University of Alberta

Relativistic Treatment of The Interactions of Electromagnetic Probes with Complex Nuclei

By
Mohammad Hedayatipoor ©

A dissertation
presented to the Faculty of Graduate Studies and Research
in partial fulfilment of the requirements for the degree
of

Doctor of Philosophy

in

Theoretical Physics
Department of Physics

Edmonton, Alberta
Spring 1997

National Library
of Canada

Acquisitions and
Bibliographic Services

395 Wellington Street
Ottawa ON K1A 0N4
Canada

Bibliothèque nationale
du Canada

Acquisitions et
services bibliographiques

395, rue Wellington
Ottawa ON K1A 0N4
Canada

Your file Votre référence

Our file Notre référence

The author has granted a non-exclusive licence allowing the National Library of Canada to reproduce, loan, distribute or sell copies of his/her thesis by any means and in any form or format, making this thesis available to interested persons.

The author retains ownership of the copyright in his/her thesis. Neither the thesis nor substantial extracts from it may be printed or otherwise reproduced with the author's permission.

L'auteur a accordé une licence non exclusive permettant à la Bibliothèque nationale du Canada de reproduire, prêter, distribuer ou vendre des copies de sa thèse de quelque manière et sous quelque forme que ce soit pour mettre des exemplaires de cette thèse à la disposition des personnes intéressées.

L'auteur conserve la propriété du droit d'auteur qui protège sa thèse. Ni la thèse ni des extraits substantiels de celle-ci ne doivent être imprimés ou autrement reproduits sans son autorisation.

0-612-21575-X

Canadä

UNIVERSITY OF ALBERTA

LIBRARY RELEASE FORM

NAME OF AUTHOR:	Mohammad Hedayatipoor
TITLE OF THESIS:	Relativistic Treatment of The Interactions of Electromagnetic Probes with Complex Nuclei
DEGREE:	Doctor of Philosophy
YEAR THE DEGREE GRANTED:	1997

Permission is hereby granted to the University of Alberta library to reproduce single copies of this thesis and to lend such copies for private, scholarly or scientific research purposes only.

The author reserves other publication rights, and neither the thesis or extensive extracts from it may be printed or otherwise reproduced without the author's written permission.

Mohammad Hedayatipoor
Department of Physics
University of Alberta
Edmonton, Alberta
T6G 2J1

Date: Jan, 17, 1997

UNIVERSITY OF ALBERTA

FACULTY OF GRADUATE STUDIES AND RESEARCH

The undersigned certify that they have read, and recommend to the Faculty of Graduate Studies and Research for acceptance, a thesis entitled "Relativistic Treatment of The Interactions of Electromagnetic Probes with Complex Nuclei" submitted by Mohammad Hedayatipoor in partial fulfilment of the requirements for the degree of Doctor of Philosophy in Theoretical Physics

Professor H.S. Sherif, Supervisor

AN Kamal
Professor A.N. Kamal

Martin Legaré
Associate Professor M. Legaré

M. R.
Professor M. Razavy

Associate Professor N.L. Rodning

M. R.
Professor Louis E. Wright, External Examiner

Date: January 9, 1997

to

my Wife

and

my Daughter.

Abstract

The interactions of electromagnetic probes with nuclei are studied. In the first part of this thesis the relationship between relativistic and nonrelativistic approaches to nucleon knock-out reactions is investigated. The relativistic amplitudes for the proton knock-out reactions (γ, p) and (e, $e'p$) on nuclei are reduced to the nonrelativistic forms using an effective Pauli reduction scheme. The reductions are carried out to second order in the inverse nucleon mass. It is found that the interaction Hamiltonians appearing in the nonrelativistic amplitude have significant dependence on the vector and scalar mean nuclear potentials. These strong medium modifications are absent in traditional nonrelativistic calculations. Detailed comparisons show that these modifications are crucial to understanding the differences between relativistic and nonrelativistic models. These differences are also examined through reduction of the relativistic Hamiltonian for the first reaction via the Foldy-Wouthuysen transformation. Similar medium modifications are obtained in this case as well. We discuss the implications of these medium modifications for the consistency of existing nonrelativistic calculations.

In the second part of this thesis, a relativistic model for photoproduction of η mesons from complex nuclei is developed. The model is used to study the exclusive reaction A($\gamma, \eta p$)A-1, leading to discrete final states in the residual nucleus. Inclusive reactions A(γ, η)X in which the η meson is the only detected particle are also studied. The ingredients of the model are: i) the nucleon wavefunctions are solutions of the Dirac wave equation with the appropriate scalar and vector strong potentials, ii) the η meson is described by solutions of the Klein-Gordon equation with appropriate optical potentials, and iii) the interactions between the fields are introduced through a covariant effective Lagrangian.

The amplitudes are used to calculate the observables for the exclusive and inclusive reactions on different target nuclei. The energy region where the $S_{11}(1535)$ resonance dominates the reaction is specified. This is the best energy region for using the η photoproduction reactions to study the properties of the above resonance in the nuclear medium. The region of phase space where the reaction has its largest cross section is also determined. Comparison with the existing nonrelativistic calculations is carried out. Detailed comparison of the inclusive reactions with the available data show that, in the energy regions studied, the quasifree η production is the main contributing process to inclusive η photoproduction reactions.

Acknowledgements

I am extremely grateful to my supervisor, Professor Helmy S. Sherif, for his continuous guidance, encouragement and the invaluable discussions in the course of this research. I wish to thank all the members of the advisory committee for their enlightening comments on my thesis. Helpful discussions with Jon I. Johansson were always invaluable sources of inspiration in all phases of this research. I am grateful to J. Ahrens, M. Benmerrouche, C. Bennhold, B. Krusche, F.X. Lee, B. Lopez Alvaredo, E. Oset, M. Roebig-Landau and M. Vineyard for helpful communications concerning their work. I am thankful to Bahman K. Darian for his assistance on Latex. I extend my appreciation to the office staff for providing an enjoyable working environment in the Physics Department. The continuing support from the Iranian Ministry of Higher Education is gratefully acknowledged. Lastly, I wish to thank my wife, Azar, without whose support, this work could not have been accomplished.

Contents

1 Introduction **1**

Bibliography 8

2 Nonrelativistic Reduction of The Relativistic Amplitude for (γ, p) Reaction on Nuclei **11**

2.1 Relativistic Direct Knock-out Mechanism 13

2.2 Effective Pauli Reduction 18

2.2.1 Formalism 18

2.2.2 Observables for (γ, p) Reaction 23

2.2.3 Results of the Effective Pauli Reduction 24

2.3 Foldy-Wouthuysen Transformation 42

2.3.1 Spin $\frac{1}{2}$ Particle Interacting with Strong and Electromagnetic Potentials 43

2.3.2 Schrödinger-like wavefunctions 46

2.3.3 Differences Between the FW and Pauli Reduction Schemes . . 48

2.3.4 Results of the FW Reduction 54

2.4 Conclusions 60

Bibliography 62

Appendix 2.A Radial and Angular Integrals 64

Appendix 2.B Observables 68

Appendix 2.C Nucleon Wavefunctions 70

3 Nonrelativistic Reduction of The (e, $e'p$) Reaction on Nuclei 73

3.1 Relativistic Amplitude for (e, $e'p$) Reactions 76

3.2 Pauli Reduction 82

3.2.1 Convergence of the Expansion 85

3.2.2 The Nonrelativistic Limit 90

3.3 Results of nonrelativistic Calculations 91

3.4 Conclusions 100

Bibliography 103

Appendix 3.A Kinematics 105

Appendix 3.B Current Operators 108

Appendix 3.C Observables 111

Appendix 3.D Factorization of The PWIA Cross section 113

4 Photoproduction of η Mesons from Complex Nuclei
I) Exclusive Reactions 117

4.1 The Reaction A(γ, ηp)A$-$1 121

4.1.1 Model Lagrangian 122

4.1.2 Reaction Amplitude 128

4.1.3 Observables 136

4.2 Results of the A(γ, ηp)A$-$1 Reactions 137

4.2.1 The ^{12}C(γ, ηp)^{11}B Reaction 142

4.2.2 The ^{16}O(γ, ηp)^{15}N Reaction 153

4.2.3 The ^{40}Ca(γ, ηp)^{39}K Reaction 156

4.3 Conclusions 160

Bibliography 162

Appendix 4.A Kinematics 165

Appendix 4.B The $\gamma + p \rightarrow \eta + p$ Reaction 167

Appendix 4.C Observables 175

Appendix 4.D Wavefunction of The η Meson 177

Appendix 4.E Approximation of The Propagators 179

5 Photoproduction of η Mesons from Complex Nuclei II) Inclusive Reactions **181**

5.1 Reaction Model 184

5.2 Results 187

5.3 Conclusions 193

Bibliography 194

Appendix 5.A Angular Integrals 195

6 Conclusions **196**

List of Figures

2.1 The Feynman diagram of the direct knock-out mechanism for the $A(\ \gamma, p\ )A-1$ reaction. The incident photon with momentum **k** is absorbed by a proton inside nucleus A and as a result the proton is ejected leaving the residual nucleus in a discrete final state. 14

2.2 Differential cross section a), and photon asymmetry b) for the reaction $^{16}O(\gamma,\ p)^{15}N$ at $E_\gamma = 60$ MeV. The final state Woods Saxon optical potentials are taken from reference [13]. The cross section data are those of Findlay and Owens [14]. Solid curve - full relativistic calculations. Dotted curve - nonrelativistic calculations using the first order Hamiltonian $H_I^{(1)}$ of equation (2.20). Dot-dashed curve - second order nonrelativistic calculations (neglecting the nuclear potentials in $H_I^{(2)}$ of equation (2.20)). These are referred to as medium-uncorrected second order calculations in the text. Dashed curve - second order nonrelativistic calculations using the full $H_I^{(2)}$. These are referred to as medium-corrected second order calculations. 28

2.3 Differential cross section (a), and photon asymmetry (b) for the reaction of Fig. 2.2 but with $E_\gamma = 100$ MeV. Curves labelled as in Fig. 2.2. 30

2.4 Differential cross section (a), and photon asymmetry (b) for the reaction of Fig. 2.2 but with $E_\gamma = 196$ MeV. The data are those of Turley *et.al* [16] Curves labelled as in Fig. 2.2. 33

2.5 Differential cross section (a), and photon asymmetry (b) for the reaction of Fig. 2.2 but with E_γ = 312 MeV. Curves labelled as in Fig. 2.2. 34

2.6 Differential cross section (a) and photon asymmetry (b) for the reaction $^{40}Ca(\gamma, p)^{39}K$ at $E_\gamma = 151 MeV$. curves labeled the same as figure (2.2). 36

2.7 Differential cross section (a) and photon asymmetry (b) for the reaction $^{40}Ca(\gamma, p)^{39}K$ at $E_\gamma = 201 MeV$. curves labeled the same as figure (2.2). 37

2.8 Differential cross section (a) and photon asymmetry (b) for the reaction $^{208}Pb(\gamma, p)^{207}Ti$ at $E_\gamma = 150 MeV$. curves labeled the same as figure (2.2). 40

2.9 Differential cross section (a) and photon asymmetry (b) for the reaction $^{208}Pb(\gamma, p)^{207}Ti$ at $E_\gamma = 257 MeV$. curves labeled the same as figure (2.2). 41

2.10 Central potentials (a) and spin-orbit potentials (b) produced in Pauli and FW schemes for a bound proton in ^{16}O. 52

2.11 Bound state wavefunctions derived in Pauli and FW schemes for a proton with quantum numbers $L_B = 1$, $J_B = 1/2$. The horizontal arrow shows the momentum transfer covered by the (γ, p) reactions for the photon energies between 196 → 312MeV. 53

2.12 Differential cross section (a), and photon asymmetry (b) for the reaction $^{16}O(\gamma,\ p)^{15}N$ at E_γ = 100 MeV. Solid curve - full relativistic calculations. Dotted curve - nonrelativistic calculations using the first order FW Hamiltonian $H_I^{(1)}$ of equation (2.46) and nucleon wavefunctions obtained from equation (2.47) using the first order and spin-orbit terms of equation (2.44). Dot-dashed curve - second order nonrelativistic FW calculations (neglecting the nuclear potentials in $H_I^{(2)'}$ from equation (2.51)), and full second order potentials to generate the wavefunctions. These are referred to as medium-uncorrected second order calculations in the text. Dashed curve - second order nonrelativistic FW calculations using the full $H_I^{(2)'}$. These are referred to as medium-corrected second order calculations. 57

2.13 Differential cross section (a), and photon asymmetry (b) for the reaction of Fig. 2.12 but with E_γ = 196 MeV. Curves labelled as in Fig. 2.12. 58

2.14 Differential cross section (a), and photon asymmetry (b) for the reaction of Fig. 2.12 but with E_γ = 312 MeV. Curves labelled as in Fig. 2.12. 59

3.1 The Feynman diagram for $A(e, e'p)A-1$ reaction 77

3.2 Observables for the reaction $^{16}O(\ e, e'p\ )^{15}N_{g.s.}$. The energy of the incident electron is 456 MeV, and the kinetic energy of the detected proton is fixed at 90 MeV with parallel kinematics. Hartree bound state wavefunctions are used [16] and the proton optical potentials are from [17]. The data are from reference [19]. (a) spectral function and (b) proton polarization. Curves are labelled according to their order in $(E+M)^{-1}$ and whether or not the medium corrections (through Dirac potentials) are included in the nuclear current operators: dotted curve – medium-uncorrected first order in $(E+M)^{-1}$; dashed curve – medium-corrected first order; dot-dashed curve – medium-uncorrected second order; dot-dot-dashed curve – medium-corrected second order; solid curve – fully relativistic calculations. 88

3.3 Observables for the reaction $^{208}Pb(\ e, e'p\ )^{207}(\ J^{\pi} = 3/2^{+}\ )$. (a) spectral function and (b) proton polarization. Curves are labelled as in figure(3.2). Potentials and data from the sources of figure (3.2). . . 89

3.4 Observables for the reaction $^{16}O(\ e, e'p\ )^{15}N_{g.s.}$. The kinematics are those of figure (3.2). Curves are labelled according to their order in $1/M$ and whether or not the Dirac potentials are included in the nuclear current operators: dotted curve – nonrelativistic calculations, medium-uncorrected first order in $(M)^{-1}$; dashed curve – medium-corrected first order; dot-dashed curve – medium-uncorrected second order; dot-dot-dashed curve – medium-corrected second order; solid curve – fully relativistic calculation. Potentials and data from the sources of figure (3.2). 93

3.5 Spectral function for $^{16}O(\ e,\ e'p\ )^{15}N_{g.s.}$. The kinematics are those of figure (3.2). Curves labelled as in figure (3.4). Potentials and data from the sources of figure (3.2). 94

3.6 Observables for $^{208}Pb(\ e,e'p\ )^{207}Tl$ where ^{207}Tl is in the $2d_{\frac{3}{2}}$ state. Curves labelled as in figure (3.4). Potentials and data from the sources of figure (3.2). 97

3.7 Observables for $^{16}O(\ e,\ e'p\ )^{15}N$ where ^{15}N is in the $1p_{\frac{1}{2}}$ state. The energy of the incident electron is 2000 MeV, and the kinetic energy of the detected proton is fixed at 400 MeV with parallel kinematics. Curves labelled as in figure (3.4). Potentials from the source of figure (3.2). 98

3.8 Asymmetry in missing momentum for $^{90}Zr(\ e,\ e'p\ )^{89}Y$ where ^{89}Y is in the $1f_{\frac{5}{2}}$ state. The energy of the incident electron is 461 MeV, and the kinetic energy of the detected proton is fixed at 100 MeV with parallel kinematics. Curves labelled as in figure (3.4). Potentials from the source of figure (3.2). 99

4.1 The Feynman diagram for an $A(\ \gamma,\eta p\ )A-1$ reaction. the incident photon with momentum **k** is absorbed by a proton inside nucleus A and as a result the proton and η meson are ejected out of the target. 122

4.2 The contributing Feynman diagrams to $A(\ \gamma,\eta p\ )A-1$ reaction. a) and b) are the s- and u-channel Born diagram respectively, c) the t-channel vector meson diagram, d) and e) are the s- and u-channel nucleon resonance poles. 123

4.3 The cross section for the $^{12}C(\ \gamma,\eta p\ )^{11}B_{g.s.}$ reaction for the regions of the phase space where the reaction has significant yield. 139

4.4 The cross section for the $^{12}C(\gamma,\eta p)^{11}B_{gs}$ reaction for the photon energies from near threshold up to 1.2 GeV. 140

4.5 Contributions of different diagrams to cross section of the $^{12}C(\gamma,\eta p)^{11}B_{gs}$ reaction at photon energies of 750 MeV. 141

4.6 Differential cross section (a), and photon asymmetry (b) for the reaction $^{12}C(\gamma,\eta p)^{11}B$ at $E_\gamma = 750$ MeV. The Hartree potentials of reference [28] are used in calculation of the bound state wavefunction. The final state energy dependent global optical potentials are taken from reference[29]. The η optical potential is the DW1 potential of Lee *et al.* [10]. Solid curve - plane wave calculations. Long dashed curve - calculations include only final state interactions of the η meson (η Distorted). Short dashed curve - calculations include only final state interactions of outgoing proton (Proton Distorted). Dotted curve - both η and proton waves are distorted (Full DW). 144

4.7 Differential cross section (a), and photon asymmetry (b) for the same reaction as figure (4.6). The final state optical potentials for the proton and the bound state potentials are fixed. Curves are shown for different choices of η optical potentials: Solid curve - DW calculations using DW1 of reference [10]. Long dashed curve - DW calculations using DW2 of reference [10]. DW calculations using the optical potential of reference [30] with the real part of the S_{11} self energy set to 50 MeV (short dashed curve), 0 Mev (dotted curve) and -50 MeV (dash-dotted curve). 146

4.8 Differential cross section (a), and photon asymmetry (b) for the same reaction as in figure (4.6) The final state optical potential for the η meson is the same as in figure (4.6). Curves are labelled for different choices of proton optical potentials: Solid curve - DW calculations using energy dependent optical potential of reference [29], long dashed curve - DW calculations using first fit of A and energy dependent optical potential of reference [29], short dashed curve - DW calculations using second fit of A and energy dependent optical potential of reference [29] and dotted curve - DW calculations using third fit of A and energy dependent optical potential of reference [29]. 148

4.9 Differential cross section (a), and photon asymmetry (b) for the same reaction as in figure (4.6) The final state optical potentials for the η meson and outgoing proton are the same as those of figure (4.6). Curves are labelled for different choices of proton bound potentials: Solid curve - DW calculations using Hartree potential of reference [28] and dashed curve - DW calculations using Woods-Saxon potential of reference [31]. 149

4.10 Differential cross section (a), and photon asymmetry (b) for the same reaction as figure (4.6). Curves are labelled as: Solid curve - relativistic PW calculations. Long dashed curve - PW calculations with the use of only upper component of the nuclear wavefunctions. Short dashed curve - nonrelativistic PW calculations of Lee *et al.* [10]. Dotted curve - relativistic DW calculations. 152

4.11 Differential cross section for the same reaction as figure (4.6). Curves are labelled as: Solid curve - DW calculations using only $S_{11}(1535)$ diagrams, labelled as S_{11}. Long dashed curve - DW calculations using all the diagrams but those of $S_{11}(1535)$ resonance, labelled as Rest. . 153

4.12 Differential cross section (a), and photon asymmetry (b) for the reaction $^{16}O(\gamma,\ \eta p)^{15}N$ at $E_\gamma = 750$ MeV. The Hartree potential of reference [28] is used in calculation of the bound state wavefunction. The final state energy dependent global optical potentials are taken from reference[29]. The η optical potential is the DW1 potential of Lee *et al.* [10]. Solid curve - plane wave calculations. Long dashed curve - calculations include only final state interactions of the η meson with nuclei (η Distorted). Short dashed curve - calculations include only final state interactions of outgoing proton (Proton Distorted). Dotted curve - both η and proton waves are distorted (DW). 155

4.13 Differential cross section (a), and photon asymmetry (b) for the reaction $^{40}Ca(\gamma,\ \eta p)^{39}K$ at $E_\gamma = 750$ MeV. The Hartree potential of reference [28] is used in the calculation of the bound state wavefunction. The final state energy dependent global optical potentials are taken from reference[29]. The η optical potential is the DW1 potential of Lee *et al.* [10]. Solid curve - plane wave calculations. Long dashed curve - calculations include only final state interactions of the η meson with nuclei (η Distorted). Short dashed curve - calculations include only final state interactions of outgoing proton (Proton Distorted). Dotted curve - both η and proton waves are distorted (DW) 158

4.14 Differential cross section (a), and photon asymmetry (b) for the same reaction as figure (4.13) The potentials are the same as those of figure (4.13). Curves are labelled as in figure (4.10). 159

4.15 The kinematics for the η photo production from nuclei. The xz plane is the reaction plane and momentum of the incoming photon defines the z axis. Direction of η meson and outgoing proton and recoil nucleus are shown by η, P and R, respectively. 166

4.16 The Feynman diagrams for an $p(\gamma,\eta)p$ reaction, the incident photon with momentum **k** is absorbed by proton and then as a result an η meson produced. 169

4.17 a) Differential cross section, b) total cross section for the η photoproduction on the proton. Coupling constants are those of table 2 of this chapter and table V of reference [6]. 174

4.18 The S-channel diagram for a half integer spin particle propagator. . . 180

5.1 Differential cross section of the $^{12}C(\gamma,\eta)X$ reaction at photon energy of a) 750 MeV,and b) 778.5 MeV. The Hartree binding potential of reference [10] is used in the calculation of the Dirac bound state wave function. The η optical potentials DW1 and DW2 of Lee *et al.* are used [3]. Solid curve - plane wave calculations. Long dashed curve - distorted wave calculations using DW1 optical potential and short dashed curve - distorted wave calculations using DW2 optical potential. Data are those of reference [7]. 189

5.2 Total cross section of the $^{12}C(\gamma,\eta)X$ reaction as a function of photon energy. The binding potential for the nucleon and the η optical potentials DW1 are from the same references as figure (5.1). The solid curve is plane wave calculation and the cross points are distorted wave calculations. Data are those of reference [7]. 190

5.3 Differential cross section of the $^{40}Ca(\gamma,\eta)X$ reaction at photon energy of a) 750 MeV and at photon energy of b) 778.5 MeV. Potentials and the data are from same references as those of figure (5.1). Curves are labelled as in figure (5.1). 191

5.4 Total cross section of the $^{40}Ca(\gamma,\eta)X$ reaction as a function of photon energy. The nucleon binding potential as well as the η optical potential DW1 are as of figure (5.1). Curves are labelled as in figure (5.2). Data are those of reference [7]. 192

Chapter 1

Introduction

Since the beginning of nuclear physics, when existence of the atomic nucleus was deduced by Rutherford from the famous experiments of α-particle scattering on a gold foil up to deep inelastic scattering experiments at Stanford by Friedman *et al.* revealing the structure of nucleons, the electromagnetic probes have always played a central role in the study of nuclear and subnuclear structures. The special role of the electromagnetic interaction in unravelling the microstructure of the world is due to the fact that (i) its properties as a classical field as well as the nature of its interaction with the constituents of nuclei (nucleons) are well known, and (ii) the electromagnetic interaction is weak enough to allow the probe to interact uniformly throughout the whole volume of the probed system, and to permit the use of lowest order perturbative treatment, resulting in simple and unique interpretations of experimental results. However, this weakness constitutes also a disadvantage: the cross sections for photoproduction and electron scattering are considerably smaller than for pure hadronic reactions.

A relativistic field theory describing a system of nucleons and mesons was introduced by Walecka. This quantum hadrodynamic model (QHD) starts from a relativistic phenomenological Lagrangian including nucleons and mesons. When it is applied to infinite nuclear matter, the meson fields are replaced with their expectation values. This replacement results in a simplified Lagrangian, the so called relativistic mean field theory (RMFT) Lagrangian [1, 2].

In addition to providing an excellent description of bulk properties of nuclear matter, RMFT has proven to be a very powerful tool for an effective microscopic study of the ground state properties of nuclei [1, 2]. It provides a unified description of the binding energy and deformation properties of nuclei and also has been used recently in a study of superheavy nuclei [3]. There are many successful relativistic phenomenological reaction models based on the RMFT, describing electromagnetic as well as hadronic interactions with nuclei. These are found to provide better descriptions of the observables, especially spin observables, than other models. [4, 5, 6, 7].

The connections of the RMFT to the effective chiral theory, derived from the fundamental theory of quantum chromodynamic, has been studied by many authors. The relation of the SU(2) × SU(2) chiral Lagrangian describing the strong interaction of the pions and nucleons to the RMFT is discussed by Gelmini *et al.* [8]. These authors show that the four nucleon terms of the chiral Lagrangian produce the same results for bulk nuclear matter as those of the Walecka mean field model. Brown and Rho obtained the parameters of the Walecka model from the chiral Lagrangian in mean field using the BR (Brown and Rho) scaling [9]. The RMFT model is also used to study chiral phase transitions [10] and chiral symmetry restoration of hadrons [11]. Aiming to merge the quantum hadrodynamics model of Walecka to effective field theory, Furnstahl *et al.* [12] introduced a chiral effective Lagrangian for nuclei. The success of the RMFT and reproduction of its results by effective theories of quantum chromodynamic encourages us to use the prescription provided by this model for the dynamics of the nucleons within the nuclear matter. The relativistic nuclear wavefunctions, in our approach to a variety of reactions, are solutions of the Dirac equation with the strong potentials derived from RMFT. These potentials for a spherical nucleus are just two functions S(r) and V(r) which transforms like mass and energy of the nucleon, respectively, and are called strong scalar and time-like vector potentials [13, 14].

In the first part of this thesis we study proton knock-out reactions using incident photon and electron beams. The interactions of the electromagnetic probes with the hadrons are described through the manifestly covariant and gauge invariant relativistic interaction Lagrangians [15].

The relativistic approach has been applied recently to the study of the knock-out mechanism for photonuclear reactions[4, 5]. The calculations result in favorable agreement with data in situations where the direct knock-out mechanism is expected to dominate. Recent nonrelativistic calculations based on more sophisticated nuclear wavefunctions have also had encouraging successes[16]. In view of these developments it is important to clarify the differences between the relativistic and nonrelativistic approaches. In particular we wish to investigate whether these approaches predict essentially the same cross sections and if so, would they lead to the same spectroscopic information? In addition, will this be the case for the spin-dependent observables?

In the nonrelativistic approach; the interaction terms are obtained from the Foldy-Wouthuysen reduction of the relativistic interaction Hamiltonian for free nucleons [17, 18], and the interacting nucleons are described via the Schrödinger wavefunctions. These wavefunctions and the above reduced interaction Hamiltonian are used to calculate the transition amplitude for the reaction [16, 19]. The success of the relativistic approach in providing better description of the spin observables than the above approach, is mainly due to the use of the Dirac wave functions for the states of the interacting nucleon. The Dirac equation is originally constructed for spin half particles, whereas for the Schrödinger equation, the spin-orbit interaction term is added manually.

In chapter II we start from the relativistic amplitude for $A(\gamma, p)A-1$ reactions and use two different nonrelativistic reduction schemes, namely Pauli and Foldy-Wouthuysen reduction schemes, to derive the nonrelativistic amplitude of the reaction. The nucleons in the reduced amplitude are described by Schrödinger-like wavefunctions. We will compare results of the reduced nonrelativistic models to the results of the relativistic one. A comparison of the two reduction schemes is also given.

It is noteworthy to comment on the main differences between photon and electron reactions or real and virtual photon processes. For real photons one has a fixed relation between energy and momentum transfer ($\vec{q}^2 = \omega^2$), whereas for the exchange of a virtual photon in electron scattering the four momentum is space-like ($\vec{q}^2 \geq \omega^2$) allowing an independent variation of energy and momentum. Real photons have only transverse polarizations whereas virtual photons have both transverse and longitudinal polarizations, allowing the charge density to contribute.

The quasifree electron scattering reactions are among the simple reactions that involve interactions of virtual photons with nuclei. An interesting aspect of the quasifree electron scattering reactions is their capability of providing information on the behavior of nuclear wavefunctions in different regions of momentum transfer to the recoil nucleus. The relativistic and nonrelativistic model calculations for quasifree electron scattering show some differences in descriptions of the observables and also the deduced spectroscopic factors [20, 21, 22, 23]. Considering the above differences, the study of the application of the relativistic and nonrelativistic approaches to the quasifree electron scattering is also of interest. This investigation is carried out in chapter III. In this chapter we apply the Pauli reduction scheme to the (e, e'p) reaction on nuclei and obtain an expansion of the relativistic amplitude which involves the two component Schrödinger-like wavefunctions. Then we show how one can recover a nonrelativistic amplitude from this expansion. We also study the role of the nuclear medium in the convergence of the expansion and the nonrelativistic amplitude above and point out the main differences between the relativistic and nonrelativistic approaches for this reaction.

In the second part of this thesis we apply the relativistic approach to the photoproduction of η mesons from complex nuclei.

The physics of the η meson has attracted considerable attention in recent years. The photo- and hadroproduction of η mesons off nucleons and nuclei at threshold is large. The π^0-η mixing is able to provide information on the mass difference of the up and down quarks. Unlike the pion whose S-wave scattering length is small and negative, the scattering length of η mesons is large and positive [24]. This large and attractive η-nucleon scattering length motivated the search for η-nucleus bound states, the so called η-mesic nuclei. Liu *et al.* [25] were the first to suggest the possible existence of such states. Their last publication in this regard concluded that, for medium and heavy nuclei ($A \geq 12$), η meson bound states are possible, but the widths of these states are larger than the difference between the energy levels [26]. Several authors have continued this theoretical investigation for different nuclei. Search for light η-mesic nuclei ($A \leq 4$) brought the lower limit for the mass number of a nucleus capable of binding an η meson, down to two, i.e. for nuclei with $A \geq 2$ there may exist quasi η bound states. However, the widths of the bound states are small only for ${}^{4}_{\eta}$He [27]. The one experiment performed so far aimed at searching of η-mesic nuclei, reported negative results [28].

The η meson is a spin and isospin zero meson, so it can only couple nucleons to their isospin $\frac{1}{2}$ resonances. Moreover there is a spin and isospin half resonance ($S_{11}(1535)$), close to the threshold of η meson production, which decays $\sim$50% of time to an η meson and a nucleon. By contrast the $S_{11}(1650)$ which has similar structure has only a decay rate of $\sim$ 1.5% to the η meson nucleon channel. This puzzle is still unsolved and presents a challenge to quark model descriptions of these resonances. Due to this selectivity, photoproduction of η mesons off nuclei is a valuable means to study the propagation and possible modification of the nucleon resonances, especially $S_{11}(1535)$, inside the nuclear medium.

The short life time of the η meson (5×10^{-19} second) excludes the possibility of having a practical η beam for scattering experiments from nuclei or other particles. Thus the study of the interaction of this meson with nuclear matter is restricted to its final state interactions. Photoproduction of η mesons off nuclei is the best candidate for such study (the electroproduction of the η meson is somewhat more complicated by comparison as it involves an off shell photon). The η meson can also be produced using hadronic beams. Photoproduction has the advantage that one of the vertices being electromagnetic whereas for the reactions involving hadronic probes, we have to deal with two hadronic vertices. However, the cross sections for latter reactions are larger than those of the former ones. Photoproduction of η mesons on nuclei can also be used to investigate photoproduction of η mesons on neutrons.

Recently Lee *et al.* have studied the photoproduction of η meson from complex nuclei and developed a quasifree DWA model for the reaction [29]. They used nonrelativistic Schrödinger wavefunctions to describe the bound and continuum nucleon and the Klein-Gordon wavefunction for the η meson. The elementary photoproduction used in this calculation is based on the use of the coupled channel isobar model for contributions from the resonances, whereas contributions of the Born and vector meson terms are calculated from the effective Lagrangian of reference [30]. Even though their model includes only contributions from the quasifree production to the reaction, these authors find good agreement with the experimental data of the inclusive reaction using a specific set of η optical potentials.

In chapter IV of this thesis we start from an effective interaction Lagrangian introduced in reference [30] and develop a relativistic model for describing photoproduction of η mesons form complex nuclei. Interacting nucleons and mesons are described by solutions of the Dirac and Klein-Gordon equations, respectively. After a general introduction of the model, we develop a model for exclusive photoproduction of η meson off different target nuclei. The contributions of each nucleon resonance, as well as the other diagrams, to the reaction, are discussed. The effects of the final state interactions of the outgoing particles with the residual nucleus are taken into account through the use of optical potentials. The sensitivity of the observables of the reaction, such as differential cross section and photon asymmetry, to the use of different potentials is studied.

Starting from the amplitude for exclusive η photoproduction, we obtain an amplitude for the inclusive photoproduction of η meson from complex nuclei. This is discussed in chapter V. The results of this model for plane wave as well as distorted wave calculations for two nuclear targets are compared with the data of the recent experiment performed at MAMI [31]. We also compare the results of our model with the work of Lee *et al.* [29].

In summary the thesis is organized as follows. The study of the Pauli and Foldy-Wouthuysen reductions of the relativistic amplitude for (γ, p) reactions on nuclei is given in chapter II. In chapter III we investigate the Pauli reduction of the relativistic amplitude for $(e, e'p)$ reactions on nuclei. We develop an exclusive model for photoproduction of η mesons form complex nuclei in chapter IV and extend the model for inclusive reactions in chapter V. Chapter VI is devoted to further discussions and our conclusions.

Bibliography

[1] J.D. Walecka, Ann. Phys. (N.Y.) **83** (1974) 491.

[2] B.D. Serot and J.D. Walecka, Advances in Nuclear Physics (J.W. Negele and E.Vogt, eds.) Vol. **16**, Plenum Press, New York (1986).

[3] G.A. Lalazissis, M.M. Sherma, P. Ring and Y.K. Gambhir, nucl-th/9608005.

[4] G.M. Lotz and H.S. Sherif, Nucl. Phys. **A537** (1992) 285; Phys. Lett. **B210** (1988) 45.

[5] J.P. McDermott, E. Rost, J.R. Shepard and C.Y. Cheung, Phys. Rev. Lett. **61** (1988) 814.

[6] J.P. McDermott, Phys. Rev. Lett. **65** (1990) 1991.

[7] B.C. Clark, R.L. Mercer and P. Schwandt, Phys .Lett. **B122** (1983) 211.

[8] G. Gelmini, B. Ritzi, Phys. Lett. **B357** (1995) 431.

[9] G. E. Brown and Mannque Rho, Nucl. Phys. **A596** (1996) 503.

[10] G. E. Brown and M. Buballa, nucl-th/9603016.

[11] J. Theis *et al.*, Phys. Rev. **D125** (1983) 2286.

[12] R.J. Furnstahl, B.D. Serot and Hua-Bin Tang, nucl-th/9608035.

[13] C.G. Horowitz and B.D. Serot, Nucl. Phys. **A368** (1986) 503.

[14] B.C. Clark, S. Hama, R.L. Mercer AIP conf. proc. N.**97**, ed: H.O. Mayer (1982)260; J. Raynal, Aust. J. Phys. **43** (1990) 9; G.Q. Li, J. Phys. **G19** (1993) 1841.

[15] James D. Bjorken and Sidney D. Drell, *Relativistic Quantum Mechanics*, McGraw-Hill Book Company (1964).

[16] J. Ryckebusch, M.Waroquier, K. Heyde and D. Ryckbosch, Phys. Lett. **B194** (1987) 453.

[17] L.L. Foldy and S.A. Wouthuysen, Phys. Rev. **78** (1950) 29.

[18] K.W. Mcvoy and L. Van Hove, Phys. Rev. **125** (1962) 1034.

[19] C.Giusti and F.D.Pacati, Lett.Nuovo Cimento **26** (1979) 622.

[20] Y. Jin, D.S. Onley and L.E. Wright, Phys. Rev. C **45** (1992) 1311.

[21] J. M. Udías, P. Sarriguren, E. Moya de Guerra, E. Garrido, and J.A. Caballero, Phys. Rev. C **48**, (1993) 2731.

[22] J. M. Udías, P. Sarriguren, E. Moya de Guerra, E. Garrido, and J.A. Caballero, Phys. Rev. C **51** , (1995) 3246.

[23] S. Boffi, C. Giusti and F.D. Pacati, Nucl. Phys. **A336** (1980) 416; Nucl. Phys. **A336** (1980) 427.

[24] B. M. K Nefkens, Few-Body Systems Suppl. **9** (1995) 193.

[25] L.C. Liu and q. Haider, Phys. Rev. **C34** (1986) 1845.

[26] H.C. Chiang, E. Oset and L.C. Liu, Phys. Rev. **C44** (1991) 738.

[27] S.A. Rakityansky, S.A. Sofianos, M. Braun, V.B. Belyaev and W. sandhas, nucl-th/9601035.

[28] R.E. Chrien *et al.*, Phys. Rev. Lett. **60** (1995) 2595.

[29] F.X. Lee, L.E Wright, C. Bennhold and L. Tiator, Nucl. Phys. **A603** (1996)345.

[30] M. Benmerrouche, Nimai C. Mukhopadhyay and J.F. Zhang, Phys. Rev. **D51** (1995) 3237.

[31] M. Roebig-Landau *et al.* Phys. Lett. **B373** (1996) 45.

Chapter 2

Nonrelativistic Reduction of The Relativistic Amplitude for (γ, p) Reaction on Nuclei [1]

Introduction

The interaction of electromagnetic probes with nuclei is valuable in investigating the nuclear matter properties. The interaction is known and its relative weakness permits the probe to interact almost uniformly through the entire nucleus; first order perturbation theory should then provide an adequate description of the process. Among these processes, the interaction of real photons with nuclei has the advantage of giving information about the high momentum behavior of nucleons inside the nucleus. The simple knock-out mechanism for the photonuclear reactions has been able to reproduce the experimental data qualitatively [1].

In the present study we concentrate on photonuclear reactions of the type A(γ, p)A-1 in which an incident photon is absorbed by the target nucleus then as a result a proton is ejected to the continuum state and the residual nucleus is left in a definite final state. There are two different approaches to calculate the observables for reactions of this type; 1) relativistic calculations in which the bound and continuum nucleons are described by Dirac wavefunctions while the nuclear current is written in the usual relativistic form[1, 2], and 2) nonrelativistic calculations based on the use of Schrödinger wavefunctions to describe the bound and continuum nucleons. In the latter case the nuclear current is obtained through a Foldy-Wouthuysen (FW) transformation of the relativistic Hamiltonian describing the interaction of a photon with a free nucleon [3, 4].

---

[1] A letter and an abbreviated version of this chapter are published in Phys. Lett. **B326** (1994) 9 and Nucl. Phys. **A 593** (1995) 377.

The results obtained from the relativistic calculations were found to be in better agreement with experimental data than those of nonrelativistic distorted wave Born approximation (DWBA) calculations [2].

Our goal in this chapter is to clarify the main differences between the relativistic and nonrelativistic calculations. We obtain the nonrelativistic amplitude from the relativistic distorted wave S-matrix through two different reduction schemes. The first of these is the Pauli reduction in which the relativistic S-matrix of the (γ, p) reaction is expressed in a form that involves Schrödinger-like wavefunctions and an effective interaction Hamiltonian. This Hamiltonian is expanded in powers of $1/(E+M)$, where M is the nucleon mass and E is its total energy. The first order terms in this expansion, in the limit $E \rightarrow M$, reproduce the form of the usual nonrelativistic amplitude. A characteristic feature of the higher order terms is the dependence of the interaction Hamiltonian on the nuclear vector and scalar potentials. The qualitative features of a similar two component reduction of the Dirac wavefunction for several generic vertices, in the presence of the nuclear interactions, has been discussed by Cooper *et al.* [5]. The emphasis in our present discussion is to present a more quantitative analysis for the case of (γ, p) reactions.

The second approach is based on the use of the Foldy-Wouthuysen transformation. The relativistic knock-out amplitude is written for a model case in which the initial bound and final continuum nucleons are described by a single Dirac Hamiltonian with real vector and scalar potentials. Through the FW reduction we are able to write a nonrelativistic limit of the amplitude to various orders in the inverse nucleon mass. Again we find that the interaction Hamiltonian is dependent on the strong nuclear potentials.

We will show that the first order nonrelativistic amplitudes obtained in both reduction schemes lead to results which are different from those of the corresponding relativistic calculations. Inclusion of the higher order corrections improves the nonrelativistic calculations only if the medium corrections (i.e. terms which involve strong potentials) are considered.

We begin section 2.1 by calculating the relativistic S-matrix describing the direct knock-out contribution to (γ, p) reactions on nuclei. In addition we provide some discussion of the Dirac equation containing strong scalar and vector potentials. In section 2.2 we discuss the formal aspects of the Pauli reduction scheme and show how the relativistic S-matrix of the (γ, p) reaction is reduced to an expansion in the inverse nucleon mass. We then show results of detailed calculations and discuss the implications of the presence of the nuclear potentials in the interaction Hamiltonian. In section 2.3 we discuss the FW transformation of a relativistic Hamiltonian describing a particle interacting with electromagnetic and strong nuclear fields, and we find the corresponding nonrelativistic amplitude to second order in the inverse nucleon mass. We discuss differences between the interaction Hamiltonians obtained through the Pauli and FW reduction schemes. The section closes with a comparison of observables calculated at different orders, and again discusses the implications of the presence of the nuclear potentials in the FW interaction Hamiltonian. Section 2.4 is devoted to conclusions.

2.1 Relativistic Direct Knock-out Mechanism

In an exclusive $A\,(\gamma, p)\,A-1$ reactions, the incident photon is absorbed by the nucleus and then as a result a proton is knocked out, leaving the residual nucleus in a definite

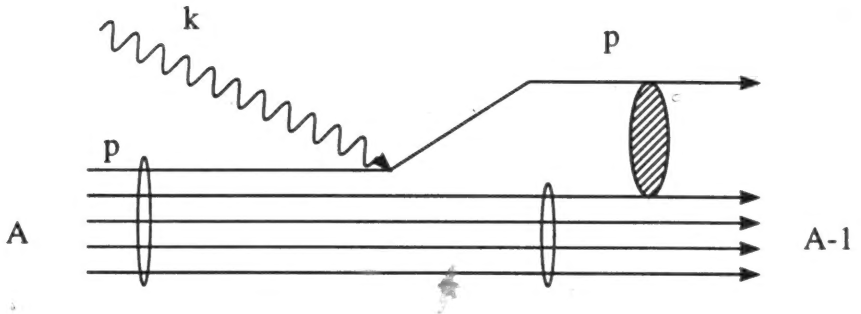

Figure 2.1: The Feynman diagram of the direct knock-out mechanism for the $A(\gamma,p)A-1$ reaction. The incident photon with momentum **k** is absorbed by a proton inside nucleus A and as a result the proton is ejected leaving the residual nucleus in a discrete final state.

final state. The assumption of the Direct knock-out model is that the incident photon is absorbed by a single bound proton which then is ejected into the continuum state. The initial bound proton is described in terms of the independent-particle shell model in which the proton moves in a potential that is the average result of its interactions with all the other nucleons, otherwise the core is essentially a spectator in the reaction. Whereas for the outgoing proton final state interactions of proton with the residual nuclei are included. Figure (2.1) shows the corresponding Feynman diagram of the reaction.

The relativistic distorted wave amplitude (S-matrix) for the reaction (γ,p) on a target nucleus in the angular momentum state $|J_iM_i\rangle$ leading to a residual nuclear state $|J_fM_f\rangle$ is obtained in first order in the interaction Hamiltonian as [1]

$$S_{fi} = \frac{-i}{(2\pi)^3}\left[\frac{1}{2\omega}\right]^{1/2}\left[\frac{M}{E_C}\right]^{1/2}$$

$$\times \sum_{J_B M_B} (J_f, J_B; M_f, M_B | J_i, M_i) \left[S_{J_i J_f}(J_B)\right]^{1/2}$$

$$\times \int \overline{\psi}^{(-)}_{S_f}(x)\, H_{em}(x)\, \psi_{J_B M_B}(x)\, d^4x, \qquad (2.1)$$

where E_C is the energy of the final state continuum proton and M is its mass. The energy of the incident photon is ω. The Dirac spinors $\psi_{J_B M_B}(x)$ and $\psi_{s_f}(x)$ describe the bound nucleon with angular momentum J_B and projection M_B, and the continuum nucleon with spin projection s_f, respectively. The Clebsch-Gordan coefficient in equation (2.1) couples the bound proton to the residual nucleus, and $S_{J_i J_f}$ is the spectroscopic factor. The electromagnetic interaction Hamiltonian is

$$H_{em}(x) = e\not{A}(x) + \frac{\kappa}{2}\frac{e}{2M}\sigma^{\mu\nu}F_{\mu\nu}(x). \qquad (2.2)$$

The 4-vector potential describing the photon is written as

$$A^{\mu}_{\xi}(x) = \epsilon^{\mu}_{\xi} e^{-ik_{\gamma}\cdot x}, \qquad (2.3)$$

where $\epsilon^{\mu}_{\xi} = (0, cos\xi, sin\xi, 0)$ is the polarization 4-vector and ξ is the corresponding polarization angle of the photon, allowing us to choose between two linear polarization states. In writing the polarization vector this way we have made a definite choice of gauge and z-axis; namely, the Coulomb gauge and the z-axis is taken along the direction of the photon momentum. Therefore the photon 4-momentum always has only two nonzero components i.e $k^{\mu}_{\gamma} = (E_{\gamma}, 0, 0, k_{\gamma})$. We thus have two linear polarization states: $\xi = 0°$ with polarization along the x-axis and $\xi = 90°$ with polarization along the y-axis.

The second term in the interaction Hamiltonian (2.2) is an anomalous magnetic moment term with $\kappa = 1.79$ for the proton. The tensor $\sigma^{\mu\nu}$ is related to the usual Dirac gamma matrices through

$$\sigma^{\mu\nu} = \frac{i}{2}\left[\gamma^{\mu},\ \gamma^{\nu}\right], \qquad (2.4)$$

and the electromagnetic field tensor $F_{\mu\nu}$ is

$$F_{\mu\nu} = \partial_\mu A_\nu - \partial_\nu A_\mu . \tag{2.5}$$

The Dirac spinors in equation (2.1) are solutions of a Dirac equation of the form

$$\{\boldsymbol{\alpha} \cdot \boldsymbol{p} + \beta [M + S(r)] + V(r)\} \psi(x) = E\psi(x), \tag{2.6}$$

where we adopt the standard representation of the 4 × 4 Dirac matrices $\{\alpha_i\}$ and β [6]. The potentials $S(r)$ and $V(r)$ are the scalar and time-like vector potentials respectively. These potentials are originally derived from the mean field Lagrangian, including nucleons, σ, and ω mesons as degrees of freedom [7]. In actual distorted wave calculations, the outgoing proton is described by a solution of the Dirac equation above, in which the scalar potential $S(r)$ and vector potential $V(r)$ are complex functions. The parameters for these potentials are determined from analyses of proton elastic scattering on nuclei [8]. For the bound nucleon, Dirac-Hartree potentials are used [9]. Detailed discussions of the Dirac equations pertaining to both bound and continuum nucleons can be found in references [1, 9].

The standard nonrelativistic amplitude for the reaction (γ, p) involves the use of Schrödinger wavefunctions to describe the initial and final nucleons. In the Pauli reduction scheme, discussed in the next section, the amplitude can be cast in a nonrelativistic form involving wavefunctions that are solutions of an equation similar to the standard Schrödinger equation. The central and spin-orbit potentials appearing in these equations are themselves functions of the Dirac scalar and vector potentials. This equation is called the Schrödinger-like wave equation and will be discussed in the rest of this section.

We write the Dirac spinors in terms of upper and lower components u and ℓ

$$\psi(x) = \begin{bmatrix} u(x) \\ \ell(x) \end{bmatrix}, \tag{2.7}$$

when this is substituted into equation (2.6), we get two coupled equations

$$\begin{aligned}
[M+S(r)-E-V(r)]\,u(x)+\boldsymbol{\sigma}\cdot\boldsymbol{p}\,\ell(x) &= 0\\
\boldsymbol{\sigma}\cdot\boldsymbol{p}\,u(x)-[M+S(r)+E-V(r)]\,\ell(x) &= 0. \qquad (2.8)
\end{aligned}$$

From the second equation we can write the lower component ℓ in terms of the upper component u as

$$\ell(x)=\frac{\boldsymbol{\sigma}\cdot\boldsymbol{p}}{E+M+S(r)-V(r)}\,u(x). \qquad (2.9)$$

Thus the Dirac spinors can be written in terms of their upper components in the form

$$\psi(x)=\begin{bmatrix} 1 \\ \dfrac{\boldsymbol{\sigma}\cdot\boldsymbol{p}}{M+E+S(r)-V(r)} \end{bmatrix} u(x). \qquad (2.10)$$

The upper component $u(x)$ of the Dirac spinor can be related to a Schrödinger-like wavefunction $\Psi_{\mathrm{Sch}}(x)$ by [10]

$$u(x)=D^{\frac{1}{2}}(r)\,\Psi_{\mathrm{Sch}}(x), \qquad (2.11)$$

and the function $D(r)$ depends on the Dirac potentials as

$$D(r)=\frac{E+M+S(r)-V(r)}{E+M}=\frac{s(r)}{E+M}. \qquad (2.12)$$

Note that for large r the nuclear potentials vanish and $D(r)$ reduces to one, so the asymptotic behavior of the upper component of the Dirac wavefunction and the Schrödinger-like wavefunction are the same. The Schrödinger-like wavefunction $\Psi_{\mathrm{Sch}}(x)$ is the solution of the Schrödinger-like equation [10].

$$\left\{-\frac{\boldsymbol{\nabla}^2}{2M}+U_{\mathrm{cent}}(r)+U_{\mathrm{so}}(r)\,\boldsymbol{\sigma}\cdot\boldsymbol{L}\right\}\Psi_{\mathrm{Sch}}=(E-M)\,\Psi_{\mathrm{Sch}}. \qquad (2.13)$$

The central and spin-orbit potentials are functions of the Dirac potentials as well as the energy of the proton, and are written explicitly as

$$U_{\mathrm{cent}}(r) = E-M+\frac{1}{2M}\left\{sd-\frac{s'}{sr}-\frac{1}{2}\frac{s''}{s}+\frac{3}{4}\frac{s'^2}{s^2}\right\}, \qquad (2.14)$$

and

$$U_{so} = -\frac{1}{2M}\frac{s'(r)}{rs(r)}. \tag{2.15}$$

In addition to the function $s(r)$ defined in equation (2.12), we have defined a function involving the difference between the nucleon's mass and energy

$$d(r) = M - E + S(r) + V(r). \tag{2.16}$$

For the bound state the "nonrelativistic" equation (2.13) provides a better description of spin orbit splitting in nuclei than the usual nonrelativistic calculations [9], and similarly for the continuum nucleon the wavefunction obtained from this equation gives an improved description of nucleon-nucleus elastic scattering data [8].

2.2 Effective Pauli Reduction

In the effective Pauli reduction scheme the relativistic distorted wave S-matrix is rewritten in terms of the above mentioned Schrödinger-like wave functions. In doing this, one finds that the interaction terms appear in an effective interaction Hamiltonian. The latter may be expanded in powers of $\frac{1}{E+M}$. The various orders can then be related, in the proper limit, to the nonrelativistic form of the amplitudes. As we show below there are, however, important differences between these and the usual nonrelativistic amplitudes.

2.2.1 Formalism

Beginning with the amplitude of equation (2.1), we write the integral in terms of Schrödinger-like wave functions using equations (2.10) and (2.11). This allows us to write

$$
\begin{aligned}
S_{fi} &= \frac{-i}{(2\pi)^3}\left[\frac{1}{2\omega}\right]^{1/2}\left[\frac{M}{E_C}\right]^{1/2} \\
&\quad \times \sum_{J_B M_B} (J_f, J_B; M_f, M_B | J_i, M_i)\left[S_{J_i J_f}(J_B)\right]^{1/2} \\
&\qquad \times \int \Psi^{\dagger(-)}_{\mathrm{Sch},s_f}(x)\, H^{eff}_{em}(x)\, \Psi_{\mathrm{Sch},J_B M_B}(x)\, d^4x, \qquad (2.17)
\end{aligned}
$$

where the Schrödinger-like wavefunctions $\Psi_{\mathrm{Sch},J_B M_B}(x)$ and $\Psi^{\dagger(-)}_{\mathrm{Sch},S_f}(x)$ describe the bound and continuum nucleons, respectively ,and the effective interaction Hamiltonian H_I^{eff} is

$$
\begin{aligned}
H_I^{eff} &= D_C^{1/2}(r)\left[1 \quad \frac{\boldsymbol{\sigma}\cdot\mathbf{p}}{M + E_C + S_C(r) - V_C(r)}\right]\gamma^0 H_{em}(x) \\
&\quad \times \left[\begin{array}{c} 1 \\ \\ \dfrac{\boldsymbol{\sigma}\cdot\mathbf{p}}{M + E_B + S_B(r) - V_B(r)} \end{array}\right] D_B^{1/2}(r), \qquad (2.18)
\end{aligned}
$$

where the labels B and C refer to the bound and continuum nucleons. The interaction Hamiltonian H_I^{eff} can be expanded in powers of $\frac{1}{E+M}$ (E is the energy of either bound or continuum nucleons) and written in the form:

$$
H_I^{eff} = H_I^{(1)} + H_I^{(2)} + \cdots . \qquad (2.19)
$$

The first and second order contributions are given by

$$
\begin{aligned}
H_I^{(1)} &= -\ \frac{e\kappa}{2M}\boldsymbol{\sigma}\cdot\nabla\times[\mathbf{A}] - e\left(\frac{1}{M+E_C} + \frac{1}{M+E_B}\right)\mathbf{A}\cdot\mathbf{p} \\
&\quad +\ ie\left(\frac{1}{M+E_C} - \frac{1}{M+E_B}\right)\boldsymbol{\sigma}\cdot\mathbf{A}\times\mathbf{p} - e\frac{\boldsymbol{\sigma}\cdot\nabla\times[\mathbf{A}]}{M+E_C}
\end{aligned}
$$

$$
\begin{aligned}
H_I^{(2)} &= -\ \frac{e}{2}\left[\frac{\kappa}{2M}\boldsymbol{\sigma}\cdot\nabla\times[\mathbf{A}] + \frac{\boldsymbol{\sigma}\cdot\mathbf{A}\boldsymbol{\sigma}\cdot\mathbf{p}}{M+E_B}\right]Q_B(r) \\
&\quad +\ e\left[Q_B(r) - \kappa\frac{1}{2M}\omega\right]\boldsymbol{\sigma}\cdot\mathbf{A}\frac{\boldsymbol{\sigma}\cdot\mathbf{p}}{M+E_B}
\end{aligned}
$$

$$
\begin{aligned}
- & \frac{e}{2}Q_C(r)\left[\frac{\kappa}{2M}\boldsymbol{\sigma}\cdot\ \boldsymbol{\nabla}\times[\mathbf{A}]+\frac{\boldsymbol{\sigma}\cdot\ \mathbf{A}\boldsymbol{\sigma}\cdot\ \mathbf{p}}{M+E_B}\right. \\
& \qquad\qquad\qquad\qquad\left.+\frac{\boldsymbol{\sigma}\cdot\ \mathbf{p}\boldsymbol{\sigma}\cdot\ \mathbf{A}}{M+E_C}\right] \\
+ & e\frac{\boldsymbol{\sigma}\cdot\ \mathbf{p}}{M+E_C}\left\{Q_C(r)-\frac{1}{2}Q_B(r)+\frac{\kappa}{2M}\omega\right\}\boldsymbol{\sigma}\cdot\ \mathbf{A},
\end{aligned}
\tag{2.20}
$$

where we have written

$$
Q_X(r)=\frac{S_X(r)-V_X(r)}{E+M}. \tag{2.21}
$$

The notation $\mathbf{O}\,[f]\cdots$ in the interaction Hamiltonians of equation (2.20) means that operator $\mathbf{O}$ acts only on function f. The appearance of the Dirac potentials, through the Q functions, in the expression for $H_I^{(2)}$ in (2.20) delineates the modification of the effective photon interaction due to the presence of the nuclear medium. This modification appears in the terms of second and higher order in the inverse of nucleon mass (more precisely the inverse of (E+M)). We will investigate the significance of this medium effect in the following section.

Using the interaction Hamiltonians (2.20) in equation (2.17) along with the nonrelativistic wavefunctions, the amplitude can be cast in a nonrelativistic form as

$$
\begin{aligned}
S_{fi}^{i} \;=\; & \frac{-i}{(2\pi)^3}\left[\frac{1}{2\omega}\right]^{1/2}\sum_{J_B M_B}(J_f,J_B;M_f,M_B|J_i,M_i)\left[S_{J_iJ_f}(J_B)\right]^{1/2} \\
& \times\int\Psi^{\dagger(-)}_{\mathrm{Sch},\mathrm{S}_f}(x)\,H_I^i(x)\,\Psi_{\mathrm{sch},J_BM_B}(x)\,d^4x,
\end{aligned}
\tag{2.22}
$$

where i refers to the highest order of the inverse of the nucleon mass in the interaction Hamiltonian which is used in the nonrelativistic amplitude, i.e.

$$
H_I^i \;=\; \sum_{l=1}^{i}H_I^{(l)} \tag{2.23}
$$

and (l) indicates the order of $\frac{1}{E+M}$ that appears in interaction Hamiltonian $H_I^{(l)}$. The amplitude (2.22), with $H_I^{(i)}=H_I^{(1)}$ in the limit $E_B,E_C\rightarrow M$ is equivalent to the standard nonrelativistic transition amplitude [11] except that the Schrödinger-like wavefunctions are used instead of the usual nonrelativistic Schrödinger wavefunctions. The amplitude obtained this way will be referred to here as the first order nonrelativistic amplitude.

The Schrödinger-like wavefunctions describing the bound nucleon can be written as

$$\Psi_{\mathrm{Sch,B}}(x) \;=\; e^{-iE_B t} f_{L_B}(r) \mathcal{Y}^{M_B}_{L_B 1/2 J_B}(\Omega), \tag{2.24}$$

while for the continuum nucleon we write

$$\begin{aligned}\Psi^{\dagger}_{\mathrm{Sch,C}}(x) \;=\; & 4\pi e^{iE_C t} \sum_{LMJ} i^{-L} Y_L^{M-S_f}(\hat{k}_f) \\ & \times (L, 1/2; M-S_f, S_f | J, M) f_{LJ}(r) \mathcal{Y}^{M\dagger}_{L1/2J}(\Omega),\end{aligned} \tag{2.25}$$

where

$$\mathcal{Y}^{M}_{L1/2J}(\Omega) \;=\; \sum_{\mu} (L, 1/2; M-\mu, \mu | J, M) Y_L^{M-\mu}(\Omega) \chi^{\mu}_{1/2}. \tag{2.26}$$

It should be emphasized here that, in order to have a standard nonrelativistic amplitude, the wavefunctions introduced in equations (2.24) and (2.25) have nonrelativistic normalization, i.e. the factor $\sqrt{\frac{E+M}{2M}}$ which comes from the Dirac spinor describing the outgoing nucleon has been set equal to one (thus a bound state wavefunction is normalized to one and the plane wave limit of the nucleon wavefunction is of the form $\Psi_{\mathrm{Sch},s_f}(x) = e^{-ik\cdot x}\chi^{s_f}_{1/2}$). In addition the factor $\sqrt{\frac{M}{E}}$ which comes from the Dirac field expansion is set equal to one (see equation (2.1)).

Using equations (2.3), (2.24) and (2.25) after evaluating the angular integration the first order amplitude can be written as

$$\begin{aligned}S^{(1)}_{fi} \;=\; & \frac{-ie}{\pi}\left[\frac{1}{2\omega}\right]^{1/2} \sum_{J_B M_B} (J_f, J_B; M_f, M_B | J_i, M_i) \left[S_{J_i J_f}(J_B)\right]^{1/2} \\ & \times \delta(E_C - E_B - \omega) \sum_{lLJ\mu} (-i)^{l+L}(2l+1)\end{aligned}$$

$$
\begin{aligned}
&\times \Big\{ (L,1/2; M_B+2\mu-S_f, S_f \mid J, M_B+2\mu) Y_L^{M_B+2\mu-S_f}(\hat{k}_f) \\
&\times \Big[\left(\frac{\kappa\omega}{2M} + \frac{\omega}{M+E_C} \right) I_{l,L,J,L_B} C^{\mu}_{l,L,J,L_B} \\
&\quad -(2\mu\cos\xi - i\sin\xi) \left(\frac{1}{M+E_C} - \frac{1}{M+E_B} \right) \\
&\qquad\qquad \times \mathcal{H}^{M_B,\mu}_{LJL_B} \big(P^{M_B,\mu,0}_{L_B+1,l,L} - \mathcal{P}^{M_B,\mu,0}_{L_B-1,l,L} \big) \Big] \\
&+ \sum_{\nu=\pm1} (L,1/2; M_B-\nu-S_f, S_f \mid J, M_B-\nu) Y_L^{M_B-\nu-S_f}(\hat{k}_f) \\
&\times \Big[\left(\frac{1}{M+E_C} + \frac{1}{M+E_B} \right) + 2\nu\mu \left(\frac{1}{M+E_C} - \frac{1}{M+E_B} \right) \Big] \\
&\times H^{M_B,\mu,\nu}_{L,J,L_B} [P^{M_B,-\mu,\nu}_{L_B+1,l,L} - \mathcal{P}^{M_B,-\mu,\nu}_{L_B-1,l,L}] \frac{\nu\cos\xi + i\sin\xi}{\sqrt{2}} \Big\}, \qquad (2.27)
\end{aligned}
$$

where I_{l,L,J,L_B}, C^{μ}_{l,L,J,L_B}, $P^{M_B,\mu,\nu}_{L_B+1,l,L}$, $\mathcal{P}^{M_B,\mu,\nu}_{L_B-1,l,L}$, $H^{M_B\mu,\nu}_{L,J,L_B}$, and $\mathcal{H}^{M_B,\mu}_{L,J,L_B}$ involve radial integrals and Clebsch-Gordan coefficients. These functions are defined in Appendix 2.A. The corresponding expression for the amplitude to second order in $\frac{1}{E+M}$ has the following form

$$
\begin{aligned}
S^{(2)}_{fi} \;=\; & \frac{-ie}{\pi} \left[\frac{1}{2\omega} \right]^{1/2} \sum_{J_B M_B} (J_f, J_B; M_f, M_B | J_i, M_i) \left[S_{J_i J_f}(J_B) \right]^{1/2} \\
& \times \delta(E_C - E_B - \omega) \sum_{lLJ\mu} (-i)^{l+L} (2l+1) \\
& \times \Big\{ (L,1/2; M_B+2\mu-S_f, S_f \mid J, M_B+2\mu) Y_L^{M_B+2\mu-S_f}(\hat{k}_f) \\
& \times [\mathcal{I}_{l,L,J,L_B} C^{\mu}_{l,L,J,L_B} + i\mathcal{H}^{M_B,\mu}_{LJL_B} (R^{M_B,\mu,0}_{L_B+1,l,L} - \mathcal{R}^{M_B,\mu,0}_{L_B-1,l,L})] \\
& \quad \times (2i\mu\cos\xi + \sin\xi) \\
& + \frac{1}{\sqrt{2}} \sum_{\nu=\pm1} (L,1/2; M_B-\nu-S_f, S_f \mid J, M_B-\nu) Y_L^{M_B-\nu-S_f}(\hat{k}_f) \\
& \times [K^{M_B,\mu,\nu}_{L_b+1,l,L} - \mathcal{K}^{M_b,\mu,\nu}_{L_b-1,l,L} + 2\nu\mu (R^{M_B,-\mu,\nu}_{L_B+1,l,L} - \mathcal{R}^{M_B,-\mu,\nu}_{L_B-1,l,L})] \\
& \quad \times H^{M_B,\mu,\nu}_{L,J,L_B} (\nu\cos\xi + i\sin\xi) \Big\} \qquad (2.28)
\end{aligned}
$$

where $\mathcal{I}_{l,L,J,L_B}$, $R^{M_B,\mu,\nu}_{L_B+1,l,L}$, $\mathcal{R}^{M_B,\mu,\nu}_{L_B-1,l,L}$, $K^{M_B,\mu,\nu}_{L_b+1,l,L}$, and $\mathcal{K}^{M_b,\mu,\nu}_{L_b-1,l,L}$ are defined in Appendix 2.A.

2.2.2 Observables for (γ, p) Reaction

Observables for the (γ, p) reaction are calculated from the S-matrix in the usual way (see Appendix 2.B for more details). To simplify the final expressions we introduce the function $Z^{i\ \xi}_{S_f,M_B}(\theta)$ which is related to the S-matrix element S^i_{fi} as follows

$$\begin{aligned} S^i_{fi} &= \frac{-ie}{\pi}\left[\frac{1}{2\omega}\right]^{1/2} \sum_{J_B M_B} (J_f, J_B; M_f, M_B | J_i, M_i) \left[S_{J_i J_f}(J_B)\right]^{1/2} \\ &\quad \times \delta(E_C - E_B - \omega) Z^{i\ \xi}_{S_f,M_b}(\theta). \end{aligned} \tag{2.29}$$

By comparing equations (2.27) and (2.29) we find that for the first order amplitude ($i = 1$), the new function can be written as

$$\begin{aligned} Z^{(1)\ \xi}_{S_f,M_B}(\theta) &= \sum_{lLJ\mu} (-i)^{l+L}(2l+1) \\ &\quad \times \Big\{ (L, 1/2; M_B + 2\mu - S_f, S_f \mid J, M_B + 2\mu) Y_L^{M_B+2\mu-S_f}(\hat{k}_f) \\ &\quad \times \Big[\left(\frac{\kappa\omega}{2M} + \frac{\omega}{M + E_C}\right) I_{l,L,J,L_B} C^{\mu}_{l,L,J,L_B} \\ &\quad -(2\mu\cos\xi - i\sin\xi)\left(\frac{1}{M + E_C} - \frac{1}{M + E_B}\right) \\ &\qquad \times \mathcal{H}^{M_B,\mu}_{LJL_B}(P^{M_B,\mu,0}_{L_B+1,l,L} - \mathcal{P}^{M_B,\mu,0}_{L_B-1,l,L})\Big] \\ &\quad + \sum_{\nu=\pm1} (L, 1/2; M_B - \nu - S_f, S_f \mid J, M_B - \nu) Y_L^{M_B-\nu-S_f}(\hat{k}_f) \\ &\quad \times \left[\left(\frac{1}{M + E_C} + \frac{1}{M + E_B}\right) + 2\nu\mu\left(\frac{1}{M + E_C} - \frac{1}{M + E_B}\right)\right] \\ &\quad \times H^{M_B,\mu,\nu}_{L,J,L_B}[P^{M_B,-\mu,\nu}_{L_B+1,l,L} - \mathcal{P}^{M_B,-\mu,\nu}_{L_B-1,l,L}] \frac{\nu\cos\xi + i\sin\xi}{\sqrt{2}} \Big\}. \end{aligned} \tag{2.30}$$

As can be seen from (2.30) $Z^{(i)\ \xi}_{S_f,M_B}(\theta)$ depends on the polarization of the incident photon ξ, spin projection of the bound nucleon M_B, spin projection of the outgoing nucleon S_f, and the direction of the outgoing nucleon θ. The resultant unpolarized cross section for the (γ, p) is

$$\frac{d\sigma^{(i)}}{d\Omega} = \frac{4\pi\alpha p E_C}{(2J_B + 1)\hbar c p_\gamma} \sum_{S_f, M_b, \xi} \mid Z^{(i)\xi}_{S_f,M_b} \mid^2 . \tag{2.31}$$

The photon asymmetry can be obtained from the cross sections for specific photon polarizations. We use the following convention [12]

$$A^{(i)}(\theta) = \frac{\frac{d\sigma^{(i)}}{d\Omega}_{\parallel} - \frac{d\sigma^{(i)}}{d\Omega}_{\perp}}{\frac{d\sigma^{(i)}}{d\Omega}_{\parallel} + \frac{d\sigma^{(i)}}{d\Omega}_{\perp}} \tag{2.32}$$

where the symbols $\parallel$ and $\perp$ refer to the cases where the polarization of the incident photon is parallel ($\xi = 0°$) and perpendicular ($\xi = 90°$) to the scattering plane respectively.

2.2.3 Results of the Effective Pauli Reduction

In the previous subsection we illustrated how the effective Pauli reduction of the relativistic amplitude for the knock-out contribution to (γ, p) reactions is performed to get an expansion in powers of $\frac{1}{E+M}$. The successive terms in this expansion can be reduced, in the appropriate limits, to forms that are equivalent to the amplitudes used in nonrelativistic calculations. This allows us to carry out quantitative comparisons between the relativistic and nonrelativistic calculations. The appropriate limits referred to above include: i) setting the nucleon total energy equal to its rest mass, ii) turning off the nuclear potentials in the second-order interaction Hamiltonian, iii) taking proper account of wavefunction normalizations. This comparison will be carried out for the differential cross section as well as the photon asymmetry at a wide range of intermediate photon energies and for three different targets.

We shall compare the following four types of calculations:

a) Full relativistic calculations using the amplitude given by equation (2.1). In the figures that follow these calculations are represented by solid curves and denoted “Relativistic”. For these calculations the relativistic (γ, p) code of Lotz has been used [13].

b) First order nonrelativistic calculations. These calculations are obtained using the amplitude $S_{fi}^{(1)}$ of equation (2.27). Note that in the limit E_B and $E_C \rightarrow M$, the interaction Hamiltonian takes on a simplified form. These calculations essentially represent the standard nonrelativistic calculations. Comparison of these results with the relativistic calculations gives the essence of the difference between the two approaches. These calculations are denoted "Pauli N.R. (First order)" in the figures. discussed in this subsection and are represented by the dotted curves.

c) The third type of calculation represents a nonrelativistic calculation carried out to second order in the inverse nucleon mass. This calculation then includes the interaction Hamiltonian $H_I^{(2)}$, but with the nuclear vector and scalar potentials set equal to zero in this Hamiltonian. This interaction will then relate to the limit in which the photon is interacting with a free nucleon. Our intention here is to clarify how much improvement in the nonrelativistic calculations can be obtained by including second order effects. We shall show that the effects are not substantial. These results are shown by the dot-dashed curves in figures presented in this subsection and are labelled "Pauli N.R. (First + Second)". We shall refer to these calculations in the text as "*medium-uncorrected*" calculations to signify the fact that they pertain to the limit in which the nuclear potentials are set to zero in the interaction Hamiltonian $H_I^{(2)}$.

d) The fourth type of calculation represents a nonrelativistic calculation using the full expression for $H_I^{(2)}$, i.e with the effect of the nuclear medium (through the presence of the potentials) taken into account. These calculations are shown by the dashed curves in figures presented in this subsection and are labelled "Pauli N.R. (First + Full Second)". They will be referred to as "*medium-corrected*" nonrelativistic calculations in the following text.

The essence of the present comparison is to show the significance of these medium effects.

Since our aim in this chapter is to compare the two theoretical models, namely relativistic and nonrelativistic, for the knock-out contribution to (γ, p) reactions, we compare the resulting observables with data just for few cases. We refer the reader to the work of Lotz and Sherif [1] for more details on the comparison of the results of the relativistic model with experiment. For the cases in which the data are presented, the "spectroscopic" factor is found by fitting the relativistic cross section (solid curve) to the data and other curves are multiplied by the same factor. In the rest of the calculated cross sections given in this chapter the spectroscopic factor takes its maximum allowable value of $(2J_B + 1)$ for both the relativistic and nonrelativistic calculations. The bound state wavefunctions used in the calculations reported in this section are generated using the Dirac-Hartree potentials of Horowitz and Serot [9].

$^{16}O\ (\ \gamma,\ p\ )\ ^{15}N$ Reaction

Figure (2.2) shows the calculated observables for the $^{16}O\ (\ \gamma,\ p\ )\ ^{15}N$ reaction at a photon energy $E_\gamma = 60$ MeV. The residual nucleus is left in its ground state which is a spin $\frac{1}{2}$ state with odd parity. The final state Woods Saxon optical potentials are taken from reference [1]. The cross section data are those of Findlay and Owens [14]. The spectroscopic factor $S = 0.908$ is found from fitting the relativistic cross section to the data. All the cross section curves, in this figure, are multiplied by this factor. Cross section curves are shown in part a) of the figure. Note the large differences between the first order nonrelativistic (dotted curve) and the relativistic calculations (solid curve). Nonrelativistic calculations lie below the relativistic calculations at all scattering angles.

Medium-uncorrected second order calculations improve the nonrelativistic calculations (dot-dashed curve)somewhat, but still there are noticeable difference between the nonrelativistic and the relativistic calculations. Medium-corrected second order calculations (dashed curve), on the other hand, bring the nonrelativistic calculations in close agreement with the relativistic ones.

Photon asymmetry calculations (Fig. 2.2-b) also show noticeable differences between the first order nonrelativistic and the relativistic calculations. These differences are more pronounced at backward angles where the nonrelativistic calculations are significantly higher than the relativistic calculations. Medium-uncorrected second order calculations move the nonrelativistic calculations even further away from the relativistic calculations, whereas the medium-corrected second order calculations bring the nonrelativistic calculations toward close agreement with the relativistic calculations. Note the large change in the second order nonrelativistic calculations, at backward angles, due to the inclusion of the nuclear medium effects.

Figure (2.3) shows similar comparisons for the reaction at a higher incident photon energy, E_γ = 100 MeV. The final state Woods Saxon optical potentials are taken from reference [13]. The cross section curves are shown in part a). Here we find large differences between the first order nonrelativistic and the relativistic calculations. Unlike the preceding case (i.e E_γ = 60 MeV) where the nonrelativistic calculations were below the relativistic ones at all scattering angles, here at forward angles the nonrelativistic calculations are almost an order of magnitude larger than the relativistic calculations, while at backward angles the nonrelativistic calculations are roughly two orders of magnitude smaller than the relativistic calculations. Medium-uncorrected second order calculations improve the nonrelativistic calculations slightly only at forward angles. Medium-corrected second order calculations, on the other hand, produce large changes in the nonrelativistic calculations. Note the large change in the magnitude for both small and large scattering angles which brings

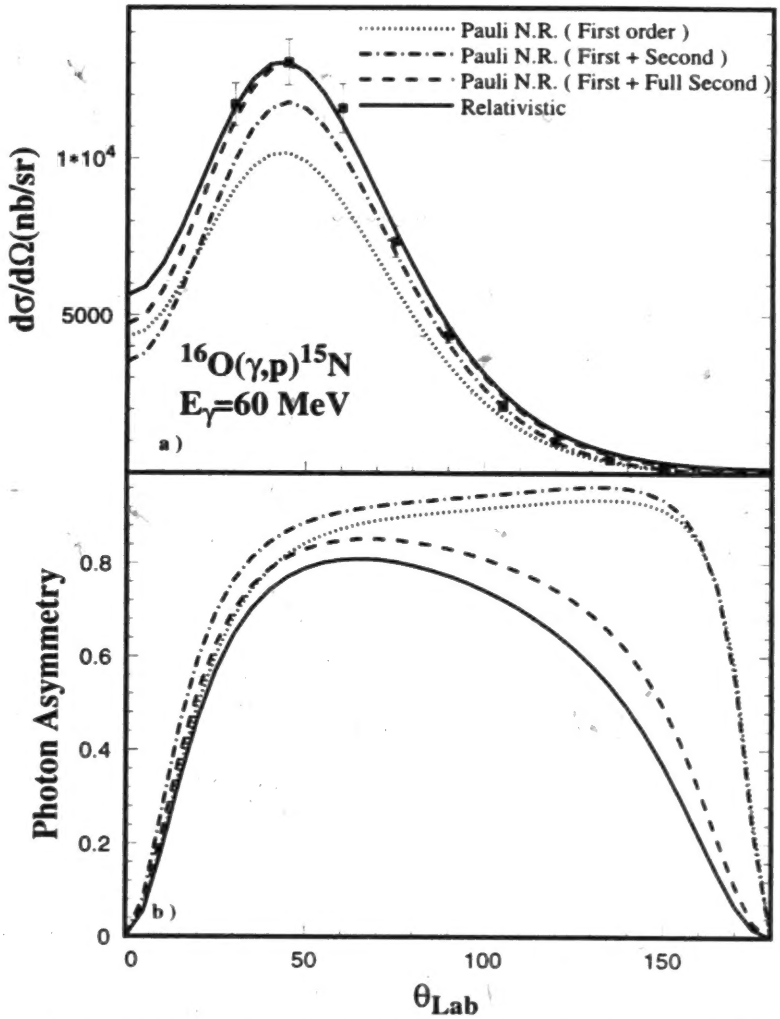

Figure 2.2: Differential cross section a), and photon asymmetry b) for the reaction $^{16}O(\gamma,\ p)^{15}N$ at $E_\gamma = 60$ MeV. The final state Woods Saxon optical potentials are taken from reference [13]. The cross section data are those of Findlay and Owens [14]. Solid curve - full relativistic calculations. Dotted curve - nonrelativistic calculations using the first order Hamiltonian $H_I^{(1)}$ of equation (2.20). Dot-dashed curve - second order nonrelativistic calculations (neglecting the nuclear potentials in $H_I^{(2)}$ of equation (2.20)). These are referred to as medium-uncorrected second order calculations in the text. Dashed curve - second order nonrelativistic calculations using the full $H_I^{(2)}$. These are referred to as medium-corrected second order calculations.

the nonrelativistic calculations into close agreement with the results of the relativistic model.

Calculations of photon asymmetry shown in Fig. (2.3-b) also exhibit noticeable differences between the first order nonrelativistic and relativistic calculations. These two calculations have different shapes and magnitudes especially for scattering angles greater than 40°. Medium-uncorrected second order calculations modify the nonrelativistic calculations slightly in magnitude while Medium-corrected second order calculations result in noticeable changes in the shape and magnitude of the nonrelativistic calculations. These changes are such that at forward angles the nonrelativistic calculations now overlap the relativistic calculations and these calculations are much closer in shape and magnitude at backward angles.

Figure (2.4) shows the same comparison as figure (2.2) at a photon energy of $E_\gamma = 196$ MeV. The final state optical potentials are those of reference [15] and the data are those of Turley *et.al* [16]. The spectroscopic factor $\mathcal{S} = 1$ is determined by matching the relativistic calculations to the data. The cross section curves of Fig. (2.4-a) show that the first order nonrelativistic calculations differ from the relativistic calculations in both shape and magnitude. The nonrelativistic calculations are above the relativistic calculations at forward angles and fall below the relativistic calculations at backward angles. Medium-uncorrected second order calculations just improve the nonrelativistic calculations at forward angles. Using the medium-corrected second order calculations brings the nonrelativistic calculations in close agreement with the relativistic calculations.

The photon asymmetry calculations (Fig. 2.4-b) also show measurable differences between the first order nonrelativistic and the relativistic calculations. Medium-uncorrected second order calculations improve the nonrelativistic results slightly at forward angles by increasing the magnitude of the asymmetry at these

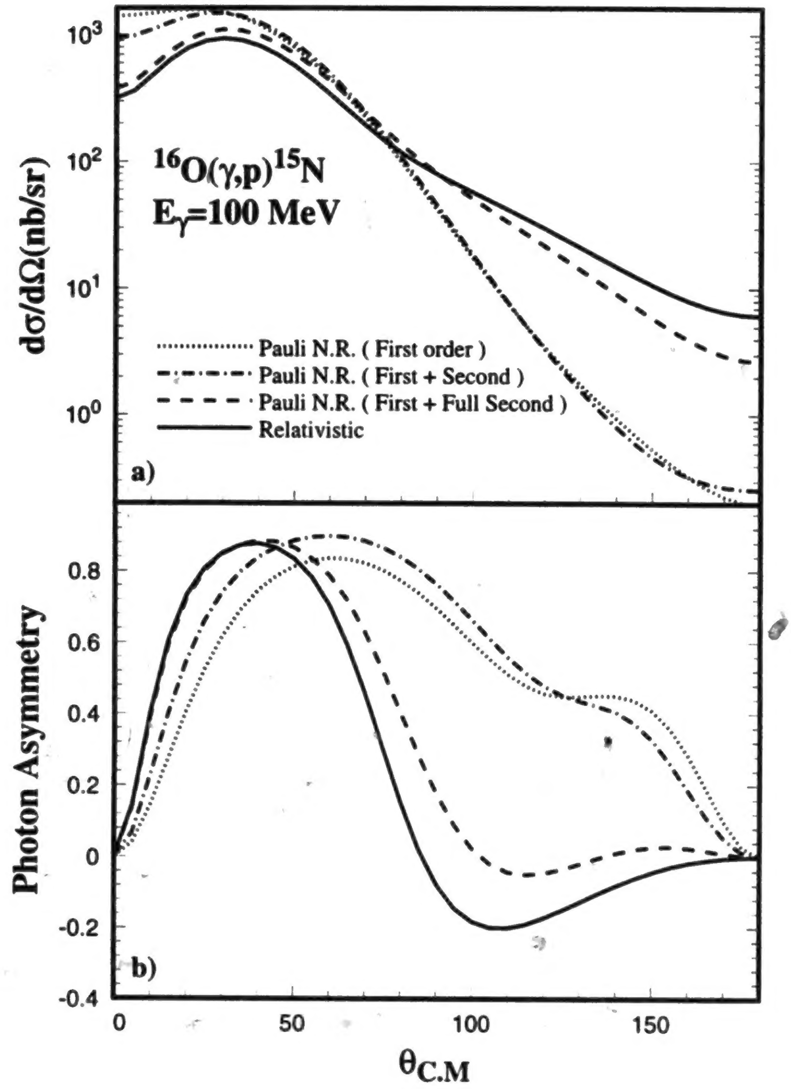

Figure 2.3: Differential cross section (a), and photon asymmetry (b) for the reaction of Fig. 2.2 but with E_γ = 100 MeV. Curves labelled as in Fig. 2.2.

angles. Medium-corrected second order calculations produce approximately the same shape and magnitude as those of the relativistic curve at all scattering angles.

Figure (2.5) shows the same comparisons for the reaction at a higher incident photon energy, $E_\gamma = 312$ MeV. The final state global optical potentials are taken from Cooper *et al.* [8]. Figure (2.5-a) shows that the cross section obtained from the first order nonrelativistic calculations has both shape and magnitude different from the results of the relativistic calculations. The nonrelativistic calculations lie above the relativistic calculations for angles smaller than 40°, whereas for other scattering angles the nonrelativistic calculations lie below the relativistic calculations by as much as an order of magnitude. Medium-uncorrected second order calculations lie closer to the relativistic calculations only at forward angles. Medium-corrected second order calculations, on the other hand, are much closer to the results of the relativistic calculations.

Calculations of the photon asymmetries of Fig.(2.5-b) show that the first order nonrelativistic results differ from the relativistic calculations in both shape and magnitude. Medium-uncorrected second order calculations improve the nonrelativistic calculations slightly at forward angles but the overall shape stays the same as that of the first order. Medium-corrected second order calculations modify the shape and magnitude of the nonrelativistic calculations at all scattering angles. It might not be clear visually that these changes bring the nonrelativistic calculations into noticeably better agreement with the relativistic ones, however a chi-squared comparison does indeed show that the medium-corrected second order calculations are closer to the relativistic calculations than medium-uncorrected second order calculations. The important point here is that there are large differences in the calculations when medium corrections are taken into account.

From the results presented for the $^{16}O\ (\ \gamma,\ p\ )\ ^{15}N$ reaction we find that the standard nonrelativistic calculations (first and second order calculations ignoring the effect of the nuclear medium in the interaction Hamiltonian) are different from the relativistic calculations. Inclusion of the medium effects, through nuclear potentials, to the interaction Hamiltonian brings the nonrelativistic results close to the results of the relativistic model.

$^{40}Ca(\gamma, p)^{39}K$ Reaction

Figure (2.6) shows the calculated observables for the $^{40}Ca(\gamma, p)^{39}K$ reaction, leading to the ground state of the residual nucleus. The shell model configuration suggests the proton is removed from a $1d_{\frac{3}{2}}$ single particle state. The incident photon energy is $E_\gamma = 151$ MeV and the final state continuum wavefunction is obtained using optical potentials from Cooper *et al* [8].

The cross section calculations (Fig.2.6-a) show that the first order nonrelativistic calculations and relativistic calculations are different in both shape and magnitude. The nonrelativistic calculations lie above the relativistic calculations at scattering angles less than 140° and then fall below the relativistic calculations at large backward angles. Medium-uncorrected second order calculations improve the nonrelativistic calculations slightly but still the nonrelativistic calculations have different shape and magnitude from the relativistic calculations .

Medium-corrected second order calculations bring the nonrelativistic calculations in close agreement with the relativistic calculations at most of the scattering angles. At large scattering angles the medium-corrected nonrelativistic calculations produce the same shape as the relativistic curve but are larger in magnitude.

Photon asymmetry calculations (Fig. 2.6-b) show that the first order nonrelativistic calculations have measurable differences from the relativistic calculations. Medium-uncorrected second order calculations improve the nonrelativistic calculation

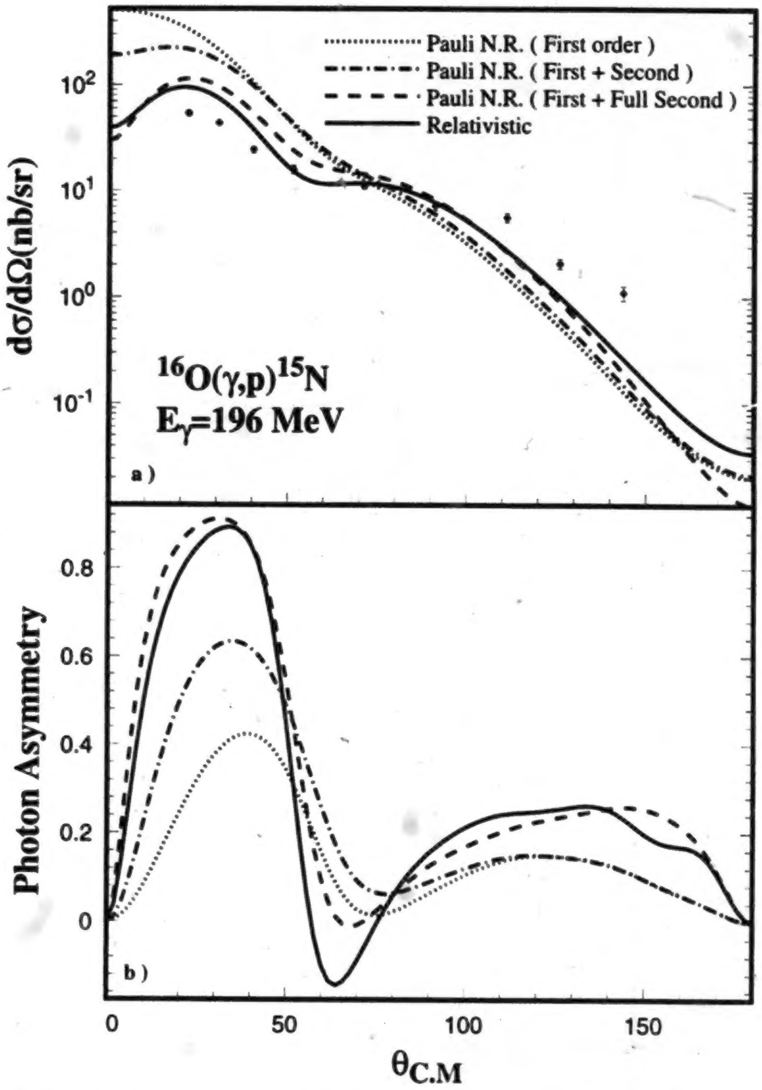

Figure 2.4: Differential cross section (a), and photon asymmetry (b) for the reaction of Fig. 2.2 but with $E_\gamma = 196$ MeV. The data are those of Turley *et.al* [16] Curves labelled as in Fig. 2.2.

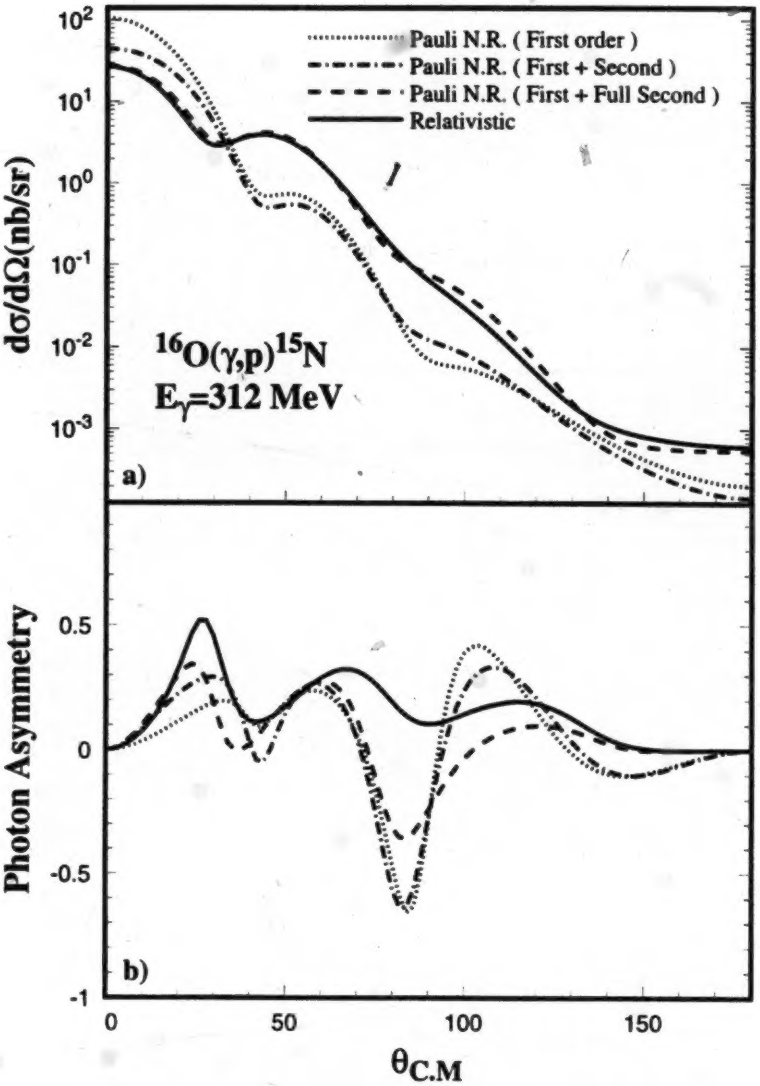

Figure 2.5: Differential cross section (a), and photon asymmetry (b) for the reaction of Fig. 2.2 but with $E_\gamma = 312$ MeV. Curves labelled as in Fig. 2.2.

slightly only at forward angles. The medium-corrected second order calculations are closer to the relativistic calculations, for forward angles of 60° and larger than about 145°.

Figure (2.7) shows the same comparison as Fig. (2.6) but at a higher incident photon energy, $E_\gamma = 201$ MeV. The final state optical potentials of Cooper *et al.* [8] are used. Nonrelativistic calculations based on the use of the first order and medium-uncorrected second order interaction terms produce results that are far from those of the relativistic calculations. On the other hand the medium-corrected second order calculations lead to a shape similar to that of the relativistic model. In addition at most scattering angles the results of the medium-corrected second order calculations are very close to those of the relativistic calculations

$^{208}Pb(\gamma, p)^{207}Ti$ Reaction

Figure (2.8) shows the calculated observables of the $^{208}Pb(\gamma, p)^{207}Ti$ reaction at an incident photon energy $E_\gamma = 150$ MeV. The final state is assumed to be a $3s_{\frac{1}{2}}$ hole state. The outgoing proton wavefunction is generated using the optical potentials of Cooper *et al* [8]. The cross section calculations of Fig.(2.8-a) show that the first order nonrelativistic calculations and the relativistic calculations are different. Note the large differences between these two calculations at forward angles. Medium-uncorrected second order calculations improve the nonrelativistic calculations somewhat at these forward as well as at backward angles. Medium-corrected second order calculations, on the other hand, overlap the relativistic calculations at most of the scattering angles.

The photon asymmetry calculations of Fig.(2.8-b) show that the relativistic and first order nonrelativistic calculations produce different results. The nonrelativistic calculations result in a bell-shaped curve whereas the relativistic calculations are

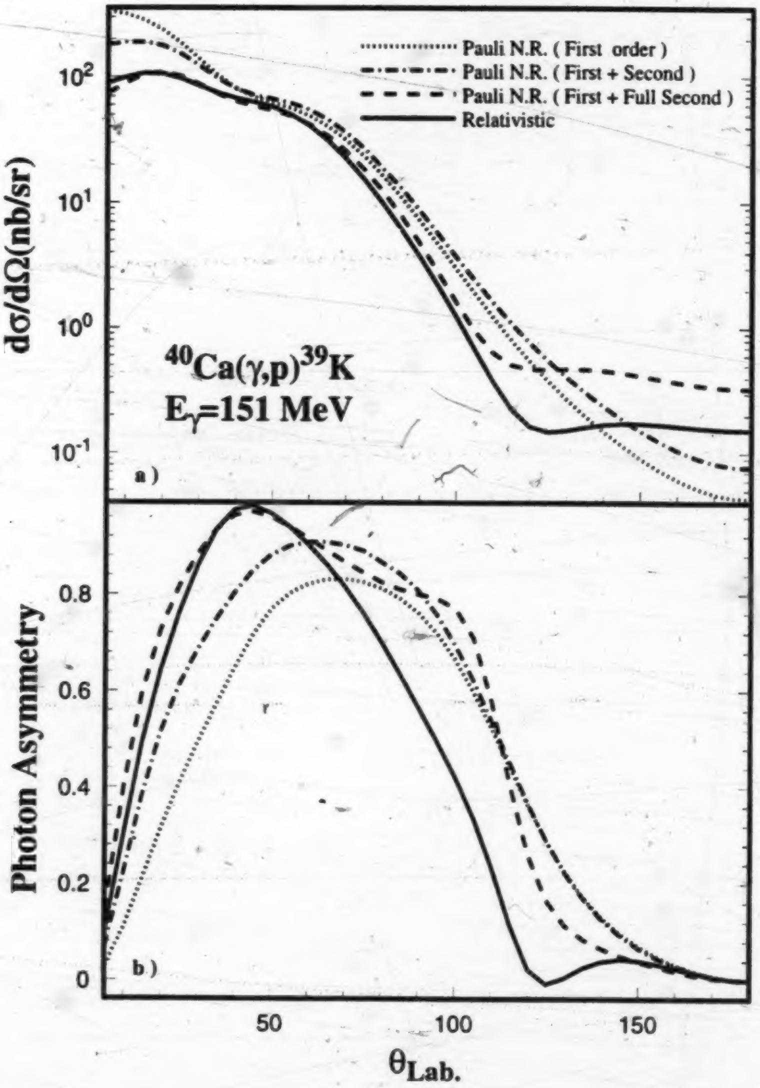

Figure 2.6: Differential cross section (a) and photon asymmetry (b) for the reaction $^{40}Ca(\ \gamma,\ p\ )^{39}K$ at $E_\gamma = 151MeV$. curves labeled the same as figure (2.2).

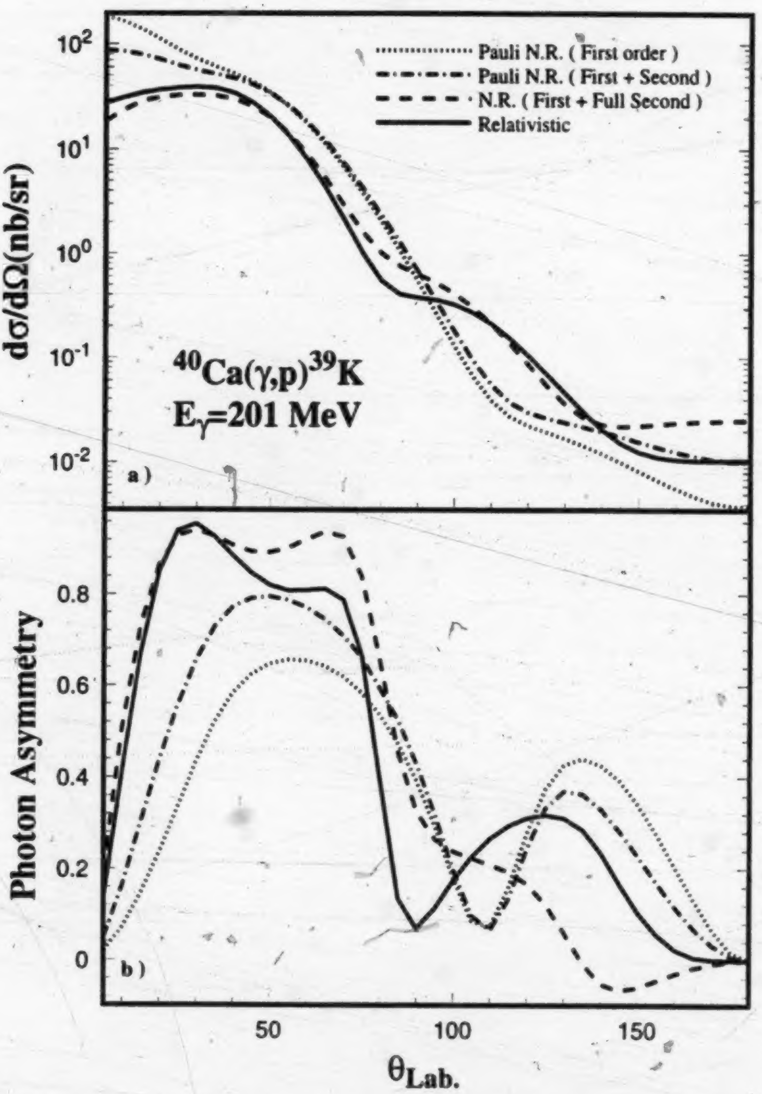

Figure 2.7: Differential cross section (a) and photon asymmetry (b) for the reaction $^{40}Ca(\ \gamma,\ p\ )^{39}K$ at $E_\gamma = 201 MeV$. curves labeled the same as figure (2.2).

not as smooth and are shifted to forward angles. Medium-uncorrected second order calculations improve the nonrelativistic calculations only at forward scattering angles. Medium-corrected second order calculations produce a curve with the same shape as the relativistic calculations. Note the changes due to the effect of the medium on the calculations specially at backward angles.

Figure (2.9) shows the same comparison as Fig. (2.8) for a higher photon energy, $E_\gamma = 257$ MeV. The qualitative features of calculated cross sections (Fig.2.9-a) are similar to those of fig.(2.8-a).

The photon asymmetry calculations of Fig.(2.9-b) show large differences between the relativistic and first order nonrelativistic calculations at backward scattering angles. Medium-uncorrected second order calculations improve the nonrelativistic calculations slightly. Medium-corrected calculations result in a large change in the nonrelativistic calculations. It is interesting that this change is toward the agreement with the relativistic calculations.

From these examples one can see that the first order nonrelativistic calculations are different from relativistic calculations. Attempts to improve the situation through the inclusion of the second order terms in which the presence of the nuclear potentials is neglected (as would normally be done in typical nonrelativistic calculations) are bound to fail in bringing the results close to the relativistic calculations. We have seen that medium-corrected second order calculations (i.e those that include the effects of the nuclear potentials on the interaction Hamiltonian) are much closer. We remind the reader that these potentials are absent in interaction terms of the usual nonrelativistic calculations even when higher order relativistic corrections are included [11]. This medium modification is the important ingredient that is missing in ordinary nonrelativistic calculations. It is this medium modification that is responsible for many of the differences between the two types of calculations. In the following section we show that the same conclusions can be reached through a procedure based on the Foldy-Wouthuysen transformation.

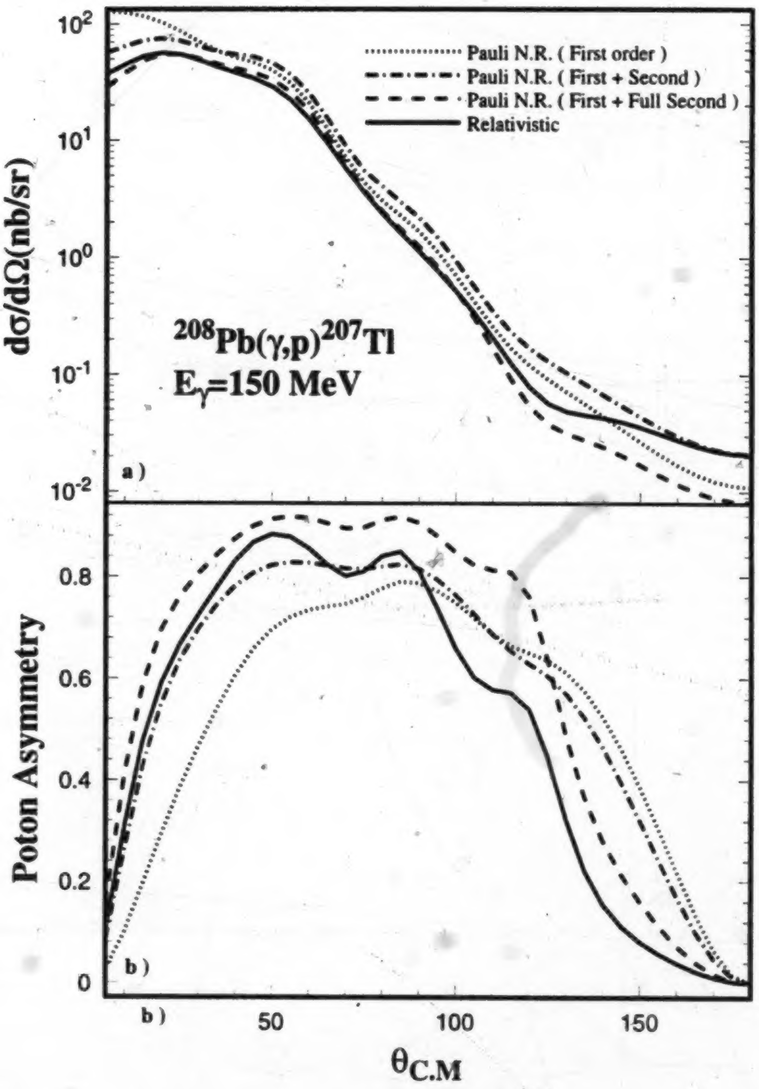

Figure 2.8: Differential cross section (a) and photon asymmetry (b) for the reaction $^{208}Pb(\ \gamma,\ p\ )^{207}Ti$ at $E_\gamma = 150 MeV$. curves labeled the same as figure (2.2).

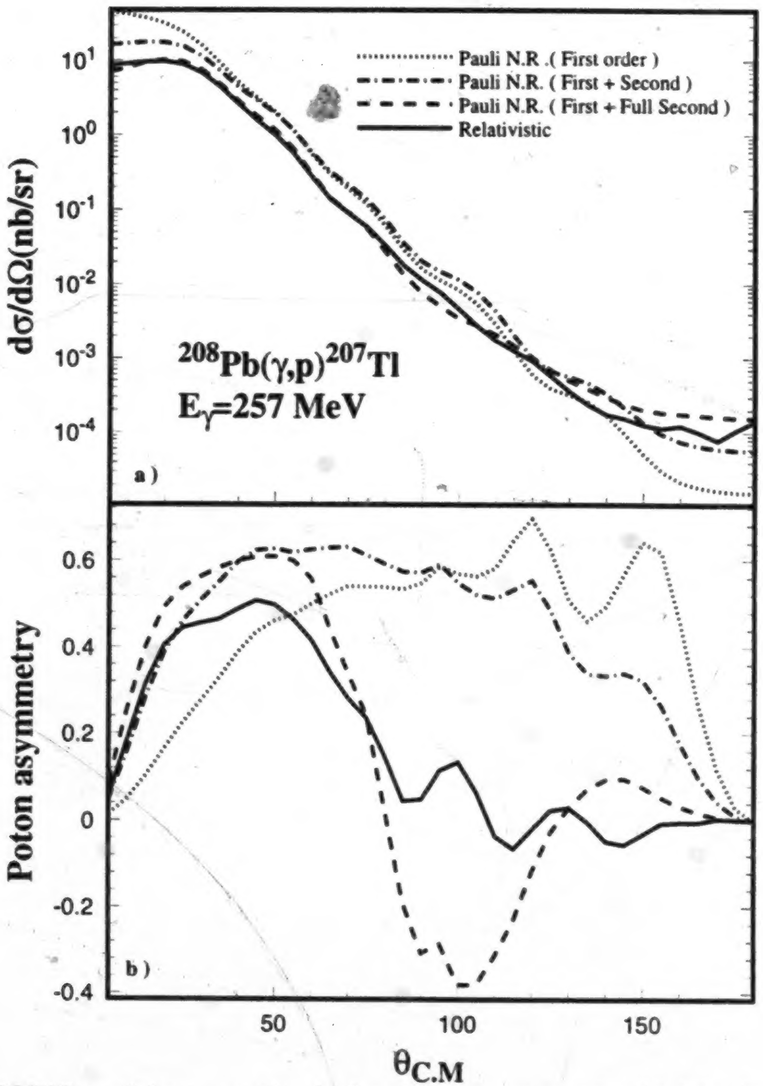

Figure 2.9: Differential cross section (a) and photon asymmetry (b) for the reaction $^{208}Pb(\ \gamma,\ p\ )^{207}Ti$ at $E_\gamma = 257 MeV$. curves labeled the same as figure (2.2).

2.3 Foldy-Wouthuysen Transformation

The Pauli nonrelativistic reduction discussed in section 2.2 is different from the nonrelativistic reduction model that is commonly used in the literature to obtain the nonrelativistic expression for the amplitude [6, 17]. Many authors construct a nonrelativistic model of photons interacting with nuclei by performing a FW transformation [18] on the relativistic Hamiltonian which involves the electromagnetic interaction with a *free* nucleon. The resulting nonrelativistic interaction Hamiltonian is then sandwiched between Schrödinger wavefunctions describing the initial and final nuclear states [17, 11]. In this section we perform a FW transformation on the relativistic Hamiltonian of a photon interacting with a nucleon *in the presence* of strong scalar and vector potentials. Similar to the effective Pauli reduction scheme studied in the previous section, we hope the study of the FW reduction also sheds more light on the role of the nuclear medium in the relativistic approach.

In the preceding discussion of the Pauli reduction scheme, our starting point was the distorted wave amplitude of equation (2.1). A feature of this amplitude for practical calculations is the use of complex vector and scalar potentials to describe the interaction of the outgoing nucleon with the residual nucleus. Moreover in the usual DWBA amplitude the initial and final states of the nucleon are described by different Hamiltonians. Since the FW transformation requires the use of only one Hamiltonian describing the whole system, it is impossible to use this reduction scheme directly for the DWBA amplitudes. We must therefore work with a model amplitude in which the bound and continuum state potentials are the same and real. It is known that such model amplitudes are inferior in their description of the data in comparison to the distorted wave amplitudes. It must be noted however that the purpose of the present investigation is not aimed at fitting data; rather we are interested in features that differentiate between the relativistic and nonrelativistic calculations. For this purpose the restricted model amplitude used here is quite appropriate.

2.3.1 Spin $\frac{1}{2}$ Particle Interacting with Strong and Electromagnetic Potentials

We first summarize the FW transformation for the case in which a Dirac particle interacts with a general field following the procedure as given in reference [6]. The results will then be applied to the case in which a nucleon interacts with an electromagnetic field while under the additional influence of strong vector and scalar potentials. The Dirac equation is written in the general form

$$i\partial_t \psi(x) = H\psi(x), \tag{2.33}$$

where the relativistic Hamiltonian H can be written in terms of even and odd operators as

$$H = \beta M + \mathcal{E} + \mathcal{O}. \tag{2.34}$$

The odd operator $\mathcal{O}$ connects the upper component of the Dirac spinor to the lower component while the even operator $\mathcal{E}$ can only connect either upper or lower components. The reduction procedure involves a unitary transformation on the wavefunction and the Hamiltonian as

$$\psi \rightarrow \psi' = U\psi \qquad\qquad H \rightarrow H' = U H U^{-1}, \tag{2.35}$$

and the unitary operator U is constructed such that all the odd operators are removed, to the desired order, from the transformed Hamiltonian. In the case of free particle one can find the exact form of operator U. On the other hand for a particle interacting with a general field one has to perform successive transformations to remove the odd terms form the Hamiltonian order by order.

Now we perform the FW transformation on the relativistic Hamiltonian (2.34) following the procedure given by Bjorken and Drell [6]. After three successive transformations we find

$$\begin{aligned} H' &= \beta M + \mathcal{E} + \frac{\beta}{2M}\mathcal{O}^2 - \frac{i}{8M^2}[\mathcal{O},\dot{\mathcal{O}}] \\ &\quad - \frac{1}{8M^2}[\mathcal{O},[\mathcal{O},\mathcal{E}]] - \frac{\beta}{8M^3}\mathcal{O}^4. \end{aligned} \tag{2.36}$$

(For simplicity the transformed Hamiltonian is denoted H', this is in fact the same as the Hamiltonian H''' in reference [6]), This result applies to any pair of even and odd operators. We are interested here in a transformed Hamiltonian containing terms which are even up to second order in the inverse of the nucleon mass so we will eventually drop the last term in equation (2.36).

The relativistic Hamiltonian for a nucleon interacting with an external electromagnetic field while under the influence of the strong vector and scalar nuclear potentials, can be written as

$$H = \boldsymbol{\alpha}\cdot\boldsymbol{\pi} + \beta\,[M + S(r)] + V(r) + \frac{e\kappa}{4M}\beta\sigma^{\mu\nu}F_{\mu\nu}, \tag{2.37}$$

where $\boldsymbol{\pi} = \mathbf{p} - e\mathbf{A}$. The above Hamiltonian, with the use of Coulomb gauge, can be written in terms of the electric and magnetic fields $\mathbf{E}$ and $\mathbf{B}$ as

$$H = \boldsymbol{\alpha}\cdot\boldsymbol{\pi} + \beta\,[M + S(r)] + V(r) + \frac{i\kappa e}{2M}(\boldsymbol{\gamma}\cdot\ \mathbf{E} + i\boldsymbol{\Sigma}\cdot\ \mathbf{B})\,, \tag{2.38}$$

where we have defined

$$\boldsymbol{\Sigma}\ = \beta\boldsymbol{\sigma}\ . \tag{2.39}$$

We rewrite the Hamiltonian (2.38) in terms of even and odd operators as in equation (2.34). In this case the even and odd operators are

$$\mathcal{E}\ =\ \beta S(r) + V(r) - \frac{\kappa e}{2M}\boldsymbol{\Sigma}\cdot\ \mathbf{B}, \tag{2.40}$$

and

$$\mathcal{O} = \boldsymbol{\alpha} \cdot \boldsymbol{\pi} + \frac{ie\kappa}{2M} \boldsymbol{\gamma} \cdot \boldsymbol{E}. \tag{2.41}$$

These even and odd operators are used in equation (2.36) in order to get the FW transformed Hamiltonian for a nucleon interacting with electromagnetic and strong potentials. The resulting Hamiltonian to second order in the inverse of the nucleon mass is a 4 × 4 block diagonal matrix

$$H' = \begin{bmatrix} H'_{11} & 0 \\ 0 & H'_{22} \end{bmatrix}. \tag{2.42}$$

The upper left element of this matrix (H'_{11}) corresponds to the transformed Hamiltonian for positive energy solutions of the Dirac equation. For the nonrelativistic limit we will use this part of the Hamiltonian which we write as

$$H'_{11} = H_0 + H_I, \tag{2.43}$$

where H_0 involves strong potentials whereas H_I carries both strong and electromagnetic interactions: we will treat the latter as a perturbation on the former. H_0 can be written to second order in $1/M$ as

$$\begin{aligned} H_0 &= \frac{\mathbf{p}^2}{2M} + M + S(r) + V(r) \\ &\quad - \frac{1}{4M^2 r} [S'(r) - V'(r)] \boldsymbol{\sigma} \cdot \mathbf{L} \\ &\quad - \frac{1}{2M^2} \left\{ S(r)\mathbf{p}^2 + \mathbf{p}[S(r)] \cdot \mathbf{p} + \frac{\mathbf{p}^2 [V(r) + S(r)]}{4} \right\}. \end{aligned} \tag{2.44}$$

The interaction Hamiltonian is written in orders of $1/M$ as

$$H_I = H_I^{(1)} + H_I^{(2)} + \cdots, \tag{2.45}$$

where for the first and second orders we have

$$H_I^{(1)} = -\frac{e}{M} \mathbf{A} \cdot \mathbf{p} - \frac{e}{2M} (1 + \kappa) \boldsymbol{\sigma} \cdot (\boldsymbol{\nabla} \times \mathbf{A}),$$

$$
\begin{aligned}
H_I^{(2)} \;=\; & \frac{e\omega}{8M^2}(1+2\kappa)\Big\{\boldsymbol{\sigma}\cdot\,\boldsymbol{\nabla}\,\times[A\,] - 2i\boldsymbol{\sigma}\cdot\,\mathbf{A}\times\mathbf{p}\Big\} \\
& +\frac{e}{4M^2}\Big\{2S(r)\mathbf{A}\cdot\mathbf{p} + 2\mathbf{A}\cdot\mathbf{p}S(r) + 2S(r)\boldsymbol{\sigma}\cdot\,\boldsymbol{\nabla}\,\times[\mathbf{A}] \\
& \qquad +\boldsymbol{\sigma}\cdot\,\mathbf{A}\times\,\boldsymbol{\nabla}\,[V(r)-S(r)] \\
& \qquad -\Big(V(r)-S(r)\Big)\boldsymbol{\sigma}\cdot\,\boldsymbol{\nabla}\,\times[\mathbf{A}]\Big\}, \qquad (2.46)
\end{aligned}
$$

where as before the notation $\mathbf{O}\,[f]\cdots$ means that operator $\mathbf{O}$ operates only on function f. From equation (2.46) we can see the first order part is not effected by the presence of the nuclear potentials. On the other hand the second order interaction Hamiltonian $H_I^{(2)}$ shows dependence on the vector and scalar potentials and their derivatives. Note the appearance of the difference between vector and scalar potentials as well as the their derivative in the two last terms of equation (2.46). Recall that the strong vector and scalar potentials have opposite sign. Now to calculate the FW amplitude we need the nonrelativistic wavefunctions. The calculations of these wavefunctions are given in the following subsection.

2.3.2 Schrödinger-like wavefunctions

The wavefunctions describing either the bound or continuum nucleons are obtained by solving the equation

$$H_0\Psi(\mathbf{r}) = E\Psi(\mathbf{r}), \qquad (2.47)$$

where H_0 is the Hamiltonian (2.44) containing terms to second order in $1/M$, and E is the total energy of the nucleon. Note that H_0 contains a first derivative term which can be eliminated using the transformation

$$\Psi_{\text{Sch}}(\mathbf{r}) = D_{\text{FW}}^{\frac{1}{2}}(r)\Psi(\mathbf{r}), \qquad (2.48)$$

where $D_{\text{FW}} = 1 - \frac{S(r)}{M}$. With this choice of D_{FW}, the two functions $\Psi(\mathbf{r})$ and $\Psi_{\text{Sch}}(\mathbf{r})$ have the same asymptotic form. After this transformation the wave equation (2.47) takes the form of the Schrödinger-like equation (2.13). The central and spin-orbit potentials in the present case are

$$\begin{aligned} U_{\text{cent}}(r) = \quad & \frac{1}{D_{\text{FW}}}\left\{S(r) + V(r) + \frac{1}{4M^2 r}\left[S'(r) + V'(r)\right] \right. \\ & \qquad\qquad \left. + \frac{1}{8M^2}\left[S''(r) + V''(r)\right]\right\} \\ & +(E - M)\left\{1 - \frac{1}{D_{\text{FW}}(r)}\right\} \\ & + \frac{1}{2Mr}\frac{D'_{\text{FW}}(r)}{D_{\text{FW}}(r)} + \frac{1}{4M}\frac{D''_{\text{FW}}(r)}{D_{\text{FW}}(r)} - \frac{1}{8M}\left(\frac{D'_{\text{FW}}(r)}{D_{\text{FW}}(r)}\right)^2, \\ U_{\text{so}}(r) = \quad & \frac{1}{D_{\text{FW}}(r)}\left\{-\frac{1}{4M^2 r}\left[S'(r) - V'(r)\right]\right\}. \end{aligned} \tag{2.49}$$

Having found the nonrelativistic effective interaction Hamiltonian and the Schrödinger-like wave equation for the initial and final nucleons, we are able to construct the nonrelativistic amplitude with all its ingredients are derived consistently from FW reduction scheme. The nonrelativistic amplitude for the knock-out contribution to the (γ, p) reaction at the desired order of $1/M$ takes the same form as given in equation (2.22). Note however that the second order amplitude obtained through the FW scheme involves wavefunctions which are solutions of equation (2.47). As we have seen above, this equation does not have the form of the usual Schrödinger wave equation because it contains a first order derivative of the wavefunction. To be consistent with the usual nonrelativistic formalism we rewrite the second order amplitude in terms of the Schrödinger-like wavefunctions $\Psi_{\text{Sch}}(\mathbf{r})$ introduced in equation (2.48). This requires that the interaction Hamiltonian be modified to

$$H'_I = D_{\text{FW}}^{-\frac{1}{2}} H_I D_{\text{FW}}^{-\frac{1}{2}}. \tag{2.50}$$

With this modification the first order terms in the interaction Hamiltonian will remain the same as $H_I^{(1)}$ in (2.46), while the second order terms in the interaction Hamiltonian become

$$
\begin{aligned}
H_I^{(2)'} &= \frac{e\omega}{8M^2}(1+2\kappa)\{\boldsymbol{\sigma}\cdot\ \boldsymbol{\nabla}\ \times[A\,] - 2\boldsymbol{\sigma}\cdot\ \mathbf{A}\times\boldsymbol{\nabla}\ \} \\
&\quad -\frac{e}{4M^2}\Big\{2\kappa S(r)\boldsymbol{\sigma}\cdot\ \boldsymbol{\nabla}\ \times[\mathbf{A}] + \boldsymbol{\sigma}\cdot\ \mathbf{A}\times\boldsymbol{\nabla}\,[V(r)-S(r)] \\
&\quad -\Big(V(r)-S(r)\Big)\boldsymbol{\sigma}\cdot\ \boldsymbol{\nabla}\ \times[\mathbf{A}]\Big\}.
\end{aligned}
\tag{2.51}
$$

The calculations of the amplitudes proceed in the same manner discussed in section 2.2. In particular the amplitude has the same form as that of equation (2.22), but now the interaction Hamiltonian $H_I^{(1)}$ is given by equation (2.46) and interaction Hamiltonian $H_I^{(2)}$ is that of equation (2.51) while the wavefunctions are solutions of a Schrödinger-like equation using the central and spin-orbit potentials of equation (2.49). Note that at first order the FW formalism does not produce an acceptable nucleon wavefunction since there is only a central potential and no spin-orbit potential, see equation (2.44).

2.3.3 Differences Between the FW and Pauli Reduction Schemes

The Pauli reduction scheme begins with the relativistic distorted wave amplitude in which the initial and final nucleons are described by Dirac wavefunctions. These are solutions of the Dirac wave equation (2.6) with different strong potentials for bound and continuum nucleons. The Pauli reduction procedure results in an expansion for the amplitude which involve Schrödinger-like wavefunctions. These wavefunctions are solutions of the Schrödinger-like equation (2.13) with central and spin-orbit potentials which in turn, are functions of the Dirac potentials $S(r)$ and $V(r)$.

The FW amplitude is constructed from the interaction Hamiltonian H_I^i along with the same Schrödinger-like wavefunctions for the initial bound and final continuum nucleons. Due to the unrealistic wavefunction used to describe the continuum nucleon, the FW calculations provide only a toy model which will be used to study the differences between the relativistic and nonrelativistic calculations.

The above statements refer to one basic difference between the two schemes. Unlike the Pauli reduction in which the wavefunctions describing nucleons are the same in all the calculations of different orders, the FW transformation involves nucleon wavefunctions that are changed in each order of calculation due to the contribution of different terms to the wave equation. Differences between these two reduction formalisms in the free nucleon limit have been studied by Fearing *et al.* [19]. They find that for the interaction of a real photon with a free particle at first order in the coupling constant the FW and Pauli reductions produce the same nonrelativistic interaction Hamiltonian.

We now discuss the differences between the Hamiltonians appearing in the two reduction schemes. In order to make instructive comparisons between the Pauli and FW Hamiltonians we need to simplify the Hamiltonians obtained through the Pauli reduction scheme of section 2.2. First the potentials describing the initial and final nucleons are taken to be the same. In addition, the energies of the bound and continuum nucleons are replaced by the nucleon mass in the Pauli interaction Hamiltonians. In this limit the first order terms in the FW and Pauli interaction Hamiltonians are exactly the same. Differences will appear in terms of order $\frac{1}{M^2}$ and higher. The difference between the interaction terms of the two schemes up to second order, with the above modifications of H_I^{Pauli}, is

$$\begin{aligned} H_I^{\mathrm{FW}} - H_I^{\mathrm{Pauli}} &= \frac{e\omega}{8M^2}\{\boldsymbol{\sigma}\cdot(\boldsymbol{\nabla}\times\boldsymbol{A}) - 2\boldsymbol{\sigma}\cdot(\mathbf{A}\times\boldsymbol{\nabla})\} \\ &\quad -\frac{e\kappa}{4M^2}\{[S(r)+V(r)]\,\boldsymbol{\sigma}\cdot(\boldsymbol{\nabla}\times\mathbf{A})\}\,. \end{aligned} \tag{2.52}$$

In the special case describing the interaction of a photon with a free nucleon, i.e in the limit when the strong potentials $S(r)$ and $V(r)$ are set equal to zero, equation (2.52) agrees with the results of Fearing *et al.* [19]. Detailed calculations show that the first term on the right hand side of equation (2.52) is very small for photon energies less than a few hundred MeV, but becomes more important at higher energies. The second term involves the sum of scalar and vector potentials. At the origin the sum of these potentials is about -100 MeV (the potentials are of opposite sign). Since this gets divided by the square of the nucleon mass, it turns out that the second term on the right hand side of the above equation also makes only a small contribution to the transition amplitude. Thus the differences between the FW and Pauli interaction Hamiltonians (in the limit imposed) appear to be small if we restrict ourselves to second order in the inverse nucleon mass.

In Appendix 2.C we give some details concerning the differences found between the potentials which generate the wavefunctions used in both schemes. Here we give a short outline. If we set $\frac{S(r)}{M} \approx -\frac{1}{3}$ (the scalar potential inside the nucleus is ~ 300 MeV) in the denominator of the spin-orbit terms, the Pauli spin-orbit potential (2.15) is approximately twice as large as the FW spin-orbit (2.49) potential. The leading terms in both central potentials are

$$\begin{aligned} U^{\text{FW}}_{\text{cent}} &\cong \frac{3}{4}\left[S(r) + V(r)\right] \\ U^{\text{Pauli}}_{\text{cent}} &\cong \frac{2}{3}\left[S(r) + V(r)\right] . \end{aligned} \tag{2.53}$$

and difference between the FW and Pauli central potential is

$$U^{\text{FW}}_{\text{cent}} - U^{\text{Pauli}}_{\text{cent}} = -\frac{1}{8M^3} S'^{\,2}(r) - \frac{3}{32M^3}\left[S'(r) - V'(r)\right]^2 \tag{2.54}$$

The differences appear in terms of order $\frac{1}{M^3}$ and higher. Figure (2.10) shows the central and spin-orbit potentials derived in both schemes for a bound proton in ^{16}O. In agreement with our analytic expressions for the leading terms in the central potentials i.e equation (2.53), Fig. (2.10-a) shows that the FW central potential is deeper than the Pauli central potential.

Fig. (2.10-b) shows relative size of the spin-orbit potentials in the two schemes. Note that as indicated above, the Pauli-spin-orbit potential is approximately two times larger than the FW spin-orbit potential at the center and surface of the nucleus.

The bound state wavefunctions for a proton with quantum numbers $L_B = 1$, $J_B = 1/2$, bound to ^{16}O, are shown in (2.11). Fig. (2.11-a) shows that the FW wavefunction is larger than the Pauli wavefunction at short distances. This is because the FW central potential is deeper than the Pauli potential in the interior region and hence the wavefunction is shifted more towards the interior of the nucleus.

The FW wavefunction leads to a binding energy of $\sim$ 13 MeV for the aforementioned state. This is larger than the one found from Pauli wavefunctions (i.e $\sim$ 9 MeV). This difference is mostly also due to the differences between the central potentials derived in the two schemes. Fig. (2.11-b) presents the wavefunctions as a function of momentum transfer. We should stress that in the range of momentum transfer covered by (γ, p) reactions at intermediate energies, these two wavefunctions are considerably different. The momentum transfer region studied by (γ, p) reactions for photon energies between 196 → 312 Mev is shown by the arrow in Fig. (2.11-b).

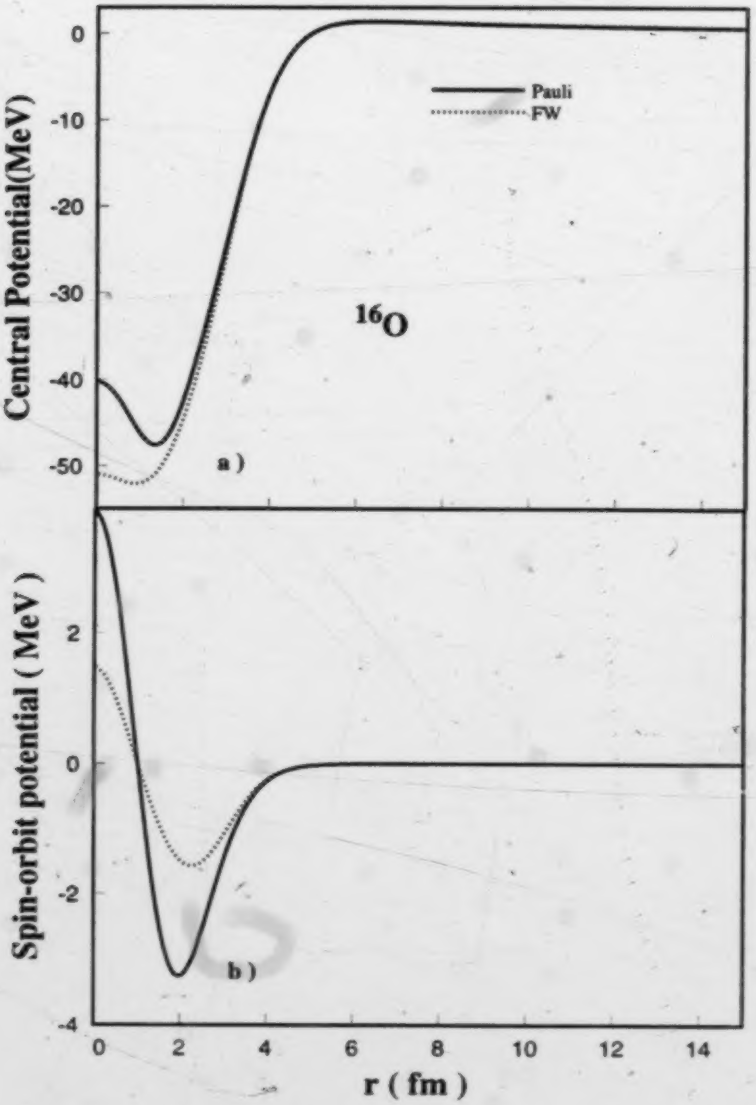

Figure 2.10: Central potentials (a) and spin-orbit potentials (b) produced in Pauli and FW schemes for a bound proton in ^{16}O.

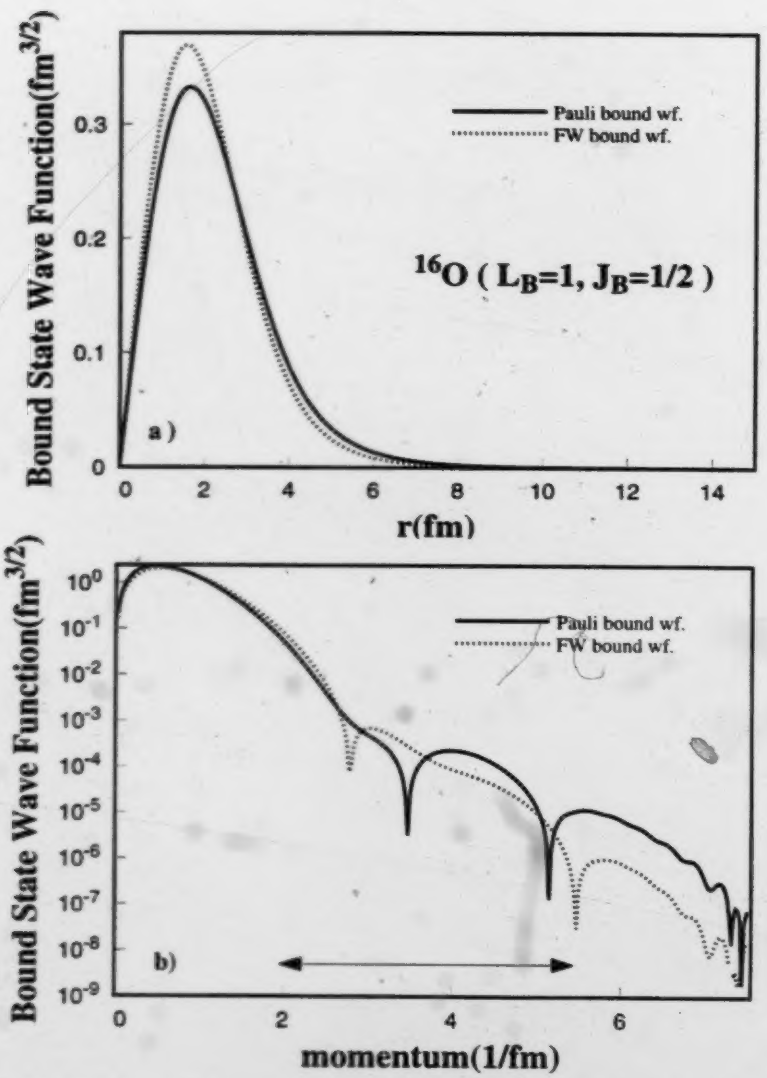

Figure 2.11: Bound state wavefunctions derived in Pauli and FW schemes for a proton with quantum numbers $L_B = 1$, $J_B = 1/2$. The horizontal arrow shows the momentum transfer covered by the $(\gamma,\ p)$ reactions for the photon energies between 196 → 312MeV.

2.3.4 Results of the FW Reduction

In this section we compare the theoretical results of the relativistic approach with those of the nonrelativistic amplitudes obtained through FW reduction. The results are shown for three different incident photon energies. As in the Pauli discussion of section 2.2.3 we present three different types of nonrelativistic calculations, namely: first order, medium-uncorrected second order and medium-corrected second order. Recall that in the first order nonrelativistic calculations the wavefunctions are solutions of equation (2.47), ignoring all the second order terms in H_0 (equation (2.44)) except for the spin-orbit potential. The spin-orbit potential is borrowed from the second order and used with the first order terms to get nucleon wavefunctions which are at least marginally realistic.

In the second order calculations the wavefunctions are obtained from equation (2.47) with all the first and second order terms in H_0 included. The Hartree potentials used in all calculations (relativistic and nonrelativistic) are from reference [9]. The graphs discussed in this section are labeled as in the Pauli discussion of section 2.2.3 except for an obvious change of notation.

Figure (2.12) shows the calculated observables for the $^{16}O\ (\gamma,p)\ ^{15}N$ reaction for a photon of energy $E_\gamma = 100$ MeV. Figure (2.12-a) shows the cross sections. At small angles the first order nonrelativistic calculations (dotted curve) are about an order of magnitude lower than the relativistic calculations (solid curve), while for large angles the first order calculations lie above the relativistic calculations. Medium-uncorrected second order calculations (dot-dashed curve; labelled First + Second) show substantial increase in the magnitude of the cross sections at small scattering angles as well as some change in the shape of the resulting curve. Medium-corrected second order calculations (dashed curve; labelled First + Full Second) produce a noticeable change in the cross sections at backward angles.

The photon asymmetry calculations of Fig. (2.12-b) also show noticeable differences between the first order nonrelativistic and relativistic calculations at backward angles. Medium-uncorrected second order calculations produce a change in the magnitude and the shape of the asymmetry for scattering angles greater than 80°. Medium-corrected second order calculations produce a shift towards larger angles resulting in a qualitatively similar shape to that of the relativistic calculations.

Figure (2.13) shows the observables for the same reaction as Fig. (2.12) but the photon energy in this case is $E_\gamma = 196$ MeV. The cross section results are shown in Fig. (2.13-a), where we note that the first order nonrelativistic calculations are generally lower than the relativistic calculations by one to two orders of magnitude. They also fail to reproduce the dip near mid-angles. Second order calculations lead to a drastic change in the cross section with large differences due to medium corrections at both forward and backward angles. Medium-corrected second order calculations are in noticeably closer agreement with relativistic calculations compared to the medium-uncorrected ones.

Similar features are observed for the photon asymmetry calculations (Fig. (2.13-b)). Here again we notice large differences between the relativistic and first-order nonrelativistic calculations. Large differences also exist between medium-corrected and medium-uncorrected calculations. The level of agreement between the second order medium-corrected calculations and the relativistic calculations is not the same as observed in the case of cross sections.

The calculations shown in Fig. (2.14) for a photon energy of $E_\gamma = 312$ MeV show essentially the same qualitative features.

One characteristic that emerges from the above discussion is that the full second order calculations (medium-corrected calculations) in the FW scheme are not as close to the relativistic results as in the Pauli reduction case at the same photon energy. This brings out an essential difference between the Pauli and FW calculations: The wavefunctions in the Pauli formalism remain the same while different orders of the amplitude result solely from the expansion of the interaction Hamiltonian. The FW calculations, on the other hand, involve an expansion affecting both the wavefunctions and the interaction Hamiltonian simultaneously. This difference is at the root of the different convergence properties of the two approaches. We find that in most cases, by second order the Pauli expansion is quite close to the fully relativistic calculations, provided medium corrections are taken into account. In the FW scheme the level of agreement at the corresponding order is inferior, indicating that the convergence in this scheme is much slower than in the Pauli case.

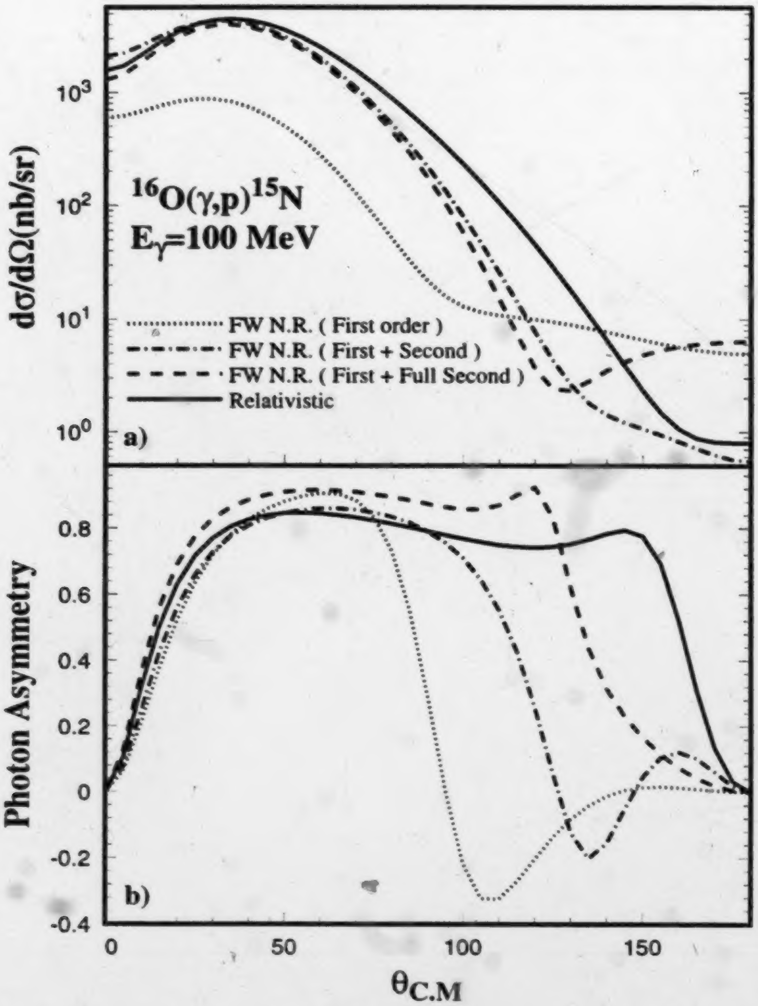

Figure 2.12: Differential cross section (a), and photon asymmetry (b) for the reaction $^{16}O(\gamma,\ p)^{15}N$ at $E_\gamma = 100$ MeV. Solid curve - full relativistic calculations. Dotted curve - nonrelativistic calculations using the first order FW Hamiltonian $H_I^{(1)}$ of equation (2.46) and nucleon wavefunctions obtained from equation (2.47) using the first order and spin-orbit terms of equation (2.44). Dot-dashed curve - second order nonrelativistic FW calculations (neglecting the nuclear potentials in $H_I^{(2)'}$ from equation (2.51)), and full second order potentials to generate the wavefunctions. These are referred to as medium-uncorrected second order calculations in the text. Dashed curve - second order nonrelativistic FW calculations using the full $H_I^{(2)'}$. These are referred to as medium-corrected second order calculations.

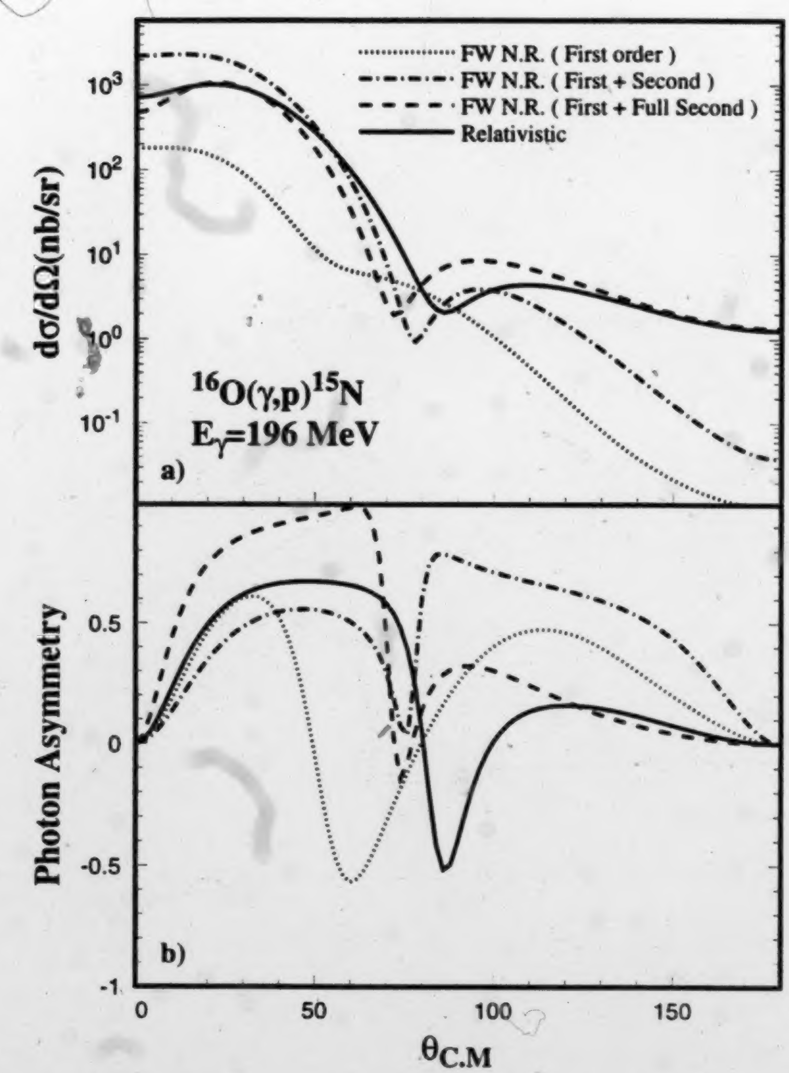

Figure 2.13: Differential cross section (a), and photon asymmetry (b) for the reaction of Fig. 2.12 but with $E_\gamma = 196$ MeV. Curves labelled as in Fig. 2.12.

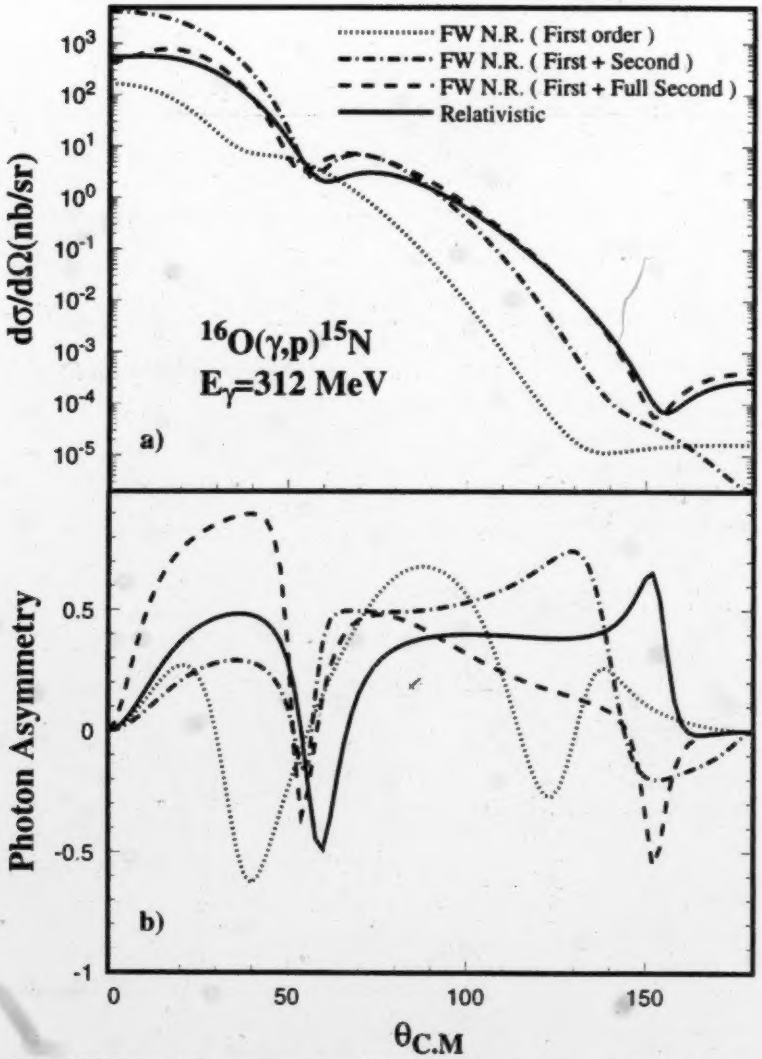

Figure 2.14: Differential cross section (a), and photon asymmetry (b) for the reaction of Fig. 2.12 but with $E_\gamma = 312$ MeV. Curves labelled as in Fig. 2.12.

2.4 Conclusions

We have described two different nonrelativistic reduction schemes of the relativistic amplitude for the knock-out contribution to (γ, p) reactions. These reductions allow us to carry out controlled comparisons between the relativistic and nonrelativistic calculations of the reaction observables. In the Pauli formalism the relativistic S matrix is written in terms of nonrelativistic two-component wavefunctions and an effective interaction Hamiltonian. The effective Hamiltonian is expanded in powers of $1/(E+M)$, where M is the nucleon mass and E is its total energy. In the limit $E \rightarrow M$, the first order interaction terms are exactly the same as those appearing in the usual nonrelativistic amplitude. The nonrelativistic wavefunctions in this scheme are solutions of the Schrödinger-like wave equation (2.13). Detailed comparisons between the relativistic and first-order nonrelativistic predictions for the differential cross sections and photon asymmetries show large differences between the two types of calculations. The inclusion of terms to second order in $1/M$ in the interaction Hamiltonian, where medium corrections effected by the nuclear potentials are left out, does not lead to any substantial improvement in the agreement between the relativistic and nonrelativistic calculations. On the other hand the expansion scheme shows explicit dependence, in the second order terms, on the nuclear potentials. When these medium corrections are taken into account the nonrelativistic calculations converge close to the relativistic results. This indicates that the essential difference between the relativistic and traditional nonrelativistic amplitudes, is the absence in the latter of the medium modification of the interaction Hamiltonian as a consequence of the presence of the strong vector and scalar potentials.

These conclusions are further supported through an analysis based on the Foldy-Wouthuysen transformation of the relativistic Hamiltonian describing a photon interacting with a nucleon embedded in the nuclear medium. The nonrelativistic wavefunctions for the bound and continuum nucleons are solutions of the wave equation obtained as a result of the transformation. The scheme leads to a nonrelativistic amplitude calculated to the desired order in $1/M$. We use these amplitudes to carry out comparisons between relativistic and nonrelativistic calculations in the manner described above for the Pauli scheme. We find that the medium modifications in the second order calculations are important and their inclusion leads in general to better agreement with the relativistic calculations. However the convergence is not as efficient at this order as in the Pauli case. The reasons for this can be understood in terms of the formal differences between the structure of the nonrelativistic amplitude obtained using this transformation as compared to the Pauli reduction case. The wavefunctions obtained through the FW reduction are different at each order in $1/M$, in contrast to the Pauli wavefunctions which are unchanged for all orders (recall that in the Pauli reduction only the interaction Hamiltonian is expanded).

The nuclear wave equations, produced in third and higher order calculations of FW scheme, involve complicated functions of the nucleon momentum such that it is most likely impossible to write these equations in the form of Schrödinger equations and solve them. On the other hand a consistent transformation requires the use the effective interaction Hamiltonian and the nuclear wavefunctions obtained at each order for calculation of the reaction amplitude. The complexity of the wave equations at higher orders in the FW transformation scheme prevents a consistent use of this scheme to reduce the relativistic distorted amplitude for photonuclear reactions.

The basic result of the present work is that standard nonrelativistic calculations of the knock-out amplitude do not properly take into account the strong medium modifications of the interaction Hamiltonian. We have clarified this point through a comparison based on nonrelativistic reduction of the relativistic amplitude using both the Pauli and Foldy-Wouthuysen reduction schemes.

Bibliography

[1] G.M. Lotz and H.S. Sherif, Phys. Lett. **B210** (1988) 45; and Nucl. Phys. **A537** (1992) 285.

[2] J.P. McDermott, E. Rost, J.R. Shepard and C.Y. Cheung, Phys. Rev. Lett. **61** (1988) 814.

[3] S. Boffi,C. Giusti and F.D. Pacati, Nucl. Phys. **A336**(1980)416

[4] C. Giusti and F.D. Pacati, Lett.Nuovo Cimento **26**(1979)622

[5] E.D. Cooper, A.O. Gattone and M.H. Macfarlane, Phys. Lett. **B130** (1983) 359.

[6] J.D. Bjorken and S.D. Drell, *Relativistic Quantum Mechanics*, (McGraw-Hill Book Company 1964).

[7] B.D. Serot and J.D. Walecka, Advances in Nuclear Physics (J.W. Negele and E. Vogt,eds.) Vol.**16**, Plenum Press, New York (1986)

[8] E.D. Cooper, S. Hama, B.C. Clark and R.L. Mercer, Phys. Rev. C **47** (1993) 297.

[9] C.J. Horowitz and B.D. Serot, Nucl. Phys. **A368** (1986) 503.

[10] B.C. Clark, S. Hama and R.L. Mercer, AIP conf. proc. N. **97**, ed: H.O. Mayer (1982) 260; J. Raynal, Aust. J. Phys. **43** (1990) 9; G.Q. Li, J. Phys. **G19** (1993) 1841.

[11] S. Boffi, C. Giusti and F.D. Pacati, Nucl. Phys. **A359** (1981) 91.

[12] V.B. Ganenko, V.A. Gushchin, Yu. V. Zhebrovskii, L. Ya. Kolesnikov, A.L. Rubashkin and P.V. Sorokin, JETP Lett. **47** (1988) 519; G.S. Blanpied *et al.*, Phys. Rev. Lett. **67** (1991) 1206.

[13] G.M. Lotz, Ph.D. thesis, University Of Alberta, 1989.

[14] D.J.S. Findlay and R.O. Owens, Nucl.Phys. **A279**(1977)385

[15] A.M. Kobos, E.D. Cooper, J.I. Johansson and H.S. Sherif, Nucl. Phys. **A445**(1985) 605.

[16] R.S. Turley, E.R. Kinnee, J.L. Matthews, W.W. Sapp, E.J. Schumacher, S.A. Wood, G.S. Adams and R.O. Owens, Phys. Lett. **B157**(1985)19

[17] K.W. Mcvoy and L.Van Hove, Phys. Rev. **125** (1962) 1034.

[18] L.L. Foldy and S.A. Wouthuysen, Phys. Rev. **78** (1950) 29.

[19] H.W. Fearing, G.I. Poulis and S. Scherer, Nuc. Phys. **A570**, (1994) 657.

Appendix 2.A Radial and Angular Integrals

In this appendix we give the explicit form of the functions involving Clebsch-Gordan coefficients and radial integrals which are introduced in the amplitude of equations (2.27) and (2.28).

$$I_{l,L,J,L_B} = (L_B, l; 0, 0 \mid L, 0) \int r^2 dr f_B(r) j_l(k_\gamma r) f_{LJ}(r),$$

$$\begin{aligned} P^{M_B,\mu,\nu}_{L_B+1,J,L} = & \sqrt{\frac{L_B+1}{2L_B+1}} (L_B+1, 1; M_B+\mu-\nu, \nu \mid L_B, M_B+\mu) \\ & \times (L_B+1, l : M_B+\mu-\nu, 0 \mid L, M_B+\mu-\nu)(L, l; 0, 0 \mid L_B+1, 0) \\ & \times \int f_{LJ}(r) j_l(k_\gamma r) \left(\frac{df_B(r)}{dr} - L_B \frac{f_B(r)}{r} \right) r^2 dr, \end{aligned}$$

$$\begin{aligned} \mathcal{P}^{M_B,\mu,\nu}_{L_B-1,J,L} = & \sqrt{\frac{L_B}{2L_B+1}} (L_B-1, 1; M_B+\mu-\nu, \nu \mid L_B, M_B+\mu) \\ & \times (L_B-1, l : M_B+\mu-\nu, 0 \mid L, M_B+\mu-\nu) \\ & \times (L, l; 0, 0 \mid L_B-1, 0) \\ & \times \int f_{LJ}(r) j_l(k_\gamma r) \left(\frac{df_B(r)}{dr} + \frac{L_B+1}{r} f_B(r) \right) r^2 dr, \end{aligned}$$

$$\begin{aligned} H^{M_B,\mu,\nu}_{L,J,L_B} = & (L, 1/2; M_B-\mu-\nu, \mu \mid J, M_B-\nu) \\ & \times (L_B, 1/2; M_B-\mu, \mu \mid J_B, M_B). \end{aligned}$$

$$\begin{aligned} \mathcal{H}^{M_B,\mu}_{L,J,L_B} = & (L, 1/2; M_B+\mu, \mu \mid J, M_B+2\mu) \\ & \times (L_B, 1/2; M_B+\mu, -\mu \mid J_B, M_B), \end{aligned}$$

$$\begin{aligned} C^{\mu}_{l,L,J,L_B} = & (L_B, 1/2; M_B+\mu, -\mu \mid J_B, M_B) \\ & \times (L, 1/2; M_B+\mu, \mu \mid J, M_B+2\mu) \\ & \times (L, l; M_B+\mu, 0 \mid L_B, M_B+\mu), \end{aligned}$$

$$\begin{aligned}
\mathcal{I}^{L_b}_{lLJ} &= (L_b, l; 0,0 \mid L,0) \left\{ \int r^2 dr f_b(r) j_l(k_\gamma r) \hat{Q}_{LJ}(r) \right. \\
&\qquad \left. + \int r^2 dr \hat{Q}_b(r) j_l(k_\gamma r) f_{LJ}(r) \right\}
\end{aligned} \tag{2.55}$$

$$\begin{aligned}
K^{M_B,\mu,\nu}_{L_B+1,l,L} &= \sqrt{\frac{L_B+1}{2L_B+1}} (L_B+1, 1; M_B-\mu-\nu, \nu \mid L_B, M_B-\mu) \\
&\quad \times (L_B+1, l : M_B-\nu-\mu, 0 \mid L, M_B-\nu-\mu) \\
&\quad \times (L, l; 0,0 \mid L_B+1, 0) \\
&\quad \times \left\{ \int \check{Q}_{LJ}(r) j_l(k_\gamma r) \left(\frac{df_B(r)}{dr} - L_B \frac{f_B(r)}{r} \right) r^2 dr \right. \\
&\quad \left. + \int f_{LJ}(r) j_l(k_\gamma r) \left(\frac{d\check{Q}_B(r)}{dr} - L_B \frac{\check{Q}_B(r)}{r} \right) r^2 dr \right\}
\end{aligned}$$

$$\begin{aligned}
\mathcal{K}^{M_B,\mu,\nu}_{L_B-1,l,L} &= \sqrt{\frac{L_B}{2L_B+1}} (L_B-1, 1; M_B-\nu-\mu, \nu \mid L_B, M_B-\mu) \\
&\quad \times (L_B-1, l : M_B-\nu-\mu, 0 \mid L, M_b-\nu-\mu) \\
&\quad \times (L, l; 0,0 \mid L_B-1, 0) \\
&\quad \left\{ \int \check{Q}_{LJ}(r) j_l(k_\gamma r) \left(\frac{df_B(r)}{dr} + \frac{L_B+1}{r} f_B(r) \right) r^2 dr \right. \\
&\quad \left. + \int f_{LJ}(r) j_l(k_\gamma r) \left(\frac{d\check{Q}_B(r)}{dr} + \frac{L_B+1}{r} \check{Q}_B(r) \right) r^2 dr \right\}
\end{aligned}$$

$$\begin{aligned}
R^{M_B,\mu,\nu}_{L_B+1,l,L} &= \sqrt{\frac{L_B+1}{2L_B+1}} (L_B+1, 1; M_B-\mu-\nu, \nu \mid L_B, M_B-\mu) \\
&\quad \times (L_B+1, l : M_B-\nu-\mu, 0 \mid L, M_B-\nu-\mu) \\
&\quad \times (L, l; 0,0 \mid L_B+1, 0) \\
&\quad \times \left\{ \int \tilde{Q}_{LJ}(r) j_l(k_\gamma r) \left(\frac{df_B(r)}{dr} - L_B \frac{f_B(r)}{r} \right) r^2 dr \right. \\
&\quad \left. + \int f_{LJ}(r) j_l(k_\gamma r) \left(\frac{d\tilde{Q}_B(r)}{dr} - L_B \frac{\tilde{Q}_B(r)}{r} \right) r^2 dr \right\}
\end{aligned}$$

$$\mathcal{R}^{M_B,\mu,\nu}_{L_B-1,l,L} = \sqrt{\frac{L_B}{2L_B+1}} (L_B-1, 1; M_b-\nu-\mu, \nu \mid L_B, M_B-\mu)$$

$$\begin{aligned}
&\times(L_B-1,l:M_B-\nu-\mu,0\mid L,M_B-\nu-\mu)\\
&\times(L,l;0,0\mid L_B-1,0)\\
&\left\{\int \tilde{Q}_{LJ}(r)j_l(k_\gamma r)\left(\frac{df_B(r)}{dr}+\frac{L_B+1}{r}f_B(r)\right)r^2dr\right.\\
&\left.+\int f_{LJ}(r)j_l(k_\gamma r)\left(\frac{d\tilde{Q}_B(r)}{dr}+\frac{L_B+1}{r}\tilde{Q}_B(r)\right)r^2dr\right\}
\end{aligned}$$

where the radial functions are

$$\begin{aligned}
\hat{Q}_b(r) &= \left\{\frac{\kappa_N}{2M}\left(1+\frac{\omega}{M+E_c}+\frac{1}{2}\frac{S(r)-V(r)}{M+E_b}\right)\right.\\
&\left.+\frac{\hbar c}{M+E_c}\left(1-\frac{S_c(r)-V_c(r)}{M+E_c}+\frac{1}{2}\frac{S(r)-V(r)}{M+E_b}\right)\right\}f_b(r) \qquad (2.56)\\
\hat{Q}_{LJ}(r) &= \left\{\frac{\kappa_N}{2M}\left(\frac{1}{2}\frac{S_c(r)-V_c(r)}{M+E_c}\right)\right.\\
&\left.+\frac{\hbar c}{M+E_c}\left(1-\frac{S_c(r)-V_c(r)}{2(M+E_c)}\right)\right\}f_{LJ}(r)\\
\check{Q}_b(r) &= \left\{\hbar c(\frac{1}{M+E_b}+\frac{1}{M+E_c})(1+\frac{1}{2}\frac{S(r)-V(r)}{M+E_b})\right.\\
&+\frac{\omega\kappa_N\hbar c}{2M}(\frac{1}{M+E_b}-\frac{1}{M+E_c})\\
&\left.-\frac{\hbar c}{(M+E_c)}\frac{S_c(r)-V_c(r)}{M+E_c}\right\}f_b(r)\\
\check{Q}_{LJ}(r) &= \left\{\frac{\hbar c}{2}(\frac{1}{M+E_b}+\frac{1}{M+E_c})\frac{S_c(r)-V_c(r)}{M+E_c}\right.\\
&\left.-\frac{\hbar c}{M+E_b}\frac{S(r)-V(r)}{M+E_b}\right\}f_{LJ}(r)\\
\tilde{Q}_b(r) &= \left\{\hbar c(\frac{1}{M+E_b}-\frac{1}{M+E_c})(1+\frac{1}{2}\frac{S(r)-V(r)}{M+E_b})\right.\\
&-\frac{\omega\kappa_N\hbar c}{2M}(\frac{1}{M+E_b}+\frac{1}{M+E_c})
\end{aligned}$$

$$- \frac{\hbar c}{(M+E_c)} \frac{S_c(r) - V_c(r)}{M+E_c} \Bigg\} f_b(r)$$

$$\begin{aligned} \tilde{Q}_{LJ}(r) \;=\; & \Bigg\{ \frac{\hbar c}{2} \Big(\frac{1}{M+E_c} - \frac{1}{M+E_b} \Big) \frac{S_c(r) - V_c(r)}{M+E_c} \\ & + \frac{\hbar c}{M+E_b} \frac{S(r) - V(r)}{M+E_b} \Bigg\} f_{LJ}(r) \end{aligned}$$

Appendix 2.B Observables

In this appendix we calculate the cross section for the resultant non-relativistic amplitudes obtained through the nonrelativistic reduction of the relativistic amplitude for (γ, p). We will start from the S-matrix given in equation (2.29) for ([illegible], p) reaction

$$S^i_{fi} = \frac{-ie}{\pi}\left[\frac{1}{2\omega}\right]^{1/2}\sum_{J_B M_B}(J_f, J_B; M_f, M_B|J_i, M_i)\left[S_{J_i J_f}(J_B)\right]^{1/2}$$

$$\times\delta(E_C - E_B - \omega)Z^{i\ \xi}_{S_f, M_B(\theta)}. \qquad (2.57)$$

Let us first square the S-matrix

$$\mid S^i_{fi}\mid^2 = \frac{e^2}{4\pi^2}[\delta(E_C - E_B - \omega)]^2 S\frac{2}{\omega}\sum_{M_B}\frac{2J_i+1}{2J_B+1}\mid Z^{i\ \xi}_{S_f, M_B}(\theta)\mid^2, \qquad (2.58)$$

where we have used the following

$$\begin{aligned}\sum_{M_B, M_f}(J_f, J_B; M_f, M_B|J_i, M_i)^2 & \qquad (2.59)\\ &= \sum_{M_B, M_f}(-1)^{2(J_f-M_f)}(J_f, J_i; M_f, -M_i \mid J_B, -M_B)^2\\ &= \sum_{M_B}(-1)^{2(J_f-M_f)}\frac{2J_i+1}{2J_B+1}.\end{aligned}$$

To calculate the δ^2 term we will follow Bjorken and Drell [6]

$$2\pi\delta(E_f - E_i) \Rightarrow \int_{\frac{-T}{2}}^{\frac{T}{2}} dt e^{i(E_f - E_i)t} = 2\frac{\sin\frac{T}{2}(E_f - E_i)}{E_f - E_i}, \qquad (2.60)$$

so for the large but finite T we have

$$[2\pi\delta(E_f - E_i)]^2 \Rightarrow 4\frac{\sin^2\frac{T}{2}(E_f - E_i)}{(E_f - E_i)^2} = f(E_f). \qquad (2.61)$$

Integration of $f(E_f)$ over the range $E_f = -\infty \rightarrow \infty$ results in $2\pi T$. So we can identify the following relation

$$[2\pi\delta(E_f - E_i)]^2 = [2\pi\delta(0)]2\pi\delta(E_f - E_i) = 2\pi T\delta(E_f - E_i). \qquad (2.62)$$

The transition rate can be found by dividing the square of the S-matrix to T (reaction time)

$$\frac{|S^i_{fi}|^2}{T} = \frac{\alpha}{2\pi^2}\delta(E_C - E_B - \omega) S \frac{2}{\omega} \sum_{M_B} \frac{2J_i + 1}{2J_B + 1} \,|\, Z^{i\,\xi}_{s_f,M_B}(\theta) \,|^2 \,. \tag{2.63}$$

To find the transition rate per incoming photon we divide the transition rate (2.63) by flux of incident photons

? $$J_{inc} = \frac{c}{(2\pi)^3} = \frac{1}{(2\pi)^3}, \tag{2.64}$$

where the last expression is in natural unit and factor $\frac{1}{(2\pi)^3}$ comes from the convention of the normalization of the photon field. Thus

$$\frac{|S^i_{fi}|^2}{J_{inc}T} = 4\pi\alpha\delta(E_C - E_B - \omega) S \frac{2}{\omega} \sum_{M_B} \frac{2J_i + 1}{2J_B + 1} \,|\, Z^{\xi}_{s_f,M_B}(\theta) \,|^2 \,. \tag{2.65}$$

Now by integrating (2.65) over the phase space we have

$$\begin{aligned} \int \frac{|S^i_{fi}|^2}{J_{inc}T} d^3p \;&=\; 4\pi\alpha \sum_{M_B} \frac{2J_i + 1}{2J_B + 1} \int \delta(E_C - E_B - \omega) \\ &\quad \times S \frac{2}{\omega} \,|\, Z^{i\,\xi}_{s_f,M_B}(\theta) \,|^2\, pEdEd\Omega. \end{aligned} \tag{2.66}$$

where we have used of $E^2 = M^2 + p^2$ or $EdE = pdp$. The cross section for the unpolarized incident photon and if the polarization of the knocked-out nucleon is not measured, is found by averaging over initial, and summing over final polarization states. Finally the non-relativistic cross section for the (γ, p) reaction is found as

$$\frac{d\sigma^i}{d\Omega} = \frac{4\pi\alpha p E_C}{(2J_B + 1)\hbar c p_\gamma} \sum_{s_f, M_B, \xi} |\, Z^{i\,\xi}_{s_f,M_B} \,|^2 \,. \tag{2.67}$$

Relativistic cross section for the (γ, p) reaction is given in reference [1].

Appendix 2.C Nucleon Wavefunctions

One basic difference between the Pauli and FW schemes, as considered in the present work, is that the nuclear wavefunctions in the Pauli scheme are the same for all orders in the expansion whereas in the FW scheme the wavefunctions change at every order. We compare here the wavefunctions of the Pauli scheme with the wavefunctions used in second order calculations of the FW scheme. In both reduction schemes the wave equation can be written in the form

$$\frac{\mathbf{p}^2}{2M}\Psi_{\rm Sch} + \{U_{\rm cent} + U_{\rm so}\boldsymbol{\sigma}\cdot \boldsymbol{L}\}\,\Psi_{\rm Sch} = (E - M)\Psi_{\rm Sch}. \tag{2.68}$$

We first consider the spin orbit potentials, from equation (2.49) for the FW scheme. We have

$$U_{\rm so}^{\rm FW} = -\frac{1}{4M^2}\frac{1}{r}\left[\frac{S'(r) - V'(r)}{1 - \frac{S(r)}{M}}\right], \tag{2.69}$$

We modify the denominator of $U_{\rm so}$ in Pauli reduction (2.15) by setting $E \to M$ and assuming the same magnitude for the strong scalar and vector potentials, so $U_{\rm so}^{\rm Pauli}$ becomes

$$U_{\rm so}^{\rm Pauli} = -\frac{1}{4M^2}\frac{1}{r}\left[\frac{S'(r) - V'(r)}{1 + \frac{S(r)}{M}}\right]. \tag{2.70}$$

If we set $\frac{S(r)}{M} \approx -\frac{1}{3}$ in the denominator of the square brackets in the above equations, we find that the Pauli spin-orbit potential is approximately twice as large as the FW spin-orbit potential. Note that if the nucleon mass were much larger than the depth of the scalar potential, these two spin-orbit potentials would be the same.

From equation (2.49), the central potential obtained in the FW transformation can be written as

$$U_{\rm cent}^{\rm FW}(r) = \frac{1}{D_{\rm FW}(r)}\left\{S(r) + V(r) + \frac{1}{4M^2 r}\left[S'(r) + V'(r)\right]\right.$$

$$
\begin{aligned}
&\qquad + \frac{1}{8M^2}\left[S''(r) + V''(r)\right]\Big\} \\
&+(E-M)\left\{1 - \frac{1}{D_{\mathrm{FW}}(r)}\right\} \\
&+\frac{1}{2Mr}\frac{D'_{\mathrm{FW}}(r)}{D_{\mathrm{FW}}(r)} + \frac{1}{4M}\frac{D''_{\mathrm{FW}}(r)}{D_{\mathrm{FW}}(r)} - \frac{1}{8M}\left(\frac{D'_{\mathrm{FW}}(r)}{D_{\mathrm{FW}}(r)}\right)^2
\end{aligned}
\tag{2.71}
$$

From equation (2.14), we write the central potential in Pauli reduction as

$$
\begin{aligned}
U^{\mathrm{Pauli}}_{\mathrm{cent}}(r) &= S(r) + \frac{E}{M}V(r) - \frac{(M-E)^2}{2M} + \frac{S^2(r) - V^2(r)}{2M} \\
&-\frac{1}{2Mr}\frac{S'(r) - V'(r)}{E + M + S(r) - V(r)} \\
&-\frac{1}{4M}\frac{S''(r) - V''(r)}{E + M + S(r) - V(r)} \\
&+\frac{3}{8M}\frac{[S'(r) - V'(r)]^2}{[E + M + S(r) - V(r)]^2}
\end{aligned}
\tag{2.72}
$$

If we set the nucleon energy equal to the nucleon mass for the sake of comparison with the FW central potential we will have

$$
\begin{aligned}
U^{\mathrm{Pauli}}_{\mathrm{cent}}(r) &= [S(r) + V(r)]\left[1 + \frac{S(r) - V(r)}{2M}\right] \\
&-\frac{1}{2Mr}\frac{S'(r) - V'(r)}{2M + S(r) - V(r)} - \frac{1}{4M}\frac{S''(r) - V''(r)}{2M + S(r) - V(r)} \\
&+\frac{3}{8M}\frac{[S'(r) - V'(r)]^2}{[2M + S(r) - V(r)]^2}.
\end{aligned}
\tag{2.73}
$$

It may be interesting to note the leading terms in both central potentials

$$
\begin{aligned}
U^{\mathrm{Pauli}}_{\mathrm{cent}}(r) &\cong [S(r) + V(r)]\left[1 + \frac{S(r) - V(r)}{2M}\right] \\
U^{\mathrm{FW}}_{\mathrm{cent}}(r) &\cong [S(r) + V(r)]\left[\frac{1}{1 - \frac{S(r)}{M}}\right]
\end{aligned}
\tag{2.74}
$$

These lead to similar modifications of the central potentials

$$
\begin{aligned}
\left[1 + \frac{S(r) - V(r)}{2M}\right] &\cong \frac{2}{3} \\
\left[\frac{1}{1 - \frac{S(r)}{M}}\right] &\cong \frac{3}{4}
\end{aligned}
\tag{2.75}
$$

The leading terms in both the FW and Pauli central potentials are then $S(r) + V(r)$, along with some constant factor. We can simplify the situation even more if we make the approximation that the potential depths are much smaller than the nucleon mass and then the central potential for both Pauli and FW wave equations can be written as

$$\begin{aligned}
U_{\text{cent}}^{\text{Pauli}}(r) &= S(r) + V(r) - \frac{1}{4M^2 r}\left[S'(r) - V'(r)\right] \\
&\quad - \frac{1}{8M^2}\left[S''(r) - V''(r)\right] + \frac{3}{32M^3}\left[S'(r) - V'(r)\right]^2 .
\end{aligned}$$

$$\begin{aligned}
U_{\text{cent}}^{\text{FW}}(r) &= S(r) + V(r) - \frac{1}{4M^2 r}\left[S'(r) - V'(r)\right] \\
&\quad - \frac{1}{8M^2}\left[S''(r) - V''(r)\right] - \frac{1}{8M^3} S'^2(r) .
\end{aligned} \tag{2.76}$$

The difference between the FW and Pauli central potentials is then

$$U_{\text{cent}}^{\text{FW}}(r) - U_{\text{cent}}^{\text{Pauli}}(r) = -\frac{1}{8M^3} S'^2(r) - \frac{3}{32M^3}\left[S'(r) - V'(r)\right]^2 \tag{2.77}$$

Therefore in the limit that the scalar and vector potentials are much smaller than the nucleon mass and if the total energy of the nucleon is replaced by its mass (the latter limit is imposed only in Pauli interaction Hamiltonian), then to order $1/M^2$ there is no difference between the two potentials.

Chapter 3

Nonrelativistic Reduction of The (e, $e'p$) Reaction on Nuclei [1]

Introduction

The quasifree process ($e, e'p$) has been used extensively to study proton hole states in nuclei and to determine single particle spectroscopic factors [1]. This reaction is advantageous because the electromagnetic interaction with the nucleon is known; the relative weakness of the interaction permits an exploration of the entire volume of the nucleus. The diagrams with the exchange of only one photon between the electron and proton are expected to be enough to describe the process. Moreover the coincidence measurements of the ($e, e'p$) reaction can provide detailed information about the single particle structure of the nucleus over a wide range of momentum transfer.

The ($e, e'p$) reaction has been studied both nonrelativistically [1, 2] and relativistically [3, 4, 5]. Both analyses begin with a Lagrangian which allows for the interaction of the photon with both electrons and protons. Nonrelativistic analyses involve the reduction of the free electron-proton interaction to a form involving two-component spinors for the nucleon. This results in a Hamiltonian which is expanded in powers of $1/M$ where M is the nucleon mass [2, 6]. The resulting interaction Hamiltonian is then used together with Schrödinger wavefunctions describing the nucleons in order to form the nuclear current. Relativistic analyses are based on the Feynman diagram for one-photon exchange between the projectile electron and a proton which is imbedded in the nucleus (see figure (3.1)). The electrons and nucleons are all described relativistically as spin 1/2 objects via the Dirac equation containing appropriate potentials [3, 4, 5].

---

[1] A short version of this chapter is published in Phys. Rev. C **51** (1995) 2044.

A long-standing problem in quasifree electron scattering has been that the spectroscopic factors extracted from nonrelativistic analyses fall widely below the expected sum rules. Spectroscopic factors which are found on the basis of the relativistic approach are generally larger than those found via the nonrelativistic approach. There are other discrepancies between the results of these approaches [3, 5].

Several groups have attempted to understand the underlying differences between these two approaches. This mainly involved looking at the sensitivity of quasifree electron scattering calculations to different optical potentials and renormalizations of the wavefunction of the outgoing proton [7, 8, 9]. This concentration on optical potentials was largely a result of the improvement in the description of proton elastic scattering observables in the framework of Dirac phenomenology.

Boffi *et al.* [7] followed a prescription in which the nonrelativistic continuum wavefunction was multiplied by a factor $\{1 + [S(r) - V(r)] / (E + M)\}^{1/2}$, where $S(r)$ is the Dirac scalar potential and $V(r)$ is the vector potential. This modification essentially changes the two-component Schrödinger wavefunction into the upper component of the Dirac wavefunction. No other changes were made in the nonrelativistic calculations. They find that extracted occupation probabilities are larger than those obtained from the [illegible]ed nonrelativistic analysis. The analysis of Udias *et al.* [8] replaces the non[illegible] bound state wavefunction with the upper component of a Dirac wave function, and the nonrelativistic continuum wavefunction is modified by factors of the same shape as the factor used by Boffi *et al.* The continuum wavefunction in this case is generated from Schrödinger-equivalent potentials [10]. The nuclear current operators are obtained in the standard way by expansion to order $1/M^4$. Their "nonrelativistic" calculations then involve nonrelativistic nuclear current operators surrounded by the upper components of Dirac wavefunctions. With these choices little difference is found between the relativistic and "nonrelativistic" calculations. These authors also performed a "standard" nonrelativistic calculation in which instead of the Schrödinger-equivalent potentials the usual nonrelativistic potentials were used to obtain the wavefunction of the knocked-out proton. Their conclusion is that differences in observed cross sections are due to the choice of optical potential. Jin and Onley [9] have presented a model which can take either relativistic or nonrelativistic optical potentials while keeping other aspects of the calculation the same. They find that different optical potentials can change the results by as much as 14%.

These results demonstrated the variability of the results associated with possible models for final state interactions. However, the issue is clouded by the occasional use of upper components of Dirac wavefunctions in a nonrelativistic calculation. We believe that the essential difference between relativistic and nonrelativistic approaches are not just in the changes in the optical potentials; these are usually phenomenological and equivalent potentials can always be found. Rather the essential difference is in the appearance of the nuclear potentials in the nuclear current operators when the relativistic amplitude is reduced to a nonrelativistic form. Such medium effects on the nuclear currents are absent in the standard nonrelativistic calculations.

In this chapter we study the differences between the relativistic and nonrelativistic approaches in calculating the amplitude for the ($e, e'p$) reaction. We do this through an effective Pauli reduction of the relativistic transition amplitude, along the same lines discussed in section 2.2 of chapter 2 for the (γ, p) reaction. An expansion of the amplitude in powers of $(E+M)^{-1}$ allows us to recover a nonrelativistic limit, which matches the standard nonrelativistic calculations, with the difference that optical potentials used to generate the distorted waves are equivalent, in the elastic channel, to those used in the relativistic calculations. We compare the two approaches and thus explain why they can still give different values for the extracted spectroscopic factors, even when equivalent optical potentials are used.

We introduce the relativistic amplitude for quasifree electron scattering in section 3.1. Section 3.2 outlines the Pauli reduction of the amplitude and some of its relevant features. In section 3.3 we compare our nonrelativistic calculations with and without nuclear potentials in the nuclear current operators, to the results of the fully relativistic calculations. Our conclusions are given in section 3.4.

3.1 Relativistic Amplitude for (e, $e'p$) Reactions

In an $A(e,e'p)A-1$ reaction the incident electron interacts with the target nucleus A and as a result a proton is knocked out of the nucleus. This proton is detected in coincidence with the scattered electron. The quasifree prescription of the reaction assumes the virtual photon is absorbed only by a single bound proton, then as a result the proton is ejected into the continuum state. The initial and final states of the interacting nucleon are described by single particle wavefunctions. We consider the one photon exchange model for the ($e,e'p$) process [5], in which a photon is exchanged between the incident electron and a target proton. The Feynman diagram describing this reaction is depicted in figure (3.1).

In this chapter we are interested in the differences between the relativistic and nonrelativistic treatment of the hadronic part of the ($e,e'p$) reaction amplitude. In the course of this discussion we do not include the Coulomb interaction in the leptonic part of the S-matrix. The present study does not impact the treatment of the electron motion which is treated in the same fashion (relativistically) for relativistic

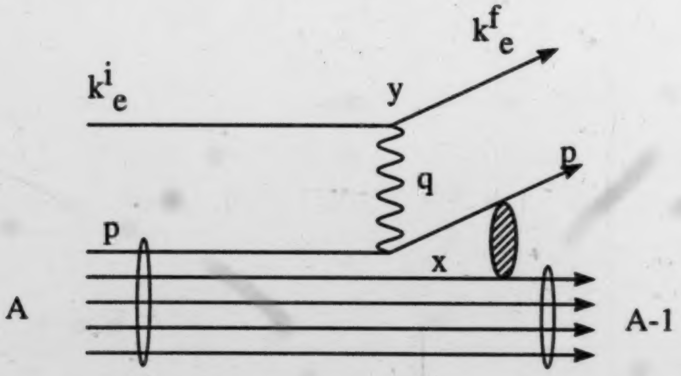

Figure 3.1: The Feynman diagram for $A(\ e, e'p\ )A-1$ reaction

and nonrelativistic calculations. The Coulomb distortions for the electrons are only important for heavier nuclei and at any rate they do not affect the present discussion.

The relativistic model for $A(\ e, e'p\ )A-1$ starts from a gauge invariant Lagrangian for electrons and protons interacting with photons. Appropriate Fock space calculations over the fields involved in the reaction lead in the first order to the S-matrix associated with figure (3.1) [11]. The relativistic expression for the S-matrix describing the quasifree electron scattering process $(\ e, e'p\ )$ is obtained as [5]

$$\begin{aligned} S_{fi} \;=\; & \frac{-ie^2}{(2\pi)^{17/2}}\left[\frac{M\,m_e^2}{E_C E_f E_i}\right]^{1/2} \sum_{J_B M_B} (J_f, J_B; M_f, M_B | J_i, M_i) \\ & \times \left[S_{J_i J_f}(J_B)\right]^{1/2} \int d^4x\, d^4y\, d^4q\, J_{e\mu}(y) \frac{e^{-iq\cdot(x-y)}}{q^2+i\epsilon} J_N^{\mu}(x), \end{aligned} \tag{3.1}$$

where J_e^{μ} and J_N^{μ} are electron and nuclear currents respectively, the Clebsch-Gordan coefficient couples the bound proton to the residual nucleus, and $S_{J_i J_f}(J_B)$ is the spectroscopic factor. M is the nucleon mass, E_C is the energy of the outgoing proton, and E_i and E_f are the energy of the initial and final electrons, respectively. The integration over d^4q is associated with the propagator of the exchanged photon. The electron current is given by

$$J_e^\mu(y) = \overline{\psi}_{e_f}(y)\,\gamma^\mu\psi_{e_i}(y)\,, \tag{3.2}$$

where ψ_{e_i} and ψ_{e_f} are the initial and final Dirac spinors for electrons. The electron wavefunctions are taken to be free Dirac spinors and the integration at the electron vertex can then be done analytically. This also allows the momentum integration for the photon propagator to be done, leaving one four-dimensional integration at the nucleon vertex. The nuclear current is similarly given by

$$J_N^\mu(x) = \overline{\psi}_{N_f}(x)\,j_N^\mu\psi_{N_B}(x)\,, \tag{3.3}$$

where the Dirac wavefunctions $\psi_{N_B}(x)$ and $\psi_{N_f}(x)$ describe the initial and final protons, respectively. For the distorted wave Born approximation (DWBA) calculations, the final state interaction of the proton with residual nucleus is included by using a Dirac distorted wave for the final state nucleon. The nuclear current operator j_N^μ in equation (3.2) is the choice $cc2$ discussed by de Forest [12]

$$j_N^\mu = F_1\left(q^2\right)\gamma^\mu + \frac{i\kappa F_2\left(q^2\right)}{2M}\sigma^{\mu\nu}q_\nu. \tag{3.4}$$

The matrix $\sigma^{\mu\nu}$ is formed from the Dirac γ-matrices, and is introduced in the previous chapter. $F_1(q^2)$ and $F_2(q^2)$ are the Dirac and Pauli form factors, respectively. These form factors are related to the electric and magnetic form factors as follows [13]

$$\begin{aligned} F_1\left(q^2\right) &= \frac{1}{1-\frac{q^2}{4M^2}}\left[G_E\left(q^2\right) - \frac{q^2}{4M^2}G_M\left(q^2\right)\right] \\ F_2\left(q^2\right) &= \frac{1}{\kappa_p\left(1-\frac{q^2}{4M^2}\right)}\left[G_M\left(q^2\right) - G_E\left(q^2\right)\right], \end{aligned} \tag{3.5}$$

where the electric $G_E(q^2)$ and magnetic $G_M(q^2)$ form factors for proton obey the following conditions

$$\begin{aligned} G_E^p(0) &= 1 \\ G_M^p(0) &= 1+\kappa_p = 2.79284. \end{aligned} \tag{3.6}$$

These form factors are parameterized as follows [13]

$$\begin{aligned} G_E^p\left(q^2\right) &= \frac{1}{(1-\frac{q^2}{M_\lambda^2})^2} \\ G_M^p\left(q^2\right) &= \frac{1+\kappa_p}{(1-\frac{q^2}{M_\lambda^2})^2}, \end{aligned} \tag{3.7}$$

where the cut-off energy of $M_\lambda = 840$ MeV is used. The variable q is the four-momentum carried by the exchanged photon.

As mentioned earlier the integration over coordinates at the electron vertex, in the S-matrix of equation (3.1), can be done analytically. This yields a Dirac δ-function giving energy and momentum conservation at the vertex so $q = k_i^e - k_f^e$. The resulting δ-function fixes the momentum of the intermediate photon so the integration over that momentum is done trivially. The integration over the time coordinate at the nucleon vertex can then be done to yield a δ-function providing overall energy conservation. The S-matrix can then be cast in the form

$$\begin{aligned} S_{fi} &= \frac{-ie^2}{(2\pi)^{7/2}}\frac{1}{q_\gamma^2}\left[\frac{M\ m_e^2}{E_C E_f E_i}\right]^{1/2}\delta\left(E_C + E_f - E_B - E_i\right) \\ &\times \sum_{J_B M_B}\left(J_f, J_B; M_f, M_B | J_i, M_i\right)\left[S_{J_i J_f}(J_B)\right]^{1/2} Z_{\nu_f \nu_i}^{\mu M_B}, \end{aligned} \tag{3.8}$$

where $Z_{\nu_f \nu_i}^{\mu M_B}$ is a function of the initial and final spin projections, momenta, etc. Specifically we have at this point

$$Z_{\nu_f \nu_i}^{\mu M_B} = e_{\nu_f \nu_i}^{\alpha} \int d^3x\ \psi_\mu^\dagger\left(k_p, \boldsymbol{x}\right)\Gamma_\alpha \psi_{J_B, M_B}\left(\boldsymbol{x}\right)\exp\left(i\boldsymbol{q}\cdot\boldsymbol{x}\right). \tag{3.9}$$

where ν_i and ν_f are the spin projections of the incoming and outgoing electrons respectively, while M_B and μ are the spin projections of the bound and continuum protons. The 4 × 4 matrix operating on the nucleon spinors is

$$\Gamma_\alpha = \gamma_0\left[F_1\left(q^2\right)\gamma_\alpha + \frac{i\kappa F_2(q^2)}{2M}\sigma_{\alpha\nu}q^\nu\right]. \tag{3.10}$$

The four-vector which comes from the electron vertex is

$$e^{\alpha}_{\nu_f\nu_i} = \left[\frac{E_f+m_e}{2m_e}\frac{E_i+m_e}{2m_e}\right]^{1/2} \times \langle 1/2,\nu_f| \left[1, \frac{\boldsymbol{\sigma}\cdot\boldsymbol{k}_f}{E_f+m_e}\right]\gamma_0\gamma^{\alpha}\left[\begin{array}{c} 1 \\ \dfrac{\boldsymbol{\sigma}\cdot\boldsymbol{k}_i}{E_i+m_e}\end{array}\right]|1/2,\nu_i\rangle . \tag{3.11}$$

and this depends on the energies and momenta of the initial and final electrons as well as their spin projections. The integration in equation (3.9) is over the nucleon vertex and in the plane wave limit can be written as the Fourier transform of the bound state wavefunction. When the appropriate factors of $\hbar$ and c are included, the relativistic expression for the triple differential cross section is related to $Z^{\mu M_B}_{\nu_f\nu_i}$ by (see Appendix 3.C for more details)

$$\frac{d^3\sigma}{d\Omega_e d\Omega_p dE_p} = \frac{2}{(2\pi)^3}\frac{\alpha^2}{\hbar c}\left[\frac{(m_e c^2)^2 Mc^2}{(q_\gamma c)^4}\frac{p_p c\, p_f c}{p_i c}\right] \times \sum_{J_B M_B \mu \nu_f \nu_i}\frac{S_{J_i J_f}(J_B)}{2J_B+1}|Z^{\mu M_B}_{\nu_f\nu_i}|^2, \tag{3.12}$$

Where α is electromagnetic coupling constant. The cross section for quasifree electron scattering in the plane wave impulse approximation can be written in a factorized form as the product of three parts [12, 2]: a kinematic factor, the cross section for the elementary process $e+p\rightarrow e'+p'$, which is evaluated off-shell, and finally a function of the energy and momentum of the nucleon inside the nucleus referred to as the spectral function. The spectral function and factorization are discussed in detail in Appendix 3.D. In the following we will discuss results of the calculations of the spectral function, proton polarization and an asymmetry parameter. The spectral function is obtained from the cross section given above by dividing by a kinematic factor and the cross section ($\frac{d\sigma}{d\Omega_e}|_{free}$) for the elementary process for $e+p\rightarrow e+p$. We write [12, 2]:

$$S\left(p_m\right) = \frac{\frac{d^3\sigma}{d\Omega_e d\Omega_C dE_C}}{E_C p_C \left.\frac{d\sigma}{d\Omega_e}\right|_{free}}, \tag{3.13}$$

where E_C and p_C are the energy and momentum of the final state proton, and p_m is the missing momentum, i.e. the momentum of the bound nucleon in the initial state. On the basis of the quasifree assumption of the reaction one is able to assign a momentum to the bound nucleon which is the negative of the momentum of the recoil nucleus. The free cross section is calculated using the nucleon current operator of equation (3.4), and is evaluated using the kinematics of the quasifree process. The energy and momentum of the initial proton in quasifree reactions does not follow the energy momentum relation of a free nucleon, so is off-shell. Note that the experimental data are always divided by the elementary cross section *cc*1 of de Forest [12], while we use the nuclear current operator which leads to his cross section *cc*2, throughout this chapter. We are not concerned with detailed comparison with experimental data in this work, so we retain a consistent approach by using the same form for the current operator in the calculation of the quasifree S-matrix and the elementary process.

The polarization of the final state proton is given by (details are given in Appendix 3.C)

$$P = -2 \frac{\operatorname{Im} \sum_{M_B \nu_f \nu_i} Z_{\nu_f \nu_i}^{1/2 M_B} \left[Z_{\nu_f \nu_i}^{-1/2 M_B} \right]^*}{\sum_{M_B \mu \nu_f \nu_i} \left| Z_{\nu_f \nu_i}^{\mu M_B} \right|^2}. \tag{3.14}$$

We also define an asymmetry parameter in the missing momentum which is calculated from the differential cross sections of equation (3.12) as

$$\mathcal{A}(p_m) = \frac{d^3\sigma(p_m > 0) - d^3\sigma(p_m < 0)}{d^3\sigma(p_m > 0) + d^3\sigma(p_m < 0)}. \tag{3.15}$$

This asymmetry is similar to the parameter defined by Bianconi, Boffi and Kharzeev [14].

3.2 Pauli Reduction

We now perform an effective Pauli reduction, as discussed in the preceding chapter, on the hadronic part of the amplitude (3.9). The electrons continue to be treated relativistically throughout. Consider the nuclear current of equation (3.3) above. Using equation (3.4) one can write:

$$J^{\mu}(x) = \overline{\psi}_{N_f}(k_p, x)\left[F_1\left(q^2\right)\gamma^{\mu} + \frac{i\kappa F_2(q^2)}{2M}\sigma^{\mu\nu}q_{\nu}\right]\psi_{N_B}(x)\,. \tag{3.16}$$

As is shown in the preceding chapter the Dirac spinors may be written in terms of a Schrödinger-like wavefunction Ψ_{Sch} as

$$\psi_N = \begin{bmatrix} 1 \\ \dfrac{\boldsymbol{\sigma}\cdot\boldsymbol{p}}{M + E + S(r) - V(r)} \end{bmatrix} D^{\frac{1}{2}}\Psi_{Sch} \tag{3.17}$$

where

$$D(r) = \frac{E + M + S(r) - V(r)}{E + M}. \tag{3.18}$$

where two-component wavefunction Ψ_{Sch} is a solution of the Schrödinger-like equation derived in chapter II. The functions $S(r)$ and $V(r)$ are the scalar and vector potentials, respectively, for either the bound or final state nucleons. The energy of the nucleon is E, and the associated momentum operator is $\boldsymbol{p}$.

The relativistic nuclear current of equation (3.16) can, with the help of equation (3.17), be written in the form

$$\begin{aligned} J^{\mu} \;=\; \Psi^{\dagger}_{Sch,C}\Bigg\{ & D_C^{1/2}(r)\left[1,\ \frac{\boldsymbol{\sigma}\cdot\boldsymbol{p}}{M + E_C + S_C(r) - V_C(r)}\right] \\ & \times\ \gamma^{o}\left[F_1\gamma^{\mu} + F_2\frac{i\kappa}{2M}\sigma^{\mu\nu}q_{\nu}\right] \\ & \times\ \begin{bmatrix} 1 \\ \dfrac{\boldsymbol{\sigma}\cdot\boldsymbol{p}}{M + E_B + S_B(r) - V_B(r)} \end{bmatrix} D_B^{1/2}(r)\Bigg\}\Psi_{Sch,B}. \end{aligned} \tag{3.19}$$

We now perform an expansion of the object between braces in equation (3.19). The usual representation of the Dirac γ-matrices is used [15] to write the 4×4 operators in terms of 2×2 Pauli matrices. The radial function $D^{1/2}(r)$ from equation (3.18) and the factor $[E + M + S(r) - V(r)]^{-1}$ coming from both the bound and continuum wavefunctions are then expanded in powers of $(E + M)^{-1}$. This procedure leads to a sum of reduced nuclear current operators for each of the contributing orders:

$$J^{\mu}(x) = \Psi^{\dagger}_{Sch,C}(x)\left[j^{\mu^{(0)}} + j^{\mu^{(1)}} + j^{\mu^{(2)}} + \cdots\right]\Psi_{Sch,B}(x). \tag{3.20}$$

The reduced current operators can be written in terms of time-like and space-like components as

$$\begin{aligned}
j^{0^{(0)}} =& \quad eF_1, \\
j^{0^{(1)}} =& \quad \frac{eF_1}{2}\left[Q_C + Q_B\right], \\
j^{0^{(2)}} =& \quad eF_1\left[\frac{Q_C Q_B}{4} - \frac{Q_C^2 + Q_B^2}{8} + \frac{\boldsymbol{\sigma}\cdot\boldsymbol{p}}{M + E_C}\frac{\boldsymbol{\sigma}\cdot\boldsymbol{p}}{M + E_B}\right] \\
&+ \frac{e\kappa F_2}{2M}\left[\frac{\boldsymbol{\sigma}\cdot\boldsymbol{q}\ \boldsymbol{\sigma}\cdot\boldsymbol{p}}{M + E_B} - \frac{\boldsymbol{\sigma}\cdot\boldsymbol{p}\ \boldsymbol{\sigma}\cdot\boldsymbol{q}}{M + E_C}\right], \\
\mathbf{j}^{(0)} =& \quad 0, \\
\mathbf{j}^{(1)} =& \quad \frac{ie\kappa F_2}{2M}\boldsymbol{\sigma}\times\boldsymbol{q} + eF_1\left[\frac{\boldsymbol{\sigma}\ \boldsymbol{\sigma}\cdot\boldsymbol{p}}{M + E_B} + \frac{\boldsymbol{\sigma}\cdot\boldsymbol{p}\ \boldsymbol{\sigma}}{M + E_C}\right], \\
\mathbf{j}^{(2)} =& \quad \frac{ie\kappa F_2}{4M}\left[Q_B + Q_C\right]\boldsymbol{\sigma}\times\boldsymbol{q} + \frac{eF_1 Q_C}{2}\left[\frac{\boldsymbol{\sigma}\ \boldsymbol{\sigma}\cdot\boldsymbol{p}}{M + E_B} + \frac{\boldsymbol{\sigma}\cdot\boldsymbol{p}\ \boldsymbol{\sigma}}{M + E_C}\right] \\
&+ \frac{eF_1}{2}\left[\frac{\boldsymbol{\sigma}\ \boldsymbol{\sigma}\cdot\boldsymbol{p}}{M + E_B} + \frac{\boldsymbol{\sigma}\cdot\boldsymbol{p}\ \boldsymbol{\sigma}}{M + E_C}\right]Q_B \\
&- eF_1\left[Q_B\frac{\boldsymbol{\sigma}\ \boldsymbol{\sigma}\cdot\boldsymbol{p}}{M + E_B} + \frac{\boldsymbol{\sigma}\cdot\boldsymbol{p}\ \boldsymbol{\sigma}}{M + E_C}Q_C\right] \\
&+ \frac{e\kappa F_2 q_o}{2M}\left[\frac{\boldsymbol{\sigma}\ \boldsymbol{\sigma}\cdot\boldsymbol{p}}{M + E_B} - \frac{\boldsymbol{\sigma}\cdot\boldsymbol{p}\ \boldsymbol{\sigma}}{M + E_C}\right],
\end{aligned} \tag{3.21}$$

where we have defined

$$Q_X(r) = \frac{S_X(r) - V_X(r)}{E_X + M}, \tag{3.22}$$

and the labels B and C refer to the bound and continuum states, respectively. Note the dependence of the nuclear current operators on the Dirac vector and scalar potentials (through the functions Q_X). This dependence appears in all orders of the reduction scheme. Thus as we go to a description in terms of the Schrödinger-like wavefunctions for the nucleon, the currents undergo a medium modification affected via the nuclear potential. This point is central to the present work.

Using the current operators from equation (3.21) up to first order in $(E+M)^{-1}$, in the S-matrix (3.1), we find that for the ($e, e'p$) reaction the S-matrix to first order in $(E+M)^{-1}$ reduces to

$$\begin{aligned} S_{fi}^{(1)} = & \frac{-ie^2}{(2\pi)^{17/2}} \left[\frac{M\, m_e^2}{E_C E_f E_i} \right]^{1/2} \\ & \times \sum_{J_B M_B} (J_f, J_B; M_f, M_B | J_i, M_i) \left[S_{J_i J_f}(J_B) \right]^{1/2} \\ & \times \int d^4x\, d^4y\, d^4q\, \frac{e^{-iq\cdot(x-y)}}{q^2+i\epsilon}\, \Psi_{Sch,C}^{\dagger}(x) \\ & \times \left\{ J_e^0(y)\, F_1\left(q^2\right) \left[1 + \frac{1}{2}(Q_C + Q_B) \right] \right. \\ & \quad - \boldsymbol{J}_e(y) \cdot \left[i\kappa F_2\left(q^2\right) \frac{\boldsymbol{\sigma} \times \boldsymbol{q}}{2M} \right. \\ & \qquad \left. \left. + F_1\left(q^2\right) \left(\frac{\boldsymbol{\sigma}\, \boldsymbol{\sigma}\cdot\boldsymbol{p}}{M+E_B} + \frac{\boldsymbol{\sigma}\cdot\boldsymbol{p}\, \boldsymbol{\sigma}}{M+E_C} \right) \right] \right\} \Psi_{Sch,B}(x) . \qquad (3.23) \end{aligned}$$

We have written this equation in a form in which the integrations over the electron coordinate and the intermediate photon momentum have not been done. The expansion method does not depend on the plane wave approximation for the electrons, and electron distortions could be included if desired. The S-matrix to second order in $(E+M)^{-1}$ is similarly found by including the second-order nuclear current as well. We shall discuss the traditional nonrelativistic limit of the amplitude in subsection 3.2.2; but will concentrate in the following subsection on clarifying the role of the nuclear potentials in the convergence properties of the Pauli expansion of the S-matrix.

3.2.1 Convergence of the Expansion

In this subsection we discuss the convergence of the expansion obtained above to the fully relativistic calculation. In these convergence calculations, all of the factors in the expansion are the original relativistic ones. *This is not yet equivalent to a standard nonrelativistic calculation*! These nonrelativistic calculations are discussed in the next subsection.

The calculations of the relativistic S-matrix require knowledge of the Dirac wavefunctions for the bound and continuum states. For the bound state Hartree bound state wavefunctions are used [16]. The continuum wavefunctions for the knocked-out proton are obtained using the energy and A dependent optical potential of Cooper *et al.* [17]. We restrict our discussion to the case where the momentum of the knocked-out proton p is parallel to the momentum transfer q. This choice of the kinematics is called parallel kinematics and discussed in Appendix 3.A. In the diagrams referred to in the following discussion the curves are labelled according to which order in $(E + M)^{-1}$ the amplitude is calculated, and whether or not the Dirac potentials are included in the nuclear current operators: i) dotted curve – first order in $(E + M)^{-1}$ without nuclear potentials, we refer to these calculations as *medium-uncorrected* first order in the text; ii) dashed curve – first order including nuclear potentials which will be referred to as *medium-corrected* first order in text; iii) dot-dashed curve – second order without nuclear potentials, we refer to these calculations as medium-uncorrected second order in text; iv) dot-dot-dashed curve – second order including nuclear potentials which will be referred to as medium corrected second order; v) solid curve – fully relativistic calculation. In doing these comparisons we are attempting to clarify the convergence of the expansion and the role of the medium correction (the nuclear potentials that appear in the nuclear currents) in the rate of convergence of this expansion. The relativistic calculations are obtained using the relativistic code of Johansson [18]. Figure (3.2) shows observables as a function of missing momentum for the reaction $^{16}O(\ e, e'p\ )^{15}N$ leading to the ground state of ^{15}N , (3.2-a) is the spectral function while (3.2-b) is the proton polarization. The ground state of the residual nucleus, ^{15}N, is assumed to be a $1p_{\frac{1}{2}}$ hole state, i.e it has spin 1/2 and negative parity. The energy of the incident electron is 456 MeV, and the kinetic energy of the detected proton is fixed at 90 MeV with parallel kinematics. The relativistic calculations of the spectral function are fitted to the peak of the data [19]; the resulting "spectroscopic factor" is then used in all the other calculations for that particular state. (We adopt this simple fitting procedure because our main concern here is comparison between the different calculations, rather than a judicious determination of the spectroscopic factors.) Note that the medium-corrected calculations converge rapidly toward the fully relativistic results in this case, with the curve for the second order calculations being very close to the relativistic results over the range of momentum transfers shown. In calculating the spectral function, the inclusion of the medium correction to the first order interaction terms brings the results closer to the fully relativistic calculation than the medium-uncorrected second order. It must be stressed that the inclusion of the medium correction brings the results close to the fully relativistic results, while the medium-uncorrected calculations are quite far from the relativistic results and do not show a strong indication for convergence to the relativistic result.

Figure (3.3) shows the spectral function and proton polarization for the reaction on the ^{208}Pb target. The residual nucleus ^{207}Tl is in an excited state with spin 3/2 and positive parity which is assumed to be a $2d_{\frac{3}{2}}$ single particle state. The energy of the incident electron is 412 MeV, and the kinetic energy of the detected proton is fixed at 100 MeV with parallel kinematics. The data are those of Lapikás [19]. The spectral functions of figure (3.3-a) show that the medium-uncorrected first and second order calculations are far from the relativistic calculations. Including the effect of the medium in the second order calculations brings them close to the results of the relativistic calculations. Note that the medium-corrected first order calculations are closer to the relativistic calculations than medium-uncorrected second order.

Proton polarization calculations of figure (3.3-b) show that the inclusion of the medium correction in the reduced amplitudes produces large changes in the results. Note the suppression of the second order calculations due to medium correction, in the low missing momentum region, which brings the calculations closer to the relativistic ones. We have seen the same feature when the residual ^{207}Tl is left in the $3s_{\frac{1}{2}}$ ground state. The calculations of the reduced amplitude for heavy targets such as ^{208}Pb do not converge as fast as for the case of lighter targets. This is, however, because the radial integrals appearing in the expansion involve nuclear potentials, so for heavy nuclei these provide terms with larger contributions and slow down the convergence of the expansion.

The above results are of course expected on simple mathematical grounds. The essential point however, is to shed light on the role of the appearance of the potentials (medium correction) in the nuclear currents. We have seen no evidence that expansions that are based on free vertices (i.e. no nuclear potentials), will converge to the fully relativistic results, even if calculations are done to higher orders in the inverse of the nucleon mass [2]. This will have implications for the comparisons with the standard nonrelativistic calculations, which we discuss next.

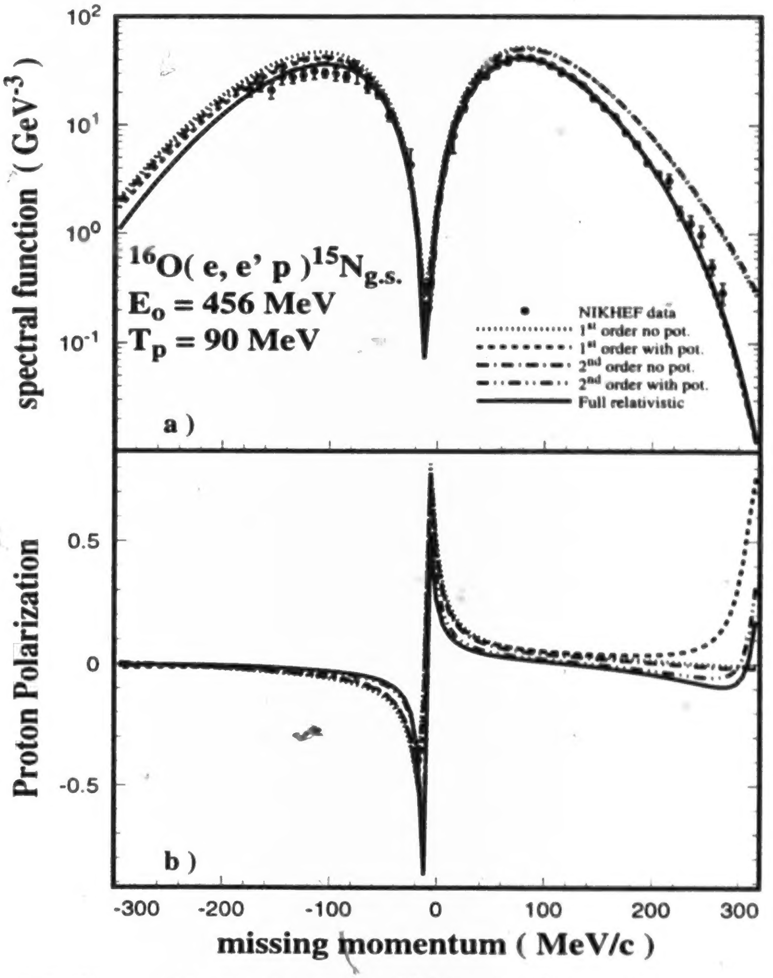

Figure 3.2: Observables for the reaction $^{16}O(\, e, e'p\,)^{15}N_{g.s.}$. The energy of the incident electron is 456 MeV, and the kinetic energy of the detected proton is fixed at 90 MeV with parallel kinematics. Hartree bound state wavefunctions are used [16] and the proton optical potentials are from [17]. The data are from reference [19]. (a) spectral function and (b) proton polarization. Curves are labelled according to their order in $(E+M)^{-1}$ and whether or not the medium corrections (through Dirac potentials) are included in the nuclear current operators: dotted curve – medium-uncorrected first order in $(E+M)^{-1}$; dashed curve – medium-corrected first order; dot-dashed curve – medium-uncorrected second order; dot-dot-dashed curve – medium-corrected second order; solid curve – fully relativistic calculations.

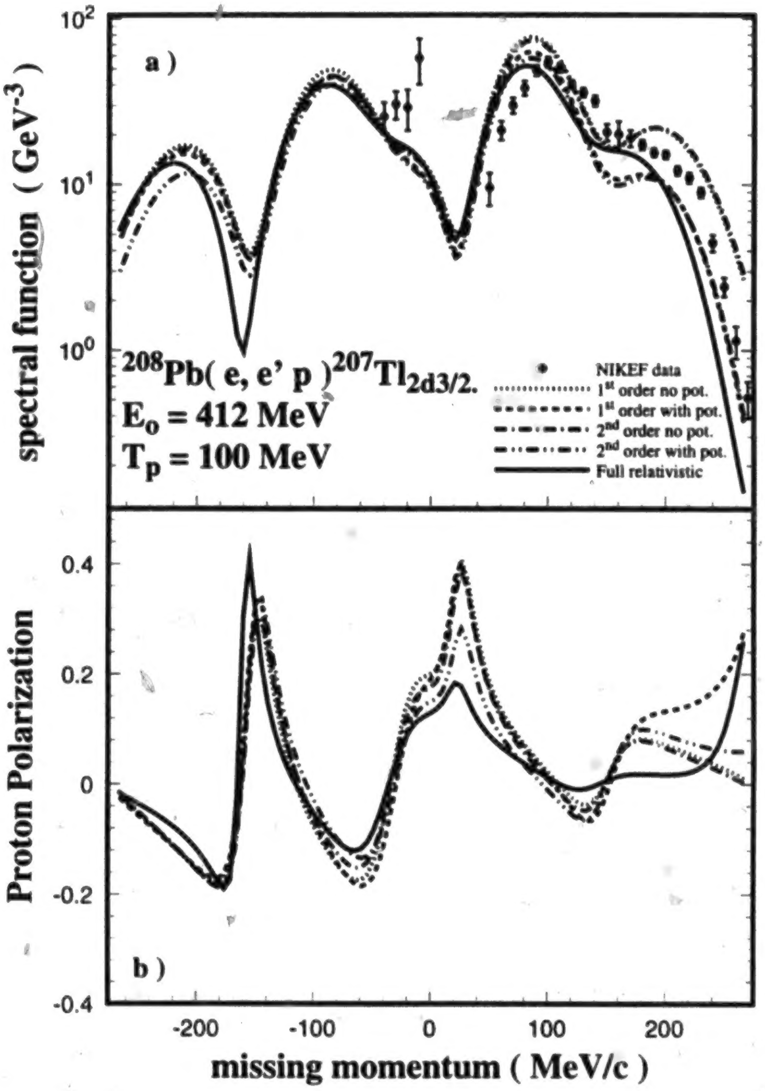

Figure 3.3: Observables for the reaction $^{208}Pb(\ e, e'p\ )^{207}(\ J^{\pi} = 3/2^{+}\ )$. (a) spectral function and (b) proton polarization. Curves are labelled as in figure(3.2). Potentials and data from the sources of figure (3.2).

3.2.2 The Nonrelativistic Limit

The expansion of the S-matrix in powers of $(E+M)^{-1}$ discussed above does not quite yield the amplitudes used in standard nonrelativistic calculations. Some care must be taken at this point in the discussion to differentiate between the correct nonrelativistic limit, and the standard operator used in nonrelativistic calculations. There are three more steps that must be followed in order to obtain the proper nonrelativistic limit from the relativistic amplitude:

> i) *The bound state wavefunction must be normalized to unity.* In the expansion obtained above, the Dirac bound state wave function is normalized to unity and the related Schrödinger-equivalent wavefunction is not. In the nonrelativistic calculations it is the Schrödinger-equivalent wave function that must be normalized.
>
> ii) *The continuum wavefunction must be normalized correctly.* The factors arising from the Dirac field and the normalization of the Dirac wave function result in a factor of $(E+M)/2E$ being set equal to one to obtain the nonrelativistic expression for the cross section, (this is equivalent to multiplying the right-hand-side of equation (3.12) by the inverse of this factor).
>
> iii) Finally, to obtain nonrelativistic expressions for the nuclear current operators from the relativistic expressions of equation (3.21), *the nucleon energies (both continuum and bound) are set equal to the nucleon mass, i.e.* $E \rightarrow M$.

It is important to note that these changes still have not yielded the standard nonrelativistic amplitudes because the nuclear current operators at this stage contain the effects of the nuclear medium, through the Dirac potentials, explicitly. This is an essential difference between the relativistic and nonrelativistic approaches, and the presence of these potentials can lead to large differences in the observables obtained via relativistic and nonrelativistic approaches. In order to obtain the usual nonrelativistic expression, the effects of the nuclear medium (i.e Dirac potentials) must be removed from the nuclear current operators. When this is done, the nonrelativistic equivalent of the S-matrix of equation (3.23) yields the usual first order nonrelativistic transition amplitude used by many authors [2, 6]. When terms to second order are included in the nonrelativistic S-matrix, and in the limit of no medium correction, there are some differences between our expression and the usual nonrelativistic second order S-matrix, which is obtained via a Foldy-Wouthuysen transformation of the interaction between electrons and free nucleons [2]. Fearing, Poulis and Scherer [20] have compared Foldy-Wouthuysen and Pauli reductions of a Dirac Hamiltonian containing a generic potential with harmonic time dependence. They found that differences do occur beyond first order in $1/M$. Detailed calculations show that these differences between the Pauli and Foldy-Wouthuysen reductions are small when the medium corrections are ignored in the nuclear current operators. This seems the only consistent way to compare the operators since we use two different Hamiltonians for the Pauli calculations.

We discuss below the effects that the medium corrections of the nonrelativistic current operators have on calculated observables.

3.3 Results of nonrelativistic Calculations

We now make comparisons between relativistic and nonrelativistic calculations based on the discussions presented above. In figure (3.4) we show results for the reaction on an ^{16}O target with the same kinematics as in figure (3.2). Figure (3.4-a) shows the spectral function while (3.4-b) shows the proton polarization. The nonrelativistic calculations show the same effects due to the inclusion of the nuclear potentials in the interaction operators that we saw in the corresponding convergence calculations of figure (3.2). Medium-uncorrected first and second order calculations (dotted and dot-dashed curves respectively) yield very similar results. This is generally true in the cases we have considered; going from first to second order in $1/M$ does little to move the results in the direction of the relativistic calculations. For the medium-corrected calculations, a somewhat larger change is noticeable in going from first order to second order calculations, particularly at larger values of missing momentum (see figure 3.4-b). Note that the nonrelativistic calculations for the spectral function converge to a lower (i.e. below the relativistic calculation) value than the simple expansion in powers of $(E+M)^{-1}$ as found in figure (3.2). This is because of the normalization of the Schrödinger-equivalent bound state wavefunction to unity (this results in the nonrelativistic expansion converging at a point which is not the relativistic one). Spin observables are not affected by changes in overall normalization, so the proton polarization calculations shown in figure (3.4-b) are very similar to those shown in figure (3.2-b), with slight differences coming from the replacement $E \rightarrow M$ in the nonrelativistic nuclear current operators.

Figure (3.5) emphasizes the behavior of the spectral function for the high missing momentum region of figure (3.4-a), with the missing momentum in the range 150 MeV/c to 300 MeV/c. In this region the medium-uncorrected first and second order calculations lie above the relativistic calculations, while the inclusion of potentials in first and second order (i.e medium-corrected) moves the results to lie below the relativistic results. Note that the the relativistic calculations were fitted to the data in the low missing momentum region, but still do rather well for high missing momenta. Medium-uncorrected calculations diverge from the relativistic calculations as the magnitude of the missing momentum is increased. On the other hand, medium-corrected calculations remain close to the relativistic results over a wide range of

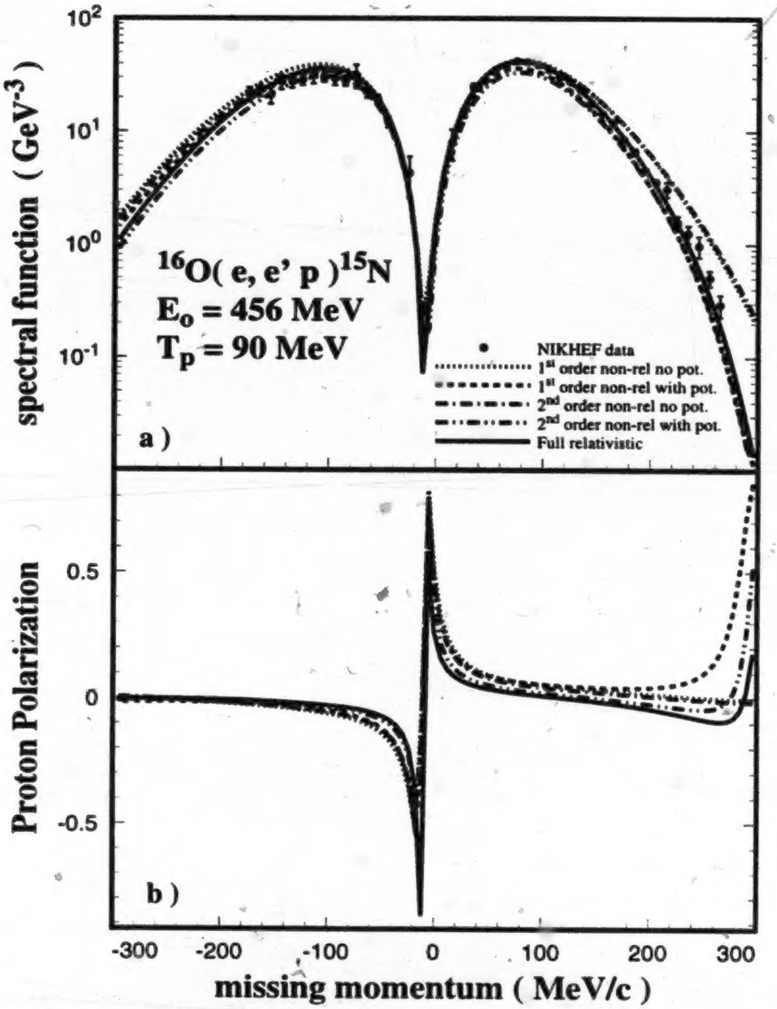

Figure 3.4: Observables for the reaction $^{16}O(\ e, e'p\ )^{15}N_{g.s.}$. The kinematics are those of figure (3.2). Curves are labelled according to their order in $1/M$ and whether or not the Dirac potentials are included in the nuclear current operators: dotted curve - nonrelativistic calculations, medium-uncorrected first order in $(M)^{-1}$; dashed curve - medium-corrected first order; dot-dashed curve - medium-uncorrected second order; dot-dot-dashed curve - medium-corrected second order; solid curve - fully relativistic calculation. Potentials and data from the sources of figure (3.2).

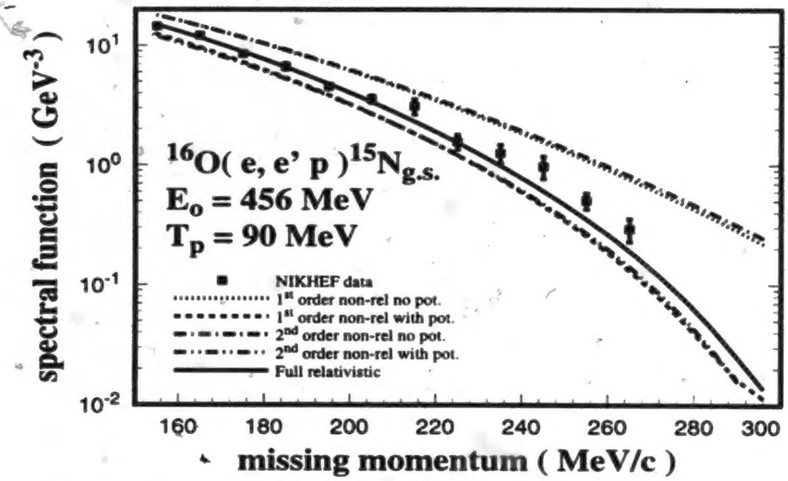

Figure 3.5: Spectral function for $^{16}O(\ e,\ e'p\ )^{15}N_{g.s.}$. The kinematics are those of figure (3.2). Curves labelled as in figure (3.4). Potentials and data from the sources of figure (3.2).

missing momenta. Note that we are only including terms to second order in the inverse mass. We have also done similar calculations for the same target but leaving the residual nucleus in an excited state (^{15}N is left in a 1p$_{3/2}$ hole state), as well as using different targets, namely ^{40}Ca and ^{90}Zr, with the residual nucleus left in both ground and excited states (for the excited states the residual nuclei ^{39}K and ^{89}Y are left in the even parity 1/2 and odd parity 5/2 states, respectively. Shell model assigns 2s$_{1/2}$ and 1f$_{5/2}$ for these states.) These calculations show the same behavior as those shown in figure (3.4).

Figure (3.6) shows similar calculations to those of figure (3.4) but for a ^{208}Pb target. The residual nucleus ^{207}Tl is left in an even parity $\frac{3}{2}$ state which is taken to be the $2d_{\frac{3}{2}}$ hole state. The kinematic conditions are those of figure (3.3). The spectral functions of figure (3.6-a) show significant changes when the effects of the nuclear medium are included in nonrelativistic calculations. Medium-corrected calculations lie blow the medium-uncorrected calculations in the entire missing momentum range considered. In the large positive missing momentum region these differences are more pronounced; medium-corrected calculations are roughly one order of magnitude lower than the medium-uncorrected calculations.

The proton polarizations (figure 3.6-b) show the same behavior as those of figure (3.3-b) except for small differences in the nonrelativistic calculations here due to the replacement $E \rightarrow M$ in the nuclear current operators. The same feature as results presented in figure (3.6) is seen for the results of the calculations of the reaction when the recoil nucleus is left in the ground state.

Figure (3.7) shows the calculations of the spectral function and proton polarization for the same reaction discussed in figure (3.4). In the present case, the energy of the incident electron is 2000 MeV, and the kinetic energy of the detected proton is fixed at 400 MeV. The larger energies allow for a much larger range of missing momenta than considered previously. Note that the medium-uncorrected first and second order calculations of the spectral function differ from the relativistic calculations by up to an order of magnitude for large missing momenta, while medium-corrected calculations are much closer to the fully relativistic results. In addition we see that for low missing momenta the convergence point is lower than the relativistic (see insert). The (γ, p) reaction, studied in the previous chapter, shows behavior consistent with these observations for ($e, e'p$) at high missing momentum. The momentum transfer in the (γ, p) reaction is generally in the range 400 MeV/c to 600 MeV/c so these two reactions can both probe this part of the single particle bound state wavefunction.

Proton polarization results are shown in figure (3.7-b). In the region of large missing momentum there are large differences between the medium-corrected and medium-uncorrected calculations. The medium corrected first and second order calculations yield results close in magnitude and shape to the results of the fully relativistic calculations. Note in particular, that in the region of the minimum and maximum in the relativistic calculations close to $p_m = -400 MeV/c$ and $p_m = 400 MeV/c$ respectively, the medium-uncorrected calculations do not reproduce the shape of the relativistic calculations at all. The effects of the medium (nuclear potentials) must be included in the nuclear current operators in order to get close to the relativistic results. In particular a measurement of the proton polarization near $p_m = -400 MeV/c$ provides a clear opportunity to differentiate between relativistic and nonrelativistic models. Note the cross section for the reaction at this missing momentum is very small. reaction.

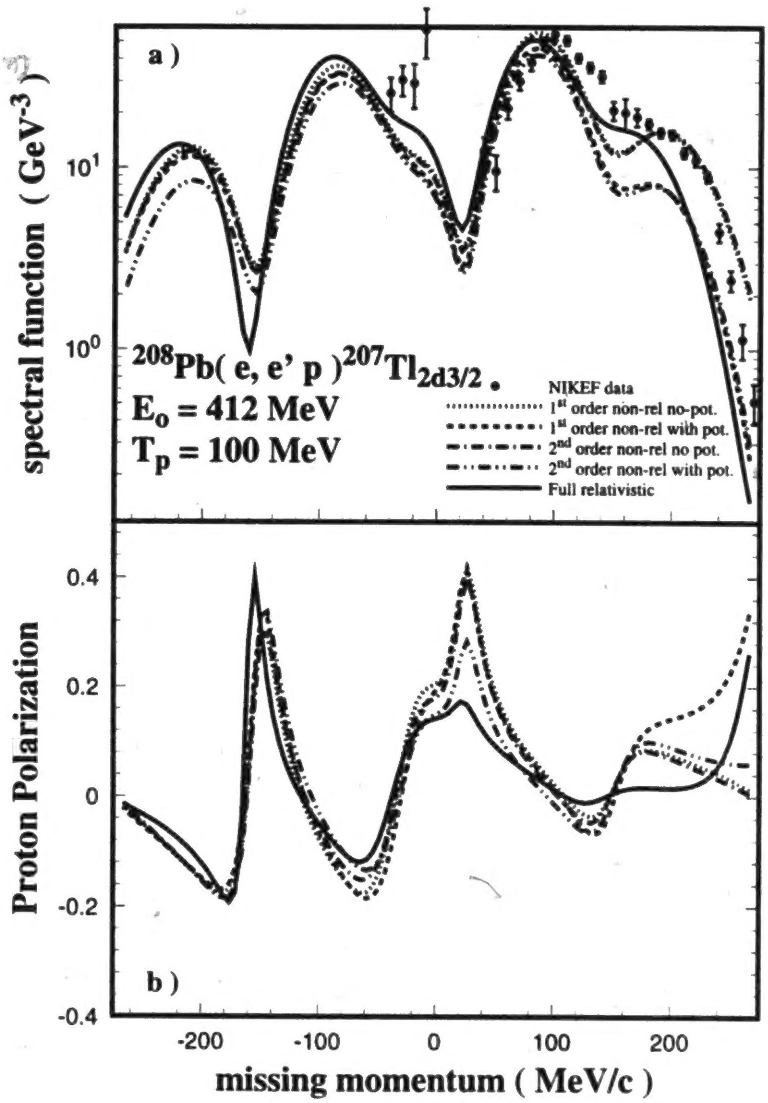

Figure 3.6: Observables for $^{208}Pb(\, e, e'p\,)^{207}Tl$ where ^{207}Tl is in the $2d_{\frac{3}{2}}$ state. Curves labelled as in figure (3.4). Potentials and data from the sources of figure (3.2).

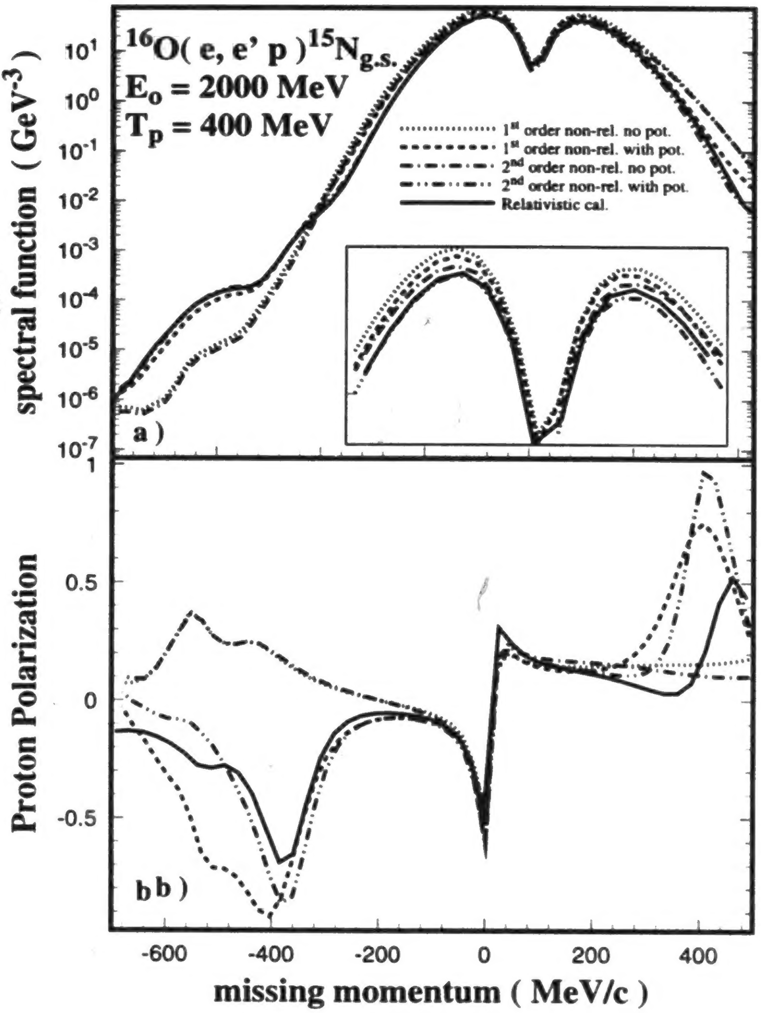

Figure 3.7: Observables for $^{16}O(\ e,\ e'p\ )^{15}N$ where ^{15}N is in the $1p_{\frac{1}{2}}$ state. The energy of the incident electron is 2000 MeV, and the kinetic energy of the detected proton is fixed at 400 MeV with parallel kinematics. Curves labelled as in figure (3.4). Potentials from the source of figure (3.2).

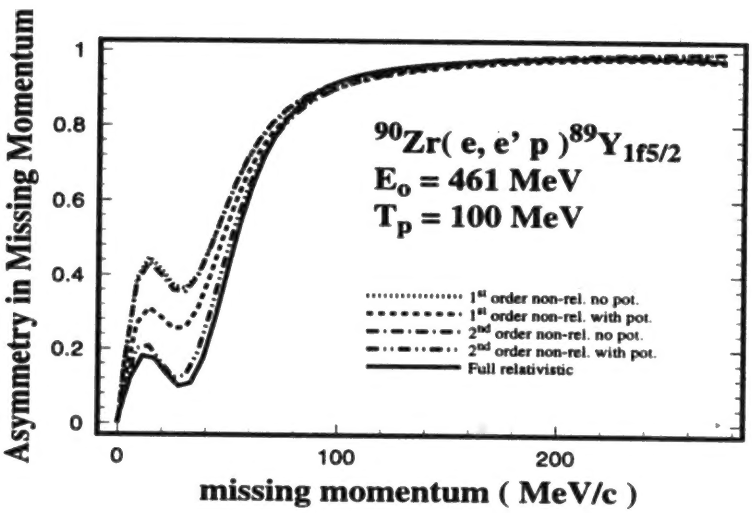

Figure 3.8: Asymmetry in missing momentum for $^{90}Zr(e, e'p)^{89}Y$ where ^{89}Y is in the $1f_{\frac{5}{2}}$ state. The energy of the incident electron is 461 MeV, and the kinetic energy of the detected proton is fixed at 100 MeV with parallel kinematics. Curves labelled as in figure (3.4). Potentials from the source of figure (3.2).

Calculations of the asymmetry parameter of equation (3.15), for small values of angular momentum L of the bound nucleon ($L \leq 2$), yield similar results for all the options under discussion whether fully relativistic; or nonrelativistic first or second order, with or without medium correction to the nuclear current operator. When the angular momentum of the bound nucleon is increased, the differences between these calculations of the asymmetry become larger, as is evident in figure (3.8). The asymmetry is calculated for a ^{90}Zr target, with the residual state in ^{89}Y assumed to be a $1f_{\frac{5}{2}}$ proton hole. The incident electron has an energy of 461 MeV, and the kinetic energy of the detected proton is fixed at 100 MeV. In this case the differences are particularly apparent for missing momenta in the neighborhood of 20 MeV/c.

3.4 Conclusions

In order to clarify the differences arising from relativistic and nonrelativistic descriptions of quasifree electron scattering [3, 5], we have discussed an expansion of the S-matrix for the reaction ($e, e'p$) in powers of $(E+M)^{-1}$ through the effective Pauli scheme. The resulting S-matrix depends on Schrödinger-like wave functions for the bound and continuum nucleons, and nuclear current operators which contain the strong Dirac potentials at the different orders. When the Dirac potentials are included in the nuclear current operators, the series essentially converges to the fully relativistic results at second order for light- to medium-mass nuclei. When the potentials are not included in the nuclear currents, the calculations can be far from the relativistic results particularly for larger missing momenta. This indicates the importance of the role played by the nuclear potentials in the modification of the currents. The convergence slows down when reactions on heavy targets like ^{208}Pb are considered. This is largely due to the effect of the size of the nucleus on the rate of convergence of the expansion.

These points were further studied in setting up a comparison between relativistic and nonrelativistic calculations. A proper nonrelativistic calculation is obtained through several steps: normalization of the bound Schrödinger-like wavefunction to unity, proper normalization of the continuum Schrödinger-like wavefunction, and setting $E = M$ in the nuclear current operators. An additional step of removing the Dirac potentials from the resulting nuclear current operators yields the standard nonrelativistic amplitude. This results in a consistent and fair comparison between the relativistic and nonrelativistic calculations. The potentials used for the bound and continuum protons yield both the relativistic and nonrelativistic wavefunctions, with normalizations handled appropriately. This eliminates any discrepancy between the results coming from the use of different potentials.

The nonrelativistic calculations we have shown for first and second order nuclear current operators without potentials give the same results that a standard nonrelativistic calculation would give if provided with the Schrödinger equivalent wavefunctions derived from the Dirac equation.

Inclusion of the nuclear potentials in the nonrelativistic nuclear current operator results in a large change in the calculated observables. In particular, calculations of the spectral function and final proton polarization using second order nuclear current operators, to a large extent, can reproduce the magnitude and shape of the fully relativistic calculations. This is true even at large missing momenta where the nonrelativistic calculations without potentials in the nuclear current operators yield very different results than the fully relativistic calculations. The polarization of the final proton is particularly sensitive to differences in the calculations, and measurements of this observable at large missing momenta could assist in the choice between the relativistic and nonrelativistic approaches.

We have also calculated the asymmetry defined in the text for the different orders, with and without potentials, and found that in cases in which the angular momentum of the bound nucleon is less than 2, there are no noticeable differences between these calculations and the fully relativistic ones. When the orbital angular momentum of the bound nucleon is greater than 2, differences between these calculations do appear. This observable thus will be useful in differentiating between relativistic and nonrelativistic models only for nuclear states with large orbital angular momentum.

Other groups have examined the sensitivity of the models to changes in the optical potentials and modifications of the wavefunctions [7, 8, 9], and have found sensitivities at the level of 15%. However, the essential differences between the relativistic and nonrelativistic approaches do not lie in modifications of the wavefunctions.

The essential difference comes from the appearance of the nuclear potentials in the nuclear current operators, as a result of the reduction of the relativistic amplitude. We emphasize that *these nuclear medium effects, characteristic of the present model, will not appear through a nonrelativistic impulse description of the process*. They are, however, inherent in the relativistic description.

Bibliography

[1] S. Frullani and J. Mougey, *Advances in Nuclear Physics*, edited by J.W. Negele and E. Vogt, **14** (1984) 1.

[2] S. Boffi, C. Giusti and F.D. Pacati, Nucl. Phys. **A336** (1980) 416; Nucl. Phys. **A336** (1980) 427.

[3] J.P. McDermott, Phys. Rev. Lett. **65** (1990) 1991.

[4] Y. Jin, D.S. Onley and L.E. Wright, Phys. Rev. C **45** (1992) 1311.

[5] J.M. Udías, P. Sarriguren, E. Moya de Guerra, E. Garrido and J.A. Caballero, Phys. Rev. C **48** (1993) 2731.

[6] K.W. McVoy and L. Van Hove, Phys. Rev. **125** (1962) 1034.

[7] S. Boffi, C. Giusti, F.D. Pacati and F. Cannata, Il Nuovo Cimento **98A** (1987) 291.

[8] J.M. Udías, P. Sarriguren, E. Moya de Guerra, E. Garrido and J.A. Caballero, Phys. Rev. C **51** (1995) 3246.

[9] Yanhe Jin and D.S. Onley, Phys. Rev. C **50** (1994) 377.

[10] H.S. Sherif, R.I. Sawafta and E.D. Cooper, Nucl. Phys.**A449** (1986) 709.

[11] F. Mandl and G. Shaw, *Quantum Field Theory*, John Wiley & Sons Publishing company, 1986

[12] T. de Forest Jr., Nucl. Phys. **A392** (1983) 232.

[13] W.S.C. Williams, *An Introduction to Elementary Particles* , secomd edition, Acadomic Press, 1971; D.H. Perkins, *Introduction to High Energy Physics*, third edition, Addison-Wesley Publishing company, 1987

[14] A. Bianconi, S. Boffi and D.E. Kharzeev, Phys. Rev. C **49** (1994) 1243.

[15] J.D. Bjorken and S.D. Drell, *Relativistic Quantum Mechanics*, McGraw-Hill Book Company (1964).

[16] C.G. Horowitz and B.D. Serot, Nucl. Phys. **A368** (1986) 503.

[17] E.D. Cooper, S. Hama, B.C. Clark and R.L. Mercer, Phys. Rev. C **47** (1993) 297.

[18] J. I. Johansson, private communication.

[19] L. Lapikás, Nucl. Phys. **A553** (1993) 297.

[20] H.W. Fearing, G.I. Poulis and S. Scherer, Nucl. Phys. **A570**, (1994) 657.

[21] M. Bernheim *et al.*, Nucl. Phys. **A375** (1982) 381

Appendix 3.A Kinematics

In this appendix we will calculate all the kinematic variables, needed for the calculations of the $A(e,\ e'p)A-1$ reaction, in terms of the four-momentum of the initial electron, four-momentum of outgoing proton , angles of final electron, and missing momentum of initial proton. It is useful to introduce the following variables,

k_i: incident electron four-momentum in the laboratory frame

k_f: outgoing electron four-momentum in the laboratory frame

p_T: target four-momentum in the laboratory frame

p_R: recoil nucleus four-momentum in the laboratory frame

q : intermediate photon four-momentum (so called momentum transfer).

p_f: ejected nucleon four-momentum in the laboratory frame

p_i: struck nucleon (in the nucleus) four-momentum in the laboratory frame (it is also called missing momentum).

In the DWIA, the residual nucleus is a spectator and its momentum is unchanged, while the reaction proceeds on the struck nucleon, so

$$\mathbf{p}_T = \mathbf{p}_i + \mathbf{p}_R \tag{3.24}$$

The 4-momentum conservation yields

$$k_i + p_T = k_f + p_f + p_R. \tag{3.25}$$

From this equation we can write the corresponding equations for energies and momenta of the particles as

$$\begin{aligned} E_i^e + M_T &= E_f^e + E_f^P + E_R \\ \boldsymbol{p}_R = \boldsymbol{k}_i - \boldsymbol{k}_f - \boldsymbol{p}_f &= \boldsymbol{q} - \boldsymbol{p}_f. \end{aligned} \tag{3.26}$$

Note for our case $\boldsymbol{p}_T = 0$. We also have

$$\boldsymbol{p}_i = \boldsymbol{p}_f - \boldsymbol{q} \tag{3.27}$$

from (3.24) and (3.27) we can write

$$\boldsymbol{q} = \boldsymbol{p}_R + \boldsymbol{p}_f \tag{3.28}$$

We have the following relation between mass of the target and recoil nucleus

$$M_R = M_T - M_P + E_B, \tag{3.29}$$

where E_B is the binding energy of the initial proton. Having defined these quantities, we now introduce the parallel kinematics used in calculations of the $(e, e'p)$ reaction.

Parallel Kinematics

In the parallel kinematics, the momentum of the final proton $\boldsymbol{p}_f$ is parallel to the momentum transfer $\boldsymbol{q}$ and $|\boldsymbol{p}_f|$ is fixed (i.e E_P is fixed). There are two values of $\boldsymbol{p}_R$ for each $\boldsymbol{p}_f$, which we assign the positive (negative) value to $\boldsymbol{p}_R$ through the condition $|\boldsymbol{q}| > |\boldsymbol{p}_f|$ ($|\boldsymbol{q}| < |\boldsymbol{p}_f|$). Distribution in $\boldsymbol{p}_R$ is obtained by varying the transformed momentum $\boldsymbol{q}$ (moving the detectors for the two outgoing particles) [21].

For these kinematic conditions the kinetic energy of the incident electron and the energy of the outgoing proton are given and we want to find the distribution of the observable quantities over the recoil momentum $\boldsymbol{p}_R$, so we have

$$\begin{aligned} E_f^e &= E_i^e + M_T - E_R - E_f^P \\ E_R &= \sqrt{\boldsymbol{p}_R^2 + M_{R^2}} \\ q^0 &= E_i^e - E_f^e \end{aligned} \tag{3.30}$$

The angle between the incident and final electron can be found as

$$cos\theta_e = \frac{k_i^2 + k_f^2 - q^2}{2k_ik_f} \tag{3.31}$$

We assume that the reaction is co-plane, i.e $\phi_e = 0$. The angle between $\boldsymbol{q}$ and the incident electron is obtained as

$$cos\theta_q = \frac{k_i - k_f cos\theta_e}{q}. \tag{3.32}$$

This is the same as θ_p, the polar angle for the outgoing proton. For the recoil nucleus

$$\begin{aligned} &\theta_R = \theta_q \qquad &\phi_R = \pi \qquad &\text{for} \qquad \boldsymbol{p}_R > 0 \\ &\theta_R = \pi - \theta_q \qquad &\phi_R = 0^0 \qquad &\text{for} \qquad \boldsymbol{p}_R < 0 \end{aligned} \tag{3.33}$$

Appendix 3.B Current Operators

In this appendix we start from equation (3.19) and obtain the reduced current used in nonrelativistic calculations. Let us rewrite the nuclear current of (3.19) as

$$
\begin{aligned}
J^{\mu} = \Psi^{\dagger}_{Sch,C} \Bigg\{ & D_C^{1/2}(r) \left[1, \frac{\boldsymbol{\sigma} \cdot \boldsymbol{p}}{M + E_C + S_C(r) - V_C(r)} \right] \\
& \times \gamma^{o} \left[F_1 \gamma^{\mu} + F_2 \frac{i\kappa}{2M} \sigma^{\mu\nu} q_{\nu} \right] \qquad (3.34) \\
& \times \begin{bmatrix} 1 \\ \dfrac{\boldsymbol{\sigma} \cdot \boldsymbol{p}}{M + E_B + S_B(r) - V_B(r)} \end{bmatrix} D_B^{1/2}(r) \Bigg\} \Psi_{Sch,B}.
\end{aligned}
$$

The corresponding equation for the zero component of the nuclear current above is

$$
\begin{aligned}
J^{o} = \Psi^{\dagger}_{Sch,C} \Bigg\{ & D_C^{1/2}(r) \left[1, \frac{\boldsymbol{\sigma} \cdot \boldsymbol{p}}{M + E_C + S_C(r) - V_C(r)} \right] \\
& \times \left[F_1 + F_2 \frac{\kappa}{2M} \boldsymbol{\gamma} \cdot \boldsymbol{q} \right] \qquad (3.35) \\
& \times \begin{bmatrix} 1 \\ \dfrac{\boldsymbol{\sigma} \cdot \boldsymbol{p}}{M + E_B + S_B(r) - V_B(r)} \end{bmatrix} D_B^{1/2}(r) \Bigg\} \Psi_{Sch,B}
\end{aligned}
$$

The effective Pauli reduction is performed on the object between the braces of the above equation. This involves expanding both $D^{1/2}(r)$ from equation (3.35) and the factor $[E + M + S(r) - V(r)]^{-1}$ in powers of $(E + M)^{-1}$, where E and M are the energy and mass of the proton respectively.

This procedure leads to an expansion of the zero component of the reduced nuclear current operators as

$$
J^{0}(x) = \Psi^{\dagger}_{Sch,C}(x) \left[j^{0}_{(0)} + j^{0}_{(1)} + j^{0}_{(2)} + \cdots \right] \Psi_{Sch,B}(x) \qquad (3.36)
$$

The time components of the reduced current operators up to second order in $\frac{1}{M}$ are.

$$\begin{aligned}
j^o_{(0)} = &\quad eF_1 \\
j^o_{(1)} = &\quad \frac{eF_1}{2}\left[Q_C + Q_B\right] \\
j^o_{(2)} = &\quad eF_1\left[\frac{Q_C Q_B}{4} - \frac{Q_C^2 + Q_B b^2}{8} + \frac{\boldsymbol{\sigma}\cdot\boldsymbol{p}}{M+E_C}\frac{\boldsymbol{\sigma}\cdot\boldsymbol{p}}{M+E_B}\right] \\
+ &\quad \frac{E\kappa F_2}{2M}\left[\frac{\boldsymbol{\sigma}\cdot\boldsymbol{q}\ \boldsymbol{\sigma}\cdot\boldsymbol{p}}{M+E_B} - \frac{\boldsymbol{\sigma}\cdot\boldsymbol{p}\ \boldsymbol{\sigma}\cdot\boldsymbol{q}}{M+E_C}\right]
\end{aligned} \tag{3.37}$$

The space components of the nuclear current equation (3.34) are

$$\begin{aligned}
J^i \;=\; \Psi^\dagger_{Sch,C} \Bigg\{ & D_C^{1/2}(r)\left[1,\ \frac{\boldsymbol{\sigma}\cdot\boldsymbol{p}}{M+E_C+S_C(r)-V_C(r)}\right] \\
\times & \left[F_1\alpha^i + F_2\frac{i\kappa}{2M}\gamma^0\sigma^{i\nu}q_\nu\right] \\
\times & \left[\begin{array}{c} 1 \\ \\ \dfrac{\boldsymbol{\sigma}\cdot\boldsymbol{p}}{M+E_B+S_B(r)-V_B(r)} \end{array}\right] D_B^{1/2}(r)\Bigg\}\Psi_{Sch,B}
\end{aligned} \tag{3.38}$$

Expanding both $D^{1/2}(r)$ from equation (3.38) and the factor $\left[E+M+S(r)-V(r)\right]^{-1}$ in powers of $(E+M)^{-1}$ as before, the following expansion is found for the space components of the nuclear current

$$\mathbf{J}(x) = \Psi^\dagger_{Sch,C}(x)\left[\mathbf{j}_{(0)} + \mathbf{j}_{(1)} + \mathbf{j}_{(2)} + \cdots\right]\Psi_{Sch,B}(x) \tag{3.39}$$

where the space components of the reduced current operators up to second order in inverse of the nucleon mass are,

$$\begin{aligned}
\mathbf{j}_{(0)} = &\quad 0 \\
\mathbf{j}_{(1)} = &\quad \frac{ie\kappa F_2}{2M}\boldsymbol{\sigma}\times\boldsymbol{q} + eF_1\left[\frac{\boldsymbol{\sigma}\ \boldsymbol{\sigma}\cdot\boldsymbol{p}}{M+E_B} + \frac{\boldsymbol{\sigma}\cdot\boldsymbol{p}\ \boldsymbol{\sigma}}{M+E_C}\right] \\
\mathbf{j}_{(2)} = &\quad \frac{ie\kappa F_2}{4M}\left[Q_B + Q_C\right]\boldsymbol{\sigma}\times\boldsymbol{q} + \frac{eF_1 Q_B}{2}\left[\frac{\boldsymbol{\sigma}\ \boldsymbol{\sigma}\cdot\boldsymbol{p}}{M+E_B} + \frac{\boldsymbol{\sigma}\cdot\boldsymbol{p}\ \boldsymbol{\sigma}}{M+E_C}\right] \\
+ &\quad \frac{eF_1}{2}\left[\frac{\boldsymbol{\sigma}\ \boldsymbol{\sigma}\cdot\boldsymbol{p}}{M+E_B} + \frac{\boldsymbol{\sigma}\cdot\boldsymbol{p}\ \boldsymbol{\sigma}}{M+E_C}\right]Q_B
\end{aligned}$$

$$
\begin{aligned}
- \quad & eF_1 \left[Q_B \frac{\boldsymbol{\sigma}\ \boldsymbol{\sigma}\cdot\boldsymbol{p}}{M+E_B} + \frac{\boldsymbol{\sigma}\cdot\boldsymbol{p}\ \boldsymbol{\sigma}}{M+E_C} Q_C \right] \\
+ \quad & \frac{e\kappa F_2 q_o}{2M} \left[\frac{\boldsymbol{\sigma}\ \boldsymbol{\sigma}\cdot\boldsymbol{p}}{M+E_B} - \frac{\boldsymbol{\sigma}\cdot\boldsymbol{p}\ \boldsymbol{\sigma}}{M+E_C} \right] \qquad (3.40)
\end{aligned}
$$

Appendix 3.C Observables

Cross section

The cross section for (e, $e'p$) reaction can be found along the same procedure as we used for the (γ, p) reaction in Appendix 2.B, with the following modifications:

1) the incident electron current is

$$j_{in} = \frac{v_e^i}{(2\pi)^3} = \frac{p_e^i}{(2\pi)^3 E_e^i}, \tag{3.41}$$

where v_e^i, p_e^i, and E_e^i are velocity, momentum, and energy of the incident electron respectively.

2) the phase space integral is

$$\int \frac{|\, S_{fi} \,|^2}{T} \frac{1}{j_{in}} d^3p_p d^3p_e, \tag{3.42}$$

where S_{fi} is S-matrix for the (e, $e'p$) reaction and T is the reaction time and p_p, p_e are momenta of the outgoing proton and electron, respectively.

Proton Polarization

Let us first define a normalized density matrix for the proton as

$$\rho_{\mu\mu'} = \frac{\sum_{\nu_f\nu_i M_B} Z^{\mu M_B}_{\nu_f\nu_i} Z^{*\mu' M_B}_{\nu_f\nu_i}}{\sum_{\nu_f\nu_i\mu M_B} |Z^{\mu M_B}_{\nu_f\nu_i}|^2}, \tag{3.43}$$

The elements of this density matrix are arranged as follow

$$\begin{bmatrix} \rho_{\frac{1}{2}\frac{1}{2}} & \rho_{\frac{1}{2}-\frac{1}{2}} \\ \rho_{-\frac{1}{2}\frac{1}{2}} & \rho_{-\frac{1}{2}-\frac{1}{2}} \end{bmatrix}. \tag{3.44}$$

The proton polarization in the y direction is then

$$\begin{aligned} P_y &= Tr < \rho\sigma_y >= Tr \begin{bmatrix} i\rho_{\frac{1}{2}-\frac{1}{2}} & -i\rho_{\frac{1}{2}\frac{1}{2}} \\ i\rho_{-\frac{1}{2}-\frac{1}{2}} & -i\rho_{-\frac{1}{2}\frac{1}{2}} \end{bmatrix} \\ &= i\left(\rho_{\frac{1}{2}-\frac{1}{2}} - \rho_{-\frac{1}{2}\frac{1}{2}}\right). \end{aligned} \tag{3.45}$$

Using equation (3.43) for ρ we can rewrite the proton polarization P_y as

$$\begin{aligned} P_y &= i\frac{\sum_{\nu_f\nu_i M_B} Z_{\nu_f\nu_i}^{\frac{1}{2}M_B} Z_{\nu_f\nu_i}^{*-\frac{1}{2}M_B} - Z_{\nu_f\nu_i}^{-\frac{1}{2}M_B} Z_{\nu_f\nu_i}^{*\frac{1}{2}M_B}}{\sum_{\nu_f\nu_i\mu M_B} |Z_{\nu_f\nu_i}^{\mu M_B}|^2} \\ &= -\frac{2Im \sum_{\nu_f\nu_i M_B} Z_{\nu_f\nu_i}^{\frac{1}{2}M_B} Z_{\nu_f\nu_i}^{*-\frac{1}{2}M_B}}{\sum_{\nu_f\nu_i\mu M_B} |Z_{\nu_f\nu_i}^{\mu M_B}|^2} \qquad (3.46) \end{aligned}$$

Appendix 3.D Factorization of The PWIA Cross section

The impulse approximation for the $(e,\ e'p)$ reaction allows us to assume that the total momentum transfer is absorbed by the knocked-out nucleon. Conservation of 4-momentum in the reaction along with the above assumption lead to the determination of the energy and momentum of the nucleon within the nucleus. Thus from the coincidence measurement of the $(e,\ e'p)$ reaction we are able to obtain the combined energy and momentum distribution of the nucleon, the so called *spectral function*, inside the nucleus.

In this appendix we show that, in the limit of the plane wave approximation (PWIA), the cross section of the $(e,\ e'p)$ reaction can be factorized to the cross section of the elementary reaction multiplied by a kinematic factor, and a function of the momentum of the initial bound proton called the spectral function.

Starting from the relativistic Lagrangian describing interaction of photons with electrons and protons, one can find the S-matrix for the the $(e,\ e'p)$ reaction as [11]

$$S_{fi} \;=\; e^2 \int d^4x d^4y < f|N\{[\bar{\psi}(x)\gamma_\alpha \psi(x)]\underline{A^\alpha(x)A^\beta(y)}[\bar{\psi}_p(y)\gamma_\beta \psi_p(y)]\}|i >. \tag{3.47}$$

where the field operators ψ_p and ψ describe the proton and electron, respectively, and N refers to the normal ordering of the field operators. $-i\underline{A^\alpha(x)A^\beta(y)}$ is the photon propagator, and initial state of the system can be specified as

$$|i >= b^\dagger_{\nu_i}(\boldsymbol{k}^e_i)|\phi^{M_i}_{J_i} > \tag{3.48}$$

where $b^\dagger_{\nu_i}(\boldsymbol{k}^e_i)$ creates an electron (charge -e) with momentum $\boldsymbol{k}^e_i$ and spin projection ν_i. $|\phi^{M_i}_{J_i} >$ is the initial nuclear state of the target nucleus with angular momentum J_i and projection M_i. The final state is described as

$$|f >= b^\dagger_{\nu_f}(\boldsymbol{k}^e_f)b^\dagger_{\mu}(\boldsymbol{k}_p)|\phi^{M_f}_{J_f} > \tag{3.49}$$

where $b^\dagger_{\nu_f}(\boldsymbol{k}^e_f)$ creates an electron (charge -e) with momentum $\boldsymbol{k}^e_f$ and spin projection ν_f. $b^\dagger_\mu(\boldsymbol{k}_p)$ creates a proton (charge +e) with momentum $\boldsymbol{k}_p$. $|\phi^{M}_{J_f} >$ describes the residual nucleus with angular quantum number J_f and projection M_f.

Let us first perform the Fock space calculations for the electron fields. Matrix elements of the electron fields are written as

$$< e_f|N[\bar{\psi}_e\psi_e]|e_i > = < 0|b_{\nu_f}(\boldsymbol{k}^e_f)N[\bar{\psi}_e(x)\psi_e(x)]b^\dagger_{\nu_i}(\boldsymbol{k}^e_i)|0 >, \tag{3.50}$$

with the following expansion for the electron fields

$$\begin{aligned} \psi_e(x) &= (2\pi)^{-\frac{3}{2}}\sum_s \int d^3k\sqrt{\frac{m}{E_k}} \\ &\times [b_s(\boldsymbol{k})u_s(k,x) + d^\dagger_s(\boldsymbol{k})v_s(k,x)] \end{aligned}$$

$$\begin{aligned} \bar{\psi}_e(x) &= (2\pi)^{-\frac{3}{2}}\sum_{s'} \int d^3k\sqrt{\frac{m}{E_k}} \\ &\times [b^\dagger_s(\boldsymbol{k})\bar{u}_s(k,x) + d_s(\boldsymbol{k})\bar{v}_s(k,x)], \end{aligned} \tag{3.51}$$

where u_s and v_s are plane wave solutions of the Dirac wave equation for positive and negative energy states, respectively, and d and $d^\dagger$ are annihilation and creation operators for the particles with negative energy or antiparticles with positive energy. The Fock space calculations for the electron fields result in the following expression

$$< 0|b_{\nu_f}(\boldsymbol{k}^e_f)N[\bar{\psi}_e(x)\psi_e(x)]b^\dagger_{\nu_i}(\boldsymbol{k}^e_i)|0 > = (2\pi)^{-3}\frac{m}{\sqrt{E_{k_i}E_{k_f}}}\bar{u}_{\nu_f}(k^e_f, x)u_{\nu_i}(k^e_i, x), \tag{3.52}$$

and the Fock space calculations for the nucleons give

$$\begin{aligned} < \phi^{M_f}_{J_f}|b_{\mu'}(\boldsymbol{k'}_p)N[\bar{\psi}_p(y)\psi_p(x)]|\phi^{M_i}_{J_i} > &= \frac{1}{(2\pi)^3}\sum_\mu \int d^3k < \phi^{M_f}_{J_f}|b_\mu(\boldsymbol{k}^*_p)|\phi^{M_i}_{J_i} > \\ &\times\sqrt{\frac{M}{E_p}}\sqrt{\frac{M^*}{E^*_p}}\bar{u}_{\mu'}(k'_p, y)u_\mu(k^*_p, y), \end{aligned} \tag{3.53}$$

where super index $*$ indicates that the initial bound particle is off shell. Using the results of the above Fock space calculations along with the usual form of the photon propagator, the S-matrix, after the integration over variable x, takes the following form,

$$S_{fi} = -ie^2 \frac{1}{(2\pi)^6} \sqrt{\frac{m_e^2}{E_f^e E_i^e} \frac{M_P}{E_P} \frac{M^*}{E_p^*}} \mathcal{E}^{\beta}_{\nu_f,\nu_i} \frac{1}{q^2}$$

$$\times \sum_{\mu} \int d^3k d^4y e^{-iq\cdot y} \bar{u}_{\mu'}(k_p, y) \gamma_\beta u_\mu(k_p^*, y) < \phi_{J_f}^{M_f} | b_\mu(\boldsymbol{k}_p^*) | \phi_{J_i}^{M_i} >, \quad (3.54)$$

where we have defined the electronic part of the matrix elements $\mathcal{E}^{\beta}_{\nu_f,\nu_i}$ as

$$\mathcal{E}^{\beta}_{\nu_f\nu_i} = \sqrt{\frac{E_f+m}{2m}\frac{E_i+m}{2m}} < \frac{1}{2}\nu_f | \left(1 \quad \frac{\boldsymbol{\sigma}\cdot\boldsymbol{k}_f}{E_f+M}\right) \gamma_0 \gamma^\beta \begin{pmatrix} 1 \\ \frac{\boldsymbol{\sigma}\cdot\boldsymbol{k}_i}{E_i+M} \end{pmatrix} | \frac{1}{2}\nu_i > . \quad (3.55)$$

In the PW limit, the impuls approximation of the reaction assigns a momentum for the initial bound nucleon, so the momentum integration in the S-matrix is removed. We rewrite the S-matrix as

$$S_{fi} = \sum_{\mu} G_1(M_f, M_i, \mu) G_2(M_f, M_i, \nu_f \nu_i) \quad (3.56)$$

where

$$G_1(M_f, M_i, \mu) = < \phi_{J_f}^{M_f} | b_\mu(\boldsymbol{k}_p^*) | \phi_{J_i}^{M_i} >$$

$$G_2(\mu', \mu, \nu_f \nu_i) = -ie^2 \frac{1}{(2\pi)^6} \sqrt{\frac{m_e^2}{E_f^e E_i^e} \frac{M_P}{E_P} \frac{M^*}{E^*}} \mathcal{E}^{\beta}_{\nu_f,\nu_i} \frac{1}{q^2}$$
$$\times \sum_{\mu} \int d^4y e^{-iq\cdot y} \bar{u}_{\mu'}(k_p, y) \gamma_\beta u_\mu(k_p^*, y) \quad (3.57)$$

Now the transition probability $|S_{fi}|^2$ takes the following form

$$|S_{fi}|^2 = \sum_{\mu,\mu} \left\{ \sum_{M_f,M_i} G_1(M_f, M_i, \mu) G_1^*(M_f, M_i, \bar{\mu}) \right.$$
$$\left. \times \sum_{\mu',\nu_f\nu_i} G_2(\mu', \mu, \nu_f\nu_i) G_2 * (\mu', \bar{\mu}, \nu_f\nu_i) \right\} \quad (3.58)$$

Defining the spectral function $S(p)$ as

$$\begin{aligned} S(p) &= \overline{\sum}_{M_f,M_i} G_1(M_f,M_i,\mu)G_1^*(M_f,M_i,\bar{\mu}) \\ &= \sum_{lj}[C^{lj}]^2\delta_{\bar{\mu},\mu} \end{aligned} \tag{3.59}$$

where C^{lj} are reduced matrix elements and do not depend on μ. The result on the second line of equation (3.59) follows from the method introduced in reference [1]. We can write the spectral function as

$$\begin{aligned} S(p) &= \sum_{M_f,M_i} G_1(M_f,M_i,\mu)G_1^*(M_f,M_i,\bar{\mu}) \\ &= \sum_{M_f,M_i} |G_1(M_f,M_i,1/2)|^2 = \frac{1}{2}\sum_{M_f,M_i,\mu} |G_1(M_f,M_i,\mu)|^2 \end{aligned} \tag{3.60}$$

The transition amplitude can be written in terms of the spectral function and the matrix elements of the elementary reaction as

$$|S_{fi}|^2 = S(p)\sum_{\mu',\nu_f\nu_i} |G_2(\mu',\mu,\nu_f\nu_i)|^2 \tag{3.61}$$

The differential cross section is defined as

$$d\sigma = \frac{|S_{fi}|^2}{T}\frac{1}{j_{\text{inc}}}d^3p_pd^3p_f^e \tag{3.62}$$

Having done the integration over phase space and using

$$\int d^3p_pd^3p_f^e = \int d\Omega_pd\Omega_f^ep_pE_pp_f^eE_f^edE_pdE_f^e \tag{3.63}$$

we can write the cross section as follows

$$\frac{d^3\sigma}{d\Omega_pd\Omega_f^edE_p} = S(p)\,p_pE_pp_f^eE_f^e\frac{|G_2(\mu',\mu,\nu_f\nu_i)|^2}{T}\frac{1}{j_{\text{inc}}} \tag{3.64}$$

Comparing with the cross section for the free reaction we find

$$\frac{d^3\sigma}{d\Omega_pd\Omega_f^edE_p} = S(p)\,p_pE_p\frac{d\sigma}{d\Omega_f^e}|_{free} \tag{3.65}$$

Chapter 4

Photoproduction of η Mesons from Complex Nuclei

I) Exclusive Reactions

Introduction

η meson production reactions explore a rich domain of phenomena at the interface of nuclear and particle physics. In the past photoproduction of the η meson has been confined to proton targets. The advent of high-duty-cycle electron accelerators at MAINZ, BATES and CEBAF, has opened up novel possibilities of performing production experiments on complex nuclei. Some results have been reported recently and there are several experiments underway [1].

The possible existence of a bound η meson-nucleus system (η-mesic nuclei) has been studied by several authors. Liu *et al.*, in a recent publication in this regard, conclude that for medium and heavy nuclei ($A \geq 12$) such bound states exist, but their widths are larger than the spacing between energy levels [2]. Rakityansky *et al.* [3] studied the formations of light η-mesic nuclei ($A \leq 4$) and found that for nuclei with $A \geq 2$, there may exist quasi η bound states, but the widths of the bound states are small only for ${}^4_\eta$He. One can also find some information on the subject of η-mesic nuclei in references [4, 5]. The study of this new type of nuclear matter has generated an interest in the interaction and production of η mesons on nuclei.

Analysis of the early experiments on the photoproduction of η mesons reveal an interesting selectivity. The isoscalar η meson can couple only to $I = \frac{1}{2}$ nucleon resonances. At energies near the threshold of η production, there is a significant preference for intermediate excitation of the $S_{11}(1535)$ resonance. This resonance decays $\sim 50\%$ of the time to an η meson and a nucleon whereas the $S_{11}(1650)$ which has similar structure has only a decay rate of $\sim 1.5\%$ to the η meson nucleon channel. This puzzle is still unsolved and presents a challenge to quark models dealing with the structure of these resonances.

The selectivity mentioned above makes η meson photoproduction reactions a suitable tool for learning more about the $S_{11}(1535)$ resonance. In addition to the study of the final state interactions of the η mesons with nuclei, the reaction on nuclei can be a means of studying the propagation of nucleon resonances in the nuclear medium.

The elementary reaction $\gamma + p \rightarrow \eta + p$ has been the subject of several studies. Benmerrouche *et al.* [6] developed an effective Lagrangian approach to study this reaction. Contributions from nucleon resonances, t-channel vector meson as well as the nucleon Born diagrams are included. Calculations were performed at the tree level and included eight free parameters, coupling of η mesons to nucleons, four parameters for spin $\frac{1}{2}$ resonances and three parameters for spin $\frac{3}{2}$ resonance. The $S_{11}(1535)$ was found to be the dominant contributor to the reaction at energies close to the threshold. In addition they concluded that there is no preference in using pseudoscalar (PS) or pseudovector (PV) coupling in introducing the interaction of η meson with nucleon and nucleon resonances. They also found an estimate close to the quark models prediction for the quantity $\Gamma_\eta^{\frac{1}{2}} A_{\frac{1}{2}}$ (Γ_η is the decay width of the resonance to the η meson and nucleon channel and $A_{\frac{1}{2}}$ is the helicity amplitude of the electromagnetic excitation of the resonance) for the $S_{11}(1535)$ resonance.

The approach followed by Bennhold *et al.* [7, 8] for η photoproduction on the nucleon is based on a coupled channel isobar model, in which the reaction is related to (γ, π), (π, η) and (η, η) reactions. They include three resonances which are thought to make the major contributions to the reaction, namely, $S_{11}(1535)$, $D_{13}(1520)$ and $P_{11}(1440)$. The resonances are parameterized based on the a Breit-Wigner-type parameterization with the masses and coupling constants of the resonances obtained by fitting the experimental data up to photon laboratory energy of 2 GeV. Each contributing partial wave is parameterized in terms of six parameters for the hadronic vertex. These are determined from a fit to the data of the reactions $\pi + N \rightarrow \pi + N$, $\pi^- + p' \rightarrow \eta + n$ and $\pi + N \rightarrow \pi + \pi + N$. The five parameters of the electromagnetic vertices are adjusted to reproduce the pion photoproduction multipoles E_0^+, E_2^- and M_2^-. The authors studied the effects of the πNN coupling on the cross section for η photoproduction on protons and found that the PS coupling of this vertex results in curves which are closer to the experimental data, for partial and total cross sections, than those for PV coupling.

The authors employed this elementary amplitude to calculate the coherent and incoherent photoproduction of η mesons from nuclei. They found the highest cross section for coherent production on nuclei ($A \geq 4$) to be associated with ^{4}He targets and in this case is dominated by $D_{13}(1520)$ resonance. On the other hand all of their cross sections for incoherent production are dominated by $S_{11}(1535)$. Note that in the coherent photoproduction of η mesons from nuclei, all the nucleons inside of the nuclear target contribute to the reaction. On the other hand for incoherent photoproduction of η mesons only nucleons that satisfy the selection rule for the angular momentum of the transition can contribute to the reaction.

Tiator *et al.* [9] extended the work of reference [7] by including Born diagram as well as ρ and ω exchange diagrams. These added diagrams are calculated using effective Lagrangians. The parameters and the coupling constants for the nucleon resonance part of the model are fixed and those of the vector mesons are obtained from available sources. The model can be used to investigate the ηNN vertex. These authors found that, for the ηNN vertex, both PS coupling with a strength of 0.1 and PV of a strength of 0.6, fit the experimental data of the total cross section equally well. On the other hand the differential cross section as well as the recoil polarization data favor the PS coupling. The resulting elementary amplitudes were subsequently used to calculate the PWIA amplitude of the photoproduction reaction on light nuclei such as D, ^{2}H, ^{3}H and ^{4}He. The largest cross sections were found to occur for productions on the trinucleon system.

The elementary amplitude above was also used by Lee *et al.* [10] to calculate the DWA amplitude for the photoproduction of η mesons on heavier nuclei such as ^{12}C and ^{40}Ca. They performed exclusive as well as inclusive reaction calculations on these targets. In this model the initial bound nucleon is described by a Harmonic oscillator wavefunction and final state interactions of the detected outgoing particles with the recoil nucleus are introduced through optical potentials. Two different optical potentials were used for η mesons. Comparisons with the experimental data of inclusive reaction appear to favor one of these sets. The authors found that the photon asymmetry is insensitive to the final state interactions of the outgoing particles as well as the size of the target nucleus.

Carrasco calculated the inclusive photoproduction of η mesons from nuclei using the effective Lagrangian approach [11]. The reaction is assumed to proceed through the formation of $S_{11}(1535)$ nucleon resonance only. The calculations were carried out using local density approximation, with Pauli blocking and Fermi motions taken into account. The final state interactions of the η meson with the residual nucleus were accounted for via a Monte Carlo program. The author showed that the total cross section experiences a large suppression due medium modifications (Fermi sea effects and the modifications of the $S_{11}(1535)$ resonance parameters) and the final state interaction of the η meson. These effects are less for the differential cross section than the total cross section. Another finding is that the total cross section grows like $A^{0.6}$ (A is the atomic number of the target nucleus).

A model for η photoproduction from complex nuclei was introduced by Hombach *et al.* [12]. The final state interaction of η meson is obtained using coupled channel Boltzmann-Uehling-Ulenbeck formalism. They found the mass dependence of the total cross section to be $A^{\frac{2}{3}}$. A recent calculation for the photoproduction of η meson off the deuteron on the basis of the effective Lagrangian is presented in reference [13].

η meson production in proton proton collisions is studied in reference [14]. There has also been many studies using hadron (proton and pion) beams for η production [15, 16, 17].

In this chapter we develop a relativistic model for the (γ, ηp) reaction on nuclei leading to residual nuclei with definite spins and parities. The effective Lagrangian of reference [6] is used for the interactions between fields. The nuclear wavefunctions are solutions of the Dirac equation with the strong scalar and vector potentials obtained from the relativistic mean field theory of Walecka [18, 19]. In the next section we derive the amplitude of the A(γ, ηp)A−1 reaction and then use it to calculate the observables for the reaction. The results of our calculations are presented in section 2 and our conclusions are given in section 3.

4.1 The Reaction A(γ, ηp)A−1

The model for the (γ, ηp) reaction on nuclei has the incident photon interacting with a bound proton through some process denoted by the blob in figure (4.1). A proton and an η meson are produced. The diagrams contributing to the blob of figure (4.1), at the tree level, are shown in figure (4.2). The Born diagrams (s- and u-channels

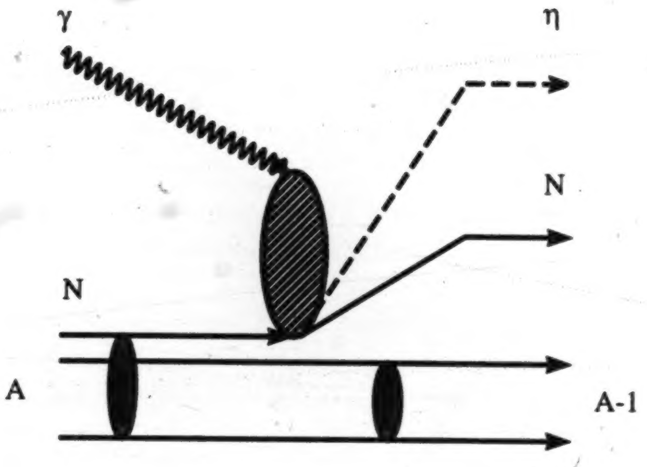

Figure 4.1: The Feynman diagram for an $A(\gamma, \eta p)A-1$ reaction, the incident photon with momentum **k** is absorbed by a proton inside nucleus A and as a result the proton and η meson are ejected out of the target.

of the nucleon propagator) are figures 4.2a) and 4.2b): the t-channel vector meson diagram is shown in figure 4.2c), figures 4.2d) and 4.2e) are the nucleon resonance poles.

The starting point in the present approach is a relativistic Lagrangian for a system of photons, nucleons and mesons from which one obtains the transition amplitude for the A(γ, ηp)A−1 reaction. The amplitude then is used to calculate the observables for the reaction.

4.1.1 Model Lagrangian

We write the total Lagrangian of a system of photons, mesons and nucleons as

$$\begin{aligned}\mathcal{L} &= \mathcal{L}_{\mathrm{MFT}} + \mathcal{L}_{\gamma} + \mathcal{L}_{\eta} \\ &+ \mathcal{L}_{\eta NN} + \mathcal{L}_{\gamma NN} + \mathcal{L}_{\gamma\eta V} + \mathcal{L}_{\gamma NV} + \mathcal{L}_{\eta NR} + \mathcal{L}_{\gamma NR} \qquad (4.1)\end{aligned}$$

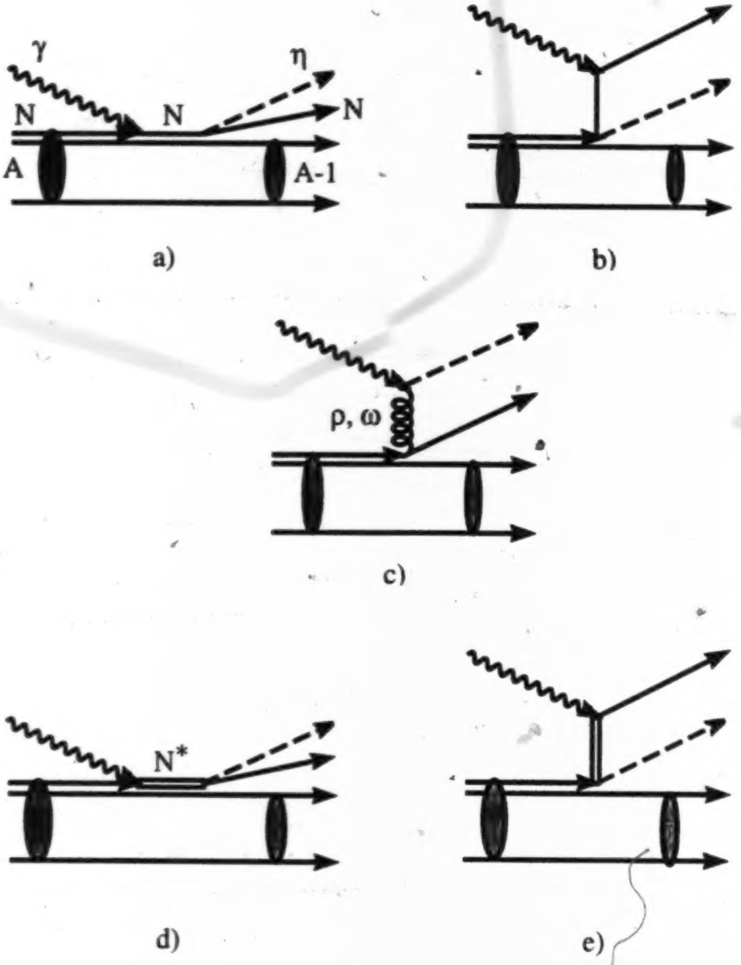

Figure 4.2: The contributing Feynman diagrams to $A(\gamma, \eta p)A-1$ reaction. a) and b) are the s- and u-channel Born diagram respectively, c) the t-channel vector meson diagram, d) and e) are the s- and u-channel nucleon resonance poles.

where the subindices of γ, η, V, N and R stand for photon, η meson, vector meson, nucleon and nucleon resonances, respectively. The dynamics of the nucleons within the nuclear matter is studied on the basis of the relativistic mean field theory of Walecka. This theory starts from a phenomenological renormalizable Lagrangian describing a system of nucleons and different types of meson, namely scalar, vector and isovector mesons. When it is applied to infinite nuclear matter, at the mean field limit ($\mathcal{L}_{\mathrm{MFT}}$), only scalar meson (σ) and neutral vector mesons (ρ and ω) survive.

$$\begin{aligned}\mathcal{L}_{\mathrm{MFT}} &= \bar{\psi}[i\partial\!\!\!/ - g_\rho \frac{1}{2}\tau_3\gamma^0 b_0 - g_v\gamma^0 V_0 - (M - g_s\phi_s)]\psi \\ &-\frac{1}{2}m_s^2\phi_s^2 + \frac{1}{2}m_v^2 V_0^2 + \frac{1}{2}m_\rho^2 b_0^2 \qquad (4.2)\end{aligned}$$

where ψ and ϕ_s are nucleon and scalar meson fields, respectively. The time-like component of the vector and neutral isovector field are shown by V_0 and b_0, respectively. M, m_s, m_v and m_ρ are the corresponding masses of the nucleon , scalar, vector and isovector field, respectively. The b_0 field vanishes when this Lagrangian is used for the ground state of nuclear matter. Then this mean field theory Lagrangian is used to derive the Dirac equation with the scalar and vector potential [20]. This mean field theory has been applied successfully to the description of bulk properties of nuclear matter, and has proven to be a very powerful tool for an effective microscopic study of the ground state properties of nuclei [18, 19]. It provides a unified description of the binding energy and deformation properties of nuclei and is also used recently in the study of super heavy nuclei [21]. There are many successful relativistic phenomenological reaction models based on this mean field theory, describing electromagnetic as well as hadronic interactions with nuclei. These are found to provide better descriptions of the observables, especially spin observables, than other models. [22, 23, 24, 25].

The wave equation for η meson is obtained under the assumption that only its interaction with nucleons through the formation of nucleon resonances is important. The corresponding Lagrangian can be written as

$$\mathcal{L}'_\eta = \mathcal{L}_\eta + \mathcal{L}_{\eta NR} = \frac{1}{2}\left(\partial_\mu \eta(x)\, \partial^\mu \eta(x) - m_\eta^2 \eta^2(x)\right) + \mathcal{L}_{\eta NR}, \tag{4.3}$$

where η is the η meson field.

Photons are described by the following Lagrangian

$$\mathcal{L}_\gamma \quad = \quad -\frac{1}{4} F_{\mu\nu}(x)\, F^{\mu\nu}(x)\,, \tag{4.4}$$

and the electromagnetic field tensor $F_{\mu\nu}$ is written in terms of the electromagnetic field A_μ as

$$F_{\mu\nu}(x) = \partial_\mu A_\nu(x) - \partial_\nu A_\mu(x). \tag{4.5}$$

We adopt the pseudoscalar form for the η meson-nucleon states coupling. The interaction Lagrangians involving the nucleon and spin $\frac{1}{2}$ resonances can be cast in the following forms [6]:

$$\mathcal{L}_{\eta NN} = \; - \; i g_\eta \bar{\psi} \gamma_5 \psi \eta$$

$$\mathcal{L}_{\gamma NN} = \; - \; e\bar{\psi}\gamma_\mu A^\mu \psi - \frac{e\kappa_p}{4M}\bar{\psi}\sigma^{\mu\nu}\psi F_{\mu\nu},$$

$$\mathcal{L}_{VNN} \; - \; g_v \bar{\psi}\gamma_\mu \psi V^\mu - \frac{g_t}{4M}\bar{\psi}\sigma_{\mu\nu}\psi V^{\mu\nu},$$

$$\mathcal{L}_{V\eta\gamma} = \; \frac{e\lambda_V}{4m_\eta}\epsilon_{\mu\nu\lambda\sigma} F^{\mu\nu} V^{\lambda\sigma}\eta,$$

$$\mathcal{L}_{\eta NR} = \; - \; i g_{\eta NR} \bar{\psi} \Gamma R \eta + h.c.$$

$$\mathcal{L}_{\gamma NR} = \; - \; \frac{e\kappa_p^R}{2(M_R + M)} \bar{R}\Gamma^{\mu\nu}\psi F_{\mu\nu} + h.c.,$$

where

$$\begin{aligned} &\text{for } S_{11} \text{ resonances} \qquad && \Gamma = 1 \ \text{ and } \Gamma^{\mu\nu} = \gamma_5\sigma^{\mu\nu} \\ &\text{for } P_{11} \text{ resonances} \qquad && \Gamma = \gamma_5 \ \text{ and } \Gamma^{\mu\nu} = \sigma^{\mu\nu} \end{aligned} \tag{4.6}$$

and κ_p is the anomalous magnetic moment of the proton, κ_p^R and M_R are the anomalous magnetic moment and the mass of the nucleon (proton) resonance, respectively. The tensor $V_{\mu\nu}(x)$ is related to the vector meson field V_μ by

$$V_{\mu\nu}(x) = \partial_\mu V_\nu(x) - \partial_\nu V_\mu(x) \tag{4.7}$$

The interaction of photons and η mesons with the spin $\frac{3}{2}$ ($D_{13}(1520)$) resonance are introduced through the following Lagrangians,

$$\begin{aligned} \mathcal{L}_{\eta NR} &= \frac{f_{\eta NR}}{m_\eta}\overline{R}^\mu \theta_{\mu\nu}(Z)\gamma_5\psi\partial^\nu\eta + h.c., \\ \mathcal{L}^1_{\gamma NR} &= -\frac{ie\kappa^1_R}{2M}\overline{R}^\mu \theta_{\mu\nu}(Y)\gamma_\lambda\psi F^{\nu\lambda} + h.c., \\ \mathcal{L}^2_{\gamma NR} &= \frac{e\kappa^2_R}{4M^2}\overline{R}^\mu \theta_{\mu\nu}(X)\partial_\lambda N F^{\nu\lambda} + h.c., \end{aligned} \tag{4.8}$$

where R^μ is the field associated with the $D_{13}(1520)$ resonance. The two anomalous magnetic moments κ^1_R and κ^2_R are used for two different electromagnetic interaction vertices introduced for this resonance, and

$$\begin{aligned} \theta_{\mu\nu}(V) &= g_{\mu\nu} + \left[-\frac{1}{2}(1+4V) + V\right]\gamma_\mu\gamma_\nu. \\ V &= X, Y, Z \end{aligned} \tag{4.9}$$

The parameter X, Y and Z, often referred to as off shell parameters, are obtained by fitting the experimental data for the elementary reaction. In addition to the $S_{11}(1535)$

Table 1: Summery of the properties of the baryon resonances included in our model. J^π is the spin parity, L is the relative angular momentum related to πN scattering state. The Subscripts I and J for the L values (third column) represent the isospin and total angular momentum assigned to the resonance, respectively. Γ is the total width of the resonance.

Resonance	J^π	L_{2I2J}	Mass(MeV)	Γ(MeV)
N*(1440)	$1/2^+$	P_{11}	1440	350
N*(1520)	$3/2^-$	D_{13}	1520	120
N*(1535)	$1/2^-$	S_{11}	1535	150
N*(1650)	$1/2^-$	S_{11}	1650	150
N*(1710)	$1/2^+$	P_{11}	1710	100

resonance, we also include four other resonances. Table 1 gives some of the properties of the 5 resonances used in the present calculations.

The authors of reference [6], through fits to existing data, provided several sets of values for the parameters and observables related to the coupling constants of the effective interaction Lagrangians of (4.6, 4.8). We copy in table 2 the values in the second column of table V of the above reference, which are the ones used in our present calculations. The parameters of table V are for a PS coupling which is the form we used here. The off-shell parameters α, β and δ given in table 2 are related to the X, Y and Z introduced in equation (4.8), as

$$\alpha = 1 + 4Z, \qquad \beta = 1 + 4y, \qquad \delta = 1 + 2X \tag{4.10}$$

The parameters A_J are the helicity amplitudes and are related to the formation of the resonances through the absorption of photons by nucleons.

Table 2: Couplings obtained by fitting the data for η photoproduction [6]. The cutoff parameter $\lambda^2 = 1.2$ GeV^2 is used for the vector meson vertex. The off shell parameter at strong vertex is fixed to α=-1. The helicity amplitudes are in units of 10^{-3} GeV$^{-1/2}$ and the quantities $\sqrt{\Gamma_\eta}A_J$ are multiplied by 1000.

$\left[\sqrt{\Gamma_\eta}A_{1/2}\right]_{S^1_{11}}$	26.2	$\left[\sqrt{\Gamma_\eta}A_{1/2}\right]_{P^1_{11}}$	-0.08	$\left[\sqrt{\Gamma_\eta}A_{1/2}\right]_{D_{13}}$	-0.2
$\left[A_{1/2}\right]_{S^1_{11}}$	95.6	$\left[A_{1/2}\right]_{P^1_{11}}$	-0.4	$\left[A_{1/2}\right]_{D_{13}}$	-9.3
$\left[\sqrt{\Gamma_\eta}A_{1/2}\right]_{S^2_{11}}$	-7.0	$\left[\sqrt{\Gamma_\eta}A_{1/2}\right]_{P^2_{11}}$	2.9	$\left[\sqrt{\Gamma_\eta}A_{3/2}\right]_{D_{13}}$	0.8
$\left[A_{1/2}\right]_{S^2_{11}}$	180.9	$\left[A_{1/2}\right]_{P^2_{11}}$	16.7	$\left[A_{3/2}\right]_{D_{13}}$	70.4
g_η	4.1	β	0.9	δ	1.0

4.1.2 Reaction Amplitude

At the tree-level the S-matrix for the A(γ, ηp)A-1 reaction is [26]

$$S_{fi} = -\frac{1}{2}\int < f|T\left[\mathcal{L}_{int}(x)\,\mathcal{L}_{int}(y)\right]|i > d^4x d^4y \tag{4.11}$$

where $|i>$ and $|f>$ are the initial and final states of the system respectively. The T in front of the square bracket denotes the time ordered product of the operators within the bracket. We shall illustrate, below, the derivation of the S-matrix for one of the contributing diagrams of figure (4.2), namely the S_{11} diagram. The same procedure can be used to derive the S-matrix for the other diagrams.

The S-matrix for the S$_{11}$ resonance diagram is written as

$$S^R_{fi} = -\int < f|T\left[\mathcal{L}_{\gamma NR}(x)\,\mathcal{L}_{\eta NR}(y)\right]|i > d^4x d^4y. \tag{4.12}$$

The amplitude (4.11) for each contributing diagram contains the product of the corresponding interaction Lagrangians twice. So in writing the S-matrix (4.12) for the

S_{11} resonance, the factor $\frac{1}{2}$ appearing in equation (4.12) is dropped. After introducing $\mathcal{L}_{\gamma NR}$ and $\mathcal{L}_{\eta NR}$ from equation (4.6) into the above expression one gets

$$\begin{aligned} S^R_{fi} = & - \frac{ie\kappa^R_p g_{\eta NR}}{2(M+M_R)} \int < f|T\Big[\Big(\bar{R}(x)\,\gamma_5\sigma_{\mu\nu}F^{\mu\nu}(x)\,\psi(x) \\ & \qquad -\bar{\psi}(x)\,\gamma_5\sigma_{\mu\nu}F^{\mu\nu}(x)\,R(x)\Big) \\ \times & \quad \Big(\bar{\psi}(y)\,R(y)\,\eta(y) - \bar{R}(y)\,\psi(y)\,\eta(y)\Big)\Big]\,|i > dx^4 dy^4. \end{aligned} \qquad (4.13)$$

Using Wick's theorem [26], the contributing terms in the reaction above are

$$\begin{aligned} S^R_{fi} = -\frac{ie\kappa^R_p g_{\eta NR}}{2(M+M_R)} \int & < f|N\Big[\bar{\psi}(y)\,\eta(y)\,\underline{R(y)\,\bar{R}(x)}\gamma_5\sigma_{\mu\nu}F^{\mu\nu}(x)\,\psi(x) \\ & +\bar{\psi}(x)\,\gamma_5\sigma_{\mu\nu}F^{\mu\nu}(x)\,\underline{R(x)\,\bar{R}(y)}\psi(y)\,\eta(y)\Big]\,|i > dx^4 dy^4. \end{aligned} \qquad (4.14)$$

Note that the application of the Wick rotation has replaced the time ordering of the the field with the normal ordering (i.e T[$\cdots$]→ N[$\cdots$]) The initial state $|i>$ contains a photon and a target nucleus with A nucleons. The latter is regarded as made up of a core and a valance nucleon. We write

$$\begin{aligned} |i> = & \quad b^\dagger_{s_\gamma}(\mathbf{k}_\gamma) \sum_{J_B M_B J} (J, J_B{:}\, M, M_B|J_i, M_i) \\ & \times\Big[\mathcal{S}_{J_i J_f}(J_B)\Big]^{1/2} b^\dagger_{J_B M_B}|\phi^M_J >, \end{aligned} \qquad (4.15)$$

where $b^\dagger_{s_\gamma}(\mathbf{k}_\gamma)$ is the creation operator for a photon with momentum $\mathbf{k}_\gamma$ and polarization s_γ, $b^\dagger_{J_B M_B}$ creates a bound nucleon with angular momentum quantum numbers J_B and M_B bound to the core $|\phi^M_J>$ and $\mathcal{S}$ is the corresponding spectroscopic factor.

The final state $|f>$, composed of an η meson, a nucleon and the residual nucleus, is written as

$$|f> = a^\dagger_\eta(\mathbf{k}_\eta)\,b^\dagger_{s_f}(\mathbf{k}_p)\,|\phi^{M_f}_{J_f}>, \qquad (4.16)$$

where $a^\dagger(\mathbf{k}_\eta)$ creates an η meson with momentum $\mathbf{k}\eta$ and $b^\dagger_s(\mathbf{k}_p)$ is the creation operator for a nucleon with spin s_f and momentum $\mathbf{k}_p$. The pseudoscalar field (η meson) is written in second quantized form as

$$\eta(x) = \frac{1}{(2\pi)^{3/2}} \int \frac{d^3k}{\sqrt{2E_\mathbf{k}}} \Big[a^\dagger(\mathbf{k})\varphi^*_\eta(k,x) + a(\mathbf{k})\varphi_\eta(k,x)\Big]. \qquad (4.17)$$

where $a(\mathbf{k})$ annihilates an η meson with the corresponding wavefunction $\varphi_\eta(k,x)$. The electromagnetic field is written in second quantized form as

$$A^\mu(x) = \frac{1}{(2\pi)^{3/2}}\sum_r \epsilon_r^\mu \int \frac{d^3k}{(2E_\mathbf{k})^{1/2}}\left[a_r(\mathbf{k})e^{-ik\cdot x} + a_r^\dagger(\mathbf{k})e^{ik\cdot x}\right], \tag{4.18}$$

where $a_r^\dagger(\mathbf{k})$ is the creation operator for a photon with momentum $\mathbf{k}$ and polarization r. The second quantized form of the nucleon field operator $\psi(x)$ is

$$\begin{aligned}\psi(x) = \quad & \sum_s \int \frac{d^3k}{(2\pi)^{3/2}}\left(\frac{M}{E_k}\right)^{1/2}\left[b_s(\mathbf{k})u_s(k,x) + d_s^\dagger(\mathbf{k})v_s(k,x)\right] \\ + \; & \sum_n [b_n u_n(x) + d_n^\dagger v_n(x)]\end{aligned} \tag{4.19}$$

where $b_s(\mathbf{k})$ is the destruction operator for a nucleon with spin s and momentum $\mathbf{k}$, and $u_s(k,x)$ is the corresponding space-time continuum wave function. The creation operator $d_s^\dagger(\mathbf{k})$ creates an antinucleon with spin s and momentum $\mathbf{k}$, $v_s(k,x)$ is the corresponding space-time continuum wave function. For bound nucleons we have b_n destroying a bound nucleon with quantum numbers denoted by n while $d_n^\dagger$ creates a bound antinucleon with quantum numbers n. The corresponding space-time wavefunctions are $u_n(x)$ and $v_n(x)$. The Fock space calculations for the fields involved in the interaction result in following

$$< 0|a_\eta(\mathbf{k}_\eta)\eta(x)|0 >= \frac{1}{(2\pi)^{2/3}}\frac{1}{(2E_\eta)^{1/2}}\varphi^*(k_\eta, x),$$

$$< 0|F^{\mu\nu}(x)a_r^\dagger(\mathbf{k}_\gamma)|0 >= \frac{2}{(2\pi)^{2/3}}\frac{1}{(2E_\gamma)^{1/2}}q_r H_\gamma, \tag{4.20}$$

where $|0>$ is the vacuum state of the corresponding fields. E_γ and E_η are energies of the photon and η meson respectively. The above result for the electromagnetic tensor is obtained using the radiation gauge. The Fock space calculations for the nucleon fields give

$$\begin{aligned}< f|N[\bar{\psi}_p(y)\psi_p(x)]|i >= \; & \frac{1}{(2\pi)^{\frac{3}{2}}} \\ \times\sqrt{\frac{M}{E_p}} & \sum_{J_B M_B}(J_f, J_B; M_f, M_B|J_i, M_i)\sqrt{S}\bar{u}_\mu(k_p, y)u_{J_B,M_B}(x),\end{aligned} \tag{4.21}$$

where M and E_p are the mass and energy of the nucleon respectively. We use the plane wave approximation for the resonance propagator (see Appendix 4.E for more details). In this approximation the propagator for a spin $\frac{1}{2}$ resonance assumes the simple form

$$\underline{R(x)\bar{R}(y)} \;=\; iS_R^F(x-y) \;=\; i\frac{\not{k}_R + M_R}{k_R^2 - M_R^2}\delta^4(x-y), \tag{4.22}$$

where $S_R^F(x-y)$ is the Feynman propagator of the nucleon resonance with the mass M_R and four momentum k_R. Putting the results of the Fock space calculations into the S-matrix of the equation (4.14), the S-matrix for the S_{11} resonance diagram can be cast in the following form

$$\begin{aligned} S_{fi}^R \quad &= \frac{e}{(2\pi)^{9/2}}\left(\frac{M}{E_p}\frac{1}{2E_\eta}\frac{1}{2E_\gamma}\right)^{1/2} \\ &\times \sum_{J_B M_B} (J_f, J_B; M_f, M_B|J_i, M_i)\left[\mathcal{S}_{J_i J_f}(J_B)\right]^{1/2} \\ &\times \int d^4x \Psi_{s_f}^{(-)\dagger}(x)\Gamma_{S_{11}}\Psi_{J_B M_B}(x)\varphi_\eta^*(x)e^{-ik_\gamma\cdot x}, \end{aligned} \tag{4.23}$$

where $\Gamma_{S_{11}}$ is a 4×4 matrix operator and contains combinations of the Dirac γ matrices, polarization of the interacting photon, mass and four momentum of the propagating resonance. The explicit form of this operator along with those of other diagrams are given below.

The structure of the total S-matrix is the same as S_{fi}^R of equation (4.23) except for $\Gamma_{S_{11}}$ which must be replaced by a sum representing contributions from all the diagrams included in the model. We have obtained the following operators for the diagrams included in our calculations:

$$\Gamma_{proton}^e = g_{\eta NN}\gamma_0\left(\gamma_5\frac{\not{k}_s + M}{k_s^2 - M^2}\not{\epsilon}_r + \not{\epsilon}_r\frac{\not{k}_u + M}{k_u^2 - M^2}\gamma_5\right),$$

$$\Gamma_{proton}^\mu = \frac{g_{\eta NN}\kappa_p}{2M}\gamma_0\left(\gamma_5\frac{\not{k}_s + M}{k_s^2 - M^2}\not{k}_\gamma\not{\epsilon}_r + \not{k}_\gamma\not{\epsilon}_r\frac{\not{k}_u + M}{k_u^2 - M^2}\gamma_5\right),$$

$$\Gamma_{S_{11}} = \frac{g_{\eta NR}\kappa_p^R}{M + M_R}\gamma_0 \left(\frac{\not{k}_s + M_R}{k_s^2 - M_R^2}\gamma_5 \not{k}_\gamma \not{\epsilon}_r + \gamma_5 \not{k}_\gamma \not{\epsilon}_r \frac{\not{k}_u + M_R}{k_u^2 - M_R^2} \right),$$

$$\Gamma_{P_{11}} = \frac{g_{\eta NR}\kappa_p^R}{M + M_R}\gamma_0 \left(\gamma_5 \frac{\not{k}_s + M_R}{k_s^2 - M_R^2} \not{k}_\gamma \not{\epsilon}_r + \not{k}_\gamma \not{\epsilon}_r \frac{\not{k}_u + M_R}{k_u^2 - M_R^2}\gamma_5 \right),$$

$$\Gamma_V^v = -i\frac{\lambda_v g_v}{m_\eta}\epsilon_{\mu\nu\lambda\sigma}\gamma_0 \frac{\epsilon^\mu k_\gamma^\nu k_\eta^\lambda \gamma^\sigma}{k_t^2 - m_V^2 + i\epsilon},$$

$$\Gamma_V^t = -\frac{\lambda_t g_t}{2Mm_\eta}\epsilon_{\mu\nu\lambda\sigma}\gamma_0 \frac{\epsilon^\mu k_\gamma^\nu \sigma^{\sigma\alpha} k_{t\alpha} k_\eta^\lambda}{k_t^2 - m_V^2 + i\epsilon},$$

$$\begin{aligned} \Gamma_{D_{13}}^{(1)} &= -\frac{f_{\eta NR}\kappa_R^{(1)}}{2Mm_\eta}\gamma_0 \\ &\times \left(\gamma_5 k_\eta^\nu \theta_{\nu\mu}(Z) \frac{\not{k}_s + M_R}{k_s^2 - M_R^2} P^{\mu\alpha}\theta_{\alpha\beta}(Y)\gamma_\lambda (k_\gamma^\beta \epsilon_r^\lambda - \epsilon_r^\beta k_\gamma^\lambda) \right. \\ &\quad \left. + \gamma_\lambda \theta_{\beta\alpha}(Y)(k_\gamma^\beta \epsilon_r^\lambda - \epsilon_r^\beta k_\gamma^\lambda) \frac{\not{k}_u + M_R}{k_u^2 - M_R^2} P^{\alpha\mu}\theta_{\mu\nu}(Z) k_\eta^\nu \gamma_5 \right), \end{aligned}$$

$$\begin{aligned} \Gamma_{D_{13}}^{(2)} &= \frac{f_{\eta NR}\kappa_R^{(2)}}{4m_\eta M^2}\gamma_0 \\ &\times \left(\gamma_5 k_\eta^\nu \theta_{\nu\mu}(Z) \frac{\not{k}_s + M_R}{k_s^2 - M_R^2} P^{\mu\alpha}\theta_{\alpha\beta}(X)(k_\gamma^\beta \epsilon_r^\lambda - \epsilon_r^\beta k_\gamma^\lambda) \left\{ k^B \right\}_\lambda \right. \\ &\quad \left. + \left\{ k_p \right\}_\lambda \theta_{\beta\alpha}(X)(k_\gamma^\beta \epsilon_r^\lambda - \epsilon_r^\beta k_\gamma^\lambda) \frac{\not{k}_u + M_R}{k_u^2 - M_R^2} P^{\alpha\mu}\theta_{\mu\nu}(Z) k_\eta^\nu \gamma_5 \right), \end{aligned}$$

$$P^{\mu\nu} = \left(g^{\mu\nu} - \frac{1}{3}\gamma^\mu\gamma^\nu - \frac{1}{2M_R}\left[\gamma^\mu k^\nu - \gamma^\nu k^\mu\right] - \frac{2}{3M_R^2}k^\mu k^\nu \right), \tag{4.24}$$

where k^B is the local momentum of the bound nucleon and

$$k_s = k_\eta + k_p, \qquad k_t = k_\gamma - k_\eta, \qquad k_u = k_p - k_\gamma. \tag{4.25}$$

To calculate the amplitude of equation (4.23) one can use either plane waves or distorted waves to describe the outgoing particles. In the plane wave approximation the final state interactions of the outgoing nucleon and η-meson, with the recoil nucleus, are ignored. The respective wavefunctions have the form

$$\begin{aligned} \psi_p(k_p, x) &= \sqrt{\frac{E+M}{2M}} \begin{pmatrix} 1 \\ \frac{\sigma \cdot \boldsymbol{k}_p}{E+M} \end{pmatrix} e^{-ik_p \cdot x} \chi_{s_f}, \\ \varphi_\eta(x) &= e^{-ik_\eta \cdot x}. \end{aligned} \tag{4.26}$$

Therefore in the plane wave approximation (PWA) the S-matrix can be written as

$$\begin{aligned} S^R_{fi} &= \frac{e}{(2\pi)^{7/2}} \left(\frac{M}{E_p} \frac{1}{2E_\eta} \frac{1}{2E_\gamma} \right)^{1/2} \delta(E_B + \omega_\gamma - E_p - \omega_\eta) \\ &\times \sum_{J_B M_B} (J_f, J_B; M_f, M_B | J_i, M_i) \left[S_{J_i J_f}(J_B) \right]^{1/2} \\ &\times \int d^3x u^\dagger_{sf}(\boldsymbol{k}_p) e^{i\boldsymbol{k}_{rec} \cdot \boldsymbol{x}} \Gamma_{S_{11}} \Psi_{J_B M_B}(\boldsymbol{x}), \end{aligned} \tag{4.27}$$

where $\boldsymbol{k}_{rec}$ is the momentum of the recoil nucleus. Equation (4.27) shows that the PWA S-matrix is made up of terms proportional to the Fourier transform of the components of the bound state wavefunction. Note that in this reaction we have control over the kinematics and hence a desirable region of the momentum transfer can be selected. If the interaction terms are well known, one can use this reaction to find the behavior of the bound state wavefunction in different regions of momentum transfer.

The rest of this section is devoted to derivation of the distorted wave approximation (DWA) S-matrix.

The continuum nucleon wavefunction with incoming boundary conditions is written as

$$\begin{aligned} \psi^{(-)\dagger}_{s_f}(x) &= 4\pi \left[\frac{E+M}{2M} \right]^{1/2} e^{iEt} \sum_{LJM} i^{-L} Y_L^{M-s_f}(\hat{\mathbf{k}}_f) \mathcal{Y}^{M\dagger}_{L1/2J}(\Omega) \\ &\times (L, 1/2; M - s_f, s_f | J, M) \, [\, f_{LJ}(r), \quad i\sigma \cdot \hat{\mathbf{r}} g_{LJ}(r) \,] \end{aligned} \tag{4.28}$$

where $\mathcal{Y}^M_{L1/2J}$ is introduced in the chapter 2. The above distorted wavefunction is a solution of the Dirac equation with the vector and scalar optical potentials obtained from comparison with proton-nucleus elastic scattering data. More details of the Dirac proton wavefunctions can be found in the previous chapters and reference [27]. The η meson wavefunction is a solution of the Klein-Gordon equation with an appropriate optical potential for the η-nucleus system. It is expanded in partial waves as

$$\varphi_{\eta}^{*}(k_{\eta},\mathbf{x}) = 4\pi \sum_{L_{\eta}M_{\eta}} i^{-L_{\eta}} v_{L_{\eta}}(k_{\eta}r) Y_{L_{\eta}}^{M_{\eta}}(\hat{\mathbf{k}}_{\eta}) Y_{L_{\eta}}^{M_{\eta}*}(\Omega) \tag{4.29}$$

In Appendix 4.D we give more information about the η wavefunction and potentials used in our calculations.

The bound state wavefunction is a solution of a Dirac equation containing strong vector and scalar potentials. We write the four-component wavefunction in terms of upper and lower components as

$$\psi_{J_B M_B}(x) = e^{-iE_B t} \begin{bmatrix} f_B(r) \\ -i g_B(r)\sigma\cdot\hat{\mathbf{r}} \end{bmatrix} \mathcal{Y}_{L_B 1/2 J_B}^{M_B}(\Omega). \tag{4.30}$$

L$_B$, J$_B$ and M$_B$ are the orbital , total and z-component of the total angular momentum of the bound nucleon. The photon momentum defines the z-axis so the photon wave can be expanded as

$$e^{-ik_{\gamma}\cdot x} \;=\; e^{-i\omega t}\sum_{l} i^{l}\sqrt{4\pi(2l+1)}\,j_{l}(k_{\gamma}r)Y_{l}^{0}(\Omega). \tag{4.31}$$

Substituting the above expressions into the amplitude of equation (4.23), one gets the DWA S-matrix as

$$\begin{aligned} S_{fi} \;=\; & \frac{e}{\pi}\left(\frac{E_p+M}{E_p E_{\eta} E_{\gamma}}\right)^{1/2} \delta(E_p+E_{\gamma}-E_B-E_{\eta}) \\ & \times \sum_{J_B M_B} (J_f, J_B; M_f, M_B | J_i, M_i) \left[S_{J_i J_f}(J_B)\right]^{1/2} \\ & \times \sum_{L J L_{\eta} L_{\gamma}} i^{L_{\gamma}-L-L_{\eta}} (2L_{\gamma}+1)^{1/2} \\ & \times \sum_{M M_{\eta}} Y_{L}^{M-s_f}\left(\hat{\mathbf{k}}_p\right) \left[Y_{L_{\eta}}^{M_{\eta}}\left(\hat{\mathbf{k}}_{\eta}\right)\right]^{*} \left(L, \frac{1}{2}; M-s_f, s_f | J, M\right) \end{aligned}$$

$$\times \left\{ R_{ff}\left[\kappa\kappa_B L_\eta L_\gamma\right] A_{11} \begin{bmatrix} \kappa & \kappa_B & L_\eta & L_\gamma & \xi \\ M & M_B & M_\eta & & \end{bmatrix} \right.$$

$$+ i R_{fg}\left[\kappa\kappa_B L_\eta L_\gamma\right] A_{12} \begin{bmatrix} \kappa & \kappa_B' & L_\eta & L_\gamma & \xi \\ M & M_B & M_\eta & & \end{bmatrix}$$

$$- i R_{gf}\left[\kappa\kappa_B L_\eta L_\gamma\right] A_{21} \begin{bmatrix} \kappa' & \kappa_B & L_\eta & L_\gamma & \xi \\ M & M_B & M_\eta & & \end{bmatrix}$$

$$\left. + R_{gg}\left[\kappa\kappa_B L_\eta L_\gamma\right] A_{22} \begin{bmatrix} \kappa' & \kappa_B' & L_\eta & L_\gamma & \xi \\ M & M_B & M_\eta & & \end{bmatrix} \right\} \tag{4.32}$$

where we have $\kappa = (L - J)(2J + 1)$ and $L' = 2J - L$. The radial integrals are given by

$$R_{CB}\left[\kappa\kappa_B L_\eta L_\gamma\right] = \int C_{LJ}(r)\, B_{L_B M_B}(r)\, v_{L_\eta}(k_\eta r)\, j_{L_\gamma}(k_\gamma r)\, r^2 dr, \tag{4.33}$$

and $C(r)$ is either upper- or lower-component radial function for the ejected proton while $B(r)$ is corresponding bound state wavefunction. The angular integrals are also given as follows

$$A_{ij} \begin{bmatrix} \kappa' & \kappa_B & L_\eta & L_\gamma & \xi \\ M & M_B & M_\eta & & \end{bmatrix} = \int \left(\mathcal{Y}^{M}_{L1/2J}\right)^\dagger \Gamma_{ij} \mathcal{Y}^{M_B}_{L_B 1/2 J_B} Y^{M_\eta}_{L_\eta}(\Omega)\, Y^{0}_{L_\gamma}(\Omega)\, d\Omega, \tag{4.34}$$

The matrix operators Γ_{ij} are the elements of the 4×4 Γ matrix operator

$$\Gamma = \begin{pmatrix} \Gamma_{11} & \Gamma_{12} \\ \Gamma_{21} & \Gamma_{22} \end{pmatrix}. \tag{4.35}$$

The DWA amplitude (4.32) is then used to calculate the observables of the reaction.

4.1.3 Observables

It is useful to define a function of the initial and final spin projections $Z^{sf}_{\xi M_B}$ by rewriting the amplitude of equation (4.32) in the form

$$\begin{aligned} S_{fi} &= \frac{e}{\pi}\left(\frac{E_p + M}{E_p E_\eta E_\gamma}\right)^{1/2} \delta(E_p + E_\gamma - E_B - E_\eta) \\ &\times \sum_{J_B M_B} (J_f, J_B; M_f, M_B | J_i, M_i) \\ &\times \left[S_{J_i J_f}(J_B)\right]^{1/2} Z^{s}_{\xi} \text{[illegible]} \end{aligned} \tag{4.36}$$

The triple differential cross section is related to $Z^{sf}_{\xi M_B}$ by

$$\begin{aligned} \frac{d^3\sigma}{d\Omega_\eta d\Omega_p dE_\eta} &= \frac{8\alpha\pi}{\hbar c}\left[\frac{E_p + Mc^2}{E_\gamma}\right] k_p c\, k_\eta c \\ &\times \frac{1}{R} \sum_{J_B M_B s f \xi} \frac{S_{J_i J_f}(J_B)}{2J_B + 1} |Z^{sf}_{\xi M_B}|^2 \end{aligned} \tag{4.37}$$

where R is a recoil factor (of the same form as that for $A(e, e'p)A-1$ reaction in chapter 3)

$$R = 1 + \frac{E_\eta}{E_r}\left(1 - \frac{k_\gamma}{k_\eta}\mathrm{Cos}\,(\theta_\eta) - \frac{k_p}{k_\eta}\mathrm{Cos}\,(\theta_{\eta p})\right), \tag{4.38}$$

and E_r is the energy of the residual nucleus.

The photon asymmetry for linearly polarized incident photons is

$$A = \frac{d\sigma_\parallel - d\sigma_\perp}{d\sigma_\parallel + d\sigma_\perp}, \tag{4.39}$$

where $d\sigma_\parallel$ and $d\sigma_\perp$ are the cross section for specified polarizations of the incident photon, namely parallel and perpendicular to the plane of the reaction.

4.2 Results of the A(γ, ηp)A−1 Reactions

Let us address two important issues regarding this reaction before discussing the results of our model. The first of these is: what is the desirable kinematic situation that maximizes the cross section for each incident photon energy? This task is very important because of the generally low cross sections for the reaction. The second point, related to the basic motivation for studying this reaction i.e. shedding more light on the behavior of the $S_{11}(1535)$ resonance within the nuclear medium, has to do with exploring the energy region where this resonance diagram is the dominant contributer to the reaction. We will accomplish these two tasks using the plane wave S-matrix (4.27) for a number of target nuclei.

Recall in our plane wave calculations outgoing proton and η meson are described by plane waves. The bound nucleon is described by a solution of the Dirac equation involving relativistic scalar and vector Hartree potentials of reference [28]. We used the maximum value for the spectroscopic factor (i.e $2J_B + 1$; J_B is the total angular momentum of the interacting bound proton) for all the calculations presented in this chapter.

Figure (4.3) shows the calculated cross section for the (γ, ηp) reaction on ^{12}C target nuclei leading to the ground state of ^{11}B which is a $1p_{3/2}$ hole state. The incident photon energy is 750 MeV and the azimuthal angles of the outgoing proton and η meson are fixed at 180° and 0°, respectively. Each three dimensional graph shows the calculations for a specific polar angle of the η meson. The polar angle of the outgoing proton is represented by the y-axis. The x-axis represents the kinetic energy of the η meson.

The calculations are performed for four different polar angles of the η meson and cover the polar angles of the outgoing protons from 0^o to 90^o. These results indicate that, for this photon energy, the cross section reaches its maximum value when both of the outgoing particles (i.e. η meson and proton) have polar angle near 30^o.

Now let us investigate the dependence on the incident photon energy in an effort to locate the region where the contributions due to S_{11} resonance are dominant. We fixed the angles of the outgoing particles at the values suggested by the above search, namely $\theta_\eta = 30^o$, $\phi_\eta = 0^o$ and $\theta_p = 30^o$, $\phi_p = 180^o$, then varied the energy of the incident photon from near threshold to the energy where contributions from the $S_{11}(1535)$ diagrams are comparable to the contributions from all other diagrams. Results of these calculations are illustrated in figure (4.4): dotted curves are the contribution of the $S_{11}(1535)$ diagrams while the contributions due to the rest of the diagrams are represented by solid curves. Note the varying scale for the cross section axes. Figure (4.4) shows that the $S_{11}(1535)$ resonance dominates the cross section from threshold up to a photon energy of 1100 Mev. The cross section is small at energies near threshold and increases with increasing photon energy reaching its largest values in the photon energy range 800-950 MeV. At energies higher than 950 MeV, cross section of the $S_{11}(1535)$ resonance decreases as photon energy increases.

We suggest the photon energy region of 700-800 MeV as the best energy region to study the behavior of the $S_{11}(1535)$ resonance within the nuclear matter. In this energy region, not only does the S_{11} dominate the cross section but also the magnitude of the cross section is relatively high.

We also use the plane wave S-matrix to look at the relative contributions of different diagrams. Figure (4.5) shows the results of these calculations for the same reaction, with the outgoing particles having the same angles as those of figure (4.4). The cross section arising from the $S_{11}(1535)$ pole diagrams, shown by the long-dashed curve, is clearly the dominant contribution. The second largest contribution is form

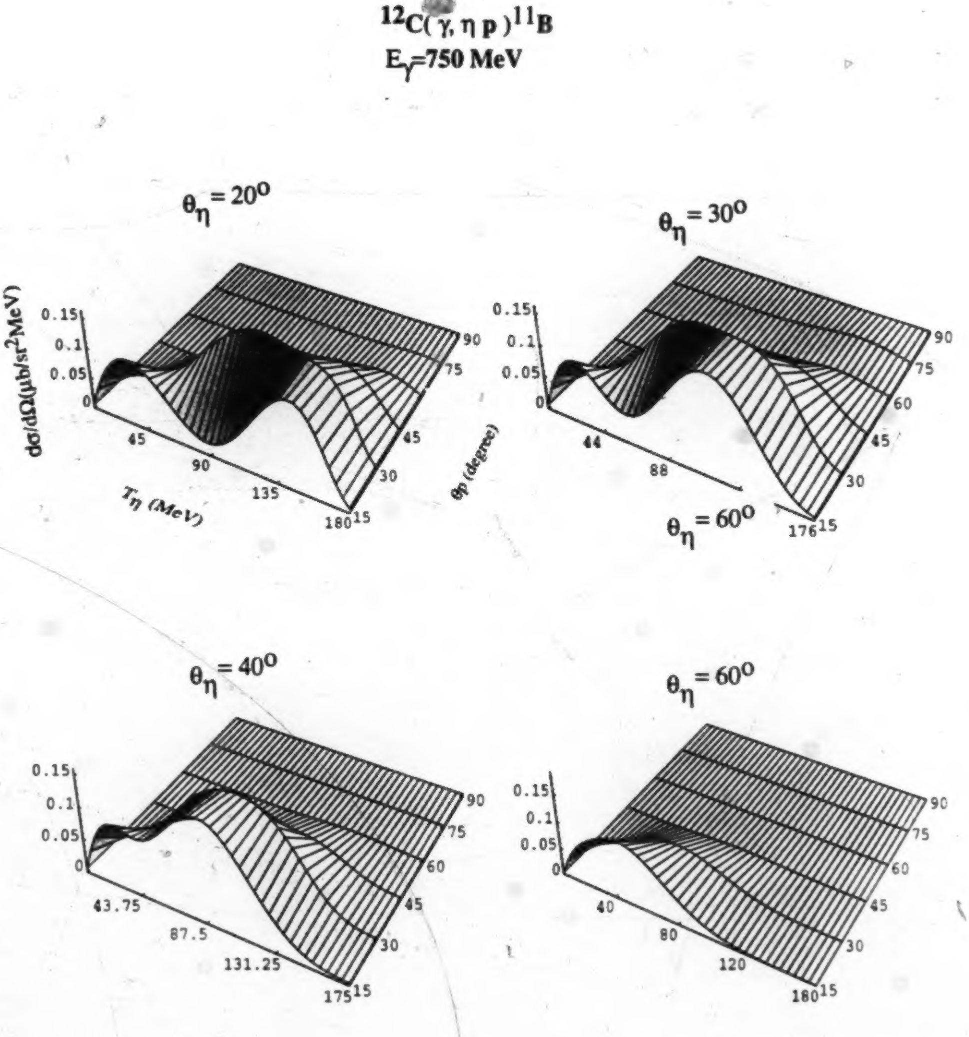

Figure 4.3: The cross section for the $^{12}C(\ \gamma, \eta p\ )^{11}B_{g.s.}$ reaction for the regions of the phase space where the reaction has significant yield.

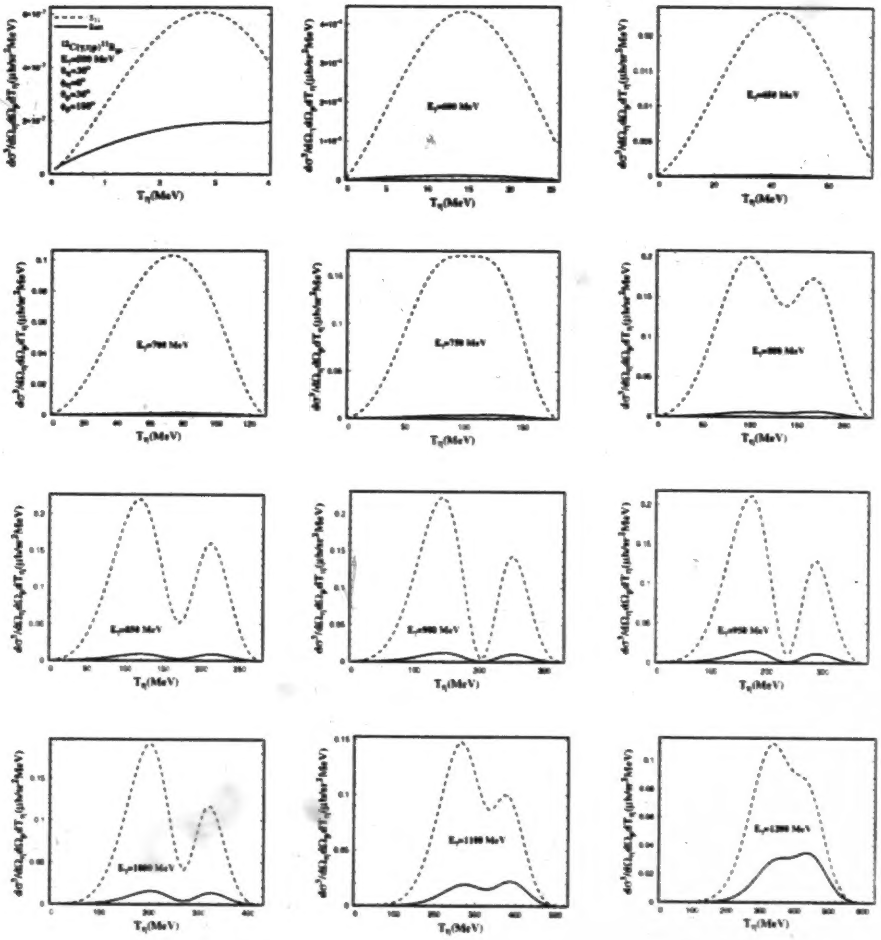

Figure 4.4: The cross section for the $^{12}C(\gamma, \eta p)^{11}B_{gs}$ reaction for the photon energies from near threshold up to 1.2 GeV.

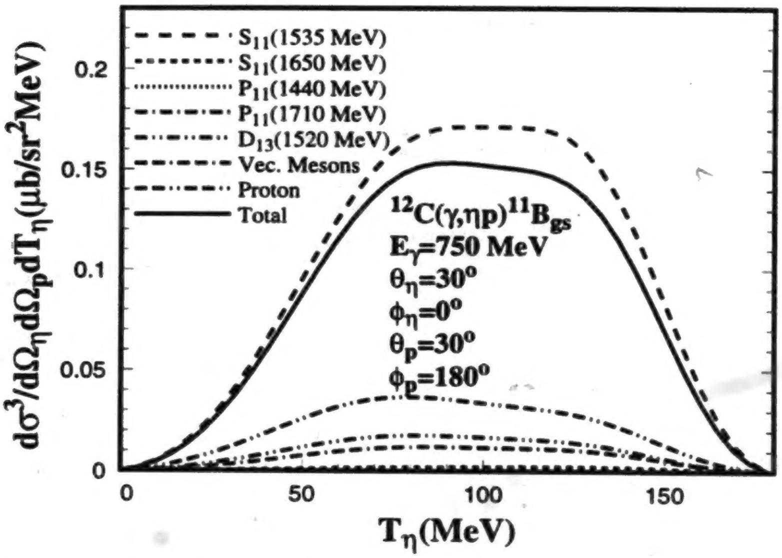

Figure 4.5: Contributions of different diagrams to cross section of the $^{12}C(\ \gamma, \eta p\ )^{11}B_{gs}$ reaction at photon energies of 750 MeV.

the proton poles; this is depicted by the double dash-double dotted curve. The results of the calculations using D$_{13}$(1520) resonance and vector mesons poles are shown by dot-dot-dashed and dot-dash-dashed curves, respectively. The other diagrams (i.e. P$_{11}$(1440), S$_{11}$(1650), P$_{11}$(1710)) do not make significant contributions to the reaction at this energy. The solid curve is the result of the plane wave calculation including contributions of all the diagrams considered in our reaction model. These results once again assure us that the main contributer in this energy region is S$_{11}$(1535) resonance.

We include the final state interactions of the outgoing particles with the recoil nucleus in our distorted wave calculations. Appropriate optical potentials are used in the calculation of the wavefunctions of the outgoing proton and η meson. In all the distorted wave calculation presented here the global optical potentials of Cooper *et.al* [29] have been used to calculate the Dirac distorted wavefunctions describing outgoing proton. For the outgoing η meson we use the Klein-Gordon wave equation together with the optical potentials of references [10, 30].

We discuss below the results of these distorted wave calculations of the (γ, ηp) reaction on three different nuclear targets, namely ^{12}C, ^{16}O and ^{40}Ca.

4.2.1 The ^{12}C(γ, ηp)^{11}B Reaction

Figure (4.6) shows the calculated observables for the ^{12}C(γ, ηp)^{11}B reaction with a photon energy of E_γ = 750 MeV. The residual nucleus is in an odd parity $1p_{3/2}$ hole state. The energy dependent Global optical potential of Cooper *et al.* [29], and the optical potential DW1 of reference [10] are used for outgoing proton and η meson, respectively.

Figure (4.6-a) compares the plane wave calculations of the cross section with those including the final state interactions of one or both of the outgoing particles with the residual nucleus.

The short dashed curve shows the suppression due to the final state interaction of the outgoing proton with the residual nucleus. This suppression is more evident at higher η energies because the energy of the outgoing proton is smaller and hence its chance for absorption is higher. This same qualitative behavior holds for the η meson distortion (dashed curve); the suppression is skewed towards smaller η energies, again because the meson gets absorbed more readily at low energies. The dotted curve is the calculated cross section when distortion effects are included for both of the outgoing particles. Inclusion of both final state interactions leads to a suppression of the cross section by about a factor of $\sim$ 0.6 relative to the plane wave calculations and produces a curve which is flat in the η kinetic energy region of 50-140 MeV.

Figure (4.6-b) shows the photon asymmetry for the above reaction. Curve labels are the same as in part a) of the figure. Plane wave calculations (solid curve) produce a flat curve for the photon asymmetry varying from 0.1 to 0.13. Distortion of outgoing η meson affects the shape and magnitude of the photon asymmetry only slightly, lowering its magnitude at small η energies and pushing it up at high η energies. Inclusion of the final state interactions of the outgoing proton results in significant changes in asymmetry. When both final state interactions are included, the resulting curve (dotted curve) has characteristics close to the case when only the proton is distorted.

Figure (4.7) shows the effects of the different η optical potentials on the calculated observables. The curves of figure (4.7) are obtained with the same bound and continuum proton potentials while different optical potentials are used for the outgoing η meson. The five different potentials used are: the DW1 and DW2 of Lee *et al.* [10], the potential of Chiang *et al.* [30] with three choices for the real part of the S_{11} self energy, namely $\mathrm{Re}\Sigma_{N^*} = (\rho/\rho_0)V_{N^*}$ and V_{N^*}=50, 0, -50 MeV (ρ and ρ_0 are the nuclear density for finite and infinite nuclear medium, respectively).

Calculated cross sections using the above potentials have similar shapes, except for the case V_{N^*}=50 MeV of the latter reference whose corresponding curve has a slightly different shape. However, the magnitude of the cross section obtained with the DW1 potential is larger than the others.

Calculations with the optical potential of reference [30], with non-vanishing values for the real part of the S_{11} potential (dashed and dotted curves), produce results which have roughly the same magnitude as those obtained with the use of potential DW2. On the other hand the cross sections obtained with the use of these two last potentials have different shape than the others. They approximately reflect relative to the η kinetic energy of 100 MeV by changing the sign of the real value of the S_{11} potential. We can make the following comments regarding to the final state

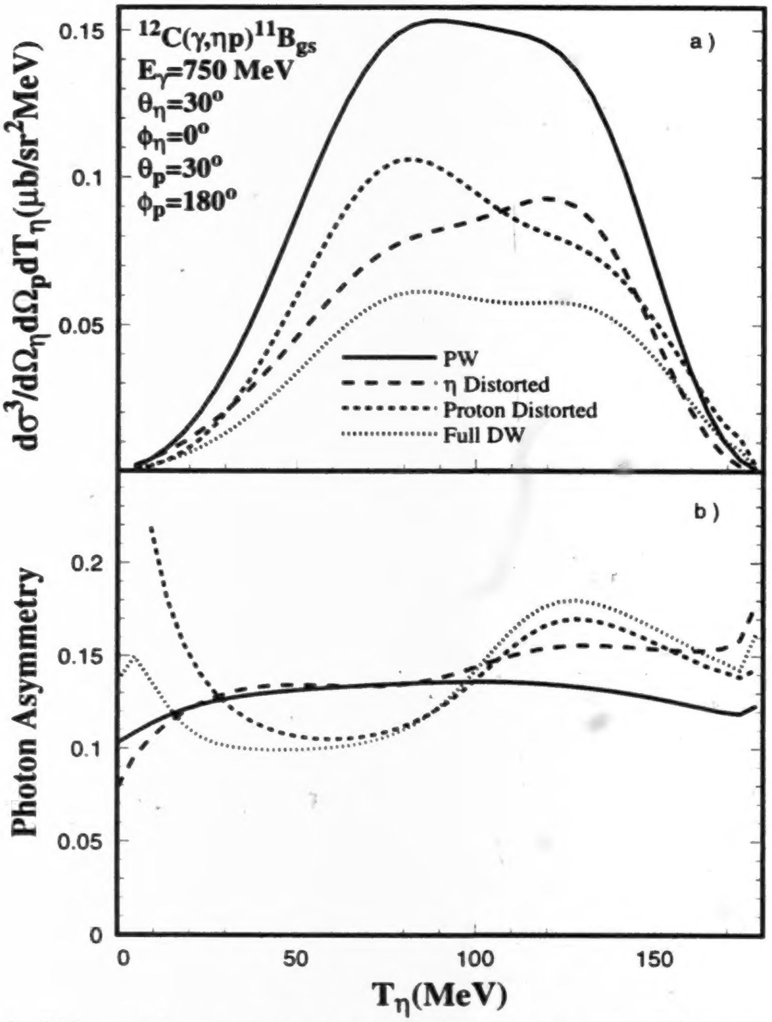

Figure 4.6: Differential cross section (a), and photon asymmetry (b) for the reaction $^{12}C(\gamma,\ \eta p)^{11}B$ at $E_\gamma = 750$ MeV. The Hartree potentials of reference [28] are used in calculation of the bound state wavefunction. The final state energy dependent global optical potentials are taken from reference[29]. The η optical potential is the DW1 potential of Lee *et al.* [10]. Solid curve - plane wave calculations. Long dashed curve - calculations include only final state interactions of the η meson (η Distorted). Short dashed curve - calculations include only final state interactions of outgoing proton (Proton Distorted). Dotted curve - both η and proton waves are distorted (Full DW).

interactions of the η meson with the residual nucleus. First, our results show the final state interactions have large effects on the calculated cross sections. Second, the different optical potentials produce different results; there can be as much as $\sim 35\%$ variation in the results.

The DW calculations for photon asymmetry with different optical potentials for the outgoing η meson are shown in figure (4.7-b). All of the optical potentials produce approximately the same shape and magnitude for the photon asymmetry. The asymmetry therefore, at least at this energy, is not particularly sensitive to the different choices of the final state interactions of η mesons.

Figure (4.8) shows the effects of the different proton optical potentials on the calculated observables of the ^{12}C(γ, ηp)^{11}B reaction with the same kinematics as those of figure (4.6). In all the calculations presented in this figure the optical potential DW1 of reference [10] is used for the final state interaction of the η meson with the residual nucleus. Since the same bound state potentials (Hartree) are used throughout, the differences between these curves come only from the effects of different optical potentials for the outgoing proton. The four potentials used for distortion of the outgoing nucleon are from reference [29]. The first of these is obtained from a fit to the proton elastic scattering data on ^{12}C from 29-1040 MeV. The last three potentials result from three different A and energy dependent (A is the mass number of the target nucleus) fits to scattering data on several nuclei from ^{12}C up to ^{208}Pb, in the proton energy range 21-1040 MeV.

Results obtained using the energy dependent global optical potential (solid curve, labelled as Energy Dep.), are slightly higher than those for the other potentials, otherwise all potentials produce the same shape for the cross sections.

Figure (4.8-b) shows the effect of the different proton optical potentials on the calculated photon asymmetry. The calculations based on different proton optical

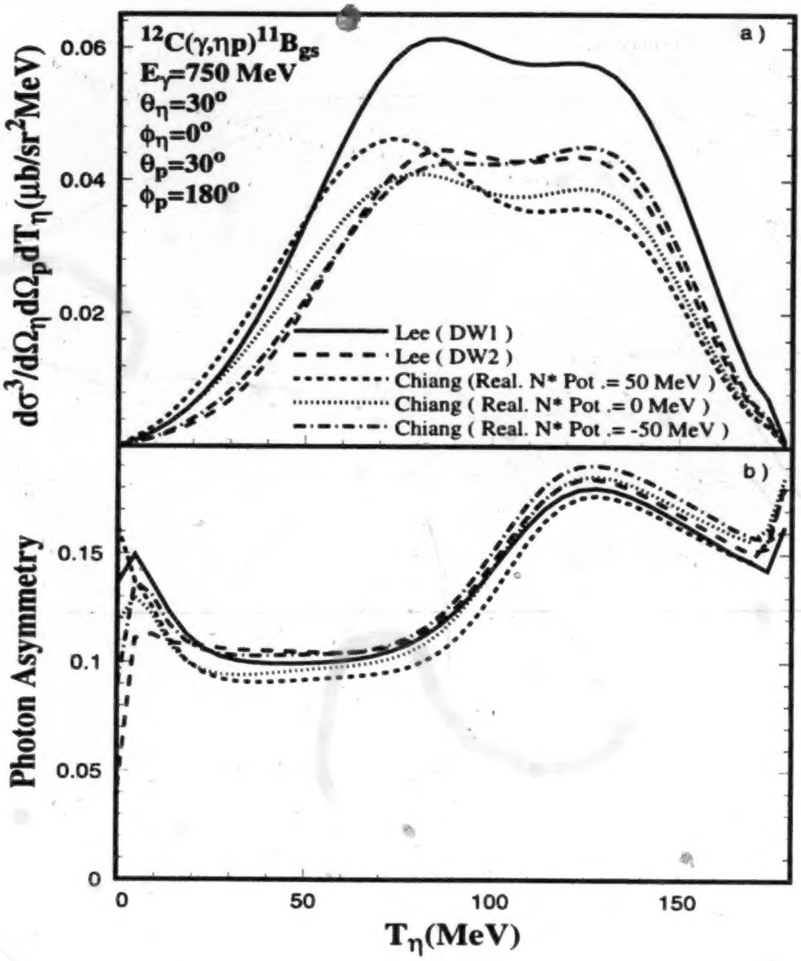

Figure 4.7: Differential cross section (a), and photon asymmetry (b) for the same reaction as figure (4.6). The final state optical potentials for the proton and the bound state potentials are fixed. Curves are shown for different choices of η optical potentials: Solid curve - DW calculations using DW1 of reference [10]. Long dashed curve - DW calculations using DW2 of reference [10]. DW calculations using the optical potential of reference [30] with the real part of the S_{11} self energy set to 50 MeV (short dashed curve), 0 Mev (dotted curve) and -50 MeV (dash-dotted curve).

potentials lead to curves with the same shape. The use of the A and energy dependent optical potentials results in curves slightly lower than the curve for the energy dependent potential, in the η kinetic energy region of 10-100 MeV.

The sensitivity of the results to the bound state potentials was evaluated by performing calculations, with the same ingredients, but for two different binding potentials. The kinematics and the optical potentials of the outgoing particles are the same as those of figure (4.6). In one of these calculations we used relativistic scalar and vector potentials of Woods Saxon shape [31] to calculate the Dirac bound state wavefunction (dashed curve). Figure (4.9-a) presents the results of this calculation along with those obtained using Hartree potentials (solid curve). Comparison of these curves indicates the level of the sensitivity of our model calculations to the bound state potentials. This comparison shows that the Hartree Bound state potentials lead to some enhancement in the calculated cross sections of ($\sim$ 10%). On the other hand the photon asymmetry calculations appear to be insensitive to different choices of the bound state potentials; the solid and dashed curves of figure (4.9-b) overlap in all the η energy range shown in this figure.

In addition to the kinematic set discussed above, we also calculated the observables of the reaction for another set of angles for the outgoing particles. The motivation for choosing this new set is to compare the results of our model with those of the nonrelativistic model of Lee *et al.* [10].

Figure (4.10) shows the results of the calculation of the (γ, ηp) reaction on the same target nucleus and the same incident photon energy as those of figure (4.6), but with the directions of outgoing particles fixed at $\theta_\eta = 20^o$, $\phi_\eta = 0^o$ and $\theta_p = 15^o$, $\phi_p = 180^o$. In all the relativistic distorted wave calculations presented in this figure we have used the energy dependent global optical potential of Cooper *et al.* [29] for the outgoing proton, and DW1 optical potential of reference [10] for η meson.

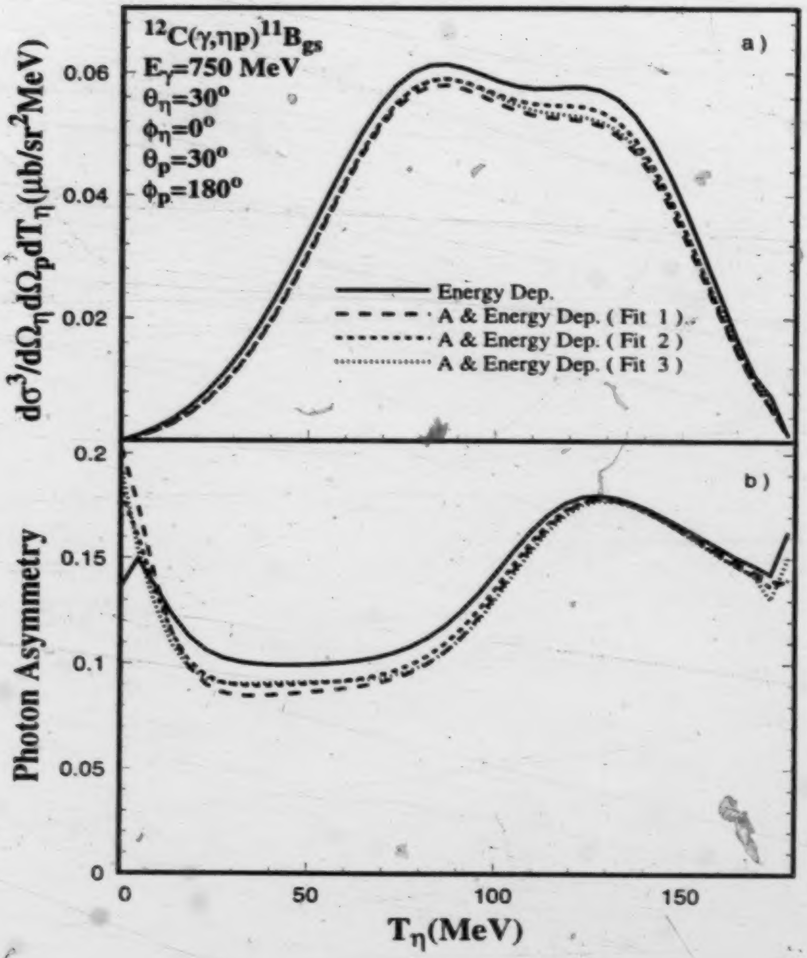

Figure 4.8: Differential cross section (a), and photon asymmetry (b) for the same reaction as in figure (4.6) The final state optical potential for the η meson is the same as in figure (4.6). Curves are labelled for different choices of proton optical potentials: Solid curve - DW calculations using energy dependent optical potential of reference [29], long dashed curve - DW calculations using first fit of A and energy dependent optical potential of reference [29], short dashed curve - DW calculations using second fit of A and energy dependent optical potential of reference [29] and dotted curve - DW calculations using third fit of A and energy dependent optical potential of reference [29].

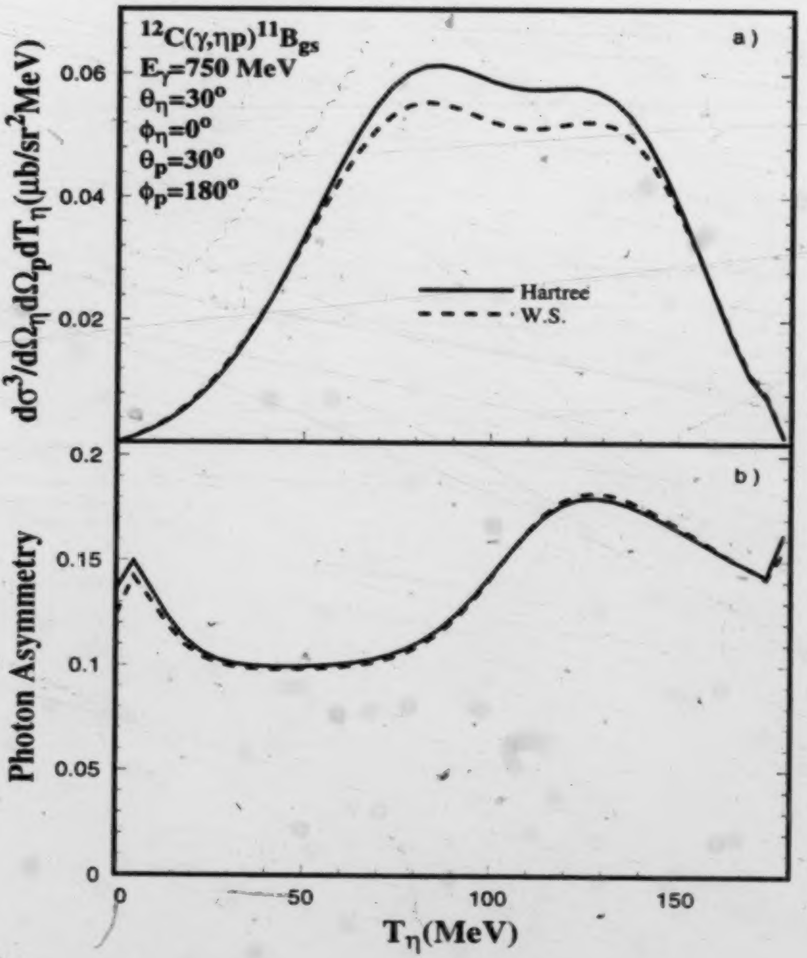

Figure 4.9: Differential cross section (a), and photon asymmetry (b) for the same reaction as in figure (4.6) The final state optical potentials for the η meson and outgoing proton are the same as those of figure (4.6). Curves are labelled for different choices of proton bound potentials: Solid curve - DW calculations using Hartree potential of reference [28] and dashed curve - DW calculations using Woods-Saxon potential of reference [31].

The Hartree binding potential is used to calculate the bound state wave function. We have also plotted the results of the plane wave calculations of Lee *et al.* [10]. Figure (4.10-a) shows the cross section and figure (4.10-b) the resulting photon asymmetry. Results of the relativistic plane wave and distorted wave calculations are shown by solid (labelled as Rel. PW) and dotted curves (labelled as Rel. DW), respectively.

The nonrelativistic plane wave calculations of Lee *et al.* are depicted by short dashed curve (labelled as Nonrel. PW (Lee et al.)). Comparison of the solid and short dashed curves indicates that both relativistic and nonrelativistic calculations produce curves with similar shape, but nonrelativistic calculations lie above the relativistic ones up to η energy of ~120 MeV. Compared to the relativistic calculations, the nonrelativistic calculations have the first peak shifted slightly toward higher energies and the second peak moved toward lower η energies.

We have also performed the relativistic plane wave calculations with the lower components of the bound and continuum nuclear wavefunctions set to zero. As we know, working with the upper component only is not equivalent to the nonrelativistic calculations (see chapters II and III). This discussion is meant to assess the role of the lower components of the nucleon wavefunctions on the observables. The results for the cross section are very close to those of the full relativistic calculations at all η energies (long dashed curves, labelled as Upper PW), except in the region of first peak. We note that in the low η energy region the proton acquires higher energies, therefore the effects of the lower components of the wavefunctions are somewhat enhanced. Note also that the elimination of the lower components brings the relativistic and nonrelativistic calculations slightly closer.

The effects of the final state interactions of the outgoing particles on the cross sections at the kinematics chosen here are slightly less than those for the kinematics of figure (4.6). Note that the distorted cross sections in figure (4.6) can only reach

$\sim \frac{2}{5}$ of their plane wave values, whereas at the first peak region in this figure the distorted wave calculations reach $\sim \frac{1}{2}$ of the relativistic plane wave values.

The plane wave relativistic and nonrelativistic calculations of the photon asymmetry yield two different results. The relativistic calculations produce a flat curve with small positive values, whereas nonrelativistic calculations result in a curve with large negative values, depending on the η energy. Moreover as stated in reference [10], the final state interactions do not have any significant effect on the asymmetry in nonrelativistic calculations. On the other hand the relativistic calculations are affected by the inclusion of the final state interaction (compare solid and dotted curves). The asymmetry is shifted down when the contributions of the lower components of the nuclear wavefunctions are removed.

Let us before discussing the results of our calculations for other target nuclei, see if the inclusion of the final state interactions of the outgoing particles preserves the dominance of the $S_{11}(1535)$ contribution to the reaction in the energy range suggested in figure (4.4). Figure (4.11) shows the results of our DWA for two calculations as explained below. The nuclear target, the photon energy, directions of the detected particles and the potentials are the same as figure (4.6). In the first calculation, it is assumed that reaction is taking place only through $S_{11}(1535)$ resonance (solid curve, labelled as S_{11}), whereas the second calculation includes the contributions of all the diagrams considered in our model but those of $S_{11}(1535)$ resonance (dashed curve, labelled as Rest). These results indicate that the $S_{11}(1535)$ resonance, as in the plane wave calculations (4.4), is the dominant contributor to the reaction in the distorted wave limit.

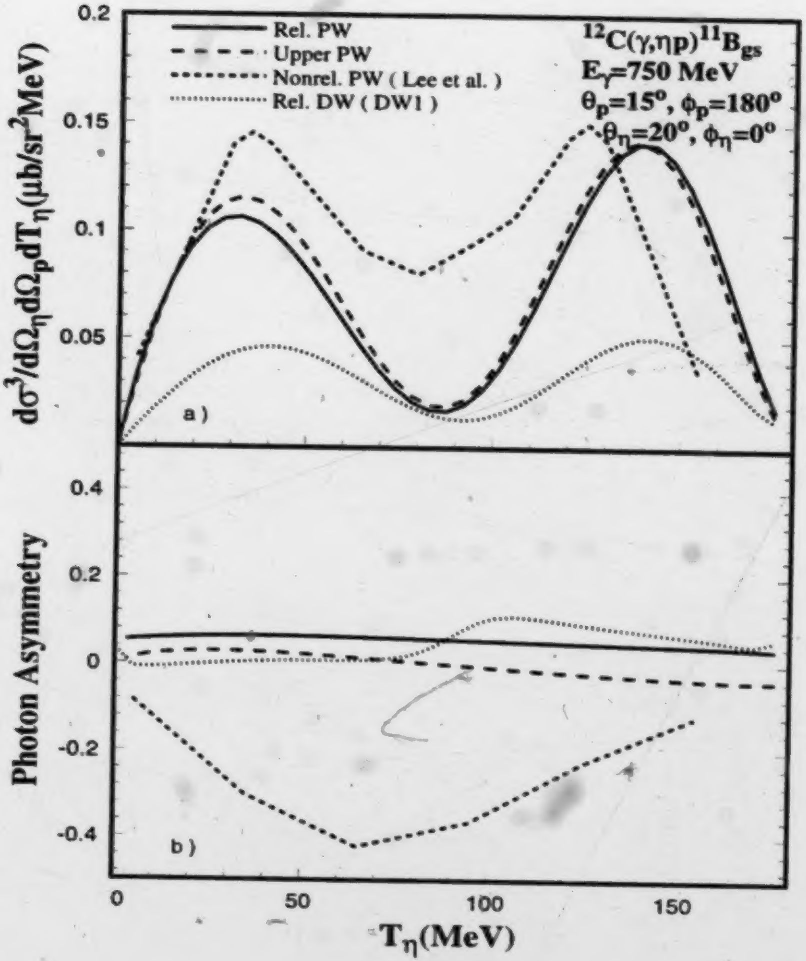

Figure 4.10: Differential cross section (a), and photon asymmetry (b) for the same reaction as figure (4.6). Curves are labelled as: Solid curve - relativistic PW calculations. Long dashed curve - PW calculations with the use of only upper component of the nuclear wavefunctions. Short dashed curve - nonrelativistic PW calculations of Lee *et al.* [10]. Dotted curve - relativistic DW calculations.

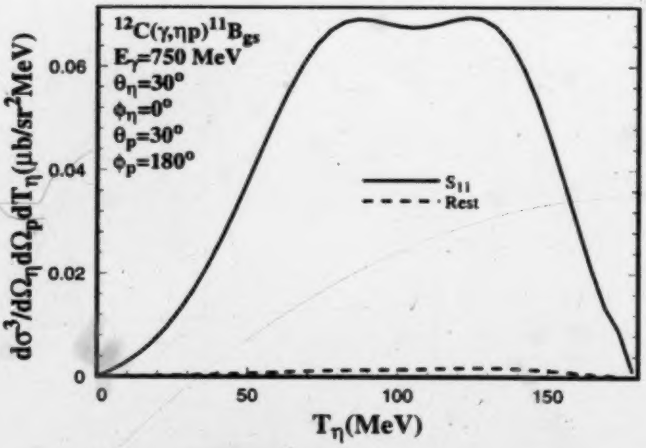

Figure 4.11: Differential cross section for the same reaction as figure (4.6). Curves are labelled as: Solid curve - DW calculations using only $S_{11}(1535)$ diagrams, labelled as S_{11}. Long dashed curve - DW calculations using all the diagrams but those of $S_{11}(1535)$ resonance, labelled as Rest.

4.2.2 The $^{16}O(\gamma, \eta p)^{15}N$ Reaction

We study the photoproduction of η meson on another target leading to different hole state from that of the ^{12}C.

Figure (4.12) shows the results of the calculations for the (γ, ηp) reaction on a ^{16}O target leading to the ground state of ^{15}N (an odd parity $1p_{1/2}$ hole state). The Hartree potential of reference [28] is used to calculate the bound state wavefunctions. The final state interactions of the outgoing proton and η meson are calculated using the energy dependent global optical potential of reference [29] and the DW1 optical potential of reference [10], respectively. The energy of the incident photon and the angels of the outgoing particles are the same as in figure (4.6)

Cross section curves show behavior similar to the ^{12}C case (i.e figure(4.6)), except that cross section is slightly suppressed for the ^{16}O target.

On the other hand the resulting photon asymmetries for this target, behave differently form those of the ^{12}C target. The distorted wave calculations here peak at lower η energies, whereas for the ^{12}C target the peak is at higher energies. Moreover asymmetries for this target have larger magnitudes. Since we are comparing the results of the reaction on the nucleons with two different states, these differences indicate that the asymmetry is nuclear state dependent.

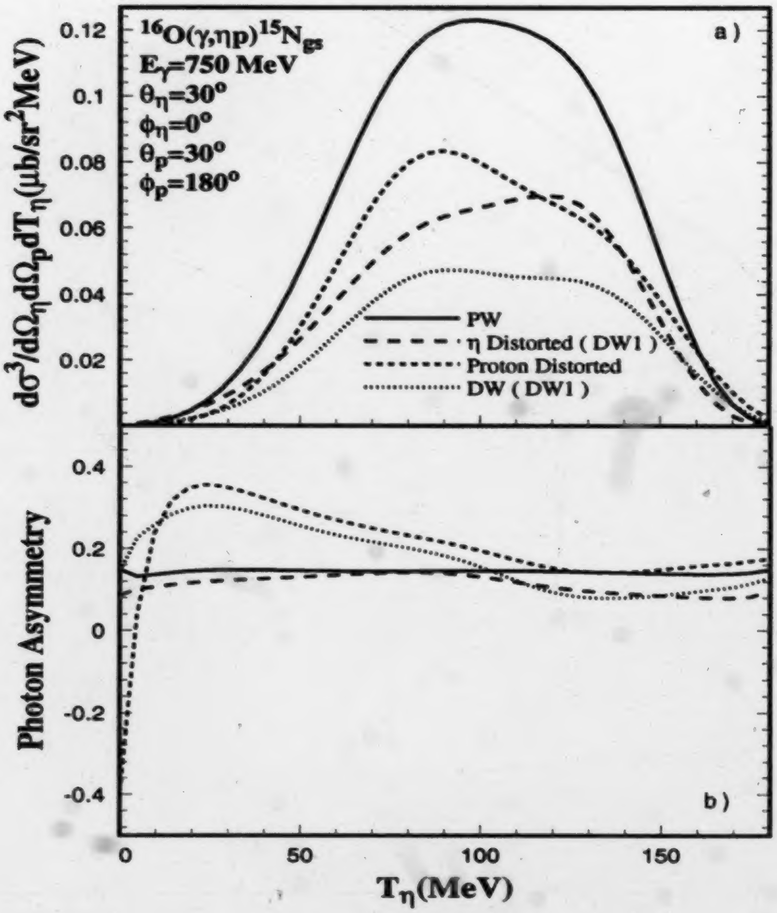

Figure 4.12: Differential cross section (a), and photon asymmetry (b) for the reaction $^{16}O(\gamma,\ \eta p)^{15}N$ at $E_\gamma = 750$ MeV. The Hartree potential of reference [28] is used in calculation of the bound state wavefunction. The final state energy dependent global optical potentials are taken from reference[29]. The η optical potential is the DW1 potential of Lee *et al.* [10]. Solid curve - plane wave calculations. Long dashed curve - calculations include only final state interactions of the η meson with nuclei (η Distorted). Short dashed curve - calculations include only final state interactions of outgoing proton (Proton Distorted). Dotted curve - both η and proton waves are distorted (DW).

4.2.3 The ^{40}Ca(γ, ηp)^{39}K Reaction

We have also used our relativistic model for calculations of the reaction on ^{40}Ca target leading to ground and excited states of ^{39}K nucleus. Similar investigations as for the ^{12}C target, searching for the energy region as well as angles of the outgoing particles which maximize the cross section and preserve the dominance of the $S_{11}(1535)$ resonance, are performed for this target. This study confirmed in the same result obtained for the ^{12}C target.

Figure (4.13) shows the results of our calculations for the ^{40}Ca(γ, ηp)^{39}K reaction. The residual nucleus is left in its ground state (an even parity $1d_{3/2}$ hole state) and the incident photon energy is 750 MeV. The angles of the outgoing particles are fixed at $\theta_\eta = 30^o$, $\phi_\eta = 0^o$, $\theta_p = 30^o$, and $\phi_p = 180^o$. The bound state Hartree potential is from reference [28]. The energy dependent global optical potential of reference [29] and the DW1 optical potential of reference [10] are used for final interactions of outgoing proton and η meson, respectively.

The calculated cross sections of figure (4.13-a) show curves with different shapes from those of the two targets studied previously. The plane wave calculations produce a curve which is peaked at two energy regions. The final state interactions of the outgoing particles suppresses the cross section more for the ^{40}Ca target. Again this is likely due to the larger distance that outgoing particles must travel inside the nuclear matter before leaving the nucleus. When considering the distortion for one of the outgoing particles, the effect of the energy of the outgoing particles on the suppression of the cross section is more pronounced for this target (compare the long- and short-dashed curves of this figure with those of figures (4.6, 4.12).

As for the other two targets, the results of the photon asymmetry calculations are sensitive to the final state interactions of the outgoing particles. This is in contrast to the predictions of the nonrelativistic model for the reaction. Comparing with the results of the calculations on the ^{12}C and ^{16}O targets, shapes and magnitudes of the asymmetries are different. For example the asymmetry for the DW calculations peaks at lower η energies, but unlike that of the ^{16}O target which reduces smoothly by increasing the η energy, here the results show sharper changes in variation of energy.

We have also used our model amplitude to calculate the observable of the reaction on a ^{40}Ca target leading to an odd parity $1p_{3/2}$ hole state of the recoil nucleus ^{39}K. The results are shown in figure (4.14).

The curves in this figure have the same features as in figure (4.10), except that the differences in the magnitude of the relativistic and nonrelativistic cross sections are larger. Also the effects of the final state interactions are more prominent for the present case.

Notice that the corresponding curves in figures (4.10-b) and (4.14-b) have approximately the same shapes. These similarities and the assumption that reaction is taking place on the same nuclear state for both calculations, support our earlier statement on the state dependency of the asymmetry.

We have also studied the sensitivity of the results to different nuclear binding and continuum potentials, for the ^{16}O and ^{40}Ca targets. The results were similar to those discussed earlier for the ^{12}C target.

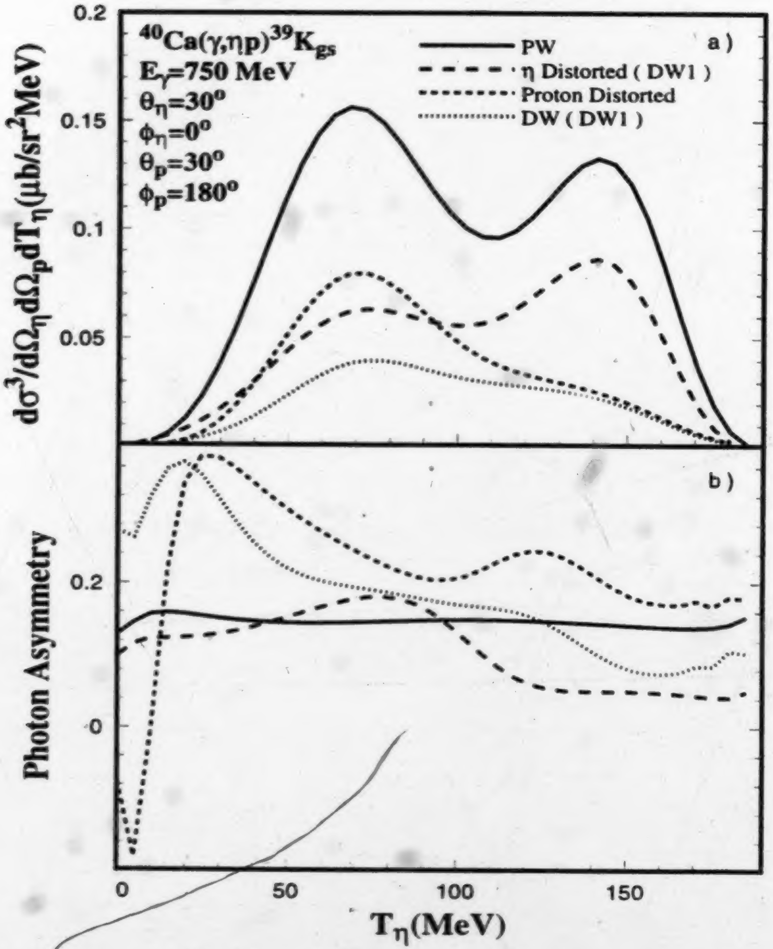

Figure 4.13: Differential cross section (a), and photon asymmetry (b) for the reaction $^{40}Ca(\gamma, \eta p)^{39}K$ at $E_\gamma = 750$ MeV. The Hartree potential of reference [28] is used in the calculation of the bound state wavefunction. The final state energy dependent global optical potentials are taken from reference[29]. The η optical potential is the DW1 potential of Lee *et al.* [10]. Solid curve - plane wave calculations. Long dashed curve - calculations include only final state interactions of the η meson with nuclei (η Distorted). Short dashed curve - calculations include only final state interactions of outgoing proton (Proton Distorted). Dotted curve - both η and proton waves are distorted (DW)

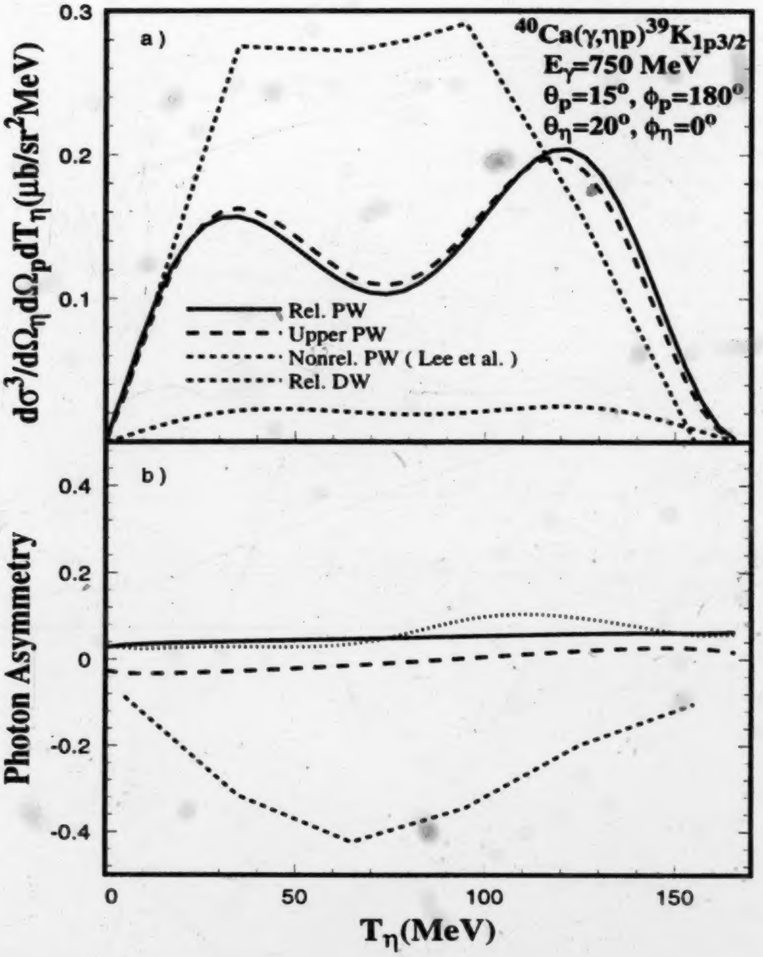

Figure 4.14: Differential cross section (a), and photon asymmetry (b) for the same reaction as figure (4.13) The potentials are the same as those of figure (4.13). Curves are labelled as in figure (4.10).

4.3 Conclusions

A relativistic model for quasifree A(γ, ηp)A-1 reaction, on the basis of a gauge and Lorentz invariant Lagrangian involving nucleons and meson fields, is constructed. The ingredients of the model are: i) the nucleon wavefunctions are solutions of the Dirac wave equation with appropriate scalar and vector strong potentials obtained from a relativistic mean field theory, ii) The η meson is described by solutions of the Klein-Gordon equation with the appropriate optical potentials, and iii) the interactions between the fields are introduced through a covariant effective Lagrangian. This model is used to calculate the cross section and photon asymmetry, for different target nuclei.

The energy region where the $S_{11}(1535)$ resonance dominates the reaction is specified. This is the best energy region for using the η photoproduction reactions to study the properties of the above resonance in the nuclear medium. We have also searched for a geometry of the outgoing particles where the cross section reaches its maximum for a given incident photon energy. This investigation results in a choice of the angles of the outgoing particles that yield differential cross sections up to 20 nb for some targets. It was shown that within the photon energy region from near threshold up to 1.1 GeV, the $S_{11}(1535)$ resonance dominates the reaction. The other diagrams which have significant contributions are proton, D_{13} resonance and vector meson poles (however their sum is really small).

The final state interactions of the outgoing particles are included through distortion of their wavefunctions using the appropriate optical potentials. The cross sections experience large suppression due to these final state interactions. Several η optical potentials were tested and lead to different results for the cross section (up to $\sim 35\%$) as well as photon asymmetry . On the other hand our model is much less sensitive to different choices of the potentials for the bound and continuum proton.

The uncertainty in η optical potentials makes it difficult to make final predictions for the cross sections. More theoretical work on the final state interactions of the η is required.

Calculations were carried out using the same kinematics as those in the recent nonrelativistic calculations of Lee *et.al* [10]. Results of our calculations for the cross section have shapes close to those of nonrelativistic calculations but the magnitudes of our results are somewhat smaller. In contrast the photon asymmetries predicted by two models differ significantly. The nonrelativistic model gives large asymmetry in the PW limit, which is insensitive tho the final state interactions of the outgoing particles. Our PW predictions for asymmetry are small and the asymmetries are strongly affected by the final state interactions of the outgoing particles.

The next steps to improve the model at the tree level approximation are: removing the plane wave approximation used for the propagators by performing finite range calculations, and including the medium modifications of the propagators.

There is need for experimental data for exclusive reactions on nuclei (currently non-existed) especially spin observables that could shed more light on the differences between the relativistic and nonrelativistic models.

Bibliography

[1] M. Roebig-Landau *et al.*, Phys. Lett. **B373** (1996) 45; M. Vineyard, private communication.

[2] H.C. Chiang, E. Oset and L.C. Liu, Phys. Rev. **C44** (1991) 738.

[3] S.A. Rakityansky, S.A. Sofianos, M. Braun, V.B. Belyaev and W. sandhas, nucl-th/9601035.

[4] S. Wycech, A.M. Green and J.A. Niskanen, Phys. Rev. **C52** (1995) 544.

[5] A.I. Lebedev and V.A. Tryasuchev, Physcs of Atomic Nuclei. Vol. 58, No. 4, 586 (1995).

[6] M. Benmerrouche, Nimai C. Mukhopadhyay and J.F. Zhang, Phys. Rev. **D51** (1995) 3237.

[7] C. Bennhold and H. Tanabe, Phys. Lett. **B243** (1990) 13

[8] C. Bennhold and H. Tanabe, Nucl. Phys. **A530** (1991)625.

[9] L. Tiator, C. Bennhold and S.S. Kamalov, Nucl. Phys. **A580** (1994) 455.

[10] F.X. Lee, L.E. Wright, C. Bennhold and L. Tiator, Nucl. Phys. **A603** (1996) 345.

[11] R.C. Carrasco, Phys. Rev. **C48** (1993) 2333.

[12] A. Hombach *et al.*, Z. Phys. **A352** (1995) 223.

[13] E. Breitmoser and H. Arenhövel, nucl-th/9608064.

[14] M. Batinić, A. Švarc and T.-S.H. Lee, nucl-th/9604043.

[15] R.S. Bhalerao and L.C. Liu, Phys. Rev. Lett. **54** (1985) 865.

[16] B.V. Krippa and J.T. Londergan, Phys. Lett. **B286** (1992) 216.

[17] B.V. Krippa and E. Ya. Paryev, Phys. Scr. **48** (1993) 79.

[18] J.D. Walecka, Ann. Phys. (N.Y.) **83** (1974) 491.

[19] B.D. Serot and J.D. Walecka, Advances in Nuclear Physics (J.W. Negele and E.Vogt, eds.) Vol. **16**, Plenum Press, New York (1986).

[20] B.D. Serot and J.D. Walecka, Advances in Nuclear Physics (J.W. Negele and E. Vogt, eds.), Vol. 16, Plenum Press, New York (1986).

[21] G.A. Lalazissis, M.M. Sherma, P. Ring and Y.K. Gambhir, nucl-th/9608005.

[22] G.M. Lotz and H.S. Sherif, Nucl. Phys. **A537** (1992) 285; Phys. Lett. **B210** (1988) 45.

[23] J.P. McDermott, E. Rost, J.R. Shepard and C.Y. Cheung, Phys. Rev. Lett. **61** (1988) 814.

[24] J.P. McDermott, Phys. Rev. Lett. **65** (1990) 1991.

[25] B.C. Clark, R.L. Mercer and P. Schwandt, Phys .Lett. **B122** (1983) 211.

[26] F. Mandl and G. Shaw, *Quantum Field Theory*, John Wiley & Sons (1984).

[27] J.I. Johansson and H.S. Sherif, Nuc. Phys. **A575** (1994) 477.

[28] C.J. Horowitz and B.D. Serot, Nuc. Phys. **A368** (1986) 503.

[29] E.D. Cooper, S. Hama, B.C. Clark and R.L. Mercer, Phys. Rev. **C47** (1993) 297.

[30] H.C. Chiang, E. Oset and L.C. Liu, Phys. Rev. **C44** (1991)734.

[31] G. Lotz, PH.D thesis, University of Alberta (1989)

[32] J.D. Bjorken and S.D. Drell, *Relativistic Quantum Mechanics*, McGraw-Hill Book Company (1964).

Appendix 4.A Kinematics

In our model for photoproduction of η meson from nuclei, direction of the incoming photon defines the z-axis. We define a reaction plane formed of momenta of incoming photon $\mathbf{k}_\gamma$ and outgoing η meson $\mathbf{k}_\eta$.

The y-axis is normal to this plane and its direction is along the $\mathbf{k}_\gamma \times \mathbf{k}_\eta$ vector. Figure (4.15) depicts the direction of the initial and final particles as well as the choice of axes used in the present calculation.

In the rest of this appendix we will calculate the kinematic quantities required for a situation in which the energies of the incoming photon and the outgoing meson as well as the direction of the outgoing detected particles are given. Let us start with writing the four vectors for incident photon and target nucleus in the lab frame as

$$\begin{aligned} k_\gamma^\mu &= (\,k_\gamma \quad 0 \quad 0 \quad k_\gamma\,) \\ k_T^\mu &= (\,M_T \quad 0 \quad 0 \quad 0\,), \end{aligned} \tag{4.40}$$

where M_T is mass of the target nucleus is related to the mass of the recoil nucleus M_r as

$$M_r = M_T - M + E_B, \tag{4.41}$$

and M and E_B are the mass and binding energy of the initial bound nucleon. Conservation of the four vector of the initial and final momenta is written as

$$k_T^\mu + k_\gamma^\mu = k_\eta^\mu + k_p^\mu + k_r^\mu. \tag{4.42}$$

This equation can be rewritten as two scalar and vector equation as follows

$$\begin{aligned} M_T + E_\gamma &= E_\eta + E_p + E_r \\ \mathbf{k}_\gamma &= \mathbf{k}_\eta + \mathbf{k}_p + \mathbf{k}_r. \end{aligned} \tag{4.43}$$

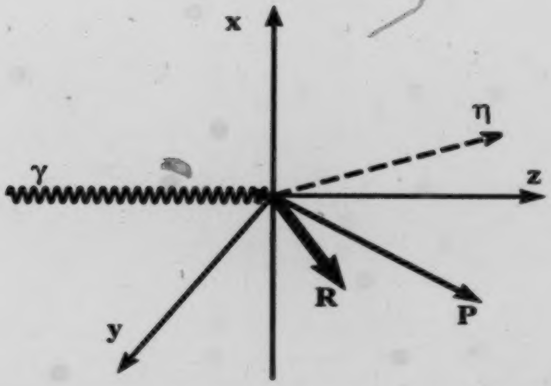

Figure 4.15: The kinematics for the η photo production from nuclei. The xz plane is the reaction plane and momentum of the incoming photon defines the z axis. Direction of η meson and outgoing proton and recoil nucleus are shown by η, P and R, respectively.

Solving these equations for the energy of the outgoing proton results in

$$E_p = \frac{\alpha\epsilon \pm \delta\sqrt{\alpha^2 - 4M(\epsilon^2 - \delta^2)}}{2(\epsilon^2 - \delta^2)}, \tag{4.44}$$

where variables α, δ and ϵ are defined as follows

$$\begin{aligned} \alpha &= \epsilon^2 - M_r^2 + M^2 - k_\gamma^2 - k_\eta^2 + 2k_\eta k_\gamma \cos(\theta_{\eta,\gamma}) \\ \delta &= k_\eta \cos(\theta_{\eta,p}) - k_\gamma \cos(\theta_{\gamma,p}) \\ \epsilon &= M_T + E_\gamma - E\eta. \end{aligned} \tag{4.45}$$

Having obtained the proton energy, we can find all the other kinematic quantities required in the calculation of the reaction amplitude and observables.

Appendix 4.B The $\gamma + p \rightarrow \eta + p$ Reaction

In this appendix we discuss an effective Lagrangian approach proposed by Benmouroushe *et al.* [6] These authors used this Lagrangian to investigate the η meson production on the nucleon. Recently Arenhövel *et al.* applied this Lagrangian to calculate the η photo production from deuteron. The Lagrangian of reference [6] was also used by the authors of reference [9] to calculate the Born and vector meson exchange diagrams of their η photo production model.

Starting from effective Lagrangian proposed in reference [6]

$$\begin{aligned}
\mathcal{L}_{\eta NN} &= - \quad i g_\eta \bar{\psi} \gamma_5 \psi \eta \\
\mathcal{L}_{\gamma NN} &= - \quad e \bar{\psi} \gamma_\mu A^\mu \psi - \frac{e\kappa_p}{4M} \bar{\psi} \sigma^{\mu\nu} \psi F_{\mu\nu}, \\
\mathcal{L}_{VNN} &= - \quad g_v \bar{\psi} \gamma_\mu \psi V^\mu - \frac{g_t}{4M} \bar{\psi} \sigma_{\mu\nu} \psi V^{\mu\nu}, \\
\mathcal{L}_{V\eta\gamma} &= \quad \frac{e\lambda_V}{4m_\eta} \epsilon_{\mu\nu\lambda\sigma} F^{\mu\nu} V^{\lambda\sigma} \eta, \\
\mathcal{L}_{\eta NR} &= - \quad i g_{\eta NR} \bar{\psi} \Gamma R \eta + h.c. \\
\mathcal{L}_{\gamma NR} &= - \quad \frac{e\kappa_p^R}{2(M_R + M)} \bar{R} \Gamma^{\mu\nu} F_{\mu\nu} + h.c.,
\end{aligned}$$

where

$$\begin{aligned}
&\text{for } S_{11} \text{ resonances} \qquad \Gamma = 1 \;\text{ and }\; \Gamma^{\mu\nu} = \gamma_5 \sigma^{\mu\nu} \\
&\text{for } P_{11} \text{ resonances} \qquad \Gamma = \gamma_5 \;\text{ and }\; \Gamma^{\mu\nu} = \sigma^{\mu\nu} \qquad (4.46)
\end{aligned}$$

Where fields and coupling constants are the same as those introduced in the chapter.

The interaction of photons and η mesons with the $N^*(1520)$ resonance are introduced through the following Lagrangians,

$$
\begin{aligned}
\mathcal{L}_{\eta NR} = & \quad \frac{f_{\eta NR}}{m_\eta}\overline{R}^{\mu}\theta_{\mu\nu}(Z)\gamma_5\psi\partial^{\nu}\eta + h.c., \\
\mathcal{L}^1_{\gamma NR} = & \quad -\frac{ie\kappa^1_R}{2M}\overline{R}^{\mu}\theta_{\mu\nu}(Y)\gamma_\lambda\psi F^{\nu\lambda} + h.c., \\
\mathcal{L}^2_{\gamma NR} = & \quad \frac{e\kappa^2_R}{4M^2}\overline{R}^{\mu}\theta_{\mu\nu}(X)\partial_\lambda N F^{\nu\lambda} + h.c.,
\end{aligned}
\tag{4.47}
$$

where

$$
\begin{aligned}
\theta_{\mu\nu}(V) &= g_{\mu\nu} + \left[-\frac{1}{2}(1+4V) + V\right]\gamma_\mu\gamma_\nu, \\
V &= X, Y, Z
\end{aligned}
\tag{4.48}
$$

and off-shell parameters X, Y and Z are expressed in terms of α, β and δ in equation (4.10). Using standard procedure [26], the S-matrix for the photoproduction of η mesons on the proton is derived. Diagrams included in this calculation are depicted in figure (4.16). The Born diagrams are figures 4.16a) and 4.16b): the t-channel vector meson diagram is shown in figure 4.16c), figures 4.16d) and 4.16e) are the resonance poles. In addition to the $S_{11}(1535)$ resonance this calculation includes the other four resonances whose characteristics are given in table (1). Coupling constants of above Lagrangian are calculated using the parameters listed in the table 2.

We illustrate the main steps of the derivation for the free reaction S-matrix for contribution due to S_{11} resonance (diagrams 4.16d) and 4.16e)). The second order amplitude is expressed in terms of the effective Lagrangian as

$$
S_{fi} = -\frac{1}{2}\int < f|T\left[\mathcal{L}_{int}(x)\,\mathcal{L}_{int}(y)\right]|i> d^4x d^4y \tag{4.49}
$$

where $|i>$ and $|f>$ are the initial and final states of the system respectively. After introducing $\mathcal{L}_{\gamma NR}$ and $\mathcal{L}_{\eta NR}$ from equation (4.48) into the above expression for the

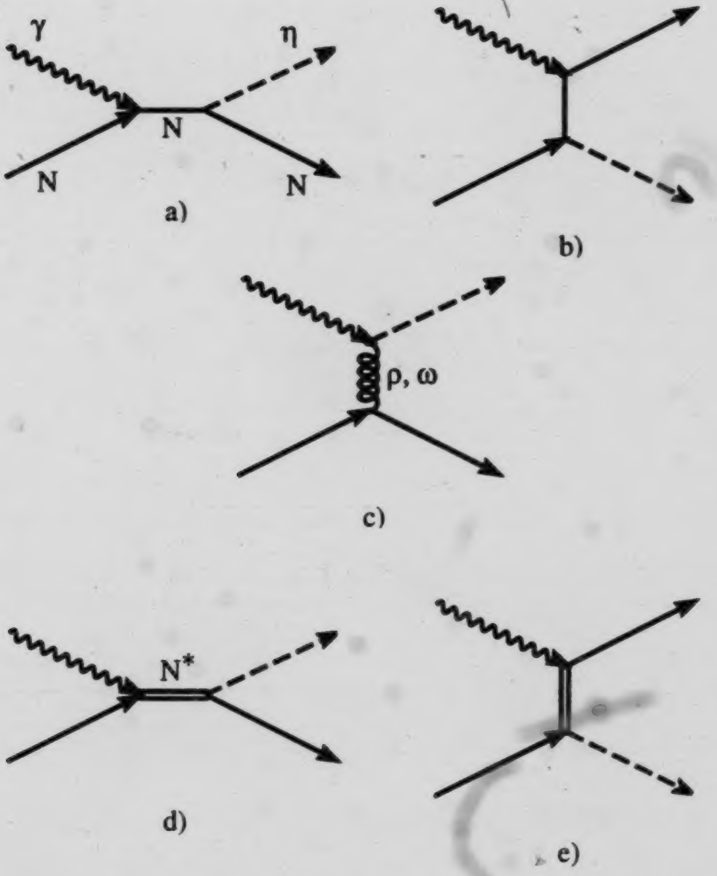

Figure 4.16: The Feynman diagrams for an $p(\gamma,\eta)p$ reaction, the incident photon with momentum **k** is absorbed by proton and then as a result an η meson produced.

S-matrix, we get

$$\begin{aligned} S^R_{fi} = & - \frac{ie\kappa^R_p g_{\eta NR}}{2(M+M_R)} \int < f|T \Big[\Big(\bar{R}(x)\,\gamma_5\sigma_{\mu\nu}F^{\mu\nu}(x)\,\psi(x) \\ & \qquad - \bar{\psi}(x)\,\gamma_5\sigma_{\mu\nu}F^{\mu\nu}(x)\,R(x) \Big) \\ \times & \Big(\bar{\psi}(y)\,R(y)\,\eta(y) - \bar{R}(y)\,\psi(y)\,\eta(y) \Big) \Big] |i > dxdy. \end{aligned} \tag{4.50}$$

Using the Wick theorem, the contributing terms for the reaction on a nucleon are

$$\begin{aligned} S^R_{fi} = -\frac{ie\kappa^R_p g_{\eta NR}}{2(M+M_R)} \int < f|N \Big[& \bar{\psi}(y)\,\eta(y)\,\underline{R(y)\,\bar{R}(x)}\gamma_5\sigma_{\mu\nu}F^{\mu\nu}(x)\,\psi(x) \\ & + \bar{\psi}(x)\,\gamma_5\sigma_{\mu\nu}F^{\mu\nu}(x)\,\underline{R(x)\,\bar{R}(y)}\psi(y)\,\eta(y) \Big] |i > dxdy. \end{aligned} \tag{4.51}$$

The initial state contains a photon and a proton

$$|i >= \quad b^\dagger_{s_\gamma}(\mathbf{k}_\gamma)\, b^\dagger_{\mu_i}(\mathbf{k}_p)|0 >, \tag{4.52}$$

where $b^\dagger_{s_\gamma}(\mathbf{k}_\gamma)$ is the creation operator for a photon with momentum $\mathbf{k}_\gamma$ and polarization s_γ, and $b^\dagger_{\mu_i}(\mathbf{k}_p)$ creates a nucleon with momentum $\mathbf{k}_p$ and spin component μ_i.

The final state $|f>$ contains an η meson and a nucleon and is written as

$$|f >= a^\dagger_\eta(\mathbf{k}_\eta)\, b^\dagger_{\mu_f}(\mathbf{k}_p)\,|0 >, \tag{4.53}$$

where $a^\dagger(\mathbf{k})$ creates an η meson with momentum $\mathbf{k}$ and $b^\dagger_{\mu_f}(\mathbf{k})$ is the creation operator for a nucleon with spin μ_f and momentum $\mathbf{k}$. The pseudo scalar field (η meson) is written in second quantized form as

$$\eta(x) = \frac{1}{(2\pi)^{3/2}} \int \frac{d^3k}{\sqrt{2E_{\mathbf{k}}}} \left[a^\dagger(\mathbf{k})e^{ik\cdot x} + a(\mathbf{k})e^{-ik\cdot x} \right]. \tag{4.54}$$

The electromagnetic field is written in second quantized form as

$$A^\mu(x) \; = \; \frac{1}{(2\pi)^{3/2}} \sum_r \epsilon^\mu_r \int \frac{d^3k}{(2E_{\mathbf{k}})^{1/2}} \times \left[a_r(\mathbf{k})e^{-ik\cdot x} + a^\dagger_r(\mathbf{k})e^{ik\cdot x} \right], \tag{4.55}$$

where $a_r^\dagger(\mathbf{k}_\gamma)$ and $a_r(\mathbf{k}_\gamma)$ are the creation and annihilation operator for a photon with momentum $\mathbf{k}_\gamma$ and polarization r. The second quantized form of the nucleon field operator $\psi(x)$ is

$$\psi(x) = \quad \sum_s \int \frac{d^3k}{(2\pi)^{3/2}} \left(\frac{M}{E_k}\right)^{1/2} \left[b_s(\mathbf{k})u_s(k,x) + d_s^\dagger(\mathbf{k})v_s(k,x)\right] \qquad (4.56)$$

where $b_s(\mathbf{k})$ is the destruction operator for a nucleon with spin s and momentum $\mathbf{k}$, and $u_s(k,x)$ is the corresponding space-time continuum wave function. The creation operator $d_s^\dagger(\mathbf{k})$ creates an anti nucleon with spin s and momentum $\mathbf{k}$, $v_s(k,x)$ is the corresponding space-time continuum wave function. The Fock space calculations for the fields involved in the interaction result in following

$$< 0|a_\eta(\mathbf{k}_\eta)\eta(x)|0 >= \frac{1}{(2\pi)^{2/3}}\frac{1}{(2E_\eta)^{1/2}}e^{ik_\eta\cdot x},$$

$$< 0|F^{\mu\nu}(x)a_r^\dagger(\mathbf{k}_\gamma)|0 >= \frac{2}{(2\pi)^{2/3}}\frac{1}{(2E_\gamma)^{1/2}}\epsilon_r^{\mu}k_\gamma^{\nu}e^{-ik_\gamma\cdot x}, \qquad (4.57)$$

where E_γ and E_η are energy of the photon and η meson respectively. Notice that the latter result is obtained in the radiation gauge. The result of the Fock space calculation for the nucleon fields is

$$< 0|b_{\mu_f}(\boldsymbol{k}_{p_f})N[\bar{\psi}_p(y)\psi_p(x)]|b_{\mu_i}^\dagger(\boldsymbol{k}_{p_i})|0 >= \frac{1}{(2\pi)^3}$$
$$\times\frac{M}{\sqrt{E_iE_f}}\bar{u}_{\mu_f}(k_{p_f},y)u_{\mu_i}(k_{p_i},x), \qquad (4.58)$$

and

$$u_{\mu_i}(k_{p_i},x) = \sqrt{\frac{E_i+M}{2M}}\begin{pmatrix} 1 \\ \frac{\sigma\cdot k_{p_i}}{E_i+M}\end{pmatrix} e^{ik_{p_i}\cdot x} \mid \frac{1}{2},\mu_i > . \qquad (4.59)$$

M, E_i and E_f are mass and energy of the initial and final nucleon respectively. Putting the results of the Fock space calculations into the S-matrix of equation (4.51) , the S-matrix for the S_{11} resonance diagram can be cast in the following form

$$S_{fi}^R \quad = \frac{1}{(2\pi)^2}\sqrt{\frac{M^2}{4E_fE_iE_\eta E_\gamma}}i\mathcal{M}_{fi}^R, \qquad (4.60)$$

where we have defined the amplitude $i\mathcal{M}^{R}_{fi}$ as follow

$$i\mathcal{M}^{R}_{fi} = \frac{e g_{\eta N R}\kappa^{R}_{p}}{M+M_R}\bar{u}_f\left(\frac{\not{k}_s + M_R}{k_s^2 - M_R^2}\gamma_5\not{k}_\gamma\not{\epsilon}_r + \gamma_5\not{k}_\gamma\not{\epsilon}_r\frac{\not{k}_u + M_R}{k_u^2 - M_R^2}\right)u_i, \tag{4.61}$$

The following expression is used for the propagator of the spin $\frac{1}{2}$ resonance.

$$\underline{R(x)\bar{R}(y)} = iS^{F}_{R}(x-y) = \frac{i}{(2\pi)^4}\int d^4p\frac{\not{p}+M}{p^2-M^2+i\epsilon}e^{-ip\cdot(x-y)}. \tag{4.62}$$

where M and p are the mass and four momentum of the propagating resonance respectively. The same steps can be applied in the calculation of other diagrams which result in S-matrices with the structure of (4.60) and different $i\mathcal{M}_{fi}$'s as listed below.

$$i\,{}^{e}\mathcal{M}^{p}_{fi} = e g_{\eta NN}\bar{u}_f\left(\gamma_5\frac{\not{k}_s + M}{k_s^2 - M^2}\not{\epsilon}_p + \not{\epsilon}_p\frac{\not{k}_u + M}{k_u^2 - M^2}\gamma_5\right)u_i,$$

$$i\,{}^{\mu}\mathcal{M}^{p}_{fi} = \frac{e g_{\eta NN}\kappa_p}{2M}\bar{u}_f\left(\gamma_5\frac{\not{k}_s + M}{k_s^2 - M^2}\not{k}_\gamma\not{\epsilon}_r + \not{k}_\gamma\not{\epsilon}_r\frac{\not{k}_u + M}{k_u^2 - M^2}\gamma_5\right)u_i,$$

$$i\mathcal{M}^{S_{11}}_{fi} = \frac{e g_{\eta N R}\kappa^{R}_{p}}{M+M_R}\bar{u}_f\left(\frac{\not{k}_s + M_R}{k_s^2 - M_R^2}\gamma_5\not{k}_\gamma\not{\epsilon}_r + \gamma_5\not{k}_\gamma\not{\epsilon}_r\frac{\not{k}_u + M_R}{k_u^2 - M_R^2}\right)u_i,$$

$$i\mathcal{M}^{P_{11}}_{fi} = \frac{e g_{\eta N R}\kappa^{R}_{p}}{M+M_R}\bar{u}_f\left(\gamma_5\frac{\not{k}_s + M_R}{k_s^2 - M_R^2}\not{k}_\gamma\not{\epsilon}_r + \not{k}_\gamma\not{\epsilon}_r\frac{\not{k}_u + M_R}{k_u^2 - M_R^2}\gamma_5\right)u_i,$$

$$i\mathcal{M}^{V_v}_{fi} = -i\frac{e\lambda_v g_v}{m_\eta}\epsilon_{\mu\nu\lambda\sigma}\bar{u}_f\frac{\epsilon^{\mu}k^{\nu}_{\gamma}k^{\lambda}_{\eta}\gamma^{\sigma}}{k_t^2 - m_V^2 + i\epsilon}u_i,$$

$$i\mathcal{M}^{V_t}_{\text{[illegible]}} = -\frac{e\lambda_t g_t}{2Mm_\eta}\epsilon_{\mu\nu\lambda\sigma}\bar{u}_f\frac{\epsilon^{\mu}k^{\nu}_{\gamma}\sigma^{\sigma\alpha}k_{t\alpha}k^{\lambda}_{\eta}}{k_t^2 - m_V^2 + i\epsilon}u_i,$$

$$i\,{}^{1}\mathcal{M}^{D_{13}}_{fi} = \frac{\text{[illegible]}^{(1)}_{R}}{2M\text{[illegible]}_{\eta}}\bar{u}_f$$

$$\times\left(\gamma_5 k^{\nu}_{\eta}\theta_{\nu\mu}(Z)\frac{\not{k}_s + M_R}{k_s^2 - M_R^2}P^{\mu\alpha}\theta_{\alpha\beta}(Y)\gamma_\lambda(k^{\beta}_{\gamma}\epsilon^{\lambda}_{r} - \epsilon^{\beta}_{r}k^{\lambda}_{\gamma})\right.$$

$$\left.+\gamma_\lambda\theta_{\beta\alpha}(Y)(k^{\beta}_{\gamma}\epsilon^{\lambda}_{r} - \epsilon^{\beta}_{r}k^{\lambda}_{\gamma})\frac{\not{k}_u + M_R}{k_u^2 - M_R^2}P^{\alpha\mu}\theta_{\mu\nu}(Z)k^{\nu}_{\eta}\gamma_5\right)u_i,$$

$$
\begin{aligned}
i\,{}^{2}\mathcal{M}_{fi}^{D_{13}} = {} & \frac{e f_{\eta N R} \kappa_R^{(2)}}{4 m_\eta M^2} \bar{u}_f \\
& \times \left(\gamma_5 k_\eta^\nu \theta_{\nu\mu}(Z) \frac{\not{k}_s + M_R}{k_s^2 - M_R^2} P^{\mu\alpha} \theta_{\alpha\beta}(X) (k_\gamma^\beta \epsilon_r^\lambda - \epsilon_r^\beta k_\gamma^\lambda) \left\{ k_{p_i} \right\}_\lambda \right. \\
& \left. + \left\{ k_{p_f} \right\}_\lambda \theta_{\beta\alpha}(X) (k_\gamma^\beta \epsilon_r^\lambda - \epsilon_r^\beta k_\gamma^\lambda) \frac{\not{k}_u + M_R}{k_u^2 - M_R^2} P^{\alpha\mu} \theta_{\mu\nu}(Z) k_\eta^\nu \gamma_5 \right) u_i ,
\end{aligned}
$$

$$
P^{\mu\nu} = \left(g^{\mu\nu} - \frac{1}{3} \gamma^\mu \gamma^\nu - \frac{1}{2M_R} \left[\gamma^\mu k^\nu - \gamma^\nu k^\mu \right] - \frac{2}{3M_R^2} k^\mu k^\nu \right), \tag{4.63}
$$

where

$$
k_s = k_\eta + k_{p_f}, \quad k_t = k_\gamma - k_\eta \quad \text{and} \quad k_u = k_{p_f} - k_\gamma . \tag{4.64}
$$

We have used the S-matrix, including contributions of all diagrams, and standard procedure, for example from reference [32], and calculated the cross section for the η photoproduction off nucleon. We obtained the following expression for the cross section.

$$
\frac{d\sigma}{d\Omega} = \frac{(\hbar c)^2}{64\,(2\pi)^2} \frac{k_\eta \,(E_i + M)(E_f + M)}{E_\gamma E_i E_f \left(1 + \frac{k_{p_i}}{E_i}\right) \left(1 + \frac{E_\eta}{E_f}\right)} \sum_{\mu_i, \mu_f, \xi} |\, \mathcal{M}_{fi} \,|^2 \tag{4.65}
$$

Figure (4.17) shows the observables for the photoproduction of η meson from proton. Curves in figure (4.17-a) represent the differential cross sections for two energies 729 MeV (solid curve) and 753 MeV (dashed curve). These results are almost uniform in all the angles because of dominance of the S_{11} resonance in this energy region. Calculations for the total cross section are shown in figure (4.17-b). This curve shows that the total cross section peaks at photon energy of 800 MeV and decreases as photon energy approaches higher values.

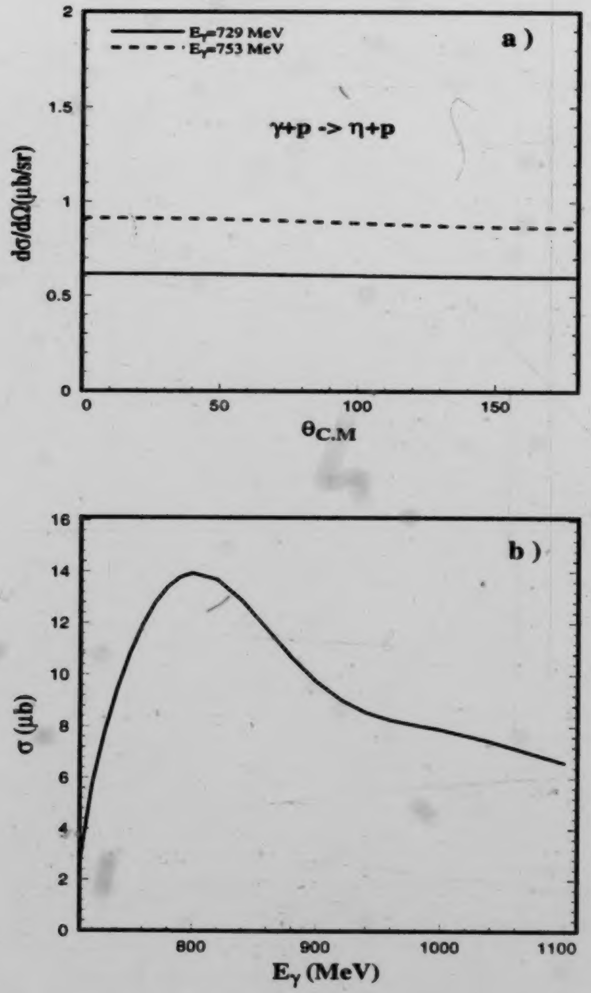

Figure 4.17: a) Differential cross section, b) total cross section for the η photoproduction on the proton. Coupling constants are those of table 2 of this chapter and table V of reference [6].

Appendix 4.C Observables

In this appendix we will relate the eta photoproduction amplitude (4.37) to the observables discussed in the chapter, namely cross section and photon asymmetry. Let us rewrite the amplitude of (4.37) as

$$\begin{aligned} S_{fi} &= \frac{e}{\pi}\left(\frac{E_p+M}{E_pE_\eta E_\gamma}\right)^{1/2}\delta(E_p+E_\gamma-E_B-E_\eta) \\ &\quad\times\sum_{J_BM_B}(J_f,J_B;M_f,M_B|J_i,M_i) \\ &\quad\times\left[S_{J_iJ_f}(J_B)\right]^{1/2}Z^{s_f}_{\xi M_B} \end{aligned} \tag{4.66}$$

The first step to calculate these observables is squaring the above amplitude to find the transition probability.

$$\begin{aligned} |S_{fi}|^2 &= \frac{\text{[illegible]}^2}{\pi^2}\left(\frac{E_p+M}{E_pE_\eta E_\gamma}\right)[\delta(E_p+E_\gamma-E_B-E_\eta)]^2 \\ &\quad\times\left\{\sum_{J_BM_B}(J_f,J_B;M_f,M_B|J_i,M_i)\left[S_{J_iJ_f}(J_B)\right]^{1/2}\right\}^2 \\ &\quad\times\ |Z^{s_f}_{\xi M_B}|^2 \end{aligned} \tag{4.67}$$

The differential cross section is related to the transition probability above as

$$d\sigma=\sum_{\substack{final\\initial}}\frac{|S_{fi}|^2}{TJ_{inc}}d^3p_\eta d^3p_p \tag{4.68}$$

Using the following relation between the delta function and its square from [32]

$$[\delta(E_p+E_\gamma-E_B-E_\eta)]^2=\frac{T}{2\pi}\delta(E_p+E_\gamma-E_B-E_\eta), \tag{4.69}$$

and the following identity for the Clebsch-Gordan coefficients

$$\sum_{M_iM_f}(J_f,J_B;M_f,M_B|J_i,M_i)(J_f,J'_B;M_f,M'_B|J_i,M_i)=\frac{2J_i+1}{2J_B+1}\delta_{J_BJ'_B}\delta_{M_BM'_B} \tag{4.70}$$

The triple differential cross section can be cast in the following form

$$\frac{d^3\sigma}{d\Omega_\eta d\Omega_p dE_\eta} = \frac{8\alpha\pi}{\hbar c}\left[\frac{E_p+Mc^2}{E_\gamma}\right]k_pc\,k_\eta c$$

$$\times \frac{1}{R} \sum_{J_B M_B s_f \xi} \frac{S_{J_i J_f}(J_B)}{2J_B + 1} |Z^{s_f}_{\xi M_B}|^2 \tag{4.71}$$

where we have used $J_{inc} = \frac{1}{(2\pi)^3}$ for the incident photon current and the recoil factor R is given by

$$R = 1 + \frac{E_\eta}{E_r}\left(1 - \frac{k_\gamma}{k_\eta}\cos(\theta_\eta) - \frac{k_p}{k_\eta}\cos(\theta_{\eta p})\right), \tag{4.72}$$

and E_r is the energy of the recoil nucleus. The photon asymmetry for linearly polarized incident photons is defined as

$$A = \frac{d\sigma_\parallel - d\sigma_\perp}{d\sigma_\parallel + d\sigma_\perp} \tag{4.73}$$

where $d\sigma_\parallel$($d\sigma_\perp$) is the cross section with the incident photon polarization parallel (perpendicular) to the scattering plane.

Appendix 4.D Wavefunction of The η Meson

The η nucleus interaction is dominated by formation of $S_{11}(1535)$ nucleon resonance. We include the final state interactions of the η meson and residual nucleus through an optical potential which is based on the contribution of the above channel [30]. We have also used the two optical potentials introduced in reference [10]. These last two potentials include contributions from two other resonances ($D_{13}(1520)$ and $P_{11}(1410)$).

The η meson is described by solutions of the Klein-Gordon equation

$$\left[\nabla^2 + \mathbf{k}_\eta^2 + V(r)\right]\phi(\mathbf{r}) = 0 \tag{4.74}$$

where

$$V(r) = -2\omega V_{opt}(r), \tag{4.75}$$

ω is the η meson energy. We expand the η wavefunction in terms of the partial waves as

$$\phi(\mathbf{r}) = 4\pi \sum_{L,M} i^L v_L(r) Y_L^M(\Omega) Y_L^{-M}\left(\hat{\mathbf{k}}_\eta\right) \tag{4.76}$$

Putting the above expansion into equation (4.74) and using the following relation

$$\nabla^2 = \frac{1}{r}\frac{\partial^2}{\partial r^2}r - \frac{L^2}{r^2}, \tag{4.77}$$

the Klein-Gordon equation reduces to the following radial equation

$$\frac{1}{r}\frac{\partial^2}{\partial r^2}(r v_L) - \frac{L(L+1)}{r^2}v_L + \left(\mathbf{k}^2 + V(r)\right)v_L = 0. \tag{4.78}$$

Using the transformation $v_L(r) = \frac{y_L(r)}{r}$, the radial equation (4.78) can be cast in a form of the Schrödinger equation for which we have a solving technique.

$$\frac{\partial^2 y_L}{\partial r^2} - \left[\frac{L(L+1)}{r^2} + f(r)\right]y_L = 0, \tag{4.79}$$

where

$$f(r) = -[\mathbf{k}_\eta^2 + V(r)] \tag{4.80}$$

Equation (4.79) is solved numerically for each partial wave of the distorted wavefunction.

Appendix 4.E Approximation of The Propagators

The DWA S-matrix for the eta photoproduction on nuclei involves eight fold integrals over the vertices involving the propagating particles as well as the partial wave expansions for the outgoing particles. Therefore we are confronting a complicated numerical calculation. We try to overcome this problem by using an approximation for the propagators which is exact in the the plane wave limit. Our aim is to illustrate this approximation in this appendix for a s-channel diagram; extensions to other channels are straightforward.

Let us consider the reaction 1 + 2 → 3 + 4 in which two particles 1 and 2 collide to form a fermion, this fermion propagates and decays to two particles 3 and 4. This process is depicted in figure (4.18).

The S-matrix for the above diagram is

$$S_{fi} = A\int d^4x d^4y \phi_4^{*}(x)\,\phi_3^{*}(x)\,\underline{\Psi(x)\,\bar{\Psi}(y)}\phi_2(y)\,\phi_1(y), \tag{4.81}$$

where A is a kinematic coefficient. The contraction of the fermion field results in the Feynman propagator

$$\underline{\Psi(x)\,\bar{\Psi}(y)} = iS_F(x-y) = \frac{i}{(2\pi)^4}\int d^4k \frac{\not{k}+M}{k^2-M^2+i\epsilon} e^{-ik\cdot(x-y)}. \tag{4.82}$$

If we assume that particles 3 and 4 are described by plane waves (in the present case these particles are the outgoing proton and eta meson), we are able to do the integration over variable x as

$$\int d^4x e^{-ix\cdot(k-k_3-k_4)} = (2\pi)^4\,\delta(k-k_3-k_4). \tag{4.83}$$

This relation restricts the 4-momentum of the propagating particle to the sum of the outgoing momenta. Using the δ function we can do the integration over momentum to find

$$S_{fi} = iA\frac{\not{k}_3+\not{k}_4+M}{(k_3+k_4)^2-M^2}\int d^4y \phi_2(y)\,\phi_1(y)\,e^{iy\cdot(k_3+k_4)}, \tag{4.84}$$

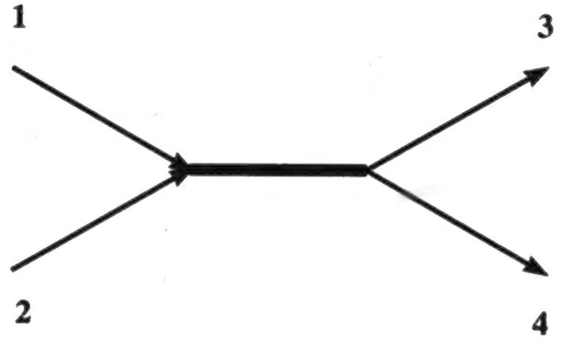

Figure 4.18: The S-channel diagram for a half integer spin particle propagator.

We obtain the same results for the S-matrix if we take the propagator to be

$$S_F(x-y) = \frac{\not{k}_3 + \not{k}_4 + M}{(k_3+k_4)^2 - M^2}\delta^4(x-y) \tag{4.85}$$

In our DWA calculations we use the expression given in (4.85) for the propagators of fermions in the s-channel. Following similar arguments one finds the corresponding simplified forms for other channels.

Chapter 5

Photoproduction of η Mesons from Complex Nuclei

II) Inclusive Reactions

Introduction

One of the current issues in intermediate energy physics is the modification of baryon properties in the nuclear medium. The nucleon resonances mainly decay to nucleons and mesons. Therefore reactions involving the production of mesons from nuclei are suitable tools for studying these modifications. Among these the photoproduction reactions are preferable. The relative weakness of the electromagnetic interaction allows photons to interact with nucleons uniformly through the entire volume of the nucleus. The amplitudes obtained on the basis of first order perturbation theory should be able to describe the reactions well.

η mesons display certain selectivity in their interactions with nucleons. Because the η meson is a spin and isospin zero particle, its coupling to nucleons can lead to the formation of only isospin $\frac{1}{2}$ baryon resonances. In addition to the study of nucleon resonances, photoproduction of η meson can be used to investigate the final state interactions of this meson with nuclei which is also of theoretical interest. The large attractive ($\sim$ 0.6 fm) scattering length of η-N system, lead to speculations about the existence of η-nucleus bound states (η-mesic nuclei) [1]. Photonuclear reactions also can be used to investigate this new type of nuclear matter. Lebedev *et* *al.* [2] used this reaction to study the formation of ${}^{12}_{\eta}$C and ${}^{16}_{\eta}$O η-mesic nuclei.

Exclusive η photoproduction reactions off nuclei are capable of providing detailed information on the propagation of nucleon resonances inside nuclei, as well as on the final state interactions of the η mesons. They suffer, however, from the disadvantage of their cross section being low. The experimental investigations of such reactions are difficult at this time. For inclusive reactions, on the other hand, the contributions of each nucleon add incoherently, so the cross sections are large compared to the exclusive ones. One can use these reactions to study the nuclear medium modifications of the nucleon resonances as well as the interaction of the η meson with nuclei.

As noted in the preceeding chapter, Lee *et al.* [3] have studied exclusive as well as inclusive photoproduction of η mesons form complex nuclei such as ^{12}C and ^{40}Ca. The initial bound nucleons are described by harmonic oscillator wavefunctions and final state interactions of the detected particles with the recoil nucleus are introduced through optical potentials. Two different optical potentials are used for the η meson. Comparison of the results with the experimental data of the inclusive reaction shows that one of the potentials produces results that are closer to the data [3]. A calculation for the inclusive photoproduction of the η meson from nuclei, based on an effective Lagrangian approach has been developed by Carrasco [4]. In this model the reaction takes place only through the formation of the $S_{11}(1535)$ resonance. In addition to a local density approximation, Pauli blocking and Fermi motion are taken into account. The final state interactions of the η meson with the residual nucleus are calculated using a Monte Carlo program. This author shows that the total cross section experiences large suppression due to medium effects (Fermi sea effects and the modifications of the $S_{11}(1535)$ resonance parameters) and the final state interactions of the η meson. These effects are less for the differential cross section than the total cross section. Another finding of this work is that the total cross section grows as $A^{0.6}$ (A is the atomic number of the target nucleus).

Chen *et al.* [5] calculated the double differential cross section for the inclusive photoproduction of η mesons from ^{12}C target. They include only the quasifree process and assume that the η is produced through the formation of the $S_{11}(1535)$ resonance. Starting with the elementary interaction on the proton these authors obtained a value for the helicity amplitude $A^{\frac{1}{2}}$ for the S_{11} resonance which is in close agreement with quark model calculations. Their calculations for the double differential inclusive cross sections on ^{12}C target predict a maximum (0.15 μb/MeV Sr) at η kinetic energy of $\sim$100 MeV. Recently a model for η photoproduction introduced by Hombach *et al.* [6], the final states interactions of η meson are obtained using the coupled channel Boltzmann-Uehling-Ulenbeck formalism. The total cross sections calculated in this model also show a mass dependence of the form $A^{\frac{2}{3}}$.

Recently the photoproduction of η mesons from complex nuclei, such as ^{12}C, ^{40}Ca, ^{93}Nb and ^{208}Pb, has been measured at MAMI. The data for the inclusive reaction are reported in [7]. This experiment confirmed the predictions of the theoretical models for the relation between the total cross sections and target mass ($A^{\frac{2}{3}}$).

In this chapter we develop an inclusive model for the photoproduction of η mesons from complex nuclei along the lines developed in the preceeding chapter. In the inclusive reaction, a photon interacts with a nucleous leading to the production of an η meson. This meson is the only detected particle and there is no restriction or information about the final nucleus. Our inclusive model includes only contributions form the quasifree channel and is thus restricted to the one hole excitations of the recoil nucleus.

In section 5.1 we describe the model calculation for the inclusive reactions: the results of our calculations for two target nuclei are given in section 5.2. Section 5.3 is devoted to discussions and conclusions.

5.1 Reaction Model

We start from the S-matrix, derived in the previous chapter (see equation 4.23), for exclusive η photoproduction from complex nuclei

$$\begin{aligned} S_{fi} &= \frac{e}{(2\pi)^{9/2}} \left(\frac{M}{E_p} \frac{1}{2E_\eta} \frac{1}{2E_\gamma} \right)^{1/2} \\ &\times \sum_{J_B M_B} (J_f, J_B; M_f, M_B | J_i, M_i) \left[S_{J_i J_f}(J_B) \right]^{1/2} \\ &\times \int d^4x \Psi_{s_f}^{(-)\dagger}(x) \Gamma^T \Psi_{J_B M_B}(x) \varphi_\eta^*(x) e^{-ik_\gamma \cdot x}, \end{aligned} \tag{5.1}$$

where all the ingredients and definitions in this equation have been given in the previous chapter. As mentioned above, the η meson is the only detected particle in the inclusive reaction; this necessitates that the above exclusive S-matrix must undergo some modifications. In plane wave calculations of the reaction we use the plane wave amplitude of the exclusive reaction and then, as it is explained below, integrate the cross section over the variables of the undetected particles.

We also carry out distorted wave calculations for the reaction. In these only the η wavefunction is distorted; the proton continues to be described by plane waves. The justification for this is as follows: an inclusive reaction implies inclusion of all possible states of the nuclear system that are not observed. That inclusion negates the necessity for using imaginary potentials. The real part of the proton optical potentials causes a change in the momentum of the outgoing protons. The effect of these changes on the production of η mesons will be minimized as we integrate over all proton directions. The reader should be reminded however, that in the present model only the quasifree production of η mesons is taken into account.

With the use of plane waves for the continuum proton and a partial wave expansion for the outgoing meson, the S-matrix of equation (5.1) can be cast in the following form

$$
\begin{aligned}
S_{fi} &= \frac{e}{\pi}\left(\frac{E_p+M}{E_pE_\eta E_\gamma}\right)^{1/2}\delta(E_p+E_\gamma-E_B-E_\eta)\\
&\times\sum_{J_BM_B}(J_f,J_B;M_f,M_B|J_i,M_i)\\
&\times\left[S_{J_iJ_f}(J_B)\right]^{1/2}Z^{s_f}_{\xi M_B}
\end{aligned}
\tag{5.2}
$$

where

$$
\begin{aligned}
Z^{s_f}_{\xi M_B} &= \sum_{L_\eta M_\eta L_q M_q} i^{L_q-l_\eta}Y^{*M_q}_{L_q}(\hat{q})\,Y^{*M_\eta}_{L_\eta}\left(\hat{k_\eta}\right)\\
&\times\left\{<\mathcal{Y}^{s_f}_{0\frac{1}{2}\frac{1}{2}}\mid\left(\Gamma^T_{11}+\frac{\sigma\cdot\mathbf{k}_{p_f}}{E_p+M}\Gamma^T_{21}\right)Y^{M_q}_{L_q}(\Omega)\,Y^{M_\eta}_{L_\eta}(\Omega)\mid\mathcal{Y}^{M_B}_{L_B\frac{1}{2}J_B}>\right.\\
&\times\int r^2dr\,j_{L_q'}(qr)\,v_{L_\eta}(r)\,f_B(r)\\
&+i<\mathcal{Y}^{s_f}_{0\frac{1}{2}\frac{1}{2}}\mid\left(\Gamma^T_{12}+\frac{\sigma\cdot\mathbf{k}_{p_f}}{E_p+M}\Gamma^T_{22}\right)Y^{M_q}_{L_q}(\Omega)\,Y^{M_\eta}_{L_\eta}(\Omega)\mid\mathcal{Y}^{M_B}_{L_B'\frac{1}{2}J_B}>\\
&\left.\times\int r^2dr\,j_{L_q}(qr)\,v_{L_\eta}(r)\,g_B(r)\right\}.
\end{aligned}
\tag{5.3}
$$

The parameters in the expression above are explained in the previous chapter except for those with subindex q: these arise from the following expansion

$$
e^{i(k_\gamma-k_{p_f})\cdot x}=e^{iq\cdot x}=4\pi\sum_{L_qM_q}i^{L_q}v_{L_q}(qr)\,Y^{*M_q}_{L_q}(\hat{\mathbf{q}})Y^{M_q}_{L_q}(\Omega)
\tag{5.4}
$$

The elements of the operator Γ^T of (5.3) can be written in terms of a scalar S and a vector A as follow

$$
\Gamma^T_{ij}+\frac{\sigma\cdot\mathbf{k}_{p_f}}{E_p+M}\Gamma^T_{kj}=SI+A\cdot\sigma=SI+(-)^\mu A_\mu\sigma^{-\mu}
\tag{5.5}
$$

where I is a 2×2 unit matrix. After putting the above expressions for the matrix elements of Γ^T in the S-matrix (5.2), the angular integrals of the types given below appear in the S-matrix.

$$
\begin{gathered}
<\mathcal{Y}^{s_f}_{0\frac{1}{2}\frac{1}{2}}\mid Y^{M_q}_{L_q}(\Omega)\,Y^{M_\eta}_{L_\eta}(\Omega)\mid\mathcal{Y}^{M_B}_{L_B\frac{1}{2}J_B}>\\
<\mathcal{Y}^{s_f}_{0\frac{1}{2}\frac{1}{2}}\mid Y^{M_q}_{L_q}(\Omega)\,Y^{M_\eta}_{L_\eta}(\Omega)\,\sigma^{-\mu}\mid\mathcal{Y}^{M_B}_{L_B\frac{1}{2}J_B}>.
\end{gathered}
\tag{5.6}
$$

The results of these angular integrals are given in Appendix 5.A. The cross section for the reaction is obtained through some modifications to that of the exclusive reaction as described below. The cross section for an exclusive reaction with the above amplitude is found to be (see Appendix 4.C)

$$\begin{aligned}\frac{d^3\sigma}{d\Omega_\eta d\Omega_p dE_\eta} &= \frac{8\alpha\pi}{\hbar c}\left[\frac{E_p + Mc^2}{E_\gamma}\right] k_{p_f}c\, k_\eta c \\ &\times \frac{1}{R} \sum_{J_B M_B s_f \xi} \frac{S_{J_i J_f}(J_B)}{2J_B+1} |Z^{s_f}_{\xi M_B}|^2,\end{aligned} \tag{5.7}$$

where R is the recoil factor introduced in the previous chapter.

Recall that in the inclusive reaction the η meson is the only detected particle. Therefore to obtain an expression for the inclusive differential cross section, which is dependent only on the energy of the η meson, we have to integrate the differential cross section (5.7) over the variables of the continuum proton as well as the angles of the η meson. These integrations are performed numerically as follows. First we take advantage of the symmetry in the dependence on the azimuthal angle ϕ_η and replace the integration over this angle by a simple multiplication of the result at the end by a factor of 2π. Integration over proton azimuthal angle is performed using a simple mid point method. For the proton and η meson's polar angles the Gaussian method is applied. The number of mesh points for each integration is varied until convergence is achieved. Good convergence (less than 1% difference) is obtained for 10 and 20 mesh points for azimuthal and polar angles, respectively. The inclusivity of the reaction requires that contributions from all the nucleons inside the target nucleus be taken into account. In the calculation of the photoproduction form neutrons, the relative factor $\frac{2}{3}$, between cross sections of η production off neutron and proton, is used. This factor is obtained experimentally [8] and is confirmed theoretically as well

[9].

We also calculated the total cross section of the inclusive η photoproduction off target nuclei by numerically integrating the differential cross section, obtained using the above procedure, over the η energy.

5.2 Results

In all the results presented in this section the Hartree potentials of reference [10] are used for calculations of the bound state nucleon wave functions. The maximum values of spectroscopic factors are used for all the nucleons involved in the reaction. Data are those of the experiment performed at MAMI [7]. Figure (5.1) shows the calculated cross section of the inclusive η photoproduction on a ^{12}C target. Curves in figure (5.1-a) are the differential cross sections of the above reaction with an incident photon energy of 750 MeV and those in figure (5.1-b) are for a photon energy of 778.5 MeV. With the exception of the data point at η energy of 90 MeV in figure (5.1-b), the results of the plane wave calculations at both photon energies produce curves with the same shapes as the data (solid curve, labelled as Plane Wave). Note the data and plane wave calculations peak at the same η energy.

The final state interactions of η meson are included using the optical potentials of reference [3]. The distorted wave calculations with the use of the optical potential DW1 of the above reference result in the long dashed curves (labelled as Distorted Wave (DW1)). These curves have roughly the same shape as the data but the calculated cross sections are lower than the data by a factor of $\sim \frac{2}{3}$.

To study the sensitivity of the model calculations to the application of different potentials, we have also performed a distorted wave calculation, at a photon energy of 750 MeV, using the DW2 optical potential of reference [3]. This calculation results in the short-dashed curve (labelled as Distorted Wave (DW2)) in figure (5.1-a). In this case we find even more suppression of the cross section than the DW1 potential (i.e. long-dashed curve of this figure).

The total cross section of the inclusive η photoproduction on a nuclear target is obtained by numerical integration of the differential cross section over the η energy. For example for the reaction on ^{12}C target the total cross section for photon energies of 750 and 778.5 MeV are calculated by integrating the differential cross sections presented in figure (5.1) over the η energy.

Figure (5.2) compares the results of our calculations for the total cross section of the reaction on ^{12}C with the data of reference [7]. The results of the plane wave calculations are shown by the solid curve: these are below the experimental data at energies near threshold and lie above the data at higher photon energies. Due to the large amount of cpu time needed for the distorted wave calculations, we have produced the total cross section only at two photon energies, namely 750 and 778.5 MeV (cross point). As was the case for the differential cross section, the total cross section is also lower than the experimental data by a factor of $\sim \frac{2}{3}$.

We have also used the present model to calculate the observables for the reaction on a ^{40}Ca target. Results of the calculations for the differential cross section are illustrated in figure (5.3). Figure (5.3-a) shows the results for an incident photon energy of 750 MeV while the curves in figure (5.3-b) are for photons with a higher energy, 778.5 MeV. The bound state potential is that of Horowitz *et al.* [10]. The optical potentials for the η meson as well as the data are from the same sources as figure (5.1). Plane wave calculations (solid curves) for this target show the same features as for ^{12}C target i.e produce curves with the same shapes as the data but magnitudes are somewhat larger. The differences in the magnitudes of the distorted wave calculations and the data are smaller for this targets than those of ^{12}C. The

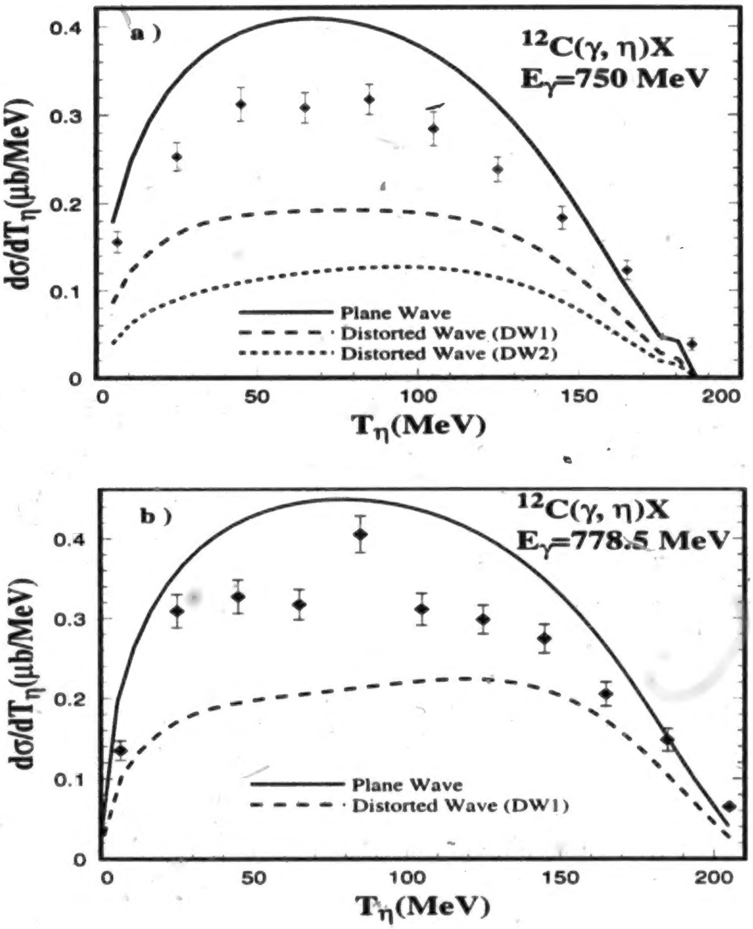

Figure 5.1: Differential cross section of the $^{12}C(\gamma,\eta)X$ reaction at photon energy of a) 750 MeV,and b) 778.5 MeV. The Hartree binding potential of reference [10] is used in the calculation of the Dirac bound state wave function. The η optical potentials DW1 and DW2 of Lee *et al.* are used [3]. Solid curve - plane wave calculations. Long dashed curve - distorted wave calculations using DW1 optical potential and short dashed curve - distorted wave calculations using DW2 optical potential. Data are those of reference [7].

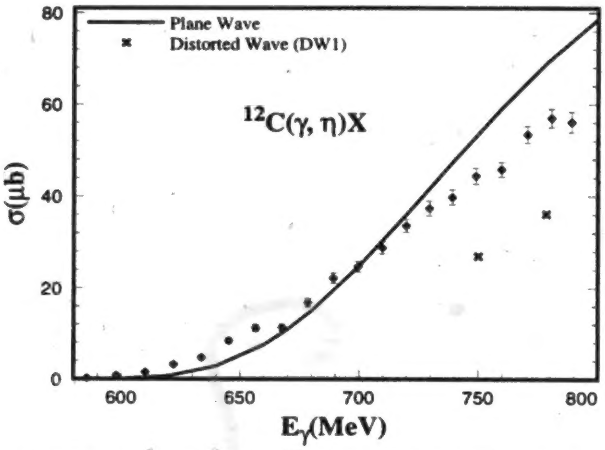

Figure 5.2: Total cross section of the $^{12}C(\gamma,\eta)X$ reaction as a function of photon energy. The binding potential for the nucleon and the η optical potentials DW1 are from the same references as figure (5.1). The solid curve is plane wave calculation and the cross points are distorted wave calculations. Data are those of reference [7].

shapes of the distorted wave calculations, however, are different from the data. The distorted wave calculations lie below the data at low η energies. At higher η energies they come close to data for one photon energy (750 MeV) and move above the data for other one (778.5 MeV).

Figure (5.4) shows the results of the calculations for the total cross section. Curves are labelled as in figure (5.2). Due to limitation of the cpu time the distorted wave calculations are performed only for two energies of the incident photon. Comparing the results presented in this figure with those for ^{12}C, the plane wave calculations for this target show larger differences with the data at higher photon energies. This can be understood in terms of the larger size of this target relative to ^{12}C. Distorted calculations for both targets are blow the data. We do not have enough distorted wave calculations results to be able to make a statement about the shape of the total cross sections. We comment here on two points regarding the discrepancy

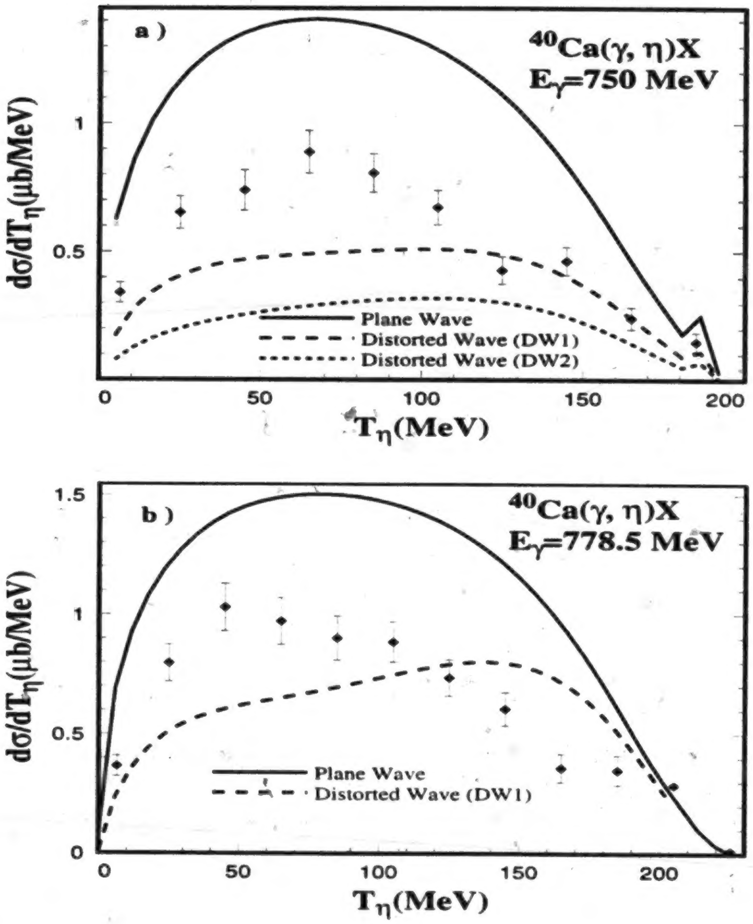

Figure 5.3: Differential cross section of the $^{40}Ca(\ \gamma, \eta)X$ reaction at photon energy of a) 750 MeV and at photon energy of b) 778.5 MeV. Potentials and the data are from same references as those of figure (5.1). Curves are labelled as in figure (5.1).

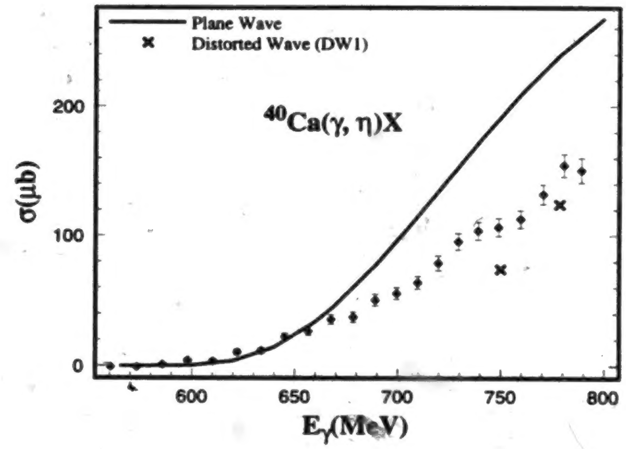

Figure 5.4: Total cross section of the $^{40}Ca(\ \gamma,\eta)X$ reaction as a function of photon energy. The nucleon binding potential as well as the η optical potential DW1 are as of figure (5.1). Curves are labelled as in figure (5.2). Data are those of reference [7].

between the data and our calculations. First, as we mentioned before, our inclusive model includes only contributions from the quasifree process. Second, we saw in the previous chapter that, using five different optical potentials for the η meson yielded five different results for the exclusive reaction. There are large uncertainties in the amount of suppression due to the final state interaction of the η meson. Therefore we believe the discrepancy between the data and our distorted calculations are mainly due to the neglect of contributions from mechanisms other than the quasifree reaction and the lack of a reliable optical potential for the η meson.

Comparison of the results of the present model with those of nonrelativistic model Lee *et al.* [3] shows that their results are larger and in better agreement with the available experimental data. Hombach *et al.*have calculated the total cross sections for inclusive reaction [6]. These authors also obtained larger results than those of our model. For example their results for the calculations including final state interactions and the medium modification of the propagating resonance is as large as the results of the plane wave calculations of this model.

5.3 Conclusions

Starting from the amplitude for an exclusive photoproduction of η mesons from complex nuclei, a model calculation for the inclusive reaction is developed. The inclusive model includes only the quasifree process and is thus restricted to single hole excitations of the residual nuclei. The cross sections for the inclusive reactions are obtained from the amplitude of the exclusive reactions using the following steps; i) removing the final state interactions for the outgoing nucleon, ii) integrating the cross sections over all the unmeasured variables, and finally iii) including the contributions from all the nucleons inside of the nuclear targets.

The model shows large sensitivity to the use of different optical potentials for the outgoing η meson (results can change by up to 50% by choosing different optical potentials for η meson). The model uses one set of parameters for the effective Lagrangian. There are in fact different sets that reproduce the data of the elementary reactions and an investigation on the sensitivity of the present model to the use of different sets of parameters is needed. This will be studied in the near feature.

The present results indicate that quasifree processes are the main contributer to the inclusive photoproduction reactions but comparison with the available data seems to suggest possible contributions from other mechanisms.

Bibliography

[1] H.C. Chiang, E. Oset and L.C. Liu, Phys. Rev. **C44** (1991) 738.

[2] A.I. Lebedev and V.A. Tryasuchev, Physcs of Atomic Nuclei. Vol.58, No.4, 586 (1995).

[3] F.X. Lee, L.E Wright, C. Bennhold and L. Tiator, Nucl. Phys. **A603** (1996)345.

[4] R.C. Carrasco, Phys. Rev. **C48** (1993)2333.

[5] Lin Chen, Huan-ching Chiang, Phys. Lett. **B329**(1994)424.

[6] A. Hombach *et al.*, Z. Phys. **A352** (1995) 223.

[7] M. Roebig-Landau *et al.*, Phys.Lett **B373** (1996) 45.

[8] B. Krusche *et al.*, Phys. Lett. **B358** (1995) 40.

[9] Nimai C. Mukhopadhyay, J.-F. Zhang and M. Benmerrouche, hep-ph/9510307

[10] C.J. Horowitz and B.D. Serot, Nuc. Phys. **A368** (1986) 503.

Appendix 5.A Angular Integrals

In this appendix we give the results of the analytical calculations for the angular integrals of equation (5.6).

$$
\begin{aligned}
&< \mathcal{Y}^{s_f}_{0\frac{1}{2}\frac{1}{2}} \mid Y^{M_q}_{L_q}(\Omega)\, Y^{M_\eta}_{L_\eta}(\Omega) \mid \mathcal{Y}^{M_B}_{L_B\frac{1}{2}J_B} > \\
&\qquad = \frac{(-)^{1+J_B+M_\eta+M_q-s_f}}{4\pi} \hat{J}_B \hat{L}_\eta \hat{L}_q \hat{L}_B \begin{pmatrix} 1/2 & J_B & L_B \\ -s_f & M_B & s_f - M_B \end{pmatrix} \\
&\qquad\qquad \times \begin{pmatrix} L_\eta & L_q & L_B \\ 0 & 0 & 0 \end{pmatrix} \begin{pmatrix} L_\eta & L_q & L_B \\ M_\eta & M_q & M_B - s_f \end{pmatrix}
\end{aligned}
$$

$$
\begin{aligned}
&< \mathcal{Y}^{s_f}_{0\frac{1}{2}\frac{1}{2}} \mid Y^{M_q}_{L_q}(\Omega)\, Y^{M_\eta}_{L_\eta}(\Omega)\, \sigma^{-\mu} \mid \mathcal{Y}^{M_B}_{L_B\frac{1}{2}J_B} > \\
&= \sqrt{\frac{3}{8\pi^2}} (-)^{J_B+1/2+s_f-M_B} \hat{J}_B \hat{L}_\eta \hat{L}_q \hat{L}_B \begin{pmatrix} J_B & L_B & 1/2 \\ M_B & \mu - M_B + s_f & -s_f - \mu \end{pmatrix} \\
&\times \begin{pmatrix} L_\eta & L_q & L_B \\ 0 & 0 & 0 \end{pmatrix} \begin{pmatrix} L_\eta & L_q & L_B \\ M_\eta & M_q & M_B - s_f - \mu \end{pmatrix} \begin{pmatrix} 1 & 1/2 & 1/2 \\ \mu & s_f & -s_f - \mu \end{pmatrix} \qquad (5.8)
\end{aligned}
$$

where $\hat{L} = \sqrt{2L+1}$.

Chapter 6

Conclusions

Two different approaches are commonly used for describing the amplitudes for the interactions of the electromagnetic probes with complex nuclei. The first of these, which has been standard in the field of nuclear physics for a long time, is based on nonrelativistic quantum mechanics. This nonrelativistic approach uses Schrödinger wavefunctions to describe the nucleons involved in the reaction. The interaction terms are obtained via Foldy-Wouthuysen transformation of the relativistic Hamiltonian of the interaction of the probe with a free nucleon.

The second approach developed only recently, is based on and uses the principles of relativistic quantum mechanics and quantum field theory. In particular, this approach is closely connected with the development of the relativistic mean field theory of Walecka. The bound and continuum nucleons are described by Dirac wavefunctions while the interaction Hamiltonians are written in Lorentz covariant forms. There are some differences in the predictions of these two approaches for observables of the above reactions. To understand the source of these differences we have carried out detailed comparisons between these approaches.

We have described the effective Pauli reduction scheme of the relativistic amplitude for the knock-out contribution to (γ, p) and $(e, e'p)$ reactions. The reduction allows us to carry out comparisons between the relativistic and nonrelativistic calculations of the reaction observables. In this formalism the relativistic S-matrix is written in terms of nonrelativistic two-component wavefunctions and an effective interaction Hamiltonian involving strong potentials. The effective Hamiltonian is expanded in powers of $1/(E+M)$, where M is the nucleon mass and E is its total energy. In the limit $E \rightarrow M$ and ignoring the strong potentials, the first order interaction terms are exactly the same as those appearing in the usual nonrelativistic amplitudes. The nonrelativistic wavefunctions appearing in the amplitude are solutions of Schrödinger-like wave equations. Detailed comparisons between the relativistic and first-order nonrelativistic predictions for the observables show large differences between the two types of calculations. The shape and magnitude of the calculated cross sections are different and these differences are more pronounced in the spin observables. We stress that for the quasifree electron scattering reactions the strong potentials appear even in the first order interaction terms and improve the nonrelativistic calculations significantly. The inclusion of terms to second order in $1/M$ in the interaction Hamiltonian, without the nuclear medium corrections, does not lead to any substantial improvement in the agreement between the relativistic and nonrelativistic calculations. There is no indication that the medium uncorrected nonrelativistic calculations are coming toward agreement with the relativistic ones. When the medium corrections are taken into account the nonrelativistic calculations converge close to the relativistic results. This indicates that the essential difference between the relativistic and traditional nonrelativistic amplitudes is the absence in the latter of medium modifications of the interaction Hamiltonian as a consequence of the presence of the strong vector and scalar potentials.

These conclusions are further supported through an analysis based on the Foldy-Wouthuysen transformation of the relativistic Hamiltonian describing a photon interacting with a nucleon embedded in the nuclear medium. The nonrelativistic wavefunctions for the bound and continuum nucleons are solutions of the wave equation obtained as a result of the transformation. The scheme leads to a nonrelativistic amplitude calculated to the desired order in $1/M$. We use these amplitudes to carry out comparisons between relativistic and nonrelativistic calculations in the same way described above for the Pauli scheme. We find that the medium modifications in the second order calculations are important and their inclusion leads in general to better agreement with the relativistic calculations. However the convergence is not as efficient at this order as in the Pauli case. The reasons for this can be understood in terms of the formal differences between the structure of the nonrelativistic amplitudes obtained using this transformation as compared to the Pauli reduction case. The wavefunctions obtained through the FW reduction are different at each order in $1/M$, in contrast to the Pauli wavefunctions which are unchanged for all orders (recall that in the Pauli reduction only the interaction Hamiltonian is expanded).

The basic result of this part of thesis is that standard nonrelativistic calculations of the knock-out amplitudes do not properly take into account the strong medium modifications of the interaction Hamiltonian. We have clarified this point through a comparison based on nonrelativistic reduction of the relativistic amplitudes for two reactions involving interactions of real and virtual photons with nuclei, using both the Pauli and Foldy-Wouthuysen reduction schemes.

In the second part of this thesis a model for photoproduction of η mesons from complex nuclei is developed. Based on what has been learnt in the first part of this thesis, a relativistic approach is adopted. The nucleon wavefunctions are solutions of the Dirac equation. The η meson is described by solutions of the Klein-Gordon equation. The interactions between fields are introduced through a relativistic effective Lagrangian which has been used by Benmerrouche *et.al* (reference [6] in chapter IV) in the study of the elementary photoproduction reaction. The model includes the production of the η meson through formation of four spin $\frac{1}{2}$ and one spin $\frac{3}{2}$ resonances, nucleon Born and t-channel vector meson diagrams. The model is used to study the quasifree (γ, ηp) reactions on nuclear targets leading to discrete final states in the residual nuclei.

We have specified the energy region in which the reaction is mainly taking place through the formation of $S_{11}(1535)$ resonance. The kinematical region in which photoproduction cross section reaches its maximum value in the neighborhood of the reaction threshold is also identified. This is of experimental interest because of the low cross section for this reaction.

Comparison of contributions due to different diagrams has shown that within the photon energy region from near threshold up to 1.1 GeV, the $S_{11}(1535)$ resonance dominates the reaction. The other diagrams which have detectable individual contributions are proton, D_{13} resonance and vector meson poles (however the sum of these contributions is very small).

The final state interactions of the outgoing particles are included through distortion of their wavefunctions using appropriate optical potentials. The inclusion of the final state interactions affects both the cross sections and photon asymmetries. It results in large suppression of the cross sections and changes in the shape and magnitude of the asymmetries. The sensitivity of results to changes in the potentials, both for the nucleons and η meson, is studied. This study showed that results are strongly sensitive to η optical potentials; for several potentials which were tested, differences of up to $\sim$ 35% are observed in the resulting cross sections as well as photon asymmetries . On the other hand the results are much less sensitive to different choices of the potentials for the bound and continuum protons.

Comparison of the results of the present model with those of the nonrelativistic model calculations were carried out using the same kinematics as those in the recent work of Lee *et.al* (see reference [10] in chapter IV). Results of the relativistic calculations for the cross section have shapes close to those of nonrelativistic calculations but the magnitudes of our results are somewhat smaller. In contrast the photon asymmetries predicted by the two models differ significantly. The nonrelativistic plane wave calculations give large asymmetries which appear to be insensitive to the final state interactions of the outgoing particles. The relativistic model, on the other hand, predicts asymmetries which are small by comparison and which are strongly affected by the final state interactions of the outgoing particles.

There is need for experimental data for exclusive reactions on nuclei (currently non-existent), especially for the spin observables. These data can shed more light on the differences between the relativistic and nonrelativistic models.

The model is also used to calculate the cross sections for the inclusive photoproduction reactions in which only the outgoing η meson is detected. The present inclusive calculations include only contributions from the quasifree process and are thus restricted to single hole excitations of the residual nuclei. The calculations show large sensitivity of the inclusive cross sections to the use of different optical potentials for the outgoing η meson (results can change by up to $\sim 50\%$ by choosing different optical potentials). The model uses one set of parameters for the effective Lagrangian. Comparison of the results of the model for the inclusive reaction with the available experimental data indicates that quasifree processes are the main contributers to the inclusive photoproduction reactions, and seems to suggest possible contributions from other mechanisms.

In making the above statement it is assumed that the coupling constants as well as the η optical potentials used in the present calculations are reliable. There are in fact different sets of coupling constants that reproduce the data of the elementary reactions and an investigation of the sensitivity of the present model to the use of different sets of parameters is suggested. The uncertainty in the η optical potential calls for more theoretical work on the final state interactions of the η meson with nuclei. The next steps towards improving the present model at the tree level approximation are: removing the plane wave approximation used for the propagator by performing finite range calculations, and including the medium modifications of the propagators.